Micromechanics of particle-modified semicrystalline polymers

Citation for published version (APA):
Dommelen, van, J. A. W. (2003). *Micromechanics of particle-modified semicrystalline polymers*. [Phd Thesis 1 (Research TU/e / Graduation TU/e), Mechanical Engineering]. Technische Universiteit Eindhoven. https://doi.org/10.6100/IR562781

DOI:
10.6100/IR562781

Document status and date:
Published: 01/01/2003

Document Version:
Publisher’s PDF, also known as Version of Record (includes final page, issue and volume numbers)

Please check the document version of this publication:

- A submitted manuscript is the version of the article upon submission and before peer-review. There can be important differences between the submitted version and the official published version of record. People interested in the research are advised to contact the author for the final version of the publication, or visit the DOI to the publisher's website.
- The final author version and the galley proof are versions of the publication after peer review.
- The final published version features the final layout of the paper including the volume, issue and page numbers.

Link to publication

General rights
Copyright and moral rights for the publications made accessible in the public portal are retained by the authors and/or other copyright owners and it is a condition of accessing publications that users recognise and abide by the legal requirements associated with these rights.

- Users may download and print one copy of any publication from the public portal for the purpose of private study or research.
- You may not further distribute the material or use it for any profit-making activity or commercial gain
- You may freely distribute the URL identifying the publication in the public portal.

If the publication is distributed under the terms of Article 25fa of the Dutch Copyright Act, indicated by the “Taverne” license above, please follow below link for the End User Agreement:

www.tue.nl/taverne

Take down policy
If you believe that this document breaches copyright please contact us at:

openaccess@tue.nl

providing details and we will investigate your claim.

Download date: 04. Oct. 2023

Micromechanics of Particle-Modified Semicrystalline Polymers

This research was financially supported by the Dutch Polymer Institute (DPI).

CIP-DATA LIBRARY TECHNISCHE UNIVERSITEIT EINDHOVEN

Dommelen, Johannes A.W. van

Micromechanics of particle-modified semicrystalline polymers / by Johannes A.W. van Dommelen. – Eindhoven : Technische Universiteit Eindhoven, 2003
Proefschrift. – ISBN 90-386-2904-4
NUR 929
Trefwoorden: deformatie / eindige elementen methode / kristal plasticiteit /
meerschalige modellen / micromechanica / microstructuur /
semi-kristallijne polymeren / taaiheid
Subject headings: deformation / finite element method / crystal plasticity /
multiscale modeling / micromechanics / microstructure / semicrystalline polymers /
toughness

Copyright ©2003 by J.A.W. van Dommelen. All rights reserved.

This thesis was prepared with the LaTeX 2ε documentation system.
Reproduction: Universiteitsdrukkerij TU Eindhoven, Eindhoven, The Netherlands.

Micromechanics of Particle-Modified Semicrystalline Polymers

PROEFSCHRIFT

ter verkrijging van de graad van doctor
aan de Technische Universiteit Eindhoven,
op gezag van de Rector Magnificus, prof.dr. R.A. van Santen,
voor een commissie aangewezen door het College voor Promoties
in het openbaar te verdedigen
op vrijdag 4 april 2003 om 16.00 uur

door

JOHANNES ANTONIUS WILHELMUS VAN DOMMELEN

geboren te Eindhoven

Dit proefschrift is goedgekeurd door de promotoren:

prof.dr.ir. F.P.T. Baaijens
en
prof.dr.ir. H.E.H. Meijer

Copromotor:
dr.ir. W.A.M. Brekelmans

Contents

Summary **ix**

Notation **xi**

1 Introduction **1**
- 1.1 General introduction . . . 1
- 1.2 Toughening mechanism . . . 2
- 1.3 Modeling strategy and outline . . . 5

2 Toughening by local anisotropy **9**
- 2.1 Introduction . . . 9
- 2.2 Constitutive model . . . 11
- 2.3 Micromechanical models . . . 12
  - 2.3.1 Axisymmetric RVE . . . 13
  - 2.3.2 Multiparticle plane strain RVE . . . 15
  - 2.3.3 Three-dimensional geometry . . . 17
- 2.4 Effect of anisotropy . . . 18
  - 2.4.1 Sensitivity to local orientation field . . . 18
  - 2.4.2 Three-dimensional structure . . . 19
  - 2.4.3 Two-dimensional RVEs . . . 21
  - 2.4.4 Failure mechanisms . . . 23
- 2.5 Unidirectional anisotropy . . . 25
- 2.6 Influence of hardening . . . 26
- 2.7 Conclusions . . . 27

3 Hard particles versus soft particles **29**
- 3.1 Introduction . . . 29
- 3.2 Model description . . . 30
- 3.3 Rubber particles . . . 32
- 3.4 Hard particles . . . 35
- 3.5 Conclusions . . . 39

4 Composite inclusion model 41
- 4.1 Introduction 41
- 4.2 Material models 43
  - 4.2.1 Kinematics 44
  - 4.2.2 Crystalline phase 45
  - 4.2.3 Amorphous phase 48
- 4.3 Micromechanical model 49
  - 4.3.1 Composite inclusion 50
  - 4.3.2 Inclusion interaction law 51
- 4.4 Solution procedure 55
  - 4.4.1 Time-integration of plastic flow 56
  - 4.4.2 Boundary value problem 56
  - 4.4.3 Morphological texture update 58
- 4.5 High density polyethylene 58
- 4.6 Monotonic uniaxial compression 61
- 4.7 Loading cycles 68
- 4.8 Effect of crystallinity 71
- 4.9 Evolution of anisotropy 73
- 4.10 Conclusions 74

5 Bridge to the macroscopic level 77
- 5.1 Introduction 77
- 5.2 Influence of aggregate-size 78
- 5.3 Finite element implementation 80
  - 5.3.1 Tangent operator 80
  - 5.3.2 Subincrementation 82
  - 5.3.3 Finite element package 83
  - 5.3.4 Output 83

6 Intraspherulitic deformation 85
- 6.1 Introduction 85
- 6.2 Mesoscopic scale: composite inclusion model 87
  - 6.2.1 Deformation modes 87
  - 6.2.2 Intraspherulitic material 88
- 6.3 Macroscopic scale: spherulitic models 90
  - 6.3.1 Axisymmetric RVE 90
  - 6.3.2 Irregular plane strain RVE 91
- 6.4 Intraspherulitic deformation and stress 92
  - 6.4.1 Axisymmetry 92
  - 6.4.2 Plane strain 97
- 6.5 Comparison with the mesoscopic model 99

6.6 Influence of spherulite size for particle-modified systems 102
6.7 Conclusions 102

7 Particle-modified semicrystalline material 105
7.1 Introduction 105
7.2 Anisotropy of preferentially oriented material 106
7.2.1 Randomly oriented material 107
7.2.2 Transcrystallized material 108
7.3 Macroscopic models 109
7.4 Effect of transcrystallized anisotropy on toughness 111
7.5 Alternative microstructure 117
7.6 Conclusions 121

8 Conclusions and recommendations 123
8.1 Conclusions 123
8.2 Recommendations 126
8.2.1 Composite inclusion model 126
8.2.2 Spherulitic modeling 128
8.2.3 Particle-modified systems 128

A Composite inclusion model 131
A.1 Introduction 131
A.2 Taylor-inclusion model 132
A.3 Sachs-inclusion model 133
A.4 $\hat{\sigma}$-inclusion model 134
A.5 $\hat{U}$-inclusion model 134

Bibliography 137

Samenvatting 145

Dankwoord / Acknowledgements 147

Curriculum Vitae 149

Summary

To enhance the toughness of semicrystalline polymeric materials, it is common practice to blend these materials with rubber particles. The present-day notion of the toughening-mechanism in semicrystalline polymers is based on a criterion, which states that toughened material behavior occurs when the average interparticle matrix ligament thickness is smaller than a critical value. This value is considered as an intrinsic material property, and is attributed to thin layers of transcrystallized material appearing in the microstructural morphology. The objective of this work is to numerically investigate the influence of the microstructural morphology on the microscopic, mesoscopic, and macroscopic behavior of particle-modified semicrystalline materials, particularly the presupposed effect of the preferentially oriented layers.

The potential of local anisotropy around dispersed particles for enhancing the material properties is investigated using anisotropic Hill plasticity for an idealized semicrystalline material. The system, containing rubber particles, which are assumed to be cavitated and are represented by voids, is described by a finite element model of a representative volume element (RVE). The system contains a length parameter, which is the ratio of the average distance between particles and an intrinsic material characteristic distance. This length parameter is represented in the calculations by the presence of a layer of anisotropic matrix material around well-dispersed particles. The applicability of different RVE models for particle-modified semicrystalline materials is investigated using three-dimensional simulations as a reference. The calculations show that local anisotropy of matrix material enveloping voids replaces localization by dispersed shear yielding and changes the nature of the occurring hydrostatic stresses. However, to achieve these improvements, a radially oriented microstructure must be pursued that provides a sufficiently large amount of anisotropy. The efficiency of this mechanism is found to be affected by the presence of hard filler particles.

To investigate whether this anisotropy can be achieved by a transcrystallized microstructure, a micromechanically-based numerical model for the elasto-viscoplastic deformation and texture evolution of semicrystalline polymers is developed. For particle-modified polymeric systems, a distinction between three different scales is made. The constitutive properties of the material are identified at the microscopic scale for the individual crystallographic lamellae and amorphous layers. At the mesoscopic scale, an aggregate of individual phases is formed, which can be a spherulite or a sheaflike aggregate of preferentially oriented material. To bridge between those scales, an elasto-viscoplastic two-phase composite inclusion model is formulated. Each composite inclusion consists of a crystalline lamella which is assumed to plastically deform by crystallographic slip, and an amorphous layer. The local inclusion-averaged deformation and stress fields are related to the mesoscopic fields of the aggregate by an interaction law. Uniaxial compression of initially isotropic high density polyethylene (HDPE) is used to assess the applicability of various interaction laws. Based on this evaluation, a hybrid interaction law is selected, that compromises between local compatibility and local equilibrium.

A full micro–meso–macrolevel bridge is obtained by using an aggregate of composite inclusions in each integration point of a macroscopic finite element model. The multiscale model is employed to study the mechanics of intraspherulitic deformation for polyethylene. Finally, multiscale calculations are performed on particle-modified HDPE. The effect of a transcrystallized structure of matrix material versus randomly oriented material is examined. A limited effect of the preferential orientations is observed. Further improved properties in a specific loading direction are obtained for a hypothesized, partly flow-induced, microstructure.

Notation

In the following definitions, a Cartesian coordinate system with unit vector base $\{\boldsymbol{e}_1,\boldsymbol{e}_2,\boldsymbol{e}_3\}$ applies and following the Einstein summation convention, repeated indices are summed from 1 to 3.

Quantities

scalar	α; a; A
vector	$\boldsymbol{a} = a_i\,\boldsymbol{e}_i$
second order tensor	$\boldsymbol{\alpha} = \alpha_{ij}\,\boldsymbol{e}_i\otimes\boldsymbol{e}_j$; $\boldsymbol{A} = A_{ij}\,\boldsymbol{e}_i\otimes\boldsymbol{e}_j$
higher (nth) order tensor	${}^{n}\boldsymbol{\mathcal{A}} = A_{ij\ldots n}\,\boldsymbol{e}_i\otimes\boldsymbol{e}_j\otimes\ldots\otimes\boldsymbol{e}_n$
column	$\underset{\sim}{a}$
matrix	$\underline{A}$

Operations

multiplication	$c = ab$; $\boldsymbol{c} = a\boldsymbol{b}$; $\boldsymbol{C} = a\boldsymbol{B}$
dyadic product	$\boldsymbol{C} = \boldsymbol{a}\otimes\boldsymbol{b} = a_i b_j\,\boldsymbol{e}_i\otimes\boldsymbol{e}_j$
cross product	$\boldsymbol{c} = \boldsymbol{a}\times\boldsymbol{b}$
inner product	$c = \boldsymbol{a}\cdot\boldsymbol{b} = a_i b_i$; $\boldsymbol{C} = \boldsymbol{A}\cdot\boldsymbol{B} = A_{ij}B_{jk}\,\boldsymbol{e}_i\otimes\boldsymbol{e}_k$
double inner product	$\boldsymbol{C} = {}^{4}\boldsymbol{\mathcal{A}}:\boldsymbol{B} = A_{ijkl}B_{lk}\,\boldsymbol{e}_i\otimes\boldsymbol{e}_j$; $c = \boldsymbol{A}:\boldsymbol{B} = A_{ij}B_{ji}$
conjugate / transpose	$\boldsymbol{C}^{\mathrm{T}} = C_{ji}\boldsymbol{e}_i\otimes\boldsymbol{e}_j$
inverse	$\boldsymbol{A}^{-1}$
determinant	$\det(\boldsymbol{A}) = (\boldsymbol{A}\cdot\boldsymbol{e}_1)\cdot(\boldsymbol{A}\cdot\boldsymbol{e}_2)\times(\boldsymbol{A}\cdot\boldsymbol{e}_3)$

trace	$\mathrm{tr}(\boldsymbol{A}) = \boldsymbol{A} : \boldsymbol{e}_i \otimes \boldsymbol{e}_i = A_{ii}$
deviatoric part	$\boldsymbol{A}^{\mathrm{d}} = \boldsymbol{A} - \frac{1}{3}\mathrm{tr}(\boldsymbol{A})\boldsymbol{e}_i \otimes \boldsymbol{e}_i$
isochoric part	$\tilde{\boldsymbol{A}} = [\,\det(\boldsymbol{A})\,]^{-\frac{1}{3}}\boldsymbol{A}$
gradient operator	$\nabla = \boldsymbol{e}_i \frac{\partial}{\partial x_i}$
tensor derivative	$\frac{\mathrm{d}\boldsymbol{A}}{\mathrm{d}\boldsymbol{B}} = \frac{\mathrm{d}A_{ij}}{\mathrm{d}B_{lk}} \boldsymbol{e}_i \otimes \boldsymbol{e}_j \otimes \boldsymbol{e}_k \otimes \boldsymbol{e}_l$
absolute value	$\lvert a \rvert$
euclidean norm	$\lvert\lvert \boldsymbol{a} \rvert\rvert = \sqrt{\boldsymbol{a} \cdot \boldsymbol{a}}$
aggregate-volume-average	$\bar{a}$
RVE-volume-average	$\langle a \rangle$

Crystallographic notation

crystallographic direction, family	$[uvw]$, $\langle uvw \rangle$
crystallographic plane, family	(hkl), $\{hkl\}$
slip system, family	$(hkl)[uvw]$, $\{hkl\}\langle uvw \rangle$

Indices

inclusion	$(\cdot)^{\mathrm{I}}$
amorphous phase	$(\cdot)^{\mathrm{a}}$
crystalline phase	$(\cdot)^{\mathrm{c}}$
arbitrary phase	$(\cdot)^{\pi}$
interface (particle/matrix)	$(\cdot)^{\mathrm{i}}$
matrix	$(\cdot)^{\mathrm{m}}$
particle	$(\cdot)^{\mathrm{p}}$
elastic	$(\cdot)_{\mathrm{e}}$
plastic	$(\cdot)_{\mathrm{p}}$

CHAPTER ONE

Introduction

Abstract / A general introduction to particle-toughening of semicrystalline polymers is presented, as well as the basic concepts of the underlying hypothesized mechanism of toughening. An overview of the approach pursued for the numerical modeling of this mechanism, involving different length scales, is given.

1.1 General introduction

Semicrystalline polymeric materials are widely used in a range of engineering applications. Despite many advantages as low cost and weight, their application is limited by some unfavorable mechanical properties. An important point of concern is their often occurring brittle response. An empirical procedure for enhancing the toughness of these materials is to blend them with rubber particles. The present-day notion of the toughening mechanism in semicrystalline polymers is based on the criterion proposed by Wu (1985), which states that a sharp brittle–to–tough transition occurs for nylon/rubber blends when the average interparticle matrix ligament thickness Λ is reduced below the critical value $\Lambda_c = 0.3\ \mu$m, as is schematically shown in Figure 1.1. The critical value was shown to be independent of the rubber volume fraction and the particle size. Later on, similar interparticle distance effects have been observed for particle-modified polyethylene (Bartczak et al., 1999a) and poly(ethylene terephthalate) (Sánchez-Solís et al., 2000; Loyens and Groeninckx, 2002, 2003). The explanation offered by Wu for this transition addressed the mutual interaction of particle-disturbed stress fields, enhancing matrix yielding. Ramsteiner and Heckmann (1985) concluded that the energy-dissipating deformation mode for rubber-modified nylon is shear yielding. Borggreve et al. (1987) confirmed the existence of a critical interparticle distance for the brittle–to–tough transition, however questioned the physical explanation by Wu. Thereafter, a modified theory was proposed, in which the critical ligament thickness corresponds to a local plane strain–

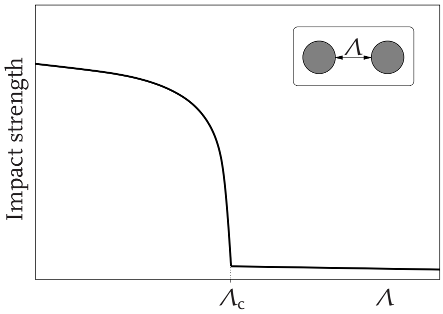

Figure 1.1 / Impact toughness of nylon/rubber blends vs. the average surface–to–surface interparticle ligament thickness Λ. Redrawn from Wu (1985).

to–plane stress transition in the matrix (Wu, 1988; Margolina and Wu, 1988). Based on their numerical investigations, Fukui et al. (1991) and Dijkstra and Ten Bolscher (1994) attributed the toughening effect to extensive shear yielding due to the interaction of stress fields. However, since the stress field theory is only effective for changes in geometrical ratios, it can be concluded that stress field interaction is incapable of explaining an absolute length scale such as a critical interparticle distance.

1.2 Toughening mechanism

A physical explanation of the absolute length parameter was offered by Muratoğlu et al. (1995a,c), who recognized the brittle–to–tough transition as a true material characteristic. It was attributed to thin layers of transcrystallized material, with a reduced plastic resistance, appearing in the microstructural morphology of particle-modified semicrystalline materials. Effectively, the crystallization behavior of the matrix is influenced by the particle/matrix interface, leading to a layer of parallel crystalline lamellae (Chacko et al., 1982; Rybnikář, 1981, 1989; Muratoğlu et al., 1995a,c; Bartczak et al., 1999a,b,c; Kim et al., 2001; Nam et al., 2001), with the crystalline planes having the lowest plastic resistance parallel to the interface. Figure 1.2 shows similar transcrystallized layers of polypropylene on a fiber (Schimanski, 2002). It was experimentally established that these transcrystalline layers have a well-defined thickness of approximately $\Lambda_c/2$. When the average matrix ligament thickness Λ is below the critical value Λ_c, the preferentially oriented material percolates through the system, bridging between the second-phase particles, as is depicted in Figure 1.3(a). Additionally, situations with $\Lambda \gg \Lambda_c$ are represented in Figure 1.3(b) and (c). The blended system consists of (i) rubber particles having a low modulus, (ii) preferentially oriented anisotropic matrix material enveloping the particles and (iii) the bulk matrix material having a randomly oriented structure and effectively having isotropic material properties. According to the toughening mechanism postulated

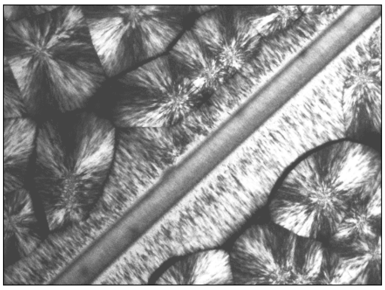

Figure 1.2 / Transcrystallized and spherulitic domains in a polypropylene matrix near an embedded fiber. Reproduced from Schimanski (2002).

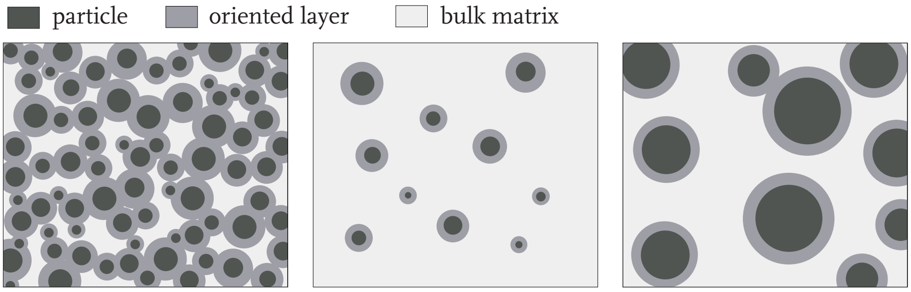

(a) $\Lambda \leq \Lambda_\mathrm{c}$ **(b)** $\Lambda \gg \Lambda_\mathrm{c}$ **(c)** $\Lambda \gg \Lambda_\mathrm{c}$

Figure 1.3 / Transcrystallized layers around second-phase particles for (a) material with a decreased plastic resistance percolating through the blend, enhancing the toughness (adopted from Muratoğlu et al. (1995c) and Bartczak et al. (1999a)), and for material with a brittle response, with (b) a smaller volume fraction and (c) the same volume fraction, but larger particles.

by Muratoğlu et al. (1995c), after cavitation of the second-phase rubber particles, the regions with a lowered yield resistance will promote large plastic deformation and thereby improve the toughness. This mechanism is schematically drawn in Figure 1.4. Tzika et al. (2000) used a micromechanical numerical model, with a staggered array of particles, to study the influence of preferentially oriented anisotropic layers, modeled with anisotropic Hill plasticity, on the deformation mechanisms under high triaxiality conditions. They observed plastic deformation in the matrix to occur diagonally away from the particles (i.e. in the matrix material between particles, parallel to the interfaces) for $\Lambda \leq \Lambda_\mathrm{c}$. The anisotropic matrix material was found to act as a nonstretching shell around the (cavitated) particles, leading to extensive shear yielding.

Bartczak et al. (1999a,b) generalized the Wu criterion to high density polyethylene (HDPE) and showed the critical interparticle distance ($\Lambda_\mathrm{c} = 0.6\ \mu\mathrm{m}$) to be an intrinsic

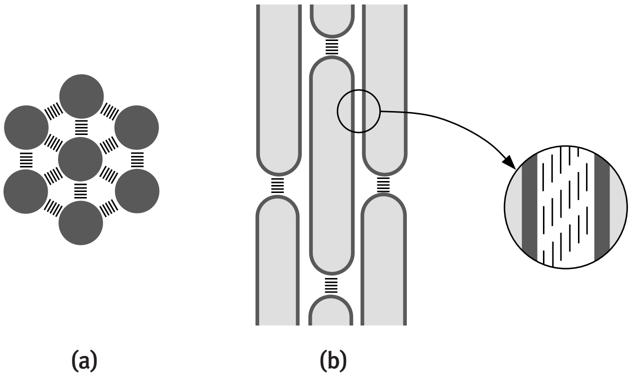

Figure 1.4 / Schematic illustration of the toughening mechanism in a particle-modified semicrystalline material, with (a) the initial configuration and (b) a uniaxially deformed state. The parallel lines denote slip planes with a low shear yield strength. Redrawn from Muratoğlu et al. (1995c) and Bartczak et al. (1999a).

property of the matrix material, thereby opening the possibility of using mineral fillers for the toughening of semicrystalline polymers, the advantage of which would be an improved modulus of the blend, as schematically indicated in Figure 1.5. They argued that

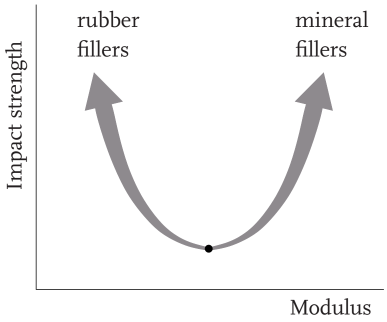

Figure 1.5 / Influence of soft (rubber) vs. hard (mineral) particles on the mechanical properties. Schematically drawn after Bartczak et al. (1999b).

debonding of hard filler particles could be an alternative for the cavitation of the rubbery phase. However, the Bartczak et al. results showed a distinct effect of processing conditions on the toughness obtained. The importance of process conditions was demonstrated by Schrauwen et al. (2001a,b, 2002), who found toughness to be dominated by flow-induced effects, see Figure 1.6. By using calcium carbonate filler particles in a nylon-6 matrix, Wilbrink et al. (2001) did not obtain the tough response of nylon/rubber

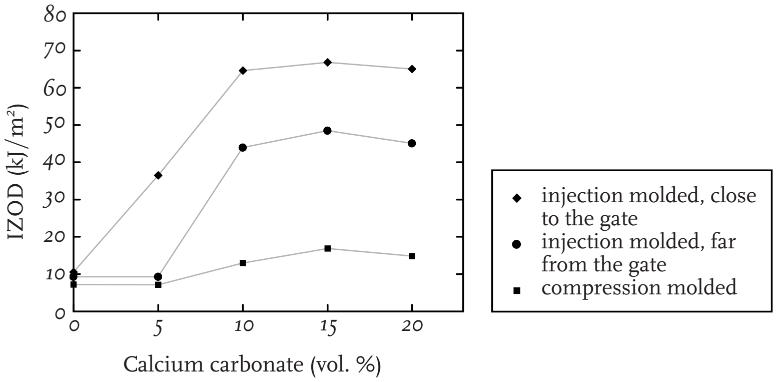

Figure 1.6 / Influence of processing conditions on toughness. Reproduced from Schrauwen et al. (2002).

blends, as was reported by Muratoğlu et al. (1995c,b), and attributed this to the development of triaxial stresses. A four times increase of the Izod impact energy was obtained by Thio et al. (2002) by incorporation of calcium carbonate particles in polypropylene, reportedly resulting from combined mechanisms of crack deflection and local plastic deformation of interparticle ligaments. Similar results have been obtained by Zuiderduin et al. (2003).

1.3 Modeling strategy and outline

The route to toughness enhancement of semicrystalline polymers, in the above context, is schematically shown in Figure 1.7. It is based on the hypothesis that local anisotropy, induced by a specific microstructure, which results from preferred crystallization of polymeric material, leads to macroscopically tough behavior. The potential validity of this hypothesis is examined by methods of micromechanical modeling. Thereby, the crystallization behavior is left out of consideration, and the starting-point is an assumed microstructure of a particle-modified system.

The deformation of polymeric materials, and thus also their either brittle or tough responses, are the result the interplay of various effects and mechanisms at different levels, such as for example (Michler, 1999) chain scission, microyielding, microcavitation, crazing, shear band formation, crack initiation and propagation, and fracture. For semicrystalline materials, also phenomena as interlamellar slip and intralamellar deformation mechanisms as crystallographic slip, twinning, and stress-induced martensitic transformation play a role (e.g. Petermann and Ebener, 1999; G'Sell and Dahoun, 1994; Lin and Argon, 1994). A quantitative prediction of toughness would require a coupled

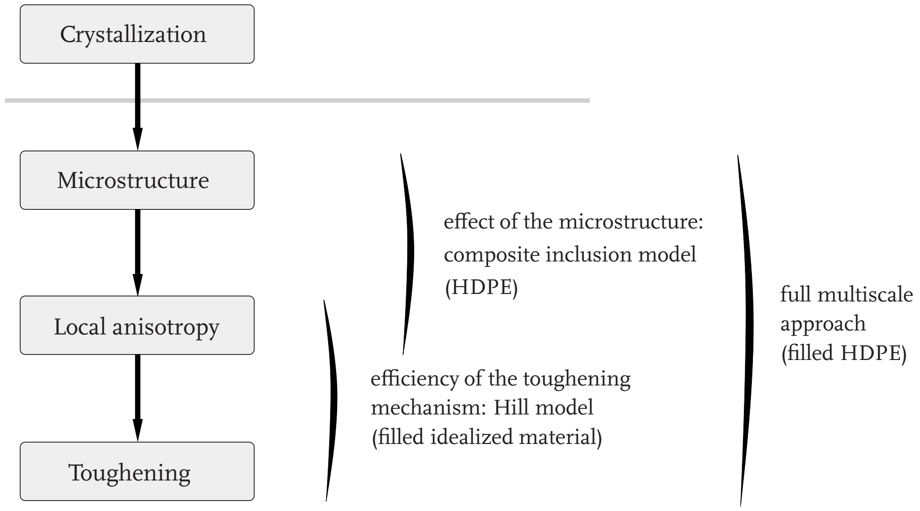
Crystallization
Microstructure
Local anisotropy
Toughening
effect of the microstructure: composite inclusion model (HDPE)
efficiency of the toughening mechanism: Hill model (filled idealized material)
full multiscale approach (filled HDPE)

Figure 1.7 / Hypothesized route to toughness and the modeling strategy.

and detailed modeling of the various deformation mechanisms and criteria for the different failure modes, which is at present still not feasible. In this thesis, the influence of the microstructure on the qualitative individual occurrence of some of these phenomena, or the conditions that may induce them, is investigated.

First, in Chapter 2, a micromechanical investigation of the potential of local anisotropy around dispersed particles for enhancing the material properties is presented. Calculations are performed on an idealized semicrystalline material, blended with rubber particles, which are assumed to be cavitated and are represented by voids. The system contains a scale parameter, which is the ratio of the average distance between particles and a critical distance. This length parameter is represented in the calculations by the relative thickness of an anisotropic layer around the particles. The simulations on the idealized polymeric material are used to investigate the applicability of various types of RVE models for particle-modified semicrystalline materials. Furthermore, with these calculations, it is ascertained (i) whether local anisotropy can potentially improve the toughness of rubber-modified systems; (ii) what is the occurring effect of anisotropy that may improve the toughness; and (iii) what type of anisotropy (i.e. mesoscopic morphology) would be required.

Simulations on a three-dimensional structure show a distinct influence of the local anisotropy on the triaxial stress field. This effect is also captured by a simplified axisymmetric RVE model of a staggered array of particles. However, for the consequence of anisotropy for the deformation mechanisms, the irregularity of the microstructure plays a crucial role. A two-dimensional multiparticle plane strain RVE with an irregular stacking of particles is used to investigate this effect. Simulations with both the axisymmetric and the multiparticle RVEs, show that local anisotropy of the matrix material around the particles can effectively replace localization by dispersed shear yielding and change the occurring hydrostatic stresses, potentially leading to toughened material behavior. However, to achieve these improvements, a morphology must be pursued with a radially oriented structure around the dispersed particles and it should, moreover, provide a sufficiently large amount of anisotropy. Furthermore, the possibility of using mineral fillers, rather than low-modulus rubber, for the toughening of semicrystalline polymers is evaluated in Chapter 3. The presence of hard, easily debonding, particles is found to affect the anisotropy-induced toughening mechanism.

Thereafter, to investigate whether the above-mentioned requirements can be achieved by a transcrystallized microstructure, a micromechanically-based numerical model for the elasto-viscoplastic deformation and texture evolution of semicrystalline polymers is developed in Chapter 4. For particle-modified polymeric systems, a distinction between three different scales is made, as is schematically depicted in Figure 1.8. The constitutive properties of the material are identified at the microscopic scale. At this scale, the individual crystallographic lamellae and amorphous layers determine the local material response. At the mesoscopic scale, an aggregate of individual phases is formed, which can be a spherulite or a sheaflike aggregate of preferentially oriented material. To bridge between those scales, an elasto-viscoplastic two-phase composite inclusion model is formulated. Each composite inclusion consists of a crystalline lamella which is assumed to plastically deform by crystallographic slip, and an amorphous layer, for which plastic flow

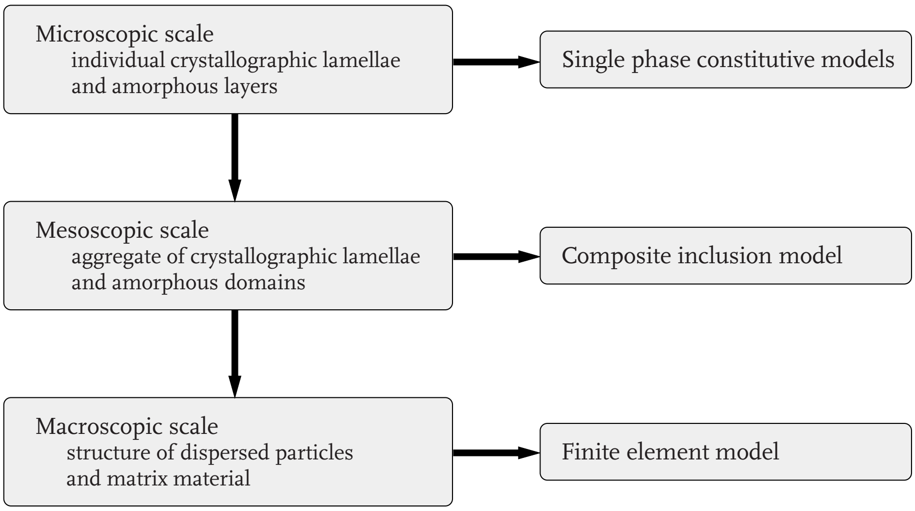
Microscopic scale
individual crystallographic lamellae
and amorphous layers
Single phase constitutive models
Mesoscopic scale
aggregate of crystallographic lamellae
and amorphous domains
Composite inclusion model
Macroscopic scale
structure of dispersed particles
and matrix material
Finite element model

Figure 1.8 / Different scales which can be identified in particle-toughened semicrystalline polymeric systems.

is modeled as a rate-dependent process with strain hardening resulting from molecular orientation. The local inclusion-averaged deformation and stress fields are related to the mesoscopic fields of the aggregate by an interaction law. Due to the anisotropy of the materials under investigation, the proper choice of this interaction law, bridging between the microscopic and the mesoscopic scales, is crucial. The interaction law should compromise between local compatibility and local equilibrium, with as extreme exponents the classical Taylor and Sachs models. The uniaxial compression of initially isotropic HDPE is used to assess the applicability of various interaction laws. A hybrid interaction law is chosen, which constitutes an intermediate approach between the Taylor and Sachs limits.

Subsequently, some aspects of the finite element implementation of the composite inclusion model, coupling all relevant length scales, are presented in Chapter 5. The mechanical behavior for an integration point is given by the average response of an entire aggregate of composite inclusions. This multiscale model is used to study the mechanics of intraspherulitic deformation and stress for polyethylene in Chapter 6. At the macroscopic scale, for particle-modified materials, a structure of dispersed particles and matrix material can be identified. In Chapter 7, this system is modeled by a finite element approach using different representative volume elements, as suggested by the anisotropic Hill simulations in Chapter 2. The effect of a transcrystallized structure of matrix material versus randomly oriented material on both mesoscopic and microscopic results is examined. A limited effect of the preferential orientations is observed. Further improved properties are obtained for a hypothesized, partly flow-induced, microstructure, if loaded in the appropriate direction. Finally, in Chapter 8, the main conclusions are recapitulated and some recommendations for future developments are discussed.

Chapter two

Toughening by local anisotropy[1]

Abstract / In this chapter, the potential of local anisotropy for the toughening of voided semicrystalline polymeric materials is investigated. The matrix material is modeled within the framework of anisotropic Hill plasticity with a rate-dependent and hardening yield stress. The applicability of different two-dimensional models is assessed by comparison to three-dimensional simulations with irregularly dispersed voids. A reduced plastic shear resistance of radially oriented material is found to be effective in inducing extensive delocalized shear deformations and alters the location of the peak tensile hydrostatic stresses.

2.1 Introduction

To enhance the toughness of semicrystalline polymers, it is common practice to blend these materials with rubber particles. The present-day notion of the toughening mechanism in these materials is expressed in the criterion proposed by Wu (1985), which states that a sharp brittle–to–tough transition occurs for nylon/rubber blends when the average interparticle matrix ligament thickness Λ is reduced below a critical value Λ_c. A physical explanation of the existence of an absolute length parameter was offered by Muratoğlu et al. (1995c,a), who recognized the brittle–to–tough transition as a true material property. It was attributed to thin layers of preferentially oriented material, with a reduced plastic resistance, appearing in the microstructural morphology of particle-modified semicrystalline materials. When the actual average matrix ligament thickness is below the critical value, the favorably oriented material percolates through the system, bridging between the second-phase particles. A blended system consists of (i) rubber particles having a low modulus, (ii) preferentially oriented anisotropic matrix material enveloping the particles and (iii) the bulk matrix material having a randomly oriented structure and with effectively isotropic material properties.

---

[1] This chapter is reproduced from Van Dommelen et al. (2003b), Van Dommelen et al. (2002a), and Van Dommelen et al. (2002b).

In this chapter, a micromechanical investigation is presented of the potential of local anisotropy around dispersed cavitated particles for enhancing material properties. Generally, particle-modified systems intrinsically have a three-dimensional structure. Fully three-dimensional numerical analyses, however, are extremely computationally demanding. Detailed simulations involving for example nonspherical particle geometries, a debonding algorithm, a realistic micromechanically-based constitutive model and/or failure criteria, require the simplification to computationally two-dimensional configurations, which restrict the analysis to either a regular stacking of particles (e.g. Socrate and Boyce, 2000; Tzika et al., 2000) or irregularly dispersed cylindrically shaped geometries (e.g. Smit et al., 1998, 1999). Since, in the current investigation, a relatively efficient Hill plasticity model is used for the anisotropic behavior of idealized material, in combination with the assumption of a spherically voided structure, three-dimensional simulations on irregular structures are feasible. These three-dimensional calculations, with either fully isotropic matrix material or strongly anisotropic material, will be taken as a reference for assessing the applicability of an axisymmetric model with a staggered array of voids and a multiparticle plane strain model having an irregular structure.

Calculations are performed on idealized semicrystalline materials, blended with rubber particles, which are assumed to be cavitated and are represented by spherical voids. The system contains a length parameter, which is the ratio of the average distance between voids and a critical distance. This length parameter is represented in the calculations by the thickness of an anisotropic layer around the voids. Each model is subjected to constant strain rate tension. Simulations on a three-dimensional structure show a distinct effect of local anisotropy on the triaxial stress field. This effect is also captured by a simplified axisymmetric model of a staggered array of voids. However, for the effect of anisotropy on the deformation mechanisms, the irregularity of the microstructure plays a crucial role. A two-dimensional irregular plane strain model is used to investigate this effect. Simulations with both the axisymmetric and the plane strain models, show that a local anisotropy of matrix material around the voids can potentially effectively transform localization into dispersed shear yielding and change the occurring hydrostatic stresses, leading to toughened material behavior. However, to achieve these improvements, a morphology must be pursued that has a radially oriented structure around the dispersed particles and provides a sufficiently large amount of anisotropy.

2.2 Constitutive model

In this chapter, the potential of plastic anisotropy for enhancing the toughness of semicrystalline polymeric materials is investigated. For this purpose, an idealized polymeric material is modeled by isotropic elasticity (characterized by a Young's modulus E^{m} and a Poisson's ratio ν^{m}) and anisotropic plasticity. During yield behavior, the anisotropic Hill yield criterion (Hill, 1950) is satisfied:

$$F(\sigma_{22}-\sigma_{33})^2+G(\sigma_{33}-\sigma_{11})^2+H(\sigma_{11}-\sigma_{22})^2+2L\sigma_{23}^2+2M\sigma_{13}^2+2N\sigma_{12}^2=\sigma_{\mathrm{y}}^2, \tag{2.1}$$

where σ_{ij} are stress components with respect to a local material vector basis and the anisotropic constants F, G, H, L, M and N are given by

$$F=\frac{1}{2}\left(\frac{1}{R_{22}^2}+\frac{1}{R_{33}^2}-\frac{3}{R_{11}^2}\right)\quad;\quad G=\frac{1}{2}\left(\frac{1}{R_{11}^2}+\frac{1}{R_{33}^2}-\frac{1}{R_{22}^2}\right)\quad; \tag{2.2}$$

$$H=\frac{1}{2}\left(\frac{1}{R_{11}^2}+\frac{1}{R_{22}^2}-\frac{1}{R_{33}^2}\right)\quad;\quad L=\frac{3}{2R_{23}^2}\quad;\quad M=\frac{3}{2R_{13}^2}\quad;\quad N=\frac{3}{2R_{12}^2}. \tag{2.3}$$

The constants R_{11}, R_{22} and R_{33} are the ratios of the actual tensile yield strength values of the anisotropic material to the actual virtual bulk tensile yield strength, σ_{y}. The constants R_{12}, R_{13} and R_{23} are the ratios of the yield strength values in shear to the shear yield strength τ_{y} of the virtual bulk material, with $\tau_{\mathrm{y}}=\sigma_{\mathrm{y}}/\sqrt{3}$. The Hill yield criterion was previously used for anisotropic polymeric material by Kobayashi and Nagasawa (1966) and Tzika et al. (2000). Here, a linear dependency of the yield strength σ_{y} on the effective plastic deformation measure $\tilde{\varepsilon}_{\mathrm{p}}$ and a power law dependency of σ_{y} on the corresponding rate $\dot{\tilde{\varepsilon}}_{\mathrm{p}}$ are assumed for the polymeric material:

$$\sigma_{\mathrm{y}}=\sigma_{\mathrm{y}_0}\left\{h\tilde{\varepsilon}_{\mathrm{p}}+q^{\frac{1}{n}}\left[1+\left(\frac{\dot{\tilde{\varepsilon}}_{\mathrm{p}}}{q\dot{\gamma}_0}\right)^2\right]^{\frac{1}{2n}}\right\}, \tag{2.4}$$

where σ_{y_0} is the reference yield strength, h is the linear hardening parameter and n is the stress exponent of the strain rate. The evolution of the yield stress with plastic deformation and strain rate is shown in Figure 2.1. A rate-independent contribution is introduced for strain rate values which are considerably smaller than the reference strain rate $\dot{\gamma}_0$, controlled by the parameter q. The plastic strain measure $\tilde{\varepsilon}_{\mathrm{p}}$ and the corresponding rate are, for anisotropic plasticity, assumed to be given by:

$$\tilde{\varepsilon}_{\mathrm{p}}=\int_0^t\dot{\tilde{\varepsilon}}_{\mathrm{p}}\,\mathrm{d}t\quad;\quad\dot{\tilde{\varepsilon}}_{\mathrm{p}}=\frac{\boldsymbol{\sigma}:\dot{\boldsymbol{\varepsilon}}_{\mathrm{p}}}{\sigma_{\mathrm{y}}}, \tag{2.5}$$

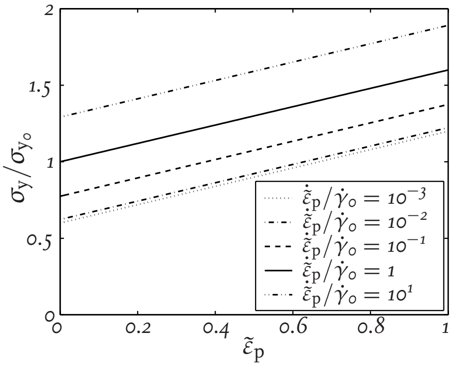

Figure 2.1 / The dependence of the yield stress on the plastic strain rate and the evolution with plastic deformation, with $h = 0.6$, $n = 9$ and $q = 10^{-2}$.

where $\boldsymbol{\sigma}$ is the Cauchy stress tensor and $\dot{\boldsymbol{\varepsilon}}_p$ is the plastic rate of deformation tensor. The material parameters that are used for the investigation of the effect of local anisotropy in particle-modified polymeric materials are summarized in Table 2.1. As mentioned earlier, the Equations (2.1)–(2.3), with the anisotropic strength ratios R_{ij}, are applied in a local coordinate system. The transcrystallized material around the voids is assumed to have a reduced plastic resistance with respect to the local 12 and 13 shear components (at the void/matrix interface, the 1-direction is defined to be perpendicular to the interface), and the reduction is controlled by the adjustable parameter ζ.

E^m [GPa]	ν^m	σ_{y_0} [MPa]	h	$\dot{\gamma}_0$ [s^{-1}]	n	q
1	0.45	25	0.6	10^{-3}	9	10^{-2}

R_{11}	R_{22}	R_{33}	R_{12}	R_{13}	R_{23}
1	1	1	$1/\zeta$	$1/\zeta$	1

Table 2.1 / Material parameters for a fictitious polymer matrix.

2.3 Micromechanical models

For particle-toughened materials, a structure of dispersed particles (here represented by voids) and matrix material can be identified. The system is described by a finite element model of a representative volume element (RVE). The particle-modified system, having a three-dimensional nature, is simplified to a computationally two-dimensional RVE, for which two different approaches are used.

For an adequate representation of the triaxial stress state around a void, an axisymmetric RVE is used, as suggested by Socrate and Boyce (2000) and Tzika et al. (2000). However, because of the regular void stacking associated to such RVEs, important effects as sequential yielding of the matrix material between the different voids (Smit et al., 1999) cannot be accounted for. In order to capture the essentially irregular nature of a system of dispersed voids, also a plane strain RVE is used. To validate the use of the simplified two-dimensional models, a comparison is made with three-dimensional calculations.

2.3.1 Axisymmetric RVE

An axisymmetric RVE model of a staggered array of voids (referred to as the *SA model*) is considered, which was previously used for the study of the micromechanics of particle-toughened polymers by Socrate and Boyce (2000) and by Tzika et al. (2000) and which resembles a body centered tetragonal stacking of voids. A schematic representation of the unit cell, with $L_o = R_o$, is shown in Figure 2.2. The axis of rotational symmetry, as well as the loading direction are horizontal. The RVE is subjected to anti-symmetry conditions (with respect to point M) along the outer radius, which were introduced by Tvergaard (1996, 1998). Axial compatibility along the radial boundary Γ_{34} is written as

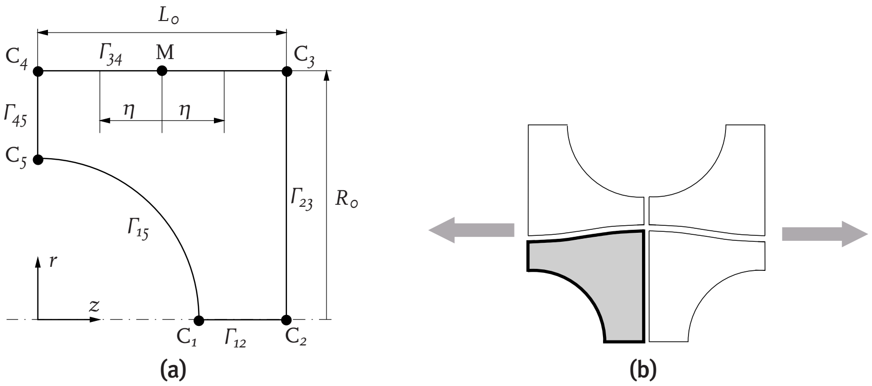

Figure 2.2 / (a) Schematic visualization of an axisymmetric RVE model of a staggered array of voids (Socrate and Boyce, 2000; Tzika et al., 2000) and (b) its position with respect to three neighboring RVEs in a deformed state.

$$u_z(z_o|_M - \eta) + u_z(z_o|_M + \eta) = 2u_z|_M. \tag{2.6}$$

The combined cross-sectional area of neighboring cells is assumed to remain constant along the axial coordinate:

$$[R_0 + u_r(z_0|_{\mathrm{M}} - \eta)]^2 + [R_0 + u_r(z_0|_{\mathrm{M}} + \eta)]^2 = 2[R_0 + u_r|_{\mathrm{M}}]^2. \tag{2.7}$$

Symmetry conditions along the right and left boundaries are written as

$$u_z|_{\Gamma_{23}} = u_z|_{\mathrm{C}_2} \tag{2.8}$$

and

$$u_z|_{\Gamma_{45}} = u_z|_{\mathrm{C}_5}, \tag{2.9}$$

respectively. Since the axis of rotational symmetry coincides with boundary Γ_{12}, the following condition is imposed on this boundary:

$$u_r|_{\Gamma_{12}} = 0. \tag{2.10}$$

The axisymmetric RVE is subjected to tension at a macroscopically constant strain rate:

$$u_z|_{\mathrm{C}_2} - u_z|_{\mathrm{C}_5} = L_0[\exp(\dot{\varepsilon}t) - 1], \tag{2.11}$$

where the deformation rate $\dot{\varepsilon}$ is set equal to the material reference shear rate $\dot{\gamma}_0$ in Equation (2.4).

The finite element mesh of the axisymmetric SA model, with void fraction $f = 0.2$, is visualized in Figure 2.3(a). In each integration point of the 196 four-noded bilinear elements, a local coordinate system is generated. Tzika et al. (2000) used a heat transfer analysis to obtain these orientations, where the local 1-direction corresponds to the direction of the heat flux vector. Here, a similar procedure is used. The 2-directions are chosen

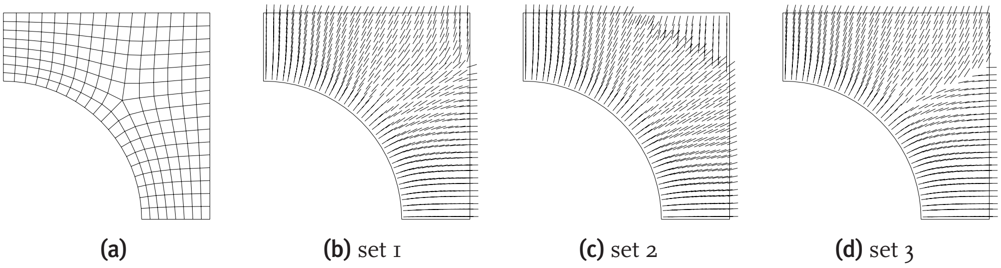
(a) **(b)** set 1 **(c)** set 2 **(d)** set 3

Figure 2.3 / (a) Finite element mesh and (b)–(d) local material orientations for the axisymmetric SA model.

perpendicular to the *1*-direction and in the plane of the mesh. The set of orientations that is obtained is referred to as set 1. The resulting field of material *1*-directions is perpendicular to the void/matrix interface, parallel to the left and lower symmetry boundaries and satisfies anti-symmetric compatibility conditions along the radial boundary. Additionally, two more sets of orientations are used, satisfying these conditions, as shown in Figure 2.3(c)–(d). Although the differences between these orientation sets seem to be small, the influence on the deformation mode that is obtained is substantial, as will be demonstrated further on.

2.3.2 Multiparticle plane strain RVE

To account for the irregular nature of particle-dispersed systems, a plane strain RVE with randomly dispersed voids (referred to as the *RD model*) is used. In Figure 2.4, a schematic illustration of this RVE is shown, as well as its arrangement with respect to the neighboring RVEs. The periodicity assumption requires full compatibility of each opposite boundary pair. The corresponding kinematic and natural boundary tyings (Smit et al., 1998) for related points on opposite boundaries are given by:

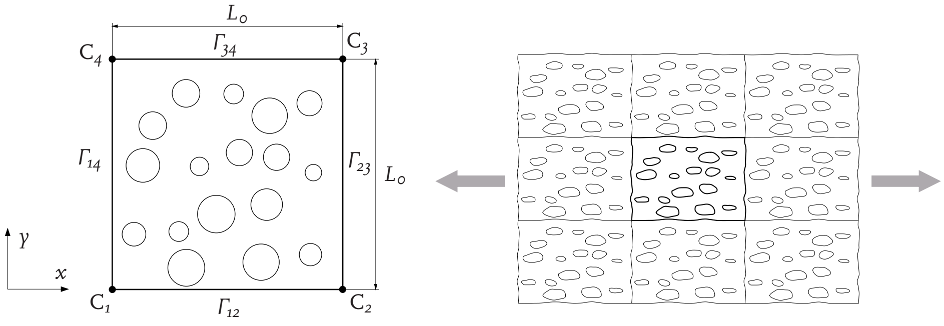

(a) (b)

Figure 2.4 / (a) Schematic visualization of a multiparticle plane strain RVE (Smit et al., 1998) and (b) its position with respect to neighboring RVEs in a deformed state.

$$\boldsymbol{u}|_{\Gamma_{34}} - \boldsymbol{u}|_{C_4} = \boldsymbol{u}|_{\Gamma_{12}} - \boldsymbol{u}|_{C_1}; \tag{2.12}$$

$$\boldsymbol{u}|_{\Gamma_{14}} - \boldsymbol{u}|_{C_1} = \boldsymbol{u}|_{\Gamma_{23}} - \boldsymbol{u}|_{C_2}; \tag{2.13}$$

$$\boldsymbol{\sigma}\cdot\boldsymbol{n}|_{\Gamma_{12}} = -\boldsymbol{\sigma}\cdot\boldsymbol{n}|_{\Gamma_{34}}; \tag{2.14}$$

$$\boldsymbol{\sigma}\cdot\boldsymbol{n}|_{\Gamma_{14}} = -\boldsymbol{\sigma}\cdot\boldsymbol{n}|_{\Gamma_{23}}, \tag{2.15}$$

where $\boldsymbol{n}$ denotes the outward unit normal of the boundary. A tensile loading condition in x-direction is prescribed:

$$u_x|_{C_2} - u_x|_{C_1} = L_0[\exp(\dot{\varepsilon}t) - 1], \tag{2.16}$$

where $\dot{\varepsilon}$ is set equal to the reference strain rate $\dot{\gamma}_0$ of the material. Furthermore, rotations are prevented by the following condition for the vertices C_1 and C_2:

$$u_y|_{C_1} = u_y|_{C_2}. \tag{2.17}$$

The relative displacements of C_4 are unspecified and follow from the analysis, whereas the displacements of C_3 are tied to the other vertices.

A structure with 20 volume percent irregularly dispersed voids is generated using a procedure from Hall (1991) and Smit et al. (1999). In order to obtain initially straight boundaries, no void is allowed to cross a boundary. The mesh with 2,622 four-noded bilinear plane strain elements is shown in Figure 2.5(a). A local orientation field is generated by taking the local 1-direction perpendicular to the closest void/matrix interface, taking into account the periodicity of the structure, and is shown in Figure 2.5(b). The obtained orientation field resembles orientation set 2 for the axisymmetric model. Since for this RVE, the results obtained are largely influenced by the irregular geometry of the structure, the RD model is qualitatively less sensitive to the choice of orientations than the SA model.

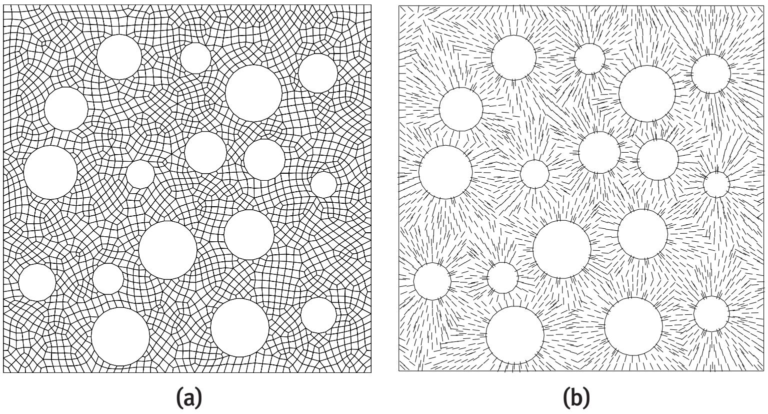

Figure 2.5 / (a) Finite element mesh and (b) local material orientations for the multiparticle plane strain RVE.

2.3.3 Three-dimensional geometry

The results obtained with the RVE models previously discussed are validated by comparison with three-dimensional calculations. To this end, a three-dimensional cube, schematically visualized in Figure 2.6(a), containing an irregular arrangement of 48 spherical voids, with volume fraction $f = 0.2$, as shown in Figure 2.6(b), is subjected to uniaxial tension in x-direction. The boundaries with their normals in the x-direction are required to remain planar:

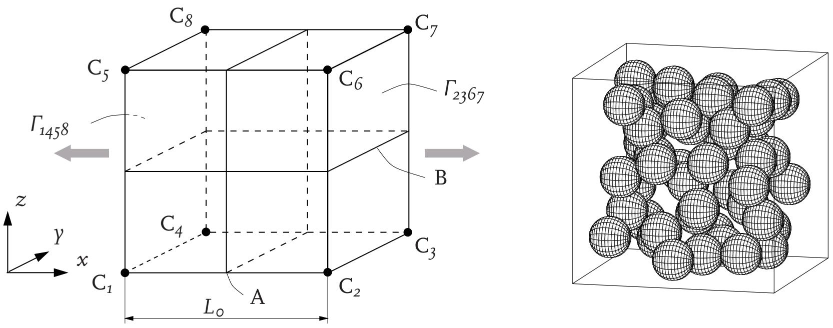

(a) (b)

Figure 2.6 / (a) Schematic visualization of the three-dimensional geometry with the position of two cross-sections and (b) the void arrangement.

$$u_x|_{\Gamma_{1458}} = u_x|_{C_1}; \tag{2.18}$$

$$u_x|_{\Gamma_{2367}} = u_x|_{C_2}. \tag{2.19}$$

The model is loaded in tension at a macroscopically constant strain rate:

$$u_x|_{C_2} - u_x|_{C_1} = L_0[\exp(\dot{\varepsilon}t) - 1], \tag{2.20}$$

with $\dot{\varepsilon} = \dot{\gamma}_0$. Additionally, rotations around the x-axis are suppressed:

$$u_y|_{C_5} = u_y|_{C_1}. \tag{2.21}$$

Results will be presented in two cross-sections, either perpendicular (A) or parallel (B) to the tensile direction, as defined in Figure 2.6(a). Figures 2.7(a) and (c) show three-dimensional views of the cross-sections. Moreover, in Figures 2.7(b) and (d) the mesh, containing 41,086 ten-noded quadratic tetrahedron elements, is shown in cross-section A and B, respectively. The local 1-directions are again taken perpendicular to the closest void/matrix interface.

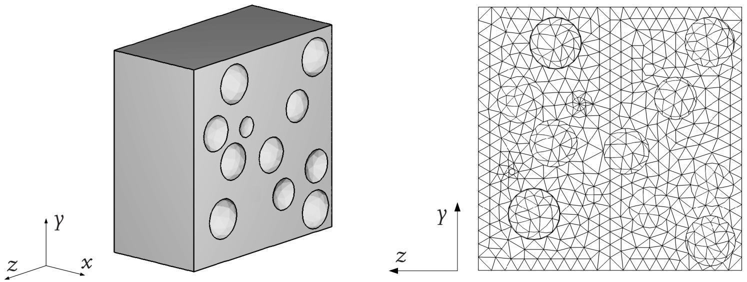

(a) cross-section A **(b)** cross-section A

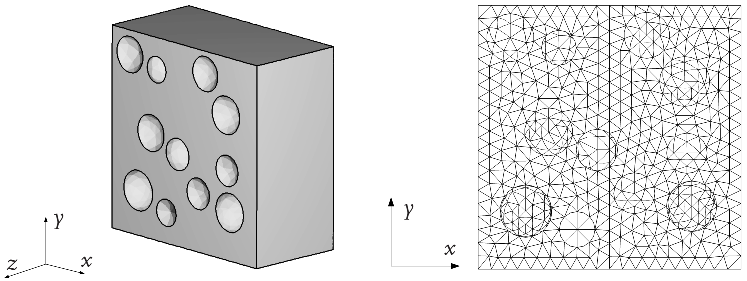

(c) cross-section B **(d)** cross-section B

Figure 2.7 / Cross-sections and the finite element mesh of the three-dimensional geometry.

2.4 Effect of anisotropy

The constitutive behavior and micromechanical models previously discussed have been implemented in the finite element package ABAQUS (HKS, 2001) to study the potential of local anisotropy enveloping dispersed voids for the toughening of semicrystalline polymers. In this section, the results are presented. First, the effect of the choice for a set of local orientations is investigated for the SA model. Thereafter, the effect of large anisotropy versus isotropy is studied for the three-dimensional configuration. The applicability of the SA and the RD model is validated by comparison to the three-dimensional calculations. The potential of toughening by local anisotropy is investigated by using different amounts of anisotropy in both the SA and the RD model.

2.4.1 Sensitivity to local orientation field

In the previous section, for the axisymmetric SA model, different sets of orientations have been presented, which are used for the local principal anisotropy directions. Here, the effect of a specific choice for these local orientations on the deformation obtained is demonstrated. Figure 2.8 shows the model sensitivity of the magnitude of plastic de-

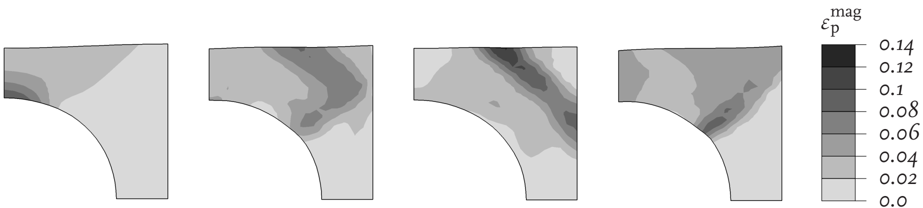

(a) $\zeta = 1$ **(b)** $\zeta = 5$, set 1 **(c)** $\zeta = 5$, set 2 **(d)** $\zeta = 5$, set 3

Figure 2.8 / The magnitude of plastic deformation, $\varepsilon_{\mathrm{p}}^{\mathrm{mag}}$, at $\dot{\varepsilon}t = 0.05$.

formation, $\varepsilon_{\mathrm{p}}^{\mathrm{mag}} = \sqrt{\frac{2}{3}\boldsymbol{\varepsilon}_{\mathrm{p}} : \boldsymbol{\varepsilon}_{\mathrm{p}}}$, with $\boldsymbol{\varepsilon}_{\mathrm{p}}$ the plastic strain tensor (HKS, 2001), to the local anisotropy directions, at $\dot{\varepsilon}t = 0.05$. The anisotropy factor ζ (see Table 2.1) is set to 5. The deformation pattern obtained largely depends on the local material orientations chosen. For the isotropic reference material, a shear band is found, originating from the area at the void surface where the surface normals are perpendicular to the loading direction, also denoted as the *equator*. The anisotropic material with orientation set 1 shows plastic deformation both in the matrix, diagonally away from the void (i.e. in the interparticle material, approximately parallel to the void surface), and in a band emanating from the void surface at an inclined off-polar region (the term *pole* refers to the location at the void surface where the surface normals are aligned with the loading direction). However, the results obtained with orientation set 2 show plastic deformation diagonally away from the void only, whereas orientation set 3 is found to produce plastic deformation in a shear band starting at the void surface in an off-polar region only.

Tzika et al. (2000) used orientations similar to orientation set 1 for their study of preferentially oriented nylon and found plastic deformation in the matrix material to occur diagonally away from the particle. However, this result is strongly related to the specific choice of orientations and, therefore, the SA model is unsuitable to simulate the distribution of plastic deformation in a particle-modified system. In the remaining, the SA model is primarily used to study the hydrostatic stress field around the void. Thereby, orientation set 2 is used, which corresponds to independently grown crystals, orthogonal to the void surface.

Due to their irregular nature, the RD model and the three-dimensional configuration are less influenced by minor changes in local anisotropy. For both models, the local 1-directions are assumed to be perpendicular to the closest void/matrix interface, which is similar to orientation set 2 for the SA model.

2.4.2 Three-dimensional structure

The three-dimensional configuration as described previously is subjected to uniaxial tension at a constant strain rate $\dot{\varepsilon} = 10^{-3}\ \mathrm{s}^{-1}$. In Figure 2.9, the magnitude of plastic deformation is presented at $\dot{\varepsilon}t = 0.05$ for both isotropic material, with $\zeta = 1$ and strongly

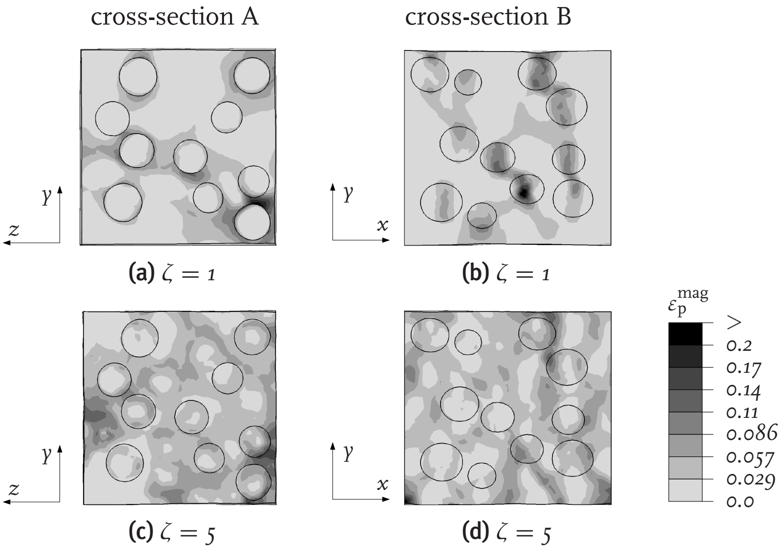

(a) $\zeta = 1$ (b) $\zeta = 1$

(c) $\zeta = 5$ (d) $\zeta = 5$

Figure 2.9 / The magnitude of plastic deformation, $\varepsilon_{\mathrm{p}}^{\mathrm{mag}}$, in a three-dimensional arrangement of voids, at $\dot{\varepsilon}t = 0.05$.

anisotropic matrix material, with $\zeta = 5$. The former corresponds to the situation where there is no significant influence of transcrystallized material around the cavitated particles, i.e. a large scale configuration where the thickness of these layers can be neglected ($\Lambda \gg \Lambda_{\mathrm{c}}$) and the material consists of randomly oriented bulk matrix material. The latter, however, resembles a small scale situation, where the matrix material completely consists of transcrystallized polymeric material ($\Lambda < \Lambda_{\mathrm{c}}$). In both cross-sections A and B, a strongly localized behavior can be observed for the isotropic material, where the majority of plastic deformation is concentrated in a distinct path of shear bands through the irregular microstructure and the highest levels of plastic deformation are reached at the void equator regions. The effect of a reduced plastic resistance in the local 12 and 13 shear directions is a more dispersed field of shear bands, with the maximum values positioned both near the voids surfaces and in the matrix and smaller than for the isotropic material. The void-bridging shear bands approach the void surface at approximately the inclined 30°–50° off-polar region, forming a double shear band at each side of a cavitated particle.

In Figure 2.10, the hydrostatic pressure field $p = -\frac{1}{3}\mathrm{tr}(\boldsymbol{\sigma})$ is represented. For the large scale ($\Lambda \gg \Lambda_{\mathrm{c}}$) isotropic material, the negative (tensile) triaxial stresses, which may induce brittle behavior, are located at the equator regions of the voids, whereas in the small scale ($\Lambda < \Lambda_{\mathrm{c}}$) anisotropic material, with $\zeta = 5$, the maximum tensile triaxial stresses are located at the void poles.

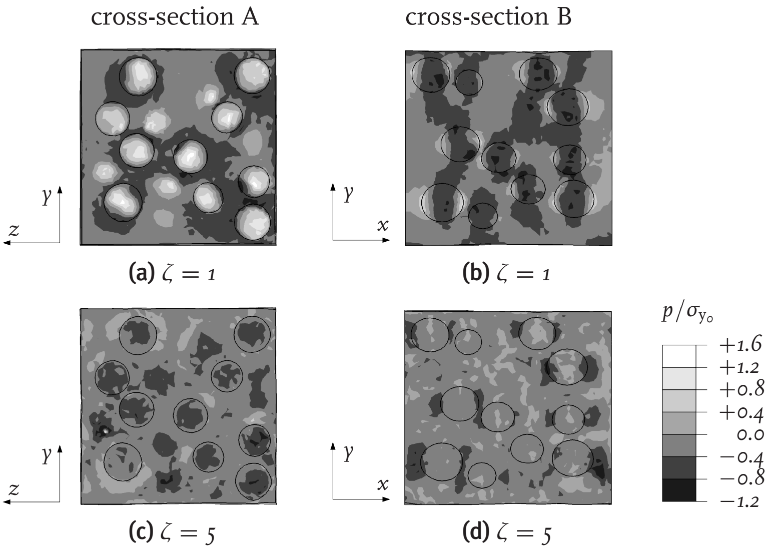

(a) $\zeta = 1$ **(b)** $\zeta = 1$

(c) $\zeta = 5$ **(d)** $\zeta = 5$

Figure 2.10 / The normalized hydrostatic pressure field p/σ_{y_0}, in a three-dimensional arrangement of voids, at $\dot{\varepsilon}t = 0.05$.

Therefore, the effect of completely transcrystallized anisotropic material, with reduced shear yield strengths, between voided inclusions is extensive, delocalized, shear yielding while the negative hydrostatic stresses are located at the polar regions rather than at the void equators.

2.4.3 Two-dimensional RVEs

In this section, both the two-dimensional RD model and the SA model are considered for the description of the particle-modified system. Isotropic material, with $\zeta = 1$, is used as a reference case for large scale, randomly crystallized material. For the small scale transcrystallized material, several levels of anisotropy are considered, ranging from $\zeta = 1.5$ to $\zeta = 5$. In Figure 2.11, the magnitude of the plastic deformation is given for the irregular plane strain model. Qualitatively, the same effect as for the three-dimensional configuration previously discussed (Figure 2.9) can be observed. For fully isotropic material, the deformation is strongly localized in a specific path through the microstructure, determined by the irregular void arrangement. For increasing anisotropy, an increasingly dispersed mode of shear yielding is observed, which is highly favorable to enhance the toughness. Maximum $\varepsilon_{\mathrm{p}}^{\mathrm{mag}}$-values are reduced, and are located both in the matrix material, away from the void surface and at the void/matrix interface for the transcrystallized material. Analogous to the three-dimensional configuration, in the largely anisotropic material, double shear bands can be observed at each side of a void, positioned at the

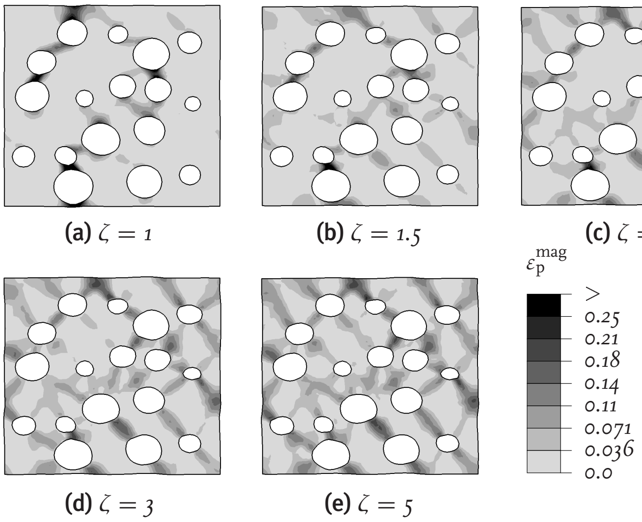

Figure 2.11 / The influence of radially oriented anisotropy on the magnitude of plastic deformation, $\varepsilon_\mathrm{p}^\mathrm{mag}$, for the irregular plane strain model, at $\dot{\varepsilon}t = 0.05$.

inclined $30°$–$50°$ off-polar regions, whereas in the isotropic material mostly single shear bands at the void equators are found. The shear yielding mechanism becomes truly effective for anisotropy ratios R_{11}/R_{12} above the value of 3.

Although not shown here, it is mentioned that for all levels of anisotropy, in the RD model, the highest tensile triaxial stresses are found at the void equator regions, which is not in agreement with the three-dimensional simulations. More realistic predictions of the triaxial stress state around dispersed voids are obtained with the axisymmetric SA model, as represented in Figure 2.12. In the isotropic material, the maximum tensile triaxial stresses are found to occur at the void equators, corresponding to the observations in the three-dimensional simulation and a second maximum is found in the matrix material between the voids. The latter is not observed in the 3D simulations. For small anisotropy

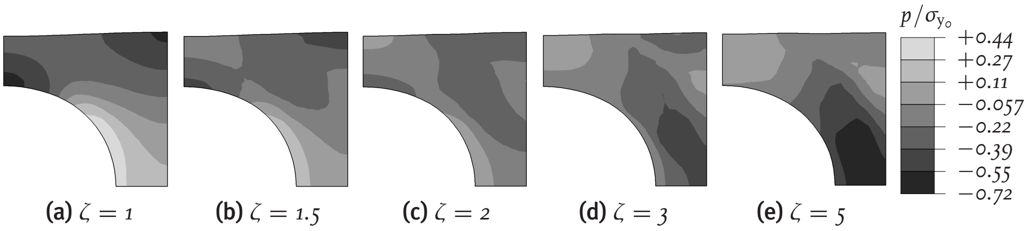

Figure 2.12 / The influence of radially oriented anisotropy on the normalized hydrostatic pressure, p/σ_{y_0}, for the axisymmetric SA model, at $\dot{\varepsilon}t = 0.05$.

levels, these negative hydrostatic pressures are reduced. At higher levels of anisotropy however, the tensile pressures again increase with increasing ζ, where the maximum now is found in the matrix material near the void pole. The SA model is in much better agreement with the three-dimensional situation than the RD model. However, the peak values of the tensile hydrostatic stress are significantly lower for the axisymmetric SA model than for the three-dimensional model. Danielson et al. (2002) found the opposite effect, when comparing their three-dimensional analysis of a BCC arrangement of voids under triaxial loading with results obtained by Socrate and Boyce (2000) with an axisymmetric BCC model.

The distinct effect of anisotropy on the triaxial stress field is also reflected in the maximum in-plane principal stress, $\sigma_{\max}$, as is shown in Figure 2.13. For the isotropic matrix material, the locations of large equivalent stress and negative hydrostatic stress coincide, leading to a relatively high maximum in-plane principal stress, concentrated at the void equators, and the void-bridging ligaments. As the anisotropy parameter ζ is increased, the values of $\sigma_{\max}$ are considerably reduced and the location of the largest $\sigma_{\max}$ changes to the void poles for $\zeta = 5$.

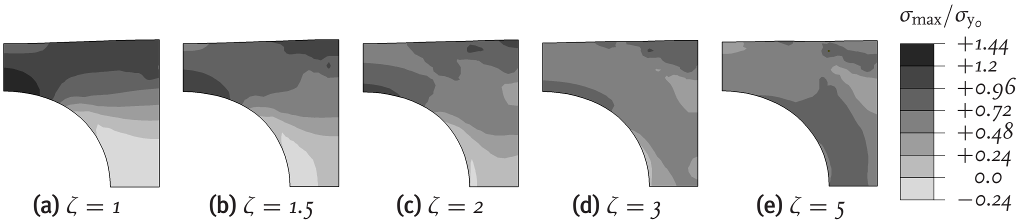

(a) $\zeta = 1$ **(b)** $\zeta = 1.5$ **(c)** $\zeta = 2$ **(d)** $\zeta = 3$ **(e)** $\zeta = 5$

Figure 2.13 / The influence of radially oriented anisotropy on the normalized maximum in-plane principal stress, $\sigma_{\max}/\sigma_{y_0}$, for the axisymmetric SA model, at $\dot{\varepsilon}t = 0.05$.

2.4.4 Failure mechanisms

Based on the investigations with both the RD and the SA model, two distinct effects of local, radially oriented, anisotropy can be observed. The influence on the triaxial stress field is a change of the position of maximum tensile values. Under high tensile triaxial stress, crazelike features, as interlamellar separation and voiding of amorphous regions (Friedrich, 1983; Narisawa and Ishikawa, 1990; Kausch et al., 1999; Michler and Godehardt, 2000), may be initiated in the semicrystalline matrix material, and upon extension and coalescence of cavities, true crazes may be formed. Although crazing may lead to brittle behavior, the crazing process itself may under certain conditions also lead to plasticity, and therefore to toughness (Argon et al., 1983, 1994).

In the simulations, the highest negative hydrostatic pressures are found at the void equators for the large scale, isotropic material. For the small scale anisotropic material however, large tensile pressures are found at the void poles. Therefore, the initiation of crazing may, for the voided system with radially oriented anisotropy, be expected to occur at the particle poles, rather than in the equator region. The growth of initiated crazes is likely to occur along planes which are perpendicular to the direction of maximum principal stress (Kramer, 1983; Narisawa and Ishikawa, 1990; Kausch et al., 1999). In Figure 2.14, the direction of the maximum in-plane principal stress is given for the SA model, for both isotropic ($\zeta = 1$) and largely anisotropic ($\zeta = 5$) material. For both situations, in the region of large tensile triaxial stress, the maximum in-plane principal stresses are relatively large, and directed parallel with the void interface. Therefore, craze growth is expected to occur perpendicular to the interface. Moreover, the large principal stresses at the particle equators of the isotropic material may lead to brittle fracture of the matrix material. The decrease of maximum in-plane principal stresses in the anisotropic material, makes this system less susceptible to brittle fracture. It is noted that in the current simulations, no failure and crazing initiation/growth criterion has been used (as for example in Tijssens et al., 2000; Estevez et al., 2000; Socrate et al., 2001). Anyhow, the observed stress and deformation phenomena are schematically represented in Figure 2.15. The actual mechanism that will occur for a specific matrix material will depend on the values of the brittle fracture strength, the resistance against craze initiation and growth and the yield strength of the material, relative to each other (Bicerano and Seitz, 1996). In the isotropic material, possible crazes are initiated at the particle equators, and grow transversely to the macroscopic tensile direction. The plastic deformation is localized in a few bands, located in crazing regions. For this large scale system, the crazes may act as precursors to cracks, and ultimately failure. For the small scale situation, with radially oriented anisotropic material around the cavitated particles, maximum tensile triaxial stresses are predominantly found in zones of limited plastic deformation. Possible crazes are initiated at the particle poles, and grow in the direction of macroscopic loading. In this situation, crazing may become a mechanism of energy-absorbing inelastic

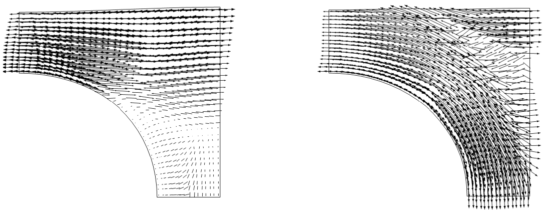

(a) $\zeta = 1$ **(b)** $\zeta = 5$

Figure 2.14 / The influence of radially oriented anisotropy on the direction and magnitude of the maximum in-plane principal stress, $\sigma_{\max}$, for the SA model, at $\dot{\varepsilon}t = 0.05$.

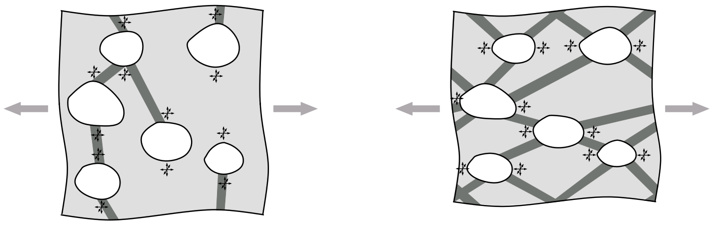

(a) isotropic **(b)** anisotropic

Figure 2.15 / Schematic illustration of the effect of radially oriented anisotropy on the occurrence of matrix shearing and triaxial stresses.

deformation. Additionally, extensive matrix yielding, which is another beneficial energy-absorbing mechanism, occurs in noncrazing regions. Therefore, by changing the nature of matrix crazing, reducing principal stresses and inducing extensive matrix shearing, a local, radially oriented, anisotropy, with sufficiently reduced shear strengths, may be a highly efficient method for the toughening of semicrystalline materials.

2.5 Unidirectional anisotropy

In the foregoing, the local principal anisotropy directions were radially oriented around the dispersed voids. Here, as an alternative, the consequences of a unidirectional orientation field are investigated. The 1-directions of the uniform field of local coordinate systems are chosen either to be aligned parallel with the macroscopic tensile direction, referred to with $\varphi = 0^\circ$, or at an angle of $\varphi = 45^\circ$ with the loading direction.

The plastic deformations obtained in the RD model are represented in Figure 2.16, for largely anisotropic material ($\zeta = 5$). The resulting mode of plastic deformation depends on the direction of the orientation field. For $\varphi = 0^\circ$, localization of deformation is found

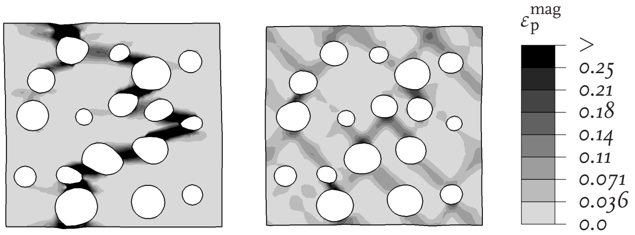

(a) $\varphi = 0^\circ$ **(b)** $\varphi = 45^\circ$

Figure 2.16 / The influence of unidirectional anisotropy on the magnitude of plastic deformation, ε_p^{mag}, at $\dot{\varepsilon}t = 0.05$, using $\zeta = 5$.

to be more severe than for the isotropic material, shown in Figure 2.11(a). Shear bands are found predominantly in either the local 1- or the local 2-direction. In the $\varphi = 45^\circ$ situation, the directions of reduced plastic resistance are oriented favorably with respect to the shear directions that are induced by the geometry of irregularly dispersed voids. Consequently, a pattern of dispersed, void-bridging, shear bands is obtained. In contrast to the radially oriented anisotropy, for this material, the shear bands are starting mainly from the void equators and have their maximum of plastic deformation at the void/matrix interface.

In Figure 2.17, the resulting hydrostatic stress fields, as obtained with the axisymmetric SA model, are represented. Again, the results depend on the angle between the principal anisotropy directions with the loading direction. When the local 1-direction coincides with the direction of the macroscopic load, a band of large tensile triaxial stress is found in the matrix material between voids, starting near the void equator, whereas for the case of $\varphi = 45^\circ$, the maximum tensile triaxial stresses, which are reduced with respect to the isotropic situation, are found in the matrix material near the void pole.

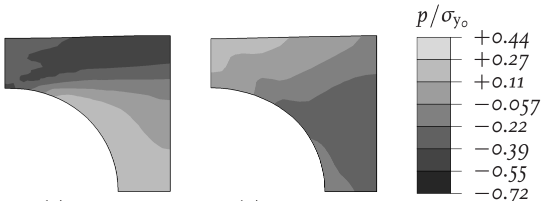

(a) $\varphi = 0^\circ$ **(b)** $\varphi = 45^\circ$

Figure 2.17 / The influence of unidirectional anisotropy on the normalized hydrostatic stress, p/σ_{y_0}, at $\dot{\varepsilon}t = 0.05$, with $\zeta = 5$.

Although a unidirectionally oriented plastic anisotropy can potentially induce a toughened behavior if loaded in the proper direction, the direction dependence of this material makes this morphology hardly suitable for improving the toughness of semicrystalline material in general.

2.6 Influence of hardening

In the numerical investigation of the effect of locally anisotropic yield properties, the hardening parameter h has been kept constant. However, increasing the postyield hardening is a known method of improving impact behavior of particle-modified polymeric material (Smit et al., 2000a,b,c). In Figure 2.18, the effect of this hardening parameter on the plastic deformation obtained is shown, for a fully isotropic matrix. Increasing the hardening reduces the localization of shear bands. Although a considerably more dispersed

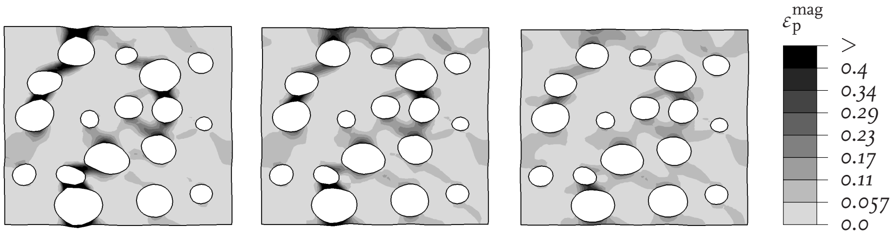

(a) $h = 0.6$ **(b)** $h = 1.9$ **(c)** $h = 6$

Figure 2.18 / Influence of postyield hardening on the magnitude of plastic deformation, $\varepsilon_{\mathrm{p}}^{\mathrm{mag}}$, at $\varepsilon = 0.1$.

pattern of plastic deformation is found for large hardening, the extensive matrix shearing in distinct shear bands, as found for the anisotropic material, see Figure 2.11(e), is not obtained. Increasing the hardening parameter has no significant effect on the triaxial stress field in the SA model.

By itself, increased hardening will indeed improve toughness, however, the toughening as obtained by local radially oriented anisotropy is potentially much larger. Nevertheless, a combination of both mechanisms, where the material behavior exhibits increased strain hardening, preferably in the local 2-direction to prevent localization in thin interparticle ligaments, in addition to a local anisotropy with reduced 12 and 13 shear strengths would be advantageous.

2.7 Conclusions

In this chapter, the effect of matrix material with a reduced yield strength in the local shear directions around well-dispersed voids has been investigated by numerical simulations of idealized systems. The local principal anisotropy directions were assumed to be radially oriented around second-phase particles. The fictitious polymeric material was modeled in the context of anisotropic Hill plasticity, where the yield strength has been taken to depend on an effective plastic deformation measure, and its time derivative. Two extreme size scales were investigated; the smallest scale having fully percolated anisotropic material and the largest scale having completely isotropic material properties.

The three-dimensional structure of the voided material was simplified to two different micromechanical models. The applicability of these computationally two-dimensional models was assessed by comparison of two reference situations with fully three-dimensional simulations. The irregular distribution of voids is captured by a multiparticle plane strain RVE. The irregular nature of this RVE is essential in capturing the effects of local anisotropy on the mechanics of plastic deformation. For the large scale, plastic deformation localizes in a specific path through the matrix material, inducing macroscopically brittle behavior, whereas for the small scale configuration, a heterogeneous field of void-bridging shear bands was found throughout the entire domain, which could lead to a macroscopically toughened behavior. The extent of shear yielding increases with increasing anisotropy. The localization of deformation vanishes due to a large reduction of local shear yield strengths. Comparison with fully three-dimensional calculations shows that the RD model is incapable of capturing the distinct effects of local anisotropy on the triaxial stress state. A better representation of the three-dimensional stress state is obtained with the axisymmetric SA model, where a regular distribution of voids is assumed. The most striking effect of local anisotropy on the hydrostatic stress field is a shift of the highest tensile triaxial stresses from the void equator region (where the surface normals are perpendicular to the loading direction) to the void polar region (the surface area where the normals are aligned with the loading direction). Consequently, the maximum principal stresses at the void equator are considerably reduced.

The calculations presented in this chapter confirm that the mechanism as proposed by Muratoğlu et al. (1995c) could indeed lead to toughened material behavior. The presence of an absolute length scale is related to the thickness of a layer of anisotropic matrix material enveloping the dispersed voids. Required for toughening by this mechanism is then (i) a structure of well-dispersed voided particles with an average surface–to–surface interparticle distance which is smaller than the critical length parameter of the matrix material; (ii) locally anisotropic material with the principal *1*-direction radially oriented with respect to the nearest void surface; and (iii) a sufficiently reduced shear yield strength in the local *12*- and *13*-directions (with R_{11}/R_{12} at least of the order of *3*). The role of voiding will be discussed in the following chapter.

It is noted that although the large potential of local anisotropy for toughening of semicrystalline polymers was shown, the origin of this anisotropy has not been addressed here. The material was merely assumed to be oriented with the principal *1*-direction of anisotropy towards the nearest void and having a finite anisotropic layer thickness. The origin of these layers is attributed to a preferred crystallization at the particle/matrix interface by Muratoğlu et al. (1995c) and Bartczak et al. (1999a,b). The consequences of such a morphology for local anisotropy will be addressed in Chapter 7.

An alternative anisotropy configuration has been investigated, having a unidirectional field of the principal material orientations. Although this microstructure can potentially induce a toughened behavior if loaded appropriately with respect to the principal anisotropy directions, the direction dependence of this material makes this toughening mechanism hardly suitable for improving semicrystalline materials. Finally, hardening of the yield strength with plastic deformation was shown to also reduce localization. However, it is concluded that local anisotropy is a more powerful tool in obtaining substantially improved material behavior. Nevertheless, when used in combination with anisotropy, an increased hardening would be beneficial for preventing localization in thin interparticle ligaments.

CHAPTER THREE

Hard particles versus soft particles[1]

Abstract / The potential of toughening of semicrystalline polymeric material by local anisotropy in combination with soft rubber and hard mineral filler particles is investigated in this chapter. The matrix material is modeled within the framework of anisotropic Hill plasticity with a rate-dependent and hardening yield stress. Various particle/matrix interface conditions are used to study the role of debonding and cavitation. The presence of debonded moderately stiff or hard fillers is found to influence the shear yielding effect of local anisotropy that was found for voided material.

3.1 Introduction

A physically-based mechanism for the toughening of semicrystalline polymeric materials due to the dispersion of particles originates from the presence of a layer of anisotropic transcrystallized material enveloping the particles, and was proposed for nylon by Muratoğlu et al. (1995c). Bartczak et al. (1999a,b) generalized this mechanism to other material (high density polyethylene) and showed the critical interparticle distance to be an intrinsic property of the matrix material, thereby opening the possibility of using mineral fillers instead of rubber particles for the toughening of semicrystalline polymers, the advantage of which would be an improved modulus of the blend. They argued that debonding of hard filler particles could be an alternative for the cavitation of the rubbery phase.

In Chapter 2, an idealized, polymeric matrix material was modeled by anisotropic Hill plasticity, and various representative volume elements were used to describe the system containing dispersed voids. It was shown that a local plastic anisotropy of matrix material around the voids can effectively replace localization by dispersed shear yielding and change the occurring hydrostatic stresses, potentially leading to toughened material behavior. However, to achieve these improvements, a morphology should be pursued that has a radially oriented structure around the dispersed voids and provides a sufficiently large amount of anisotropy.

---

[1] This chapter is based on Van Dommelen et al. (2003g).

In this chapter, the consequence of using moderately stiff rubber fillers or hard mineral particles for the toughening of semicrystalline polymers is investigated. For this purpose, again the anisotropic Hill model is used, with a rate-dependent and hardening yield stress. The system contains a scale parameter, which is the ratio of the average distance between particles and a critical distance. The value of this parameter is represented in the calculations by the relative thickness of an anisotropic layer around the particles. Large and small scale configurations are modeled by entirely isotropic or anisotropic matrix material, respectively. Debonding particles with various interface strengths, precavitated rubber shell-structures, and fully bonded hard particles are used. The combination of local anisotropy and precavitated rubber shell-structures is found to promote matrix shear yielding. The presence of easily debonding hard particles is found to partly disturb the anisotropy-based toughening mechanism, whereas fully bonded particles induce large tensile hydrostatic stresses.

3.2 Model description

In this chapter, the potential of plastic anisotropy, in combination with moderate or high stiffness filler particles, for enhancing the toughness of a particle-modified semicrystalline polymeric material is investigated. For this purpose, an idealized polymeric material is modeled by isotropic elasticity and anisotropic plasticity. For the yield behavior, the anisotropic Hill yield criterion (Hill, 1950) is used, with a rate-dependent and hardening yield stress, as discussed in Chapter 2. Also the material parameters of the fictitious polymer matrix are similar as in the previous chapter. The transcrystallized material around the particles is assumed to have a reduced plastic resistance in the local *12* and *13* shear directions (at the particle/matrix interface, the *1*-direction is perpendicular to the interface), and the reduction is controlled by the adjustable parameter $\zeta = R_{11}/R_{12}$. Rubber particles are modeled with a neo-Hookean hyperelastic model (HKS, 2001), characterized by a shear modulus $G^{\mathrm{p}} = 30$ MPa and a bulk modulus $\kappa^{\mathrm{p}} = 1$ GPa. The mineral filler particles are modeled as linearly elastic, with Young's modulus $E^{\mathrm{p}} = 80$ GPa and Poisson's ratio $\nu^{\mathrm{p}} = 0.3$.

Particle-modified material is again described by a finite element model of a representative volume element (RVE). The particle-modified system, having a three-dimensional nature, is simplified to a two-dimensional RVE, for which two different approaches are used, as discussed in Chapter 2, where a comparison with fully three-dimensional calculations was presented. To account for the irregular nature of particle-dispersed systems, a multi-particle plane strain RVE with randomly dispersed particles (referred to as the *RD model*) is used. The meshes with 2,622 4-noded bilinear plane strain matrix elements and either 324 elements for the precavitated rubber shell or 796 filler particle elements, are shown in Figure 3.1(a) and (b), respectively. A local orientation field for the matrix material is generated by taking the local 1-direction perpendicular to the closest particle/matrix interface, taking into account the periodicity of the structure, as was shown in Figure 2.5(b). The RVE will be subjected to tensile loading in x-direction.

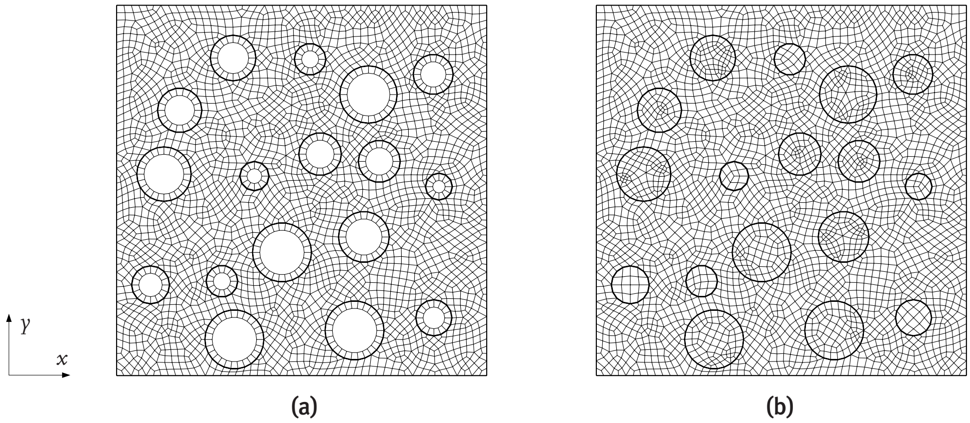

Figure 3.1 / Finite element mesh of multiparticle plane strain RVE model including (a) precavitated and (b) uncavitated particles.

An axisymmetric RVE model of a staggered array of particles (referred to as the *SA model*) is considered, which was previously used for the investigation of the micromechanics of particle-toughened polymers by Socrate and Boyce (2000) and by Tzika et al. (2000) and which resembles a body centered tetragonal stacking of particles (see Section 2.3.1). The finite element meshes of the axisymmetric SA model with 20 volume percent particles are shown in Figure 3.2. The matrix material is represented by 196 4-noded bilinear

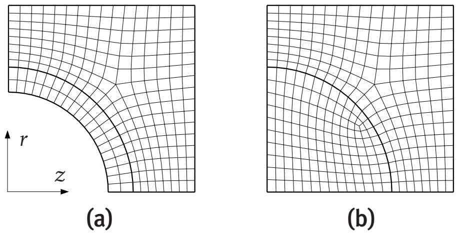

Figure 3.2 / Finite element mesh of the axisymmetric RVE model of a staggered array of particles including (a) precavitated and (b) uncavitated particles.

elements, whereas the precavitated rubber shell and the uncavitated particle regions are modeled by 40 and 136 elements, respectively. The local *1*-directions are assumed to be perpendicular to the closest particle/matrix interface (i.e. corresponding to set 2 in Chapter 2). The RVE will be subjected to tensile loading along the horizontal symmetry axis.

In the following, the influence of dispersed rubber (i.e. soft) inclusions versus mineral (i.e. hard) filler particles in semicrystalline polymeric material is investigated, and particularly the effect of these fillers on the mechanism of toughening by locally induced anisotropy. As a reference situation, voided matrix material will be used. A distinction is made between fully bonded particles, for which a tied particle/matrix interface is used, and debonding particles. For the latter, a contact algorithm (HKS, 2001) with a relatively low maximum tensile strength $\sigma^{\mathrm{i}}/\sigma_{\mathrm{y}_0} = 0.4$ is used to describe the particle/matrix interaction.

3.3 Rubber particles

For rubber inclusions with a relatively low stiffness, the effect of the presence of either debonded or cavitated particles with respect to the stress and deformation fields is negligible. These systems may be modeled by voided matrix material. For voided polymeric material, the effect of a local, radially oriented, anisotropy (see Chapter 2) is (i) a transition from localized deformation for isotropic material to dispersed shear yielding; and (ii) a relocation of hydrostatic stresses from the equator region (the particle *equator* is defined as the location where the interface normal is perpendicular to the loading direction) for isotropic material to the polar region (the term *pole* denotes the region where the interface normal is in line with the loading direction).

Rubber filler particles with a moderately high stiffness will have an effect on the deformation mechanisms. To investigate the effect of anisotropy in the presence of rubber filler particles on the triaxial stress field and local principal stresses, the SA model is used. The influence of rubber particles on the observed hydrostatic pressure, $p = -\frac{1}{3}\mathrm{tr}(\boldsymbol{\sigma})$, is shown in Figure 3.3 for both isotropic ($\zeta = 1$, i.e. large scale) and locally anisotropic ($\zeta = 3$, i.e. small scale) material. Results are shown for voided (i.e. low modulus fillers), debonded, precavitated, and well-bonded uncavitated fillers. For the latter, either debonding or cavitation may occur. This is due to tensile triaxial stresses in the rubber particle region and depends on the interface strength and the cavitation resistance. The cavitation process itself is not modeled; instead, precavitated particles are represented by a rubber shell, as was previously done by Smit et al. (2000b). For the isotropic systems, little difference in tensile triaxial pressure between the voided, debonded and cavitated RVEs is observed in the matrix. For the anisotropic systems, maximum negative pressures are found in the polar area; however these are slightly higher when a relatively stiff rubber particle is included. Crazelike features, such as interlamellar separation and voiding of amor-

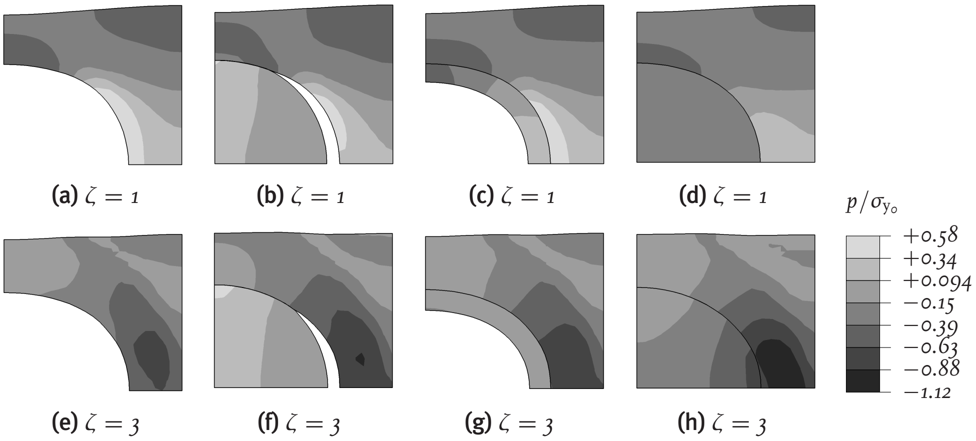

Figure 3.3 / Normalized hydrostatic pressure, p/σ_{y_0}, for the SA model with (a), (e) voids, (b), (f) rubber particles with interface strength $\sigma^{i}/\sigma_{y_0} = 0.4$, (c), (g) precavitated rubber particles, and (d), (h) fully bonded rubber particles, at $\dot{\varepsilon}t = 0.1$.

phous regions (Kausch et al., 1999), may be initiated in the semicrystalline matrix material under high tensile triaxial stress. For the anisotropic systems with both debonded and cavitated relatively stiff rubber inclusions, the maximum principal stresses are directed parallel to the matrix interface (i.e. perpendicular to the loading direction) in the area of maximum tensile triaxial stress. Therefore, crazing is expected to occur parallel to this loading direction, rather than perpendicular, as for the isotropic systems.

The mechanism of shear yielding is captured by the irregular plane strain RVE, as discussed in Section 2.4.3. For the voided systems (i.e. low modulus fillers), a distinct transition from localization in isotropic matrix material to massive dispersed shear yielding in the anisotropic system is observed (Chapter 2). This effect is shown in Figure 3.4, where the obtained magnitude of plastic deformation, $\varepsilon_p^{\text{mag}} = \sqrt{\frac{2}{3}\boldsymbol{\varepsilon}_p : \boldsymbol{\varepsilon}_p}$, with $\boldsymbol{\varepsilon}_p$ the plastic strain tensor (HKS, 2001), is displayed. Moderately stiff rubber inclusions were found

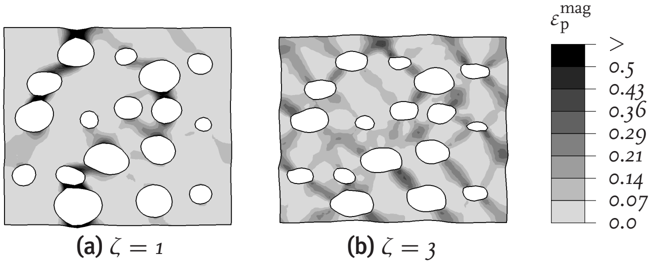

Figure 3.4 / The magnitude of plastic deformation, $\varepsilon_p^{\text{mag}}$, for the RD model with voids, at $\dot{\varepsilon}t = 0.1$.

to have only a small influence on the matrix hydrostatic pressure. Smit et al. (2000b) found precavitated load bearing particles to stabilize local yield zones and promote matrix shear yielding for rubber-modified polystyrene, which shows pronounced strain softening before strain hardening. In Figure 3.5, the consequences of either debonded or cavitated rubber inclusions on the plastic deformation, as predicted by the multiparticle RD model, are displayed for both isotropic and anisotropic systems. Prior to cavitation or debonding, plastic shearing remains dispersed through the matrix material for both the isotropic and the anisotropic system. However, the axisymmetric simulations indicate tensile triaxial stresses within the fully bonded and uncavitated inclusions, which will induce either debonding or cavitation of rubber particles. With debonded moderately stiff rubber particles included, the effect of anisotropy is reduced. For this system, both matrix shear yielding and localized deformation in relatively thin ligaments are observed. The presence of well-bonded precavitated inclusions has a stabilizing effect on matrix yielding in thin ligaments, as was reported by Smit et al. (2000b). Therefore, for polymer toughening by local anisotropy with moderately stiff rubber inclusions, cavitation of particles is preferred over debonding. Finally, the combined effect of moderate anisotropy ($\zeta = 1.5$) and included rubber shell-structures is shown in Figure 3.6. For this system, localized yielding in thin interparticle ligaments is replaced by dispersed matrix shear yielding.

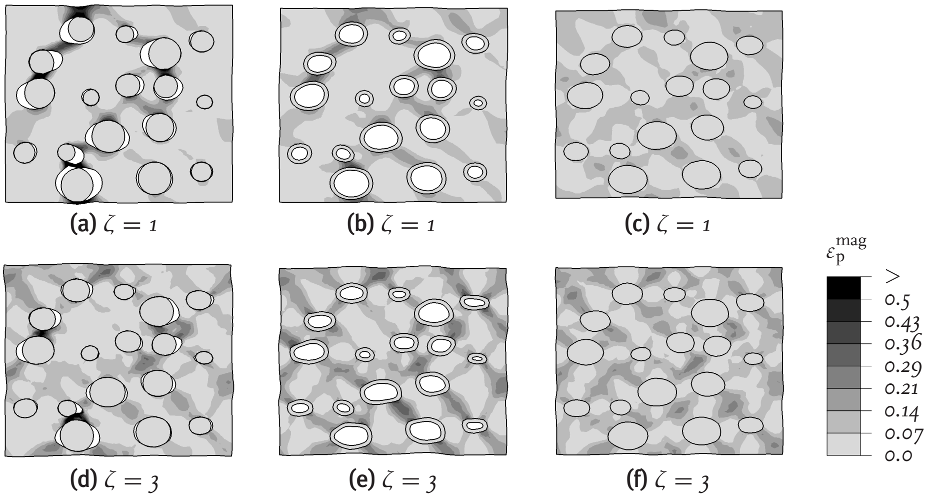

Figure 3.5 / The magnitude of plastic deformation, ε_p^{mag}, for the RD model with (a), (d) debonding rubber particles, (b), (e) precavitated rubber particles, and (c), (f) fully bonded rubber particles, at $\dot{\varepsilon}t = 0.1$.

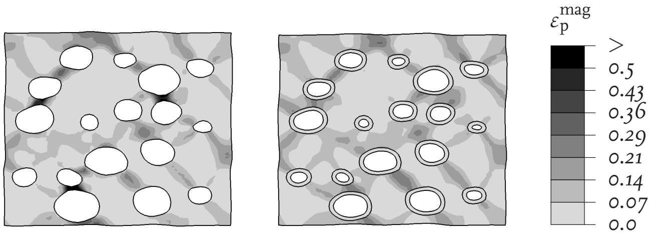

(a) (b)

Figure 3.6 / The magnitude of plastic deformation, $\varepsilon_{\mathrm{p}}^{\mathrm{mag}}$, for the RD model with (a) voids, and (b) cavitated rubber particles, at $\dot{\varepsilon}t = 0.1$, with $\zeta = 1.5$.

3.4 Hard particles

In Figure 3.7, the obtained magnitudes of plastic deformation as obtained by the RD model are shown for systems containing both debonded and fully bonded hard filler particles, for both isotropic ($\zeta = 1$, i.e. large scale) and anisotropic ($\zeta = 3$, i.e. small scale) matrix material, respectively. For the voided isotropic matrix material (Figure 3.4(a)), the macroscopic contraction in the y-direction is small, corresponding to the growth of voids, due to stretching of relatively thin ligaments. Therefore, for this matrix material, the inclusion of easily debonding hard particle fillers has no significant effect on the deformation observed, as can be seen by comparison with Figure 3.7(a), where the interface strength σ^{i} is negligibly small. For radially oriented anisotropic voided material, a dis-

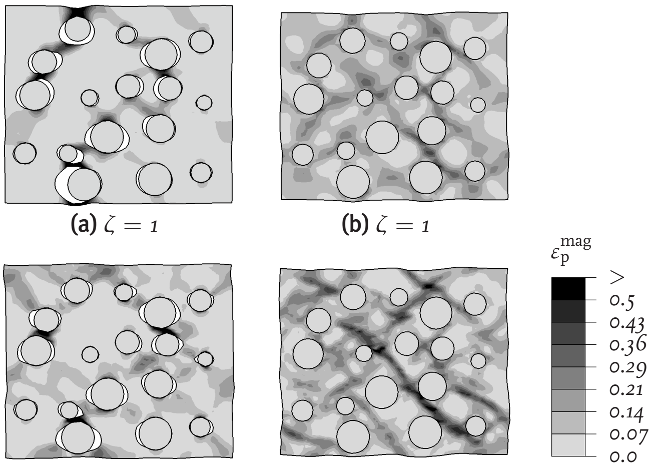

(a) $\zeta = 1$ (b) $\zeta = 1$

(c) $\zeta = 3$ (d) $\zeta = 3$

Figure 3.7 / The magnitude of plastic deformation, $\varepsilon_{\mathrm{p}}^{\mathrm{mag}}$, for the RD model with (a), (c) easily debonding hard particles, and (b), (d) fully bonded hard particles, at $\dot{\varepsilon}t = 0.1$.

persed mode of massive shear yielding is observed, with double shear bands at each side of a particle. As a result of matrix shearing, for the voided anisotropic system, however, the voids become smaller in the macroscopically free direction, see Figure 3.4(b). Consequently, the presence of hard mineral fillers interferes with the mechanism of matrix shearing, as can be observed in Figure 3.7(c). Therefore, although there is some effect of anisotropy, the mechanism of toughening by locally induced anisotropy is expected to be considerably less efficient for nonadhering hard fillers than for low modulus rubber particles. For material filled with well-bonded stiff particles, which is shown in Figure 3.7(b) and (d), massive shear yielding is found for both isotropic and anisotropic matrix behavior.

In Figure 3.8, the effect of hard filler particles on the normalized hydrostatic pressure, p/σ_{y_o}, as predicted by the SA model, is displayed for (large scale) isotropic and (small scale) anisotropic matrix material. For voided systems, the effect of anisotropy on the triaxial stress field is a change of the position of maximum tensile values. The highest negative (tensile) hydrostatic pressures are found at the particle equators for the isotropic material (Figure 3.8(a)). For the anisotropic material however, large tensile pressures are found in the polar regions (Figure 3.8(d)). Therefore, the initiation of crazing may, for the voided system with radially oriented anisotropy, be expected to occur at the particle poles, rather than in the equator region. For easily debonding hard particles, a similar effect of local anisotropy on the tensile triaxial stresses is observed, with an increase of the peak value for the anisotropic situation. The well-bonded configurations both show peak tensile triaxial stresses at the poles. Moreover, the peak values are substantially larger than for the well-bonded stiff rubber particles. The growth of initiated crazes is likely to occur along planes which are perpendicular to the direction of the maximum principal stress.

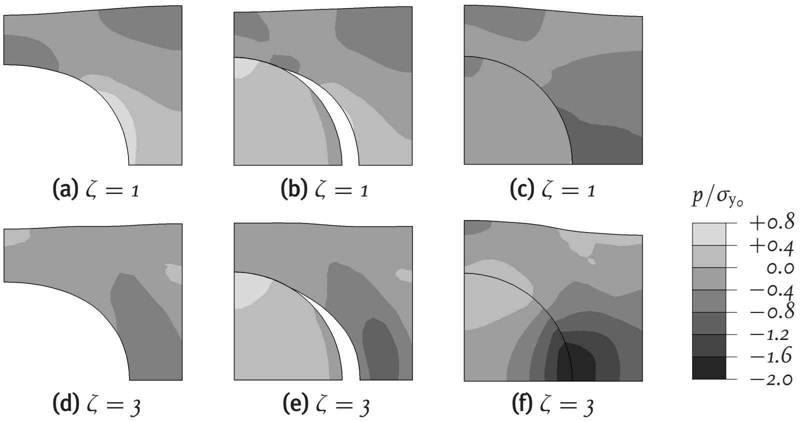

Figure 3.8 / The normalized hydrostatic pressure, p/σ_{y_o}, for the SA model, with (a), (d) voids, (b), (e) easily debonding hard particles, and (c), (f) fully bonded hard particles, at $\dot{\varepsilon}t = 0.1$.

In Figure 3.9, the normalized maximum in-plane principal stress, $\sigma_{\mathrm{max}}/\sigma_{\mathrm{y}_0}$ is depicted for the SA model, for both isotropic ($\zeta = 1$) and anisotropic ($\zeta = 3$) material, with either a void, or easily debonding or adhering hard particles. Moreover, in Figure 3.10, the direction of the maximum in-plane principal stress is given for the systems containing a hard particle. For both nonadhering situations, the maximum in-plane principal stresses in the region of large tensile triaxial stress, are parallel with the rubber/matrix interface. Therefore, craze growth is expected to occur perpendicular to the interface, i.e. perpendicular to the loading direction for the isotropic material and parallel to the loading direction for the anisotropic system. However, for the well-bonded systems, which did show advantageous shear yielding for both the isotropic and the anisotropic configuration, the maximum principal stresses in the polar region (where the largest tensile triaxial stresses

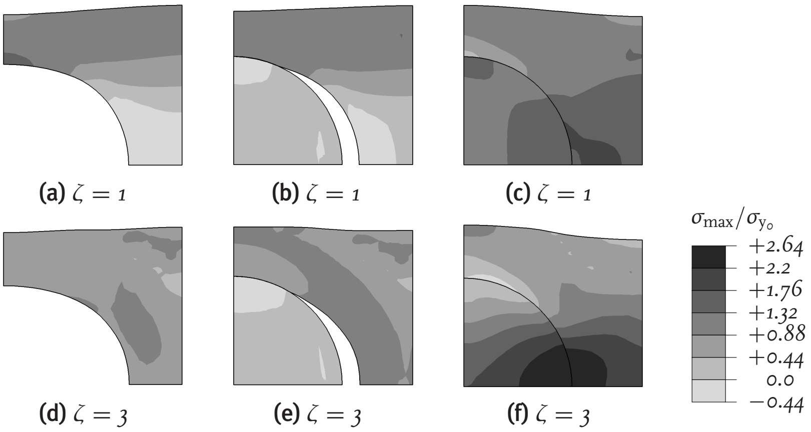

(a) $\zeta = 1$ **(b)** $\zeta = 1$ **(c)** $\zeta = 1$

(d) $\zeta = 3$ **(e)** $\zeta = 3$ **(f)** $\zeta = 3$

Figure 3.9 / The normalized maximum in-plane principal stress, $\sigma_{\mathrm{max}}/\sigma_{\mathrm{y}_0}$, for the SA model, with (a), (d) voids, (b), (e) easily debonding hard particles, and (c), (f) fully bonded hard particles, at $\dot{\varepsilon}t = 0.1$.

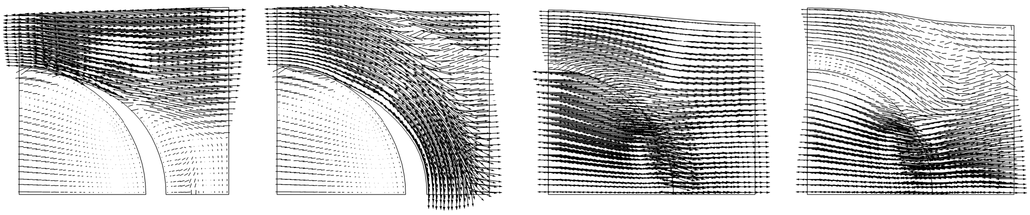

(a) $\zeta = 1$ **(b)** $\zeta = 3$ **(c)** $\zeta = 1$ **(d)** $\zeta = 3$

Figure 3.10 / The direction (and magnitude) of the maximum in-plane principal stress, σ_{max}, for (a), (b) easily debonding hard fillers, and (c), (d) well-bonded particles, at $\dot{\varepsilon}t = 0.1$.

are observed) are directed approximately in the loading direction. Consequently, for these systems craze growth or microcracking may be expected to occur perpendicular to the loading direction, thereby possibly leading to macroscopic failure. Anyhow, for the systems containing well-bonded hard particles, an isotropic matrix seems to be favorable over locally anisotropic material.

A secondary potential effect of hard mineral filler particles is an increase of the modulus of the particle-modified system (Bartczak et al., 1999b). In Figure 3.11, the influence of hard fillers, with various interface conditions, on the normalized equivalent volume-averaged stress

$$\langle\sigma\rangle^{\mathrm{eq}} = \sqrt{\frac{3}{2}\langle\boldsymbol{\sigma}\rangle^{\mathrm{d}} : \langle\boldsymbol{\sigma}\rangle^{\mathrm{d}}} \quad ; \quad \langle\boldsymbol{\sigma}\rangle^{\mathrm{d}} = \langle\boldsymbol{\sigma}\rangle - \frac{1}{3}\mathrm{tr}(\langle\boldsymbol{\sigma}\rangle)\boldsymbol{I}, \tag{3.1}$$

with

$$\langle\boldsymbol{\sigma}\rangle = \frac{1}{V}\int\limits_{\boldsymbol{x}\in V} \boldsymbol{\sigma}(\boldsymbol{x})\,\mathrm{d}V \tag{3.2}$$

the volume-averaged Cauchy stress (Smit et al., 1998), versus the imposed deformation is represented for the RD model. For both the isotropic and the anisotropic material with a reduced shear yield strength, an increase of the elastic modulus is observed for the fully bonded systems with respect to the voided situation. The particles with low interface strength ($\sigma^{\mathrm{i}}/\sigma_{\mathrm{y_0}} = 0.4$) are debonding early in the elastic region. For an increase of the modulus in the entire elastic regime, the interface strength must be sufficiently high, for particles to remain bonded prior to macroscopic yielding. The volume-averaged

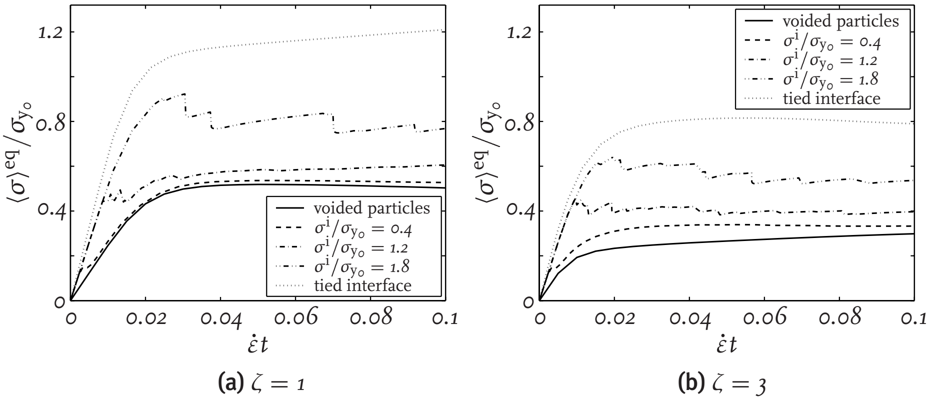

(a) $\zeta = 1$

(b) $\zeta = 3$

Figure 3.11 / The normalized equivalent volume-averaged stress, $\langle\sigma\rangle^{\mathrm{eq}}/\sigma_{\mathrm{y_0}}$, vs. the imposed deformation, $\dot{\varepsilon}t$, for the RD model, for both voids and hard particles, with variable interface conditions.

response is also shown for two situations with elevated interface strength. The stress-drops for these curves correspond to individual interface debonding events. The local anisotropy, which is achieved by a reduction of the shear yield resistances, trivially results in a reduction of the overall yield stress.

3.5 Conclusions

Fictitious, idealized, polymeric matrix materials were modeled by anisotropic Hill plasticity in Chapter 2, where the distinct effect of local plastic anisotropy of matrix material around the voids was shown, viz. an effective replacement of localization by dispersed shear yielding and a change of the occurring hydrostatic stresses, potentially leading to toughened material behavior. In this chapter, a similar modeling approach was used to investigate the influence of rubber and mineral (moderate and high modulus, respectively) filler particles on this toughening mechanism.

Moderately stiff inclusions, which are either debonded or precavitated, were found to have little effect on the triaxial stresses. Rubber shell inclusions however, stabilize local deformation zones and promote matrix shear yielding, whereas debonded rubber particles have a disturbing effect on the anisotropy-induced shear yielding mechanism. The use of mineral filler particles for toughening of polymeric materials requires debonding in order to prevent excessive tensile hydrostatic stresses. These debonded hard particles show a relocation of tensile triaxial stresses to the particle polar areas by local anisotropy, similarly to anisotropic voided systems, with the maximum principal stresses directed such that crazes or microcracks are expected parallel to the loading direction. However, the anisotropy-induced shear yielding mechanism is affected by the presence of stiff inclusions.

The potential of particle-toughening of semicrystalline polymeric materials by local anisotropy is schematically indicated in Figure 3.12, which is a refinement of the originally hypothesized diagram (Figure 1.5). Although some effect of anisotropy is observed,

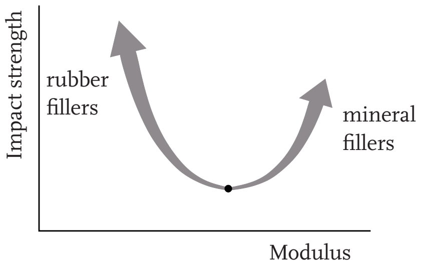

Figure 3.12 / The potential of particle-toughening of semicrystalline polymeric materials by local anisotropy for soft (rubber) and hard (mineral) particles.

the mechanism of toughening by local anisotropy is less effective for nonadhering hard particles, which have the advantage of increasing the blend modulus, than for low stiffness rubber fillers.

CHAPTER FOUR

Composite inclusion model[1]

Abstract / A micromechanically-based constitutive model for the elasto-viscoplastic deformation and texture evolution of semicrystalline polymers is developed. The model idealizes the microstructure to consist of an aggregate of two-phase layered composite inclusions. The crystalline lamellae are modeled as anisotropically elastic with plastic flow occurring via crystallographic slip. The amorphous phase is modeled as isotropically elastic with plastic flow being a rate-dependent process where strain hardening results from molecular orientation. The volume-averaged deformation and stress within the inclusions are related to the mesoscopic fields by various interaction models. The uniaxial compression of initially isotropic high density polyethylene (HDPE) is taken as a case study. The ability of the model to capture the elasto-plastic stress–strain behavior during monotonic and cyclic loading, the evolution of anisotropy, and the effect of crystallinity on the initial modulus, yield stress, postyield behavior and unloading–reloading behavior are evaluated.

4.1 Introduction

The mechanical performance of semicrystalline polymeric materials, as characterized by elasto-viscoplastic deformation, is strongly dependent on the underlying microstructure (Lin and Argon, 1994; G'Sell and Dahoun, 1994; Petermann, 1996; Peacock, 2000). Semicrystalline polymers consist of both amorphous and crystalline domains, where the percentage crystallinity in commercially available materials can vary from 10 to 90 percent. The elastic and the viscoplastic behavior depend on the percentage crystallinity, the initial crystallographic and morphological texture, as well as the evolution of this microstructure with ongoing deformation. Furthermore, the folded chain structure of polymer crystals limits the ability of the crystalline domains to accommodate arbitrary plastic deformations. Thus, the interplay between the amorphous and crystalline domains in responding to imposed deformation is a key issue in determining the mechanical behavior of semicrystalline polymers based on the structure and the behavior of the underlying amorphous and crystalline constituents.

---

[1] This chapter is based on Van Dommelen et al. (2003c) and Van Dommelen et al. (2000b).

In recent years, much research has been focused on understanding the viscoplastic behavior of semicrystalline polymers with experimental and modeling studies focused on the evolution of crystallographic texture during plastic straining up to large strains (e.g. Parks and Ahzi, 1990; Dahoun et al., 1991; Bartczak et al., 1992b; Galeski et al., 1992; Lee et al., 1993a,b, 1995; Ahzi et al., 1994; Schoenfeld et al., 1995; Argon, 1997). However, semicrystalline polymers may exhibit substantial elastic strains which play an important role in the overall mechanical behavior. The yield point itself is typically not very clearly defined since there is considerable nonlinearity prior to any clear rollover or plateauing of stress to signify yield. The contribution of the amorphous and crystalline domains to the initial elastic response and the transition of this elastic response to viscoplastic behavior with increasing strain has been unexplored yet. Elastic deformation continues to play a role during large strain deformation and, furthermore, the elastic behavior of a semicrystalline polymer evolves in an anisotropic manner during large strain deformation due to crystallographic texturing of the elastically anisotropic crystals.

The elastic behavior of each phase and, importantly, the interplay between the elasto-viscoplastic behavior of the phases govern the processing behavior and determine end-use properties. During processing, polymeric materials are often subjected to large plastic deformations, giving rise to preferential orientation of macromolecules and morphology, which may result in high anisotropy. Furthermore, in thin films, a preferred orientation of the crystalline component, produced by transcrystallization during cooling and/or by spin casting, can give rise to strong anisotropy and therefore can have a profound influence on the mechanical properties of these films (Elsner et al., 1990; Muratoğlu et al., 1995a; Bartczak et al., 1999c). This anisotropy is a general phenomenon that plays a significant role in various thin film technologies which are widely used in, for example, the micro-electronics industry. Similar conditions, namely a thin layer of preferentially oriented material, may appear in the microstructural morphology of particle-modified polymers (e.g. Chacko et al., 1982; Muratoğlu et al., 1995c; Bartczak et al., 1999a,b; Kim et al., 2001; Nam et al., 2001).

When focusing on larger strains, different stages of deformation of semicrystalline materials can be distinguished (Peterlin, 1971; Petermann and Ebener, 1999). In stage one, the original lamellar structure of the material is continuously deformed by mechanisms of intralamellar and interlamellar deformation. The second stage comprises a discontinuous transformation of the original structure into a fibrillar structure, with the molecular chains parallel to the drawing direction. In the final stage, the fibrillar structure is further deformed.

In this chapter, a micromechanically-based numerical model for the deformation and texture evolution of semicrystalline polymers is developed for the elastic and moderately plastic strain range (i.e. for the first stage of deformation). The new model is formulated within an elasto-plastic deformation framework. The model builds on previous contributions by Lee et al. (1993a,b) to the micromechanical modeling of rigid/viscoplastic deformation of amorphous/crystalline aggregates. The model idealizes the microstructure to consist of an aggregate of two-phase layered composite inclusions. A new framework for the composite inclusion model is formulated to facilitate the use of finite deformation elasto-viscoplastic constitutive models for each constituent phase. The crystalline lamellae are modeled as anisotropically elastic with plastic flow occurring via crystallographic slip. The amorphous phase is modeled as isotropically elastic with plastic flow being a rate-dependent process with strain hardening resulting from molecular orientation. The volume-averaged deformation and stress within the inclusions are related to the mesoscopic[2] fields by several interaction models. The uniaxial compression of initially isotropic HDPE is taken as a case study to investigate the effectiveness of various interaction models.

The model presented provides the ability to calculate the initial anisotropy properties, and the evolution thereof, for specifically preoriented semicrystalline polymers. Furthermore, the volumetric response and hydrostatic stresses, which, in combination with the micromechanics of the material, play an important role in the failure of polymeric material are accounted for. The mechanics and micromechanics of loading–unloading–reloading hysteresis are explored. The model is also used to investigate the influence of the percentage crystallinity on the initial elastic stiffness, the yield and the postyield behavior, and loading cycles. Finally, the ability of the model to capture the effects of an anisotropic microstructure on the mechanical behavior is demonstrated.

4.2 Material models

Viscoplastic Taylor-type models have been used by, for example, Parks and Ahzi (1990) and Lee et al. (1995) for the prediction of texture evolution for semicrystalline polymeric material. A self-consistent viscoplastic approach was used by Dahoun et al. (1991). In these studies, the influence of the amorphous phase was neglected. An elasto-viscoplastic polycrystalline model for low symmetry crystals, such as polymeric crystals, was presented by Schoenfeld et al. (1995), also exclusively for idealized 100 percent crystalline materials. However, for many semicrystalline materials, the contribution of the amorphous phase can be substantial. For example the typical crystallinities of HDPE and nylon-6 are 70 percent and 40 percent, respectively. Since the elastic behavior of polyethylene at ambient temperature is dominated by its rubbery amorphous phase, with an elastic shear modulus which is several orders lower than the crystalline modulus, the Schoenfeld et al. model, with its purely crystalline elasticity, shows an overly stiff overall stress–strain behavior. To account for the amorphous phase, Lee et al. (1993a,b) used a rigid/viscoplastic composite inclusion model. Following this Lee et al. work, a layered two-phase composite inclusion model is formulated. Each composite inclusion consists of a crystalline lamella which is assumed to deform plastically by crystallographic slip, and an amorphous layer for which a power law constitutive relation is used in conjunction with a back-stress tensor to account for orientation-induced hardening (Boyce et al., 1988). In contrast to the rigid/viscoplastic composite inclusion model of Lee et al. (1993a,b), an elasto-viscoplastic[3] formulation is used, with anisotropic elasticity for the crystalline phase. In this section, the kinematical framework, and the material models that are used to describe the constitutive behavior of each respective phase are discussed. In the following, the superscripts "a" and "c" denote the amorphous layer and the crystalline lamella, respectively.

---

[2] In the context of the three-level approach that is presented in this thesis, the term *mesoscopic* will be used for the averaged fields of an aggregate.

4.2.1 Kinematics

For a microstructural elasto-viscoplastic constitutive description of both the crystalline and the amorphous phase, the deformation gradient tensor $\boldsymbol{F}^{\pi} = (\nabla_0 \otimes \boldsymbol{x}^{\pi})^{\mathrm{T}}$ of each constituent phase $\pi = \mathrm{a, c}$, where the superscript "T" indicates the transpose, is decomposed into a plastic and an elastic component, denoted by the subscripts "p" and "e", respectively (Lee, 1969):

$$\boldsymbol{F}^{\pi} = \boldsymbol{F}_{\mathrm{e}}^{\pi} \cdot \boldsymbol{F}_{\mathrm{p}}^{\pi} \quad ; \quad \pi = \mathrm{a, c}. \tag{4.1}$$

This multiplicative decomposition considers the concept of a local intermediate stress-free state $\bar{\Omega}^{\pi}$, which results from instantaneous unloading of the current configuration Ω^{π}, as is schematically illustrated in Figure 4.1. The deformation gradient $\boldsymbol{F}_{\mathrm{p}}^{\pi}$ is supposed to be invariant, i.e. upon a superimposed rigid body motion

$$\boldsymbol{x} \in \Omega^{\pi} \;\mapsto\; \boldsymbol{x}^{+} = \boldsymbol{v} + \boldsymbol{Q} \cdot \boldsymbol{x}, \tag{4.2}$$

with $\boldsymbol{v}$ a rigid body translation and $\boldsymbol{Q}$ an orthogonal mapping, the respective deformation gradients are transformed to:

$$\boldsymbol{F}_{\mathrm{e}}^{\pi^{+}} = \boldsymbol{Q} \cdot \boldsymbol{F}_{\mathrm{e}}^{\pi} \quad \text{and} \quad \boldsymbol{F}_{\mathrm{p}}^{\pi^{+}} = \boldsymbol{F}_{\mathrm{p}}^{\pi}. \tag{4.3}$$

---

[3] A thermo-elasto-viscoplastic extension of this formulation is presented in Van Dommelen et al. (2000b).

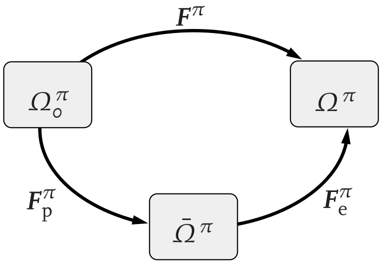

Figure 4.1 / Schematic representation of the local reference, intermediate and current configurations, based on a multiplicative decomposition of the deformation gradient tensor.

The velocity gradient tensor $\boldsymbol{L}^{\pi} = \dot{\boldsymbol{F}}^{\pi} \cdot \boldsymbol{F}^{\pi-1}$ is decomposed according to:

$$\boldsymbol{L}^{\pi} = \boldsymbol{L}_{\mathrm{e}}^{\pi} + \boldsymbol{F}_{\mathrm{e}}^{\pi} \cdot \boldsymbol{L}_{\mathrm{p}}^{\pi} \cdot \boldsymbol{F}_{\mathrm{e}}^{\pi-1} \quad ; \quad \pi = \mathrm{a}, \mathrm{c}, \tag{4.4}$$

where the elastic and the plastic parts of the velocity gradient are defined as

$$\boldsymbol{L}_{\mathrm{e}}^{\pi} = \dot{\boldsymbol{F}}_{\mathrm{e}}^{\pi} \cdot \boldsymbol{F}_{\mathrm{e}}^{\pi-1} \quad \text{and} \quad \boldsymbol{L}_{\mathrm{p}}^{\pi} = \dot{\boldsymbol{F}}_{\mathrm{p}}^{\pi} \cdot \boldsymbol{F}_{\mathrm{p}}^{\pi-1} \quad ; \quad \pi = \mathrm{a}, \mathrm{c}, \tag{4.5}$$

respectively. Within this framework, a constitutive model is defined for each constituent phase in terms of the elastic and viscoplastic behavior, based on micromechanical considerations.

4.2.2 Crystalline phase

The crystalline domain of polymeric material consists of regularly ordered molecular chains, which results in (i) anisotropically elastic behavior, where the elastic properties are given with respect to the crystallographic directions; and (ii) plastic deformation, governed primarily by crystallographic slip on a limited number of slip planes (e.g. G'Sell and Dahoun, 1994; Argon, 1997). The orthorhombic crystal structure of polyethylene is shown in Figure 4.2.

Elasticity

The elastic component of the deformation in the crystalline phase is characterized by a fourth-order anisotropically elastic modulus tensor ${}^4\boldsymbol{\mathcal{C}}^{\mathrm{c}}$ which linearly relates the elastic Green–Lagrange strain tensor $\boldsymbol{E}_{\mathrm{e}}^{\mathrm{c}}$ and the second Piola–Kirchhofflike stress measure $\boldsymbol{\tau}^{\mathrm{c}}$:

$$\boldsymbol{\tau}^{\mathrm{c}} = {}^4\boldsymbol{\mathcal{C}}^{\mathrm{c}} : \boldsymbol{E}_{\mathrm{e}}^{\mathrm{c}}, \tag{4.6}$$

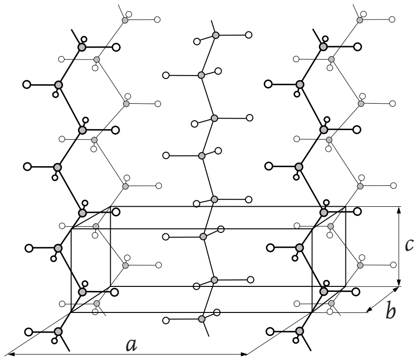

Figure 4.2 / Orthorhombic crystal structure of HDPE, after G'Sell and Dahoun (1994).

where $\boldsymbol{\tau}^{\mathrm{c}}$ and $\boldsymbol{E}_{\mathrm{e}}^{\mathrm{c}}$ are defined as

$$\boldsymbol{\tau}^{\mathrm{c}} = J_{\mathrm{e}}^{\mathrm{c}}\, \boldsymbol{F}_{\mathrm{e}}^{\mathrm{c}^{-1}} \cdot \boldsymbol{\sigma}^{\mathrm{c}} \cdot \boldsymbol{F}_{\mathrm{e}}^{\mathrm{c}^{-\mathrm{T}}} \quad \text{and} \quad \boldsymbol{E}_{\mathrm{e}}^{\mathrm{c}} = \frac{1}{2}\left(\boldsymbol{F}_{\mathrm{e}}^{\mathrm{c}^{\mathrm{T}}} \cdot \boldsymbol{F}_{\mathrm{e}}^{\mathrm{c}} - \boldsymbol{I}\right), \tag{4.7}$$

respectively, with $J_{\mathrm{e}}^{\mathrm{c}} = \det(\boldsymbol{F}_{\mathrm{e}}^{\mathrm{c}})$, $\boldsymbol{\sigma}^{\mathrm{c}}$ the Cauchy stress tensor and $\boldsymbol{I}$ the second-order identity tensor. The anisotropically elastic properties are coupled to the crystallographic lattice directions in the intermediate configuration $\bar{\Omega}^{\mathrm{c}}$.

Viscoplasticity

The microstructural processes that control the mechanical behavior of the crystalline phase in semicrystalline polymers are assigned primarily to crystallographic slip and secondarily to mechanical twinning or stress-induced martensitic phase transformations (Young and Bowden, 1974; Lin and Argon, 1994; G'Sell and Dahoun, 1994). Since crystallographic slip is assumed to be of most importance, in the modeling process the latter two mechanisms are left out of consideration.

For the viscoplastic behavior of the crystalline phase, a rate-dependent crystal plasticity model is used. In this model, the plastic flow rate of the crystalline lamella, consisting of a single crystal, is composed of the contributions of all N_{s} physically distinct slip systems and is given by

$$\boldsymbol{L}_{\mathrm{p}}^{\mathrm{c}} = \sum_{\alpha=1}^{N_{\mathrm{s}}} \dot{\gamma}^{\alpha} \boldsymbol{P}_{0}^{\alpha} \quad ; \quad \boldsymbol{P}_{0}^{\alpha} = \boldsymbol{s}_{0}^{\alpha} \otimes \boldsymbol{n}_{0}^{\alpha}, \tag{4.8}$$

where the nonsymmetric Schmid tensor $\boldsymbol{P}_{0}^{\alpha}$ is given by the dyadic product of the unit slip direction $\boldsymbol{s}_{0}^{\alpha}$ and the unit slip plane normal $\boldsymbol{n}_{0}^{\alpha}$ of the αth slip system, both given in the reference configuration Ω_{0}^{c}. The shear rate $\dot{\gamma}^{\alpha}$ of each slip system is assumed to be related to the corresponding shear stress, defined as $\tau^\alpha = \boldsymbol{\tau}^{\mathrm{c}} \cdot \boldsymbol{C}^{\mathrm{c}}_{\mathrm{e}} : \boldsymbol{P}^\alpha_0$, via the viscoplastic power law relation (Hutchinson, 1976; Asaro and Needleman, 1985):

$$\dot{\gamma}^\alpha = \dot{\gamma}^{\mathrm{c}}_0 \frac{\tau^\alpha}{g^\alpha} \left| \frac{\tau^\alpha}{g^\alpha} \right|^{n^{\mathrm{c}}-1}, \tag{4.9}$$

where g^α is the shear strength associated with the αth slip system, which is assumed to be constant (hardening is neglected). Furthermore, $\dot{\gamma}^{\mathrm{c}}_0$ is a reference shear rate, and n^{c} is the rate exponent.

Crystallographic slip in polymer crystals can occur either by *affine* or *fine* slip, where the deformation is equally distributed over a large number of parallel slip planes, or by *coarse* or *block* slip, with large deformation on a few slip planes (Young, 1988; Lin and Argon, 1994). These slip mechanism are schematically represented in Figure 4.3. During the early stages of deformation, affine slip, which changes the angle between the molecular chains and the amorphous/crystalline interface normal, is considered to be the predominant mode of plastic deformation in the crystalline phase, whereas coarse slip, leaving the chain tilt angle unaltered, becomes more important at larger strains. Here, all slip is considered to be of the affine type. The resulting change of the interface normal orientation will be discussed in Section 4.4.3.

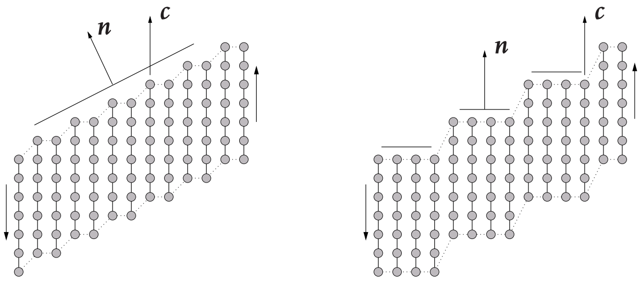

(a) affine slip **(b)** coarse slip

Figure 4.3 / Schematic illustration of chain slip mechanisms, after Young (1988).

To potentially impose any arbitrary volume-invariant plastic deformation to a crystal structure by the mechanism of crystallographic slip, a set of five linearly independent slip systems is needed, as was first pointed out by Von Mises (1928) and later by for example Groves and Kelly (1963). High-symmetry crystals, e.g. cubic metal crystals, generally possess a relatively large number of physically distinct slip systems of which a set of five independent slip systems can be composed. However, in case of low-symmetry crystals, such as for example many polymeric crystals, less than five independent slip systems may be present, in which case these materials have limited deformation possibilities. For most polymers, the chain direction is inextensible and therefore, these crystals cannot accommodate plastic deformation in the direction of the molecular chain. (Van Dommelen et al., 1999a,b, 2000a).

4.2.3 Amorphous phase

The amorphous phase of semicrystalline polymeric material consists of an assembly of disordered macromolecules, which are morphologically constrained by the neighboring crystalline lamellae. At room temperature, the amorphous phase of HDPE, which is the material of interest in this work, is in the rubbery regime, with the glass transition temperature T_g near −70 °C. However, the amorphous phase of other semicrystalline polymers, e.g. nylon, with a higher glass transition temperature, need to be modeled as elasto-viscoplastic. For purpose of generality, an elasto-viscoplastic approach[4] is presented.

Elasticity

The initial elastic resistance of the rubbery amorphous phase is well below the elastic resistance of the crystalline domain. Consequently, elastic deformations can be considerably large and are modeled by a generalized neo-Hookean hyperelastic relationship:

$$\boldsymbol{\sigma}^{\mathrm{a}} = \frac{G^{\mathrm{a}}}{J^{\mathrm{a}}} \tilde{\boldsymbol{B}}_{\mathrm{e}}^{\mathrm{a}^{\mathrm{d}}} + \kappa^{\mathrm{a}}(J^{\mathrm{a}} - 1)\boldsymbol{I}, \tag{4.10}$$

where the superscript "d" indicates the deviatoric part, $J^{\mathrm{a}} = J_{\mathrm{e}}^{\mathrm{a}} = \det(\boldsymbol{F}_{\mathrm{e}}^{\mathrm{a}})$ is the volume ratio, $\tilde{\boldsymbol{F}}_{\mathrm{e}}^{\mathrm{a}} = J_{\mathrm{e}}^{\mathrm{a}^{-\frac{1}{3}}} \boldsymbol{F}_{\mathrm{e}}^{\mathrm{a}}$ is the isochoric elastic deformation gradient tensor, and $\tilde{\boldsymbol{B}}_{\mathrm{e}}^{\mathrm{a}} = \tilde{\boldsymbol{F}}_{\mathrm{e}}^{\mathrm{a}} \cdot \tilde{\boldsymbol{F}}_{\mathrm{e}}^{\mathrm{a}^{\mathrm{T}}}$ is the isochoric elastic left Cauchy–Green deformation tensor. The parameters G^{a} and κ^{a} denote the shear modulus and bulk modulus, respectively.

Viscoplasticity

A relatively strain rate-insensitive power law relation between an effective shear strain rate $\dot{\gamma}_{\mathrm{p}}^{\mathrm{a}}$ and the effective shear stress τ^{a} (Lee et al., 1993a) is used:

$$\dot{\gamma}_{\mathrm{p}}^{\mathrm{a}} = \dot{\gamma}_{0}^{\mathrm{a}} \left(\frac{\tau^{\mathrm{a}}}{\tau_{0}^{\mathrm{a}}} \right)^{n^{\mathrm{a}}} \quad \text{with} \quad \tau^{\mathrm{a}} = \sqrt{\frac{1}{2} \boldsymbol{\sigma}_{\star}^{\mathrm{a}^{\mathrm{d}}} : \boldsymbol{\sigma}_{\star}^{\mathrm{a}^{\mathrm{d}}}}\,, \tag{4.11}$$

---

[4] By using a purely rubberlike model, such as pure neo-Hookean elasticity or the Arruda–Boyce eight-chain network rubber elastic model (Arruda and Boyce, 1993), mesoscopically less significant yielding and/or stress-plateauing is observed. A viscoplastic contribution is required for a reasonable mesoscopic stress–strain behavior. As an alternative to the model that is used here, the time-dependent Bergström–Boyce model for elastomeric materials (Bergström and Boyce, 1998) may be employed.

where $\dot{\gamma}_0^{\mathrm{a}}$ is a reference shear rate, τ_0^{a} is a reference strength, n^{a} is the rate exponent, and $\boldsymbol{\sigma}_\star^{\mathrm{a}^{\mathrm{d}}}$ represents the deviatoric part of the rotation-neutralized driving stress tensor $\boldsymbol{\sigma}_\star^{\mathrm{a}}$, which is defined as (Boyce et al., 1992)

$$\boldsymbol{\sigma}_\star^{\mathrm{a}} = \boldsymbol{R}_{\mathrm{e}}^{\mathrm{a}^{\mathrm{T}}} \cdot \boldsymbol{\sigma}^{\mathrm{a}} \cdot \boldsymbol{R}_{\mathrm{e}}^{\mathrm{a}} - \boldsymbol{H}^{\mathrm{a}}. \tag{4.12}$$

The rotation tensor $\boldsymbol{R}_{\mathrm{e}}^{\mathrm{a}}$ is obtained from the polar decomposition of $\boldsymbol{F}_{\mathrm{e}}^{\mathrm{a}}$. Furthermore, $\boldsymbol{H}^{\mathrm{a}}$ is a back-stress tensor which accounts for orientation-induced strain hardening (Boyce et al., 1988). The plastic rate of stretching, $\boldsymbol{D}_{\mathrm{p}}^{\mathrm{a}}$, is then defined by the associated flow rule

$$\boldsymbol{D}_{\mathrm{p}}^{\mathrm{a}} = \frac{\dot{\gamma}_{\mathrm{p}}^{\mathrm{a}}}{\tau^{\mathrm{a}}} \boldsymbol{\sigma}_\star^{\mathrm{a}^{\mathrm{d}}}. \tag{4.13}$$

By choosing the plastic spin to equal zero, the plastic velocity gradient is given by $\boldsymbol{L}_{\mathrm{p}}^{\mathrm{a}} = \boldsymbol{D}_{\mathrm{p}}^{\mathrm{a}}$. Using the Arruda–Boyce eight-chain network model of rubber elasticity (Arruda and Boyce, 1993), the back-stress tensor is expressed as

$$\boldsymbol{H}^{\mathrm{a}} = \mu_{\mathrm{R}} \frac{\sqrt{N}}{\lambda_{\mathrm{ch}}} \mathcal{L}^{-1}\left(\frac{\lambda_{\mathrm{ch}}}{\sqrt{N}}\right) \left(\boldsymbol{B}_{\mathrm{p}}^{\mathrm{a}} - \lambda_{\mathrm{ch}}^2 \boldsymbol{I}\right), \tag{4.14}$$

where N represents the number of rigid links between entanglements and μ_{R} is proportional to the initial stiffness. Furthermore, $\boldsymbol{B}_{\mathrm{p}}^{\mathrm{a}} = \boldsymbol{F}_{\mathrm{p}}^{\mathrm{a}} \cdot \boldsymbol{F}_{\mathrm{p}}^{\mathrm{a}^{\mathrm{T}}}$ is the plastic left Cauchy–Green deformation tensor, $\lambda_{\mathrm{ch}} = \sqrt{\frac{1}{3}\mathrm{tr}(\boldsymbol{B}_{\mathrm{p}}^{\mathrm{a}})}$ is the stretch of each chain in the eight-chain network model and $\mathcal{L}^{-1}$ is the inverse[5] of the Langevin function $\mathcal{L}(\beta) = \coth(\beta) - 1/\beta$.

4.3 Micromechanical model

When cooled from the melt, many polymers, such as for example polyethylene, possess a semicrystalline structure. These materials often show a spherulitic morphology (Bassett and Hodge, 1981; Bassett et al., 1981; G'Sell and Dahoun, 1994). Each spherulite consists of a radial assembly of thin crystalline lamellae which are separated by amorphous layers. Furthermore, in thin films crystallized on a substrate, a sheaflike morphology with preferentially-oriented crystalline lamellae is found (Bartczak et al., 1999c).

---

[5] The inverse Langevin function is approximated by (Bergström and Boyce, 2001):

$$\mathcal{L}^{-1}(x) = \begin{cases} 1.31446 \tan(1.58986\, x) + 0.91209\, x & \text{if} \quad |x| < 0.84136 \\ \dfrac{1}{\mathrm{sign}(x) - x} & \text{if} \quad 0.84136 \leq |x| < 1 \end{cases}$$

4.3.1 Composite inclusion

The mechanical behavior of the microscopically heterogeneous material is modeled by an aggregate of layered two-phase composite inclusions as was used by Lee et al. (1993a,b, 1999, 2002) for rigid/viscoplastic material behavior. Each separate composite consists of a crystalline lamella which is mechanically coupled to its corresponding amorphous layer, as is represented in Figure 4.4. The stress and deformation fields within each phase are assumed to be piecewise homogeneous; however, they may differ between the two coupled phases. The volume fractions of the respective phases are given by the relative thicknesses f^{a} and $f^{\mathrm{c}} = 1 - f^{\mathrm{a}}$, which, because of elastic dilatations, are given by

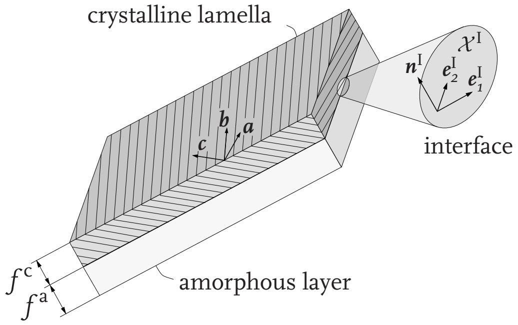

Figure 4.4 / Schematic illustration of a layered two-phase composite inclusion.

$$f^{\pi} = \frac{f^{\pi}_{o} J^{\pi}}{f^{\mathrm{a}}_{o} J^{\mathrm{a}} + (1 - f^{\mathrm{a}}_{o}) J^{\mathrm{c}}} \quad ; \quad \pi = \mathrm{a}, \mathrm{c}, \tag{4.15}$$

with $J^{\pi} = \det(\boldsymbol{F}^{\pi})$ the actual volume ratio of each constituent phase and f^{π}_{o}, the corresponding initial volume fraction. The inclusion-averaged deformation gradient $\boldsymbol{F}^{\mathrm{I}}$, where the superscript "I" denotes the composite inclusion, and the inclusion-averaged Cauchy stress $\boldsymbol{\sigma}^{\mathrm{I}}$ are given by the volume-weighted average of the respective phases:

$$\boldsymbol{F}^{\mathrm{I}} = f^{\mathrm{a}}_{o} \boldsymbol{F}^{\mathrm{a}} + (1 - f^{\mathrm{a}}_{o}) \boldsymbol{F}^{\mathrm{c}}, \tag{4.16}$$

$$\boldsymbol{\sigma}^{\mathrm{I}} = f^{\mathrm{a}} \boldsymbol{\sigma}^{\mathrm{a}} + (1 - f^{\mathrm{a}}) \boldsymbol{\sigma}^{\mathrm{c}}. \tag{4.17}$$

On the interface between the crystalline lamella and the amorphous layer, kinematical coupling is maintained by enforcing compatibility on the deformation gradients. Let $\boldsymbol{n}^{\mathrm{I}}_{o} = \boldsymbol{e}^{\mathrm{I}}_{o3}$ denote the unit normal vector of the interface in the reference configuration Ω_o, with $\boldsymbol{e}^{\mathrm{I}}_{oi}$ a local orthonormal vector basis. Furthermore, let $\boldsymbol{x}^{\mathrm{I}}_{o}$ denote an arbitrary vector in the plane of the interface $\mathcal{X}^{\mathrm{I}}_{0}$, spanned by $\boldsymbol{e}^{\mathrm{I}}_{01}$ and $\boldsymbol{e}^{\mathrm{I}}_{02}$. Then, the interface compatibility condition, in combination with volume-averaging, can be written as

$$\boldsymbol{F}^{\mathrm{c}}\cdot\boldsymbol{x}^{\mathrm{I}}_{0} = \boldsymbol{F}^{\mathrm{a}}\cdot\boldsymbol{x}^{\mathrm{I}}_{0} = \boldsymbol{F}^{\mathrm{I}}\cdot\boldsymbol{x}^{\mathrm{I}}_{0} \quad \forall\, \boldsymbol{x}^{\mathrm{I}}_{0} \in \mathcal{X}^{\mathrm{I}}_{0}. \tag{4.18}$$

Moreover, traction continuity on the interface is given by

$$\boldsymbol{\sigma}^{\mathrm{c}}\cdot\boldsymbol{n}^{\mathrm{I}} = \boldsymbol{\sigma}^{\mathrm{a}}\cdot\boldsymbol{n}^{\mathrm{I}} = \boldsymbol{\sigma}^{\mathrm{I}}\cdot\boldsymbol{n}^{\mathrm{I}}, \tag{4.19}$$

with $\boldsymbol{n}^{\mathrm{I}}$ the unit normal of the interface in the current configuration Ω. A similar deformation gradient-based framework for compatibility and averaging within two-phase laminates has been used by Ortiz et al. (2000) and Evers et al. (2001, 2002) for metallic materials.

4.3.2 Inclusion interaction law

To relate the volume-averaged mechanical behavior of each composite inclusion to the imposed deformation for an aggregate of inclusions, a local–global interaction law is formulated. The most widely used interaction law in polycrystal plasticity, is the Taylor interaction model (Taylor, 1938; Hutchinson, 1976; Asaro and Needleman, 1985). This model however, may lead to unreasonably high stresses since the crystalline phase of the polymer material under consideration is strongly anisotropic. Because of the chain inextensibility in the crystalline phase, Lee et al. (1993a,b) proposed a Sachs-type interaction model and two more hybrid interaction models to relate the volume-averaged deformation and stress within the inclusion to the mesoscopic fields. In the Sachs interaction model (Sachs, 1928; Lee et al., 1993a), micromechanical equilibrium is addressed in a stronger sense, in combination with a weakened measure of compatibility. Nikolov et al. recently used a two-phase composite inclusion model based on a self-consistent homogenization method (Nikolov and Doghri, 1998, 2000) and a Sachs-type method (Nikolov et al., 2002) for the micromechanically-based small strain constitutive behavior of HDPE. In this thesis, the ability of four interaction models (Taylor, Sachs, and two Taylor/Sachs hybrids) to simulate the elasto-viscoplastic stress–strain behavior of semicrystalline polymers is investigated. The class of hybrid-inclusion models was introduced by Lee et al. (1993a,b) for rigid/viscoplastic composite inclusions in a rate formulation; here, it is developed in a deformation gradient-based framework. This framework is suitable for use in a finite element context, is virtually independent of the particular choice of the interaction model, and includes arbitrary constitutive models for the constituent components.

The self-consistency conditions (Hill, 1972) for global equilibrium and compatibility require the mesoscopic fields to equal the appropriately averaged local quantities. Within the current framework, the mesoscopic deformation gradient, $\bar{\boldsymbol{F}}$, of an aggregate composed of N_{I} inclusions, is assumed to be given by:

$$\left(\frac{\bar{J}}{J_{\Sigma}}\right)^{\frac{1}{3}} \sum_{i=1}^{N_{\mathrm{I}}} f_{\mathrm{o}}^{\mathrm{I}^i} \boldsymbol{F}^{\mathrm{I}^i} = \bar{\boldsymbol{F}}, \tag{4.20}$$

with

$$\bar{J} = \sum_{i=1}^{N_{\mathrm{I}}} f_{\mathrm{o}}^{\mathrm{I}^i} J^{\mathrm{I}^i} \quad \text{and} \quad J_{\Sigma} = \det\left(\sum_{i=1}^{N_{\mathrm{I}}} f_{\mathrm{o}}^{\mathrm{I}^i} \boldsymbol{F}^{\mathrm{I}^i}\right), \tag{4.21}$$

with $f_{\mathrm{o}}^{\mathrm{I}^i} = 1/N_{\mathrm{I}}$ the initial volume fraction of the ith inclusion and $J^{\mathrm{I}^i} = \det(\boldsymbol{F}^{\mathrm{I}^i})$. The scaling factor $\left(\bar{J}/J_{\Sigma}\right)^{\frac{1}{3}}$ is added to assure volumetric consistency[6], which is written as

$$\bar{V} = \sum_{i=1}^{N_{\mathrm{I}}} V^{\mathrm{I}^i}, \tag{4.22}$$

with $\bar{V}$ the actual global volume and V^{I^i} the actual volume of the ith inclusion. The mesoscopic Cauchy stress tensor, $\bar{\boldsymbol{\sigma}}$, is assumed to be given by:

$$\sum_{i=1}^{N_{\mathrm{I}}} f^{\mathrm{I}^i} \boldsymbol{\sigma}^{\mathrm{I}^i} = \bar{\boldsymbol{\sigma}}, \tag{4.23}$$

where, because of elastic dilatations, the volume fractions of the inclusions evolve as

$$f^{\mathrm{I}^i} = \frac{f_{\mathrm{o}}^{\mathrm{I}^i} J^{\mathrm{I}^i}}{\sum_{j=1}^{N_{\mathrm{I}}} f_{\mathrm{o}}^{\mathrm{I}^j} J^{\mathrm{I}^j}} \quad ; \quad i = 1, \ldots, N_{\mathrm{I}}. \tag{4.24}$$

Taylor-inclusion model

The Taylor interaction law assumes that the local inclusion-averaged deformation for each composite inclusion is equal to the mesoscopically imposed deformation of the aggregate:

$$\boldsymbol{F}^{\mathrm{I}^i} = \bar{\boldsymbol{F}} \quad ; \quad i = 1, \ldots, N_{\mathrm{I}}. \tag{4.25}$$

---

[6] For the Taylor-inclusion model, both volumetric consistency and consistency of work are trivially satisfied. For the Sachs-inclusion and the hybrid-inclusions models, in the current formulation, a correction term is used to enforce volumetric consistency; consistency of work is, however, not satisfied.

This assumption assures local kinematical compatibility. The mesoscopic Cauchy stress tensor is taken to be the volume-averaged Cauchy stress of the aggregate, Equation (4.23), where, due to assumption (4.25), the volume fraction f^{I^i} remains constant. In this model, global equilibrium is provided by the global volume-average, whereas local equilibrium of the inclusions is not addressed.

Sachs-inclusion model

The Sachs interaction law assumes that the volume-averaged Cauchy stress of each inclusion is equal to the mesoscopic Cauchy stress of the aggregate:

$$\boldsymbol{\sigma}^{\mathrm{I}^i} = \bar{\boldsymbol{\sigma}} \quad ; \quad i = 1, \dots, N_{\mathrm{I}}, \tag{4.26}$$

which provides local equilibrium between the composite inclusions. Global kinematical compatibility is provided by the assumption that the mesoscopic deformation equals the appropriately scaled volume-average of all inclusion-averaged deformations, viz. Equations (4.20) and (4.21). To complete the interaction model, the rotation of each inclusion is assumed to equal the mesoscopically imposed rotation:

$$\boldsymbol{R}^{\mathrm{I}^i} = \bar{\boldsymbol{R}} \quad ; \quad i = 1, \dots, N_{\mathrm{I}}, \tag{4.27}$$

where $\boldsymbol{R}^{\mathrm{I}^i}$ and $\bar{\boldsymbol{R}}$ are the rotation tensors obtained from the polar decomposition of the deformation gradients $\boldsymbol{F}^{\mathrm{I}^i}$ and $\bar{\boldsymbol{F}}$, respectively. Then, Equation (4.20) can be rewritten in terms of the corresponding right stretch tensors:

$$\left(\frac{\bar{J}}{J_{\Sigma}}\right)^{\frac{1}{3}} \sum_{i=1}^{N_{\mathrm{I}}} f_{o}^{\mathrm{I}^i} \boldsymbol{U}^{\mathrm{I}^i} = \bar{\boldsymbol{U}}. \tag{4.28}$$

Hybrid-inclusion models

In this paragraph, a class of hybrid interaction models is discussed. These hybrid-inclusion models for lamellar composites, which were introduced by Lee et al. (1993a,b), constitute an intermediate approach between the upper bound Taylor- and the lower bound Sachs-inclusion models. In the hybrid interaction models, local–global compatibility conditions are assumed for the projections of the inclusion-averaged fields for which intrainclusion equilibrium conditions were formulated. Inversely, local–global equilibrium conditions are chosen for the components of the inclusion-averaged fields that are subjected to intrainclusion compatibility.

Let the following fourth-order subspace projection tensors, based on the orientation of the amorphous/crystalline interface plane $\mathcal{X}^{\mathrm{I}^i}$ of the ith inclusion, be defined as

$$ {}^4\mathcal{P}_{\mathrm{n}}^{\mathrm{I}^i} = \sum_{j=1}^{3} \boldsymbol{e}_j^{\mathrm{I}^i} \otimes \boldsymbol{n}^{\mathrm{I}^i} \otimes \boldsymbol{n}^{\mathrm{I}^i} \otimes \boldsymbol{e}_j^{\mathrm{I}^i}, \tag{4.29} $$

$$ {}^4\mathcal{P}_{\mathrm{x}}^{\mathrm{I}^i} = {}^4\mathcal{I} - {}^4\mathcal{P}_{\mathrm{n}}^{\mathrm{I}^i}, \tag{4.30} $$

with ${}^4\mathcal{I}$ the fourth-order identity tensor. The interface conditions, Equation (4.18) and (4.19), can be rewritten in terms of the following subspace projections:

$$ {}^4\mathcal{P}_{\mathrm{x}_0}^{\mathrm{I}^i} : \boldsymbol{F}^{\mathrm{c}^i} = {}^4\mathcal{P}_{\mathrm{x}_0}^{\mathrm{I}^i} : \boldsymbol{F}^{\mathrm{a}^i} = {}^4\mathcal{P}_{\mathrm{x}_0}^{\mathrm{I}^i} : \boldsymbol{F}^{\mathrm{I}^i} \quad ; \quad i = 1, \ldots, N_{\mathrm{I}}, \tag{4.31} $$

$$ {}^4\mathcal{P}_{\mathrm{n}}^{\mathrm{I}^i} : \boldsymbol{\sigma}^{\mathrm{c}^i} = {}^4\mathcal{P}_{\mathrm{n}}^{\mathrm{I}^i} : \boldsymbol{\sigma}^{\mathrm{a}^i} = {}^4\mathcal{P}_{\mathrm{n}}^{\mathrm{I}^i} : \boldsymbol{\sigma}^{\mathrm{I}^i} \quad ; \quad i = 1, \ldots, N_{\mathrm{I}}, \tag{4.32} $$

where the subscript "0" refers to the lamellar orientation in the reference configuration. Since the interface condition (4.31) acts upon the ${}^4\mathcal{P}_{\mathrm{x}_0}^{\mathrm{I}^i}$ subspace projection of the deformation gradient, and provides certain constraints on these components of the inclusion-averaged deformation, a Sachslike interaction law is assumed for the ${}^4\mathcal{P}_{\mathrm{x}}^{\mathrm{I}^i}$ subspace projections of the inclusion-averaged stress. Furthermore, since a certain measure of equilibrium is provided for the inclusion-averaged stress by the interface condition (4.32), acting on the ${}^4\mathcal{P}_{\mathrm{n}}^{\mathrm{I}^i}$ subspace projections of $\boldsymbol{\sigma}^{\mathrm{I}^i}$, a Taylorlike interaction law is assumed for the corresponding ${}^4\mathcal{P}_{\mathrm{n}_0}^{\mathrm{I}^i}$ subspace projection of the inclusion-averaged deformation.

A consistent set of boundary conditions must be prescribed for the mesoscopic deformation and stress fields. Let the mesoscopic rotations $\bar{\boldsymbol{R}}$ be prescribed. Then, additionally, a total of six components of $\bar{\boldsymbol{U}}$ and $\bar{\boldsymbol{\sigma}}$ must be prescribed. The remaining six components need to be determined by the inclusion model.

In the Taylor-inclusion model, the mesoscopic compatibility conditions are satisfied trivially, whereas in the Sachs-inclusion model, the mesoscopic equilibrium conditions are satisfied trivially. Since the inclusion-averaged rotations are assumed to equal the mesoscopic rotations, $\boldsymbol{R}^{\mathrm{I}^i} = \bar{\boldsymbol{R}}$, the mesoscopic compatibility conditions reduce to (4.28). The six unknown mesoscopic components can be obtained from the remaining self-consistency conditions. However, for the hybrid interaction models that are considered here, neither conditions (4.23) or (4.28) are satisfied trivially. In order to satisfy the 12 conditions of consistency, six more auxiliary unknowns must be introduced (Lee et al., 1993a). Different choices for these auxiliary unknowns can be made, leading to different versions of an hybrid interaction model.

Some considerations about the consequences of the hybrid formulations for the conditioning of the problem in combination with initial and current textures will be given in Chapter 8.

$\hat{\boldsymbol{\sigma}}$-inclusion model

In the $\hat{\boldsymbol{\sigma}}$-inclusion model, a Taylorlike assumption is used for the ${}^4\mathcal{P}^{\mathrm{I}^i}_{\mathrm{n_o}}$ subspace projection of $\boldsymbol{U}^{\mathrm{I}^i}$. Furthermore, an auxiliary unknown symmetric tensor $\hat{\boldsymbol{\sigma}}$, with the dimension of stress, is introduced. Then, the subspace projection ${}^4\mathcal{P}^{\mathrm{I}^i}_{\mathrm{x}}$ of the inclusion averaged Cauchy stress is assumed to equal the corresponding subspace projection of $\hat{\boldsymbol{\sigma}}$. The interaction model is completed by assuming the rotation of each inclusion to equal the mesoscopically prescribed rotation:

$$
\begin{aligned}
{}^4\mathcal{P}^{\mathrm{I}^i}_{\mathrm{x}} : \boldsymbol{\sigma}^{\mathrm{I}^i} &= {}^4\mathcal{P}^{\mathrm{I}^i}_{\mathrm{x}} : \hat{\boldsymbol{\sigma}} \quad ; \quad i = 1, \ldots, N_{\mathrm{I}}, && (4.33)\\
{}^4\mathcal{P}^{\mathrm{I}^i}_{\mathrm{n_o}} : \boldsymbol{U}^{\mathrm{I}^i} &= {}^4\mathcal{P}^{\mathrm{I}^i}_{\mathrm{n_o}} : \bar{\boldsymbol{U}} \quad ; \quad i = 1, \ldots, N_{\mathrm{I}}, && (4.34)\\
\boldsymbol{R}^{\mathrm{I}^i} &= \bar{\boldsymbol{R}} \quad ; \quad i = 1, \ldots, N_{\mathrm{I}}. && (4.35)
\end{aligned}
$$

$\hat{\boldsymbol{U}}$-inclusion model

In the $\hat{\boldsymbol{U}}$-inclusion model, six auxiliary deformationlike unknowns are introduced. Then, a Sachslike interaction law is used for the ${}^4\mathcal{P}^{\mathrm{I}^i}_{\mathrm{x}}$ subspace projection of the inclusion-averaged stress. The ${}^4\mathcal{P}^{\mathrm{I}^i}_{\mathrm{n_o}}$ subspace projection of the inclusion-averaged stretch is assumed to equal the corresponding subspace projection of the auxiliary unknowns $\hat{\boldsymbol{U}}$. Again, also the inclusion-averaged rotations are prescribed:

$$
\begin{aligned}
{}^4\mathcal{P}^{\mathrm{I}^i}_{\mathrm{x}} : \boldsymbol{\sigma}^{\mathrm{I}^i} &= {}^4\mathcal{P}^{\mathrm{I}^i}_{\mathrm{x}} : \bar{\boldsymbol{\sigma}} \quad ; \quad i = 1, \ldots, N_{\mathrm{I}}, && (4.36)\\
{}^4\mathcal{P}^{\mathrm{I}^i}_{\mathrm{n_o}} : \boldsymbol{U}^{\mathrm{I}^i} &= {}^4\mathcal{P}^{\mathrm{I}^i}_{\mathrm{n_o}} : \hat{\boldsymbol{U}} \quad ; \quad i = 1, \ldots, N_{\mathrm{I}}, && (4.37)\\
\boldsymbol{R}^{\mathrm{I}^i} &= \bar{\boldsymbol{R}} \quad ; \quad i = 1, \ldots, N_{\mathrm{I}}. && (4.38)
\end{aligned}
$$

4.4 Solution procedure

In this section, some numerical aspects concerning the solution procedure for the composite inclusion model are outlined. For this purpose, the time domain is subdivided into discrete time steps. First, the time-integration of the viscoplastic deformation of the respective phases is discussed. For each discrete time step, a set of nonlinear equations, comprising the interaction law, the local interface conditions and the volume-averaging equations, is solved. Thereafter, the interface normals are explicitly updated, based on convected material vectors within the planar interface.

4.4.1 Time-integration of plastic flow

The plastic deformation gradient of each phase is obtained from time-integration of the plastic flow rule $\dot{\boldsymbol{F}}_{\rm p}^{\pi} = \boldsymbol{L}_{\rm p}^{\pi} \cdot \boldsymbol{F}_{\rm p}^{\pi}$, with $\pi = {\rm a, c}$, denoting either the amorphous phase or the crystalline phase. If $\boldsymbol{L}_{\rm p}^{\pi}$ is assumed to be constant during an increment with length Δt, the plastic deformation at the end of this increment, at time level $t_{n+1} = t_n + \Delta t$, is given by

$$\boldsymbol{F}_{\rm p}(t_{n+1}) = \exp(\Delta t \boldsymbol{L}_{\rm p}) \cdot \boldsymbol{F}_{\rm p}(t_n), \tag{4.39}$$

where the superscript π is omitted. The tensor exponential is numerically evaluated by the Padé approximation (Weber, 1988), so that the incremental plastic deformation gradient is given by

$$\boldsymbol{F}_{\rm p_{inc}} = \exp(\Delta t \boldsymbol{L}_{\rm p}) \approx \left(\boldsymbol{I} - \frac{\Delta t}{2} \boldsymbol{L}_{\rm p} \right)^{-1} \cdot \left(\boldsymbol{I} + \frac{\Delta t}{2} \boldsymbol{L}_{\rm p} \right). \tag{4.40}$$

For finite increments, the determinant of the approximated exponential term may deviate slightly from unity, which is corrected by the following normalization:

$$\boldsymbol{F}_{\rm p}(t_{n+1}) = \tilde{\boldsymbol{F}}_{\rm p_{inc}} \cdot \boldsymbol{F}_{\rm p}(t_n) \quad \text{with} \quad \tilde{\boldsymbol{F}}_{\rm p_{inc}} = \left[\det(\boldsymbol{F}_{\rm p_{inc}}) \right]^{-\frac{1}{3}} \boldsymbol{F}_{\rm p_{inc}}. \tag{4.41}$$

4.4.2 Boundary value problem

For an aggregate of composite inclusions, a set of boundary conditions is prescribed for the global deformation and stress fields. Consider the right polar decomposition $\bar{\boldsymbol{F}} = \bar{\boldsymbol{R}} \cdot \bar{\boldsymbol{U}}$ of the volume-averaged deformation gradient. Then, certain components of $\bar{\boldsymbol{R}}$, $\bar{\boldsymbol{U}}$ and $\bar{\boldsymbol{\sigma}}$ are prescribed. For example, for uniaxial compression or tension in $\boldsymbol{e}_1$-direction, the following set of boundary conditions is imposed with respect to an orthonormal vector basis $\boldsymbol{e}_i$:

$$\bar{\boldsymbol{R}} = \boldsymbol{I} \quad ; \quad \bar{U}_{11} = \lambda(t), \tag{4.42}$$

$$\bar{\sigma}_{22} = \bar{\sigma}_{33} = \bar{\sigma}_{12} = \bar{\sigma}_{13} = \bar{\sigma}_{23} = 0. \tag{4.43}$$

Given these boundary conditions, a complete set of equations can be formed from the equations for interface compatibility (4.31) and traction equilibrium (4.32) in combination with the interaction laws (e.g. Equations (4.36) to (4.38) for the $\hat{\boldsymbol{U}}$-inclusion model), into which the equations for intrainclusion and interinclusion volume-averaging, (4.16)–(4.17), and (4.23), (4.21), and (4.28), respectively, are substituted. With the multiplicative decomposition given by Equation (4.1) and the material models discussed in Section 4.2, all these equations can be expressed in terms of the elastic deformation gradients $\boldsymbol{F}_{\mathrm{e}}^{\pi^i}$ of each phase $\pi = \mathrm{a}, \mathrm{c}$ of all N_{I} inclusions i. Figure 4.5 shows how these different aspects of the model are interconnected. Moreover, in Appendix A, the complete set of equations that are simultaneously solved is given for each interaction model.

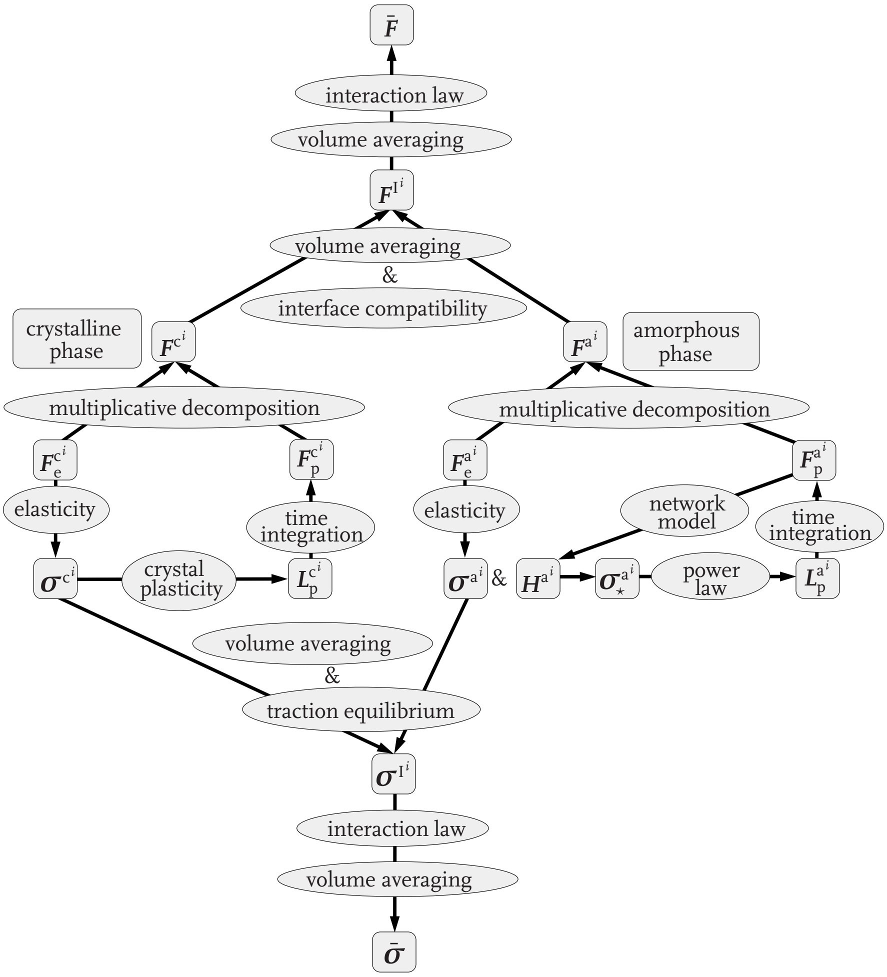
$\bar{\boldsymbol{F}}$
interaction law
volume averaging
$\boldsymbol{F}^{\mathrm{I}^i}$
volume averaging
&
interface compatibility
crystalline phase
$\boldsymbol{F}^{\mathrm{c}^i}$
$\boldsymbol{F}^{\mathrm{a}^i}$
amorphous phase
multiplicative decomposition
multiplicative decomposition
$\boldsymbol{F}_{\mathrm{e}}^{\mathrm{c}^i}$
$\boldsymbol{F}_{\mathrm{p}}^{\mathrm{c}^i}$
$\boldsymbol{F}_{\mathrm{e}}^{\mathrm{a}^i}$
$\boldsymbol{F}_{\mathrm{p}}^{\mathrm{a}^i}$
elasticity
time integration
elasticity
network model
time integration
$\boldsymbol{\sigma}^{\mathrm{c}^i}$
crystal plasticity
$\boldsymbol{L}_{\mathrm{p}}^{\mathrm{c}^i}$
$\boldsymbol{\sigma}^{\mathrm{a}^i}$ & $\boldsymbol{H}^{\mathrm{a}^i}$
$\boldsymbol{\sigma}_{\star}^{\mathrm{a}^i}$
power law
$\boldsymbol{L}_{\mathrm{p}}^{\mathrm{a}^i}$
volume averaging
&
traction equilibrium
$\boldsymbol{\sigma}^{\mathrm{I}^i}$
interaction law
volume averaging
$\bar{\boldsymbol{\sigma}}$

Figure 4.5 / Schematic overview of the elasto-viscoplastic composite inclusion model.

For each increment, this set of nonlinear equations is solved by a Newton–Raphson iteration procedure. For numerical efficiency, the unprescribed mesoscopic stretches and unprescribed mesoscopic stress components are considered as extra unknowns for the $\hat{\boldsymbol{\sigma}}$-inclusion and the $\hat{\boldsymbol{U}}$-inclusion model, respectively.

4.4.3 Morphological texture update

The evolution of the morphological texture, i.e. the change of orientation of the amorphous/crystalline interfaces, is accounted for explicitly. During an increment, the orientations of the lamellar normals are fixed. After each increment, the inclusion normals are updated, based on convected material vectors within the planar interface (Lee et al., 1993a). For this purpose, let $\boldsymbol{x}_{01}^{\mathrm{I}^i}$ and $\boldsymbol{x}_{02}^{\mathrm{I}^i}$ be two independent vectors at time $t = 0$ in the amorphous/crystalline interface $\mathcal{X}_0^{\mathrm{I}^i}$ of the ith composite. At the current time t, these vectors are convected to

$$\boldsymbol{x}_1^{\mathrm{I}^i} = \boldsymbol{F}^i \cdot \boldsymbol{x}_{01}^{\mathrm{I}^i} \quad \text{and} \quad \boldsymbol{x}_2^{\mathrm{I}^i} = \boldsymbol{F}^i \cdot \boldsymbol{x}_{02}^{\mathrm{I}^i}, \tag{4.44}$$

where $\boldsymbol{F}^i$ can be either $\boldsymbol{F}^{\mathrm{a}^i}$, $\boldsymbol{F}^{\mathrm{c}^i}$ or $\boldsymbol{F}^{\mathrm{I}^i}$. The interface unit normal $\boldsymbol{n}^{\mathrm{I}^i}$ is then obtained by

$$\boldsymbol{n}^{\mathrm{I}^i} = \frac{(\boldsymbol{F}^i \cdot \boldsymbol{x}_{01}^{\mathrm{I}^i}) \times (\boldsymbol{F}^i \cdot \boldsymbol{x}_{02}^{\mathrm{I}^i})}{\| (\boldsymbol{F}^i \cdot \boldsymbol{x}_{01}^{\mathrm{I}^i}) \times (\boldsymbol{F}^i \cdot \boldsymbol{x}_{02}^{\mathrm{I}^i}) \|}. \tag{4.45}$$

Since $(\boldsymbol{F}^i \cdot \boldsymbol{x}_{01}^{\mathrm{I}^i}) \times (\boldsymbol{F}^i \cdot \boldsymbol{x}_{02}^{\mathrm{I}^i}) = \det(\boldsymbol{F}^i) \boldsymbol{F}^{i^{-\mathrm{T}}} \cdot \boldsymbol{n}_0^{\mathrm{I}^i}$, Equation (4.45) can be rewritten as

$$\boldsymbol{n}^{\mathrm{I}^i} = \frac{\boldsymbol{F}^{i^{-\mathrm{T}}} \cdot \boldsymbol{n}_0^{\mathrm{I}^i}}{\| \boldsymbol{F}^{i^{-\mathrm{T}}} \cdot \boldsymbol{n}_0^{\mathrm{I}^i} \|}. \tag{4.46}$$

4.5 High density polyethylene

In the following sections, the presented elasto-viscoplastic composite inclusion models are used to simulate the mechanical behavior of initially isotropic HDPE. The spherulitic structure of melt-crystallized HDPE is represented by an aggregate of 125 composite inclusions with randomly generated initial orientations of the crystallographic phases. The HDPE crystal lattice, which was shown in Figure 4.2, is orthorhombic, with the $\boldsymbol{c}$-axis corresponding to the molecular chain direction, and with lattice parameters $a = 7.4$ Å, $b = 4.9$ Å, and $c = 2.5$ Å (G'Sell and Dahoun, 1994; Mandelkern and Alamo, 1999). The initially random distribution of orientations of the principal lattice directions is represented by equal area pole figures in Figure 4.6(a)–(c). Experimental studies of melt-crystallized polyethylene show that lamellar surfaces are of the $\{h0l\}$-type, where the angle between the chain direction $\boldsymbol{c}$ and the lamellar normal $\boldsymbol{n}$ varies between 20° and 40° (Keller and Sawada, 1964; Bassett and Hodge, 1981). Gautam et al. (2000) have found by molecular simulations the $\{201\}$ planes to provide the lowest amorphous/crystalline interface energy. In this thesis, the initial angle between $\boldsymbol{c}_0$ and $\boldsymbol{n}_0^{\mathrm{I}}$ is set at 35°, corresponding to the $\{201\}$ planes. The resulting initial orientations of the lamellar normals are shown in Figure 4.6(d).

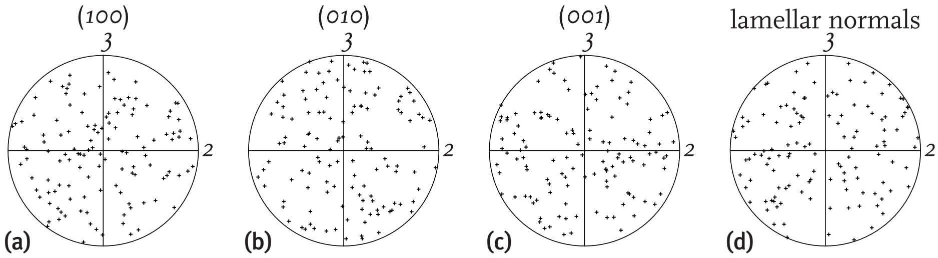

Figure 4.6 / Equal area projection pole figures representing the initially random orientation distribution of (a)–(c) the principal crystallographic lattice directions, and (d) the lamellar interface normals. The projection direction corresponds to the axial loading direction for uniaxial compression or tension.

In the crystalline phase of HDPE, eight physically distinct slip systems[7] can be distinguished, which are summarized in Table 4.1. This set of slip systems effectively comprises four independent deformation modes (Cotton et al., 1991). The molecular chain axis, $\boldsymbol{c}$, is a constrained direction and therefore in this direction no plastic deformation is possible. The two most easily activated slip systems are the (100)[001] chain slip system and the (100)[010] transverse slip system. In Table 4.1, also the resistances g^α at room temperature of all slip systems are given, normalized to $\tau_0 \equiv g^{(100)[001]} = 8$ MPa, the lowest slip resistance (Bartczak et al., 1992a; Lee et al., 1993a). Strain hardening on the slip systems of the crystalline lamellae is neglected.

	Slip system	g^α/τ_0
Chain slip	(100)[001]	1.0
	(010)[001]	2.5
	{110}[001]	2.5
Transverse slip	(100)[010]	1.66
	(010)[100]	2.5
	$\{110\}\langle 1\bar{1}0\rangle$	2.2

Table 4.1 / Slip systems of HDPE and the normalized resistances (Bartczak et al., 1992a; Lee et al., 1993a).

---

[7] Using the Miller index notation system (e.g. Kocks et al., 1998), the six displayed systems in Table 4.1, represent eight physically distinct slip systems.

The elastic behavior of the crystalline phase is anisotropic, with a relatively high stiffness in the molecular chain direction. The elastic moduli used for the crystalline domains are given in Table 4.2 (using Voigt's notation for Equation (4.6)).

C_{11}	C_{33}	C_{12}	C_{13}	C_{44}	C_{66}
7	81	3.8	4.7	1.5	1.6

Table 4.2 / Elastic constants [GPa] for the crystalline domains (Choy and Leung, 1985).

Following Lee et al. (1993a), the viscoplastic rate exponents of the amorphous and the crystalline phase are set to an equal value of $n = 9$. Moreover, also the reference shear rate of the amorphous phase is set equal to that of the crystalline phase, $\dot{\gamma}_0 = 10^{-3}\,\mathrm{s}^{-1}$. The reference initial shear strength of the amorphous phase is written as $\tau_0^{\mathrm{a}} \equiv a\tau_0$. The viscoplastic parameters of the amorphous phase, taken from Lee et al. (1993a), are summarized in Table 4.3. The typical crystallinity of HDPE is 70 percent; therefore the initial amorphous volume fraction is set to $f_0^{\mathrm{a}} = 0.3$.

$\dot{\gamma}_0$ [s^{-1}]	n	a	μ_{R} [MPa]	N
10^{-3}	9	1.2	1.6	49

Table 4.3 / Viscoplastic properties of the amorphous phase (Lee et al., 1993a).

For the elastic behavior of the amorphous phase, an isotropic generalized neo-Hookean relationship is used. In this model, the material is characterized by the bulk modulus κ^{a} and the shear modulus G^{a}. The bulk modulus is chosen to be 2 GPa. The influence of the amorphous shear modulus on the initial mesoscopic behavior is presented in Figure 4.7 for constant strain rate uniaxial compression, with stretch ratio history $\lambda(t) = \exp(-\dot{\varepsilon}t)$ and $\dot{\varepsilon} = 10^{-3}\,\mathrm{s}^{-1}$, for each interaction model. For the Taylor-inclusion model, the initial mesoscopic elastic modulus is approximately linearly dependent on the shear modulus of the amorphous phase, with $\bar{E} \to 1.9$ GPa as G^{a} approaches zero. For the Sachs-inclusion model however, the mesoscopic elastic behavior depends on the local amorphous elastic behavior in a nonlinear way, with $\bar{E} \to 0$ for $G^{\mathrm{a}} \to 0$. For the $\hat{\boldsymbol{\sigma}}$-inclusion model, the initial mesoscopic elastic behavior approximately equals the behavior of the Taylor-inclusion model. The $\hat{\boldsymbol{U}}$-inclusion model however, shows a dependency that is in between the extreme Taylor- and Sachs-inclusion models. In the following investigations, the shear modulus of the amorphous phase is selected to be $G^{\mathrm{a}} = 35$ MPa.

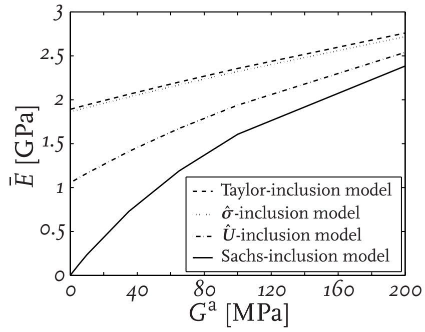

Figure 4.7 / The mesoscopically observed initial modulus in uniaxial compression, as a function of the shear modulus of the amorphous phase, for each interaction law.

4.6 Monotonic uniaxial compression

In this application, the initially isotropic HDPE material is subjected to constant strain rate uniaxial compression with $\dot{\varepsilon} = 10^{-3}\ \mathrm{s}^{-1}$. Figure 4.8(a) shows the equivalent mesoscopic stress $\bar{\sigma}^{\mathrm{eq}} = \sqrt{\frac{3}{2}\bar{\boldsymbol{\sigma}}^{\mathrm{d}} : \bar{\boldsymbol{\sigma}}^{\mathrm{d}}}$, with $\bar{\boldsymbol{\sigma}}^{\mathrm{d}} = \bar{\boldsymbol{\sigma}} + \bar{p}\boldsymbol{I}$ the mesoscopic deviatoric stress tensor and $\bar{p} = -\frac{1}{3}\mathrm{tr}(\bar{\boldsymbol{\sigma}})$ the mesoscopic hydrostatic pressure, as a function of the imposed mesoscopic strain $\dot{\varepsilon}t = -\ln(\lambda)$ for each model. Table 4.4 provides a summary of the initial modulus and the 5 percent strain yield strength as computed by each model.

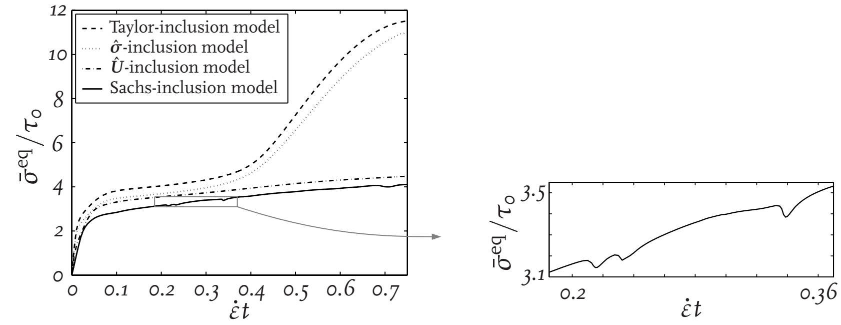

(a) **(b)**

Figure 4.8 / (a) The normalized equivalent mesoscopic stress, $\bar{\sigma}^{\mathrm{eq}}/\tau_0$, vs. the imposed mesoscopic logarithmic strain, $\dot{\varepsilon}t$, for HDPE in uniaxial compression, as predicted by the Taylor-inclusion model, the Sachs-inclusion model and the hybrid-inclusion models, and (b) an enlargement of the stress-dips exhibited by the Sachs-inclusion model.

In the Taylor-inclusion model, all inclusions are forced to undergo the same deformation, whereas in the Sachs-inclusion model, the mesoscopic deformation is accommodated mainly by relatively *weak* inclusions. Therefore, the Taylor-inclusion model shows

Model	$\bar{E}$ [GPa] at $\dot{\varepsilon}t = 0$	$\bar{\sigma}^{\mathrm{eq}}/\tau_0$ at $\dot{\varepsilon}t = 0.05$
Taylor-inclusion	2.0	3.4
Sachs-inclusion	0.73	2.6
$\hat{\boldsymbol{\sigma}}$-inclusion	2.0	3.0
$\hat{\boldsymbol{U}}$-inclusion	1.4	3.0

Table 4.4 / The mesoscopically observed initial elastic modulus $\bar{E}$ [GPa] and the normalized equivalent mesoscopic stress $\bar{\sigma}^{\mathrm{eq}}/\tau_0$ at $\dot{\varepsilon}t = 0.05$ as obtained by the Taylor-inclusion model, the Sachs-inclusion model and the hybrid-inclusion models in uniaxial compression.

a significantly higher initial modulus and postyield stress–strain behavior than the Sachs-inclusion model. In the rigid/viscoplastic Sachs-inclusion model of Lee et al. (1993a), using the same viscoplastic and hardening parameters, an initial yield stress of $\bar{\sigma}^{\mathrm{eq}}/\tau_0 = 2.9$ is found. In the present elasto-viscoplastic Sachs-inclusion model, plastic deformation starts at a lower stress. For relatively small strains in the plastic region ($\dot{\varepsilon}t = 0.05$ to 0.3), the stress–strain behavior of the two hybrid-inclusion models is approximately equal and is in between the Taylor- and the Sachs-inclusion model, which is in contrast with the results of Lee et al. (1993a) for the rigid/viscoplastic hybrid-inclusion models, which closely resemble the behavior of the rigid/viscoplastic Sachs-inclusion model. For mesoscopic strains higher than approximately 40 percent, both the Taylor-inclusion model and the $\hat{\boldsymbol{\sigma}}$-inclusion model, which is the most Taylorlike of the two hybrid models, show a strong strain hardening originating from the straining in the crystalline domains of inclusions with the crystallographic [001]-direction, which is the plastically inextensible molecular chain direction, approximately parallel to the corresponding interface normal and perpendicular to the compression direction.

In Figure 4.9, the equivalent phase-volume-averaged stresses and the phase-volume-averaged hydrostatic pressures are represented for all interaction models as obtained by the following definition of the phase-volume-averaged Cauchy stress tensor for each phase:

$$\bar{\boldsymbol{\sigma}}^{\pi} = \frac{1}{\bar{f}^{\pi}} \sum_{i=1}^{N_{\mathrm{I}}} f^{\mathrm{I}^i} f^{\pi^i} \boldsymbol{\sigma}^{\pi^i} \quad ; \quad \pi = \mathrm{a}, \mathrm{c}, \tag{4.47}$$

where the volume-averaged volume fractions of the amorphous and crystalline phase are defined as

$$\bar{f}^{\mathrm{a}} = \sum_{i=1}^{N_{\mathrm{I}}} f^{\mathrm{I}^i} f^{\mathrm{a}^i} \quad \text{and} \quad \bar{f}^{\mathrm{c}} = 1 - \bar{f}^{\mathrm{a}}, \tag{4.48}$$

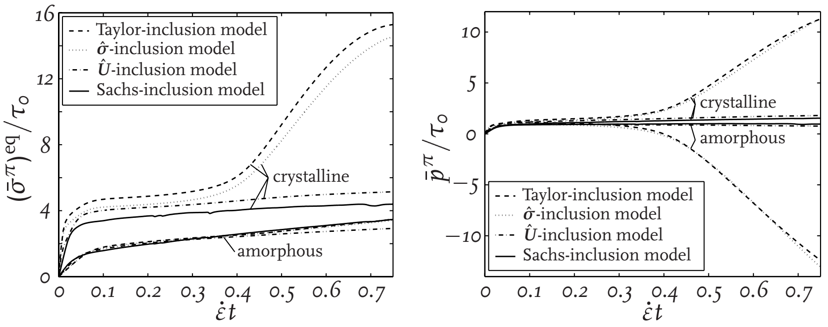

(a) (b)

Figure 4.9 / (a) The normalized equivalent phase-volume-averaged stress, $(\bar{\sigma}^{\pi})^{\mathrm{eq}}/\tau_0$, and (b) the normalized phase-volume-averaged hydrostatic pressure, $\bar{p}^{\pi}/\tau_0$, vs. the imposed mesoscopic strain $\dot{\varepsilon}t$ for HDPE in uniaxial compression, for the crystalline and the amorphous phase separately.

respectively. Then, the volume-averaged Cauchy stress tensor can be written as

$$\bar{\boldsymbol{\sigma}} = \bar{f}^{\mathrm{a}}\bar{\boldsymbol{\sigma}}^{\mathrm{a}} + (1-\bar{f}^{\mathrm{a}})\bar{\boldsymbol{\sigma}}^{\mathrm{c}}. \tag{4.49}$$

Figure 4.9(a) shows that the difference in equivalent stress–strain behavior between the models is due mainly to the response of the anisotropic crystalline phase. Moreover, Figure 4.9(b) shows that when the strong textural hardening sets in for the Taylor- and the $\hat{\boldsymbol{\sigma}}$-inclusion models, for $\dot{\varepsilon}t > 0.4$, also the phase-volume-averaged hydrostatic pressure in the crystalline phase strongly increases, which is partly compensated by a large negative hydrostatic pressure in the amorphous phase.

In Figure 4.10, the statistical variation in the normalized equivalent inclusion-averaged stress difference[8], $(\Delta\sigma^{\mathrm{I}^i})^{\mathrm{eq}}/\bar{\sigma}^{\mathrm{eq}}$, is shown, which is defined as

$$\Delta\boldsymbol{\sigma}^{\mathrm{I}^i} = \boldsymbol{\sigma}^{\mathrm{I}^i} - \bar{\boldsymbol{\sigma}} \quad ; \quad i = 1, \ldots, N_{\mathrm{I}}. \tag{4.50}$$

For the Taylor- and $\hat{\boldsymbol{\sigma}}$-inclusion models, a strong variation in equivalent inclusion-averaged stress is found for imposed mesoscopic strains larger than 0.4. For each inclusion, the angle between the molecular chains and the lamellar normal has initially been set to 35°. Upon deformation, the evolution of crystalline and morphological texture changes these angles. The strong increase of the equivalent inclusion-averaged stress for certain inclusions, corresponds to the alignment of molecular chains in the lamellar normal direction. For $\dot{\varepsilon}t > 0.4$, this angle is found to be smaller than 10° for the inclusions with relatively high equivalent stresses in the Taylor- and the $\hat{\boldsymbol{\sigma}}$-inclusion models. Moreover, these *stiff* inclusions are oriented with their lamellar normals, and thus

---

[8] The normalized equivalent inclusion-averaged stress difference is trivially zero for the Sachs-inclusion model.

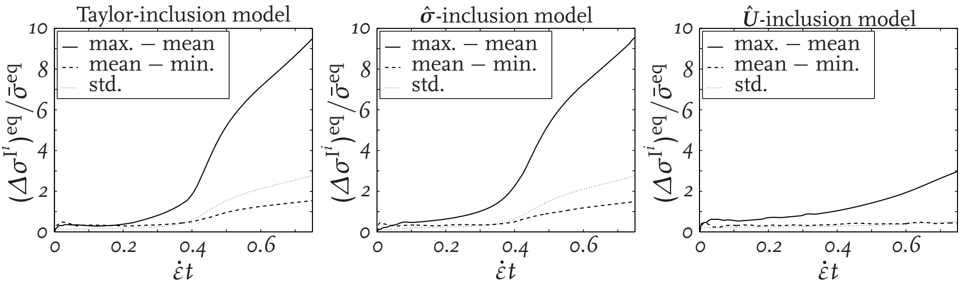

(a) (b) (c)

Figure 4.10 / Statistical variation in the normalized equivalent inclusion-averaged stress difference $(\Delta\sigma^{\mathrm{I}^i})^{\mathrm{eq}}/\bar{\sigma}^{\mathrm{eq}}$ in uniaxial compression for various interaction models. In each figure, the (maximum − mean) and (mean − minimum)-values are represented, along with the corresponding standard deviation.

the molecular chains in the crystalline phase, approximately in the transverse global direction. This direction corresponds with the directions of the maximum principal plastic stretch in the amorphous phase, corresponding to the evolution in the orientation of the molecular chains in the amorphous network model. The large variation in local stresses results in a severe deviation from local equilibrium. Consequently, for these conditions, the Taylor assumption is not appropriate. On the same account, also the hybrid $\hat{\boldsymbol{\sigma}}$-inclusion model is found to be unsuitable for the modeling of these anisotropic materials. The Sachs assumption states that all inclusion-averaged stresses equal the mesoscopic volume-averaged stress. Consequently, for this interaction model, no variation in stress is found. However, some small temporary reductions of the equivalent mesoscopic stress are found. These *stress-dips*, which are enlarged in Figure 4.8(b), are caused by relatively weak inclusions, which momentarily accommodate most of the prescribed deformation, as is shown in Figure 4.11, which represents the statistical variation in the normalized equivalent inclusion-averaged rate of deformation difference[9] per inclusion for all inclusion models, defined by

$$\Delta\dot{\boldsymbol{\varepsilon}}^{\mathrm{I}^i} = \dot{\boldsymbol{\varepsilon}}^{\mathrm{I}^i} - \dot{\bar{\boldsymbol{\varepsilon}}} \quad ; \quad i = 1, \ldots, N_{\mathrm{I}}. \tag{4.51}$$

For the Sachs-inclusion model, a large variation in strain rate is found, where the extreme rates correspond to the weak inclusions that cause the stress-dips. These inclusions are initially oriented with the molecular chains of their crystalline phases almost parallel to the compression direction and the initial (100) poles in the outer regions of the pole figure. In Figure 4.12, the crystallographic textures are given for all inclusion models at a mesoscopically prescribed strain $\dot{\varepsilon}t = 0.75$. To enrich the information shown in the

---

[9] The normalized equivalent inclusion-averaged rate of deformation difference is trivially zero for the Taylor-inclusion model.

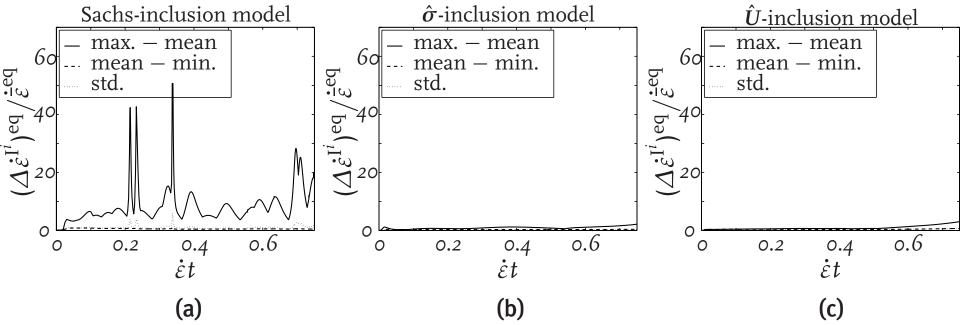

Figure 4.11 / Statistical variation in normalized equivalent strain rate difference per inclusion $(\Delta\dot{\varepsilon}^{I^i})^{\text{eq}}/\dot{\varepsilon}^{\text{eq}}$ in uniaxial compression for various interaction models. In each figure, the (maximum − mean) and (mean − minimum)-values are represented, along with the corresponding standard deviation.

plots, the mirror location of each pole with respect to the central point of the pole figure is also given. Upon deformation, for the (100) poles, the general tendency is to move towards the center and for the (001) poles to migrate towards a transverse direction. For the above-mentioned inclusions, these poles thereby pass through the 45° orientation, which corresponds to the most favorable orientation for crystallographic slip. In this weak orientation, this particular inclusion experiences a relatively large rate of plastic deformation. As a result of this deformation, the orientation of the inclusion changes to a less weak configuration, terminating the reduction of stress. For small strains, the stress prediction of the the $\hat{\boldsymbol{U}}$-inclusion model lies between the Taylor- and the Sachs-inclusion model. However, for larger strains, this model does not show the strong strain hardening as observed in the Taylor-inclusion model. Moreover, this model does not exhibit any stress-dips, as does the Sachs-inclusion model.

The Sachs-inclusion model exhibits the most distinct evolution of crystallographic texturing (see Figure 4.12). For the inclusions that accommodate most deformation, i.e. that are the most *active,* in the Sachs-inclusion model, the crystalline phase is found to initially deform mainly along the two easiest slip systems, i.e. the (100)[001] chain slip system and the (100)[010] transverse slip system, which is in agreement with observations by Bartczak et al. (1992b). In the Taylor-inclusion model however, all inclusions are forced to be active. This is accomplished by deformation on other slip systems than mentioned above for relatively stiff inclusions. The same behavior is observed for the $\hat{\boldsymbol{\sigma}}$-inclusion model, whereas in the $\hat{\boldsymbol{U}}$-inclusion model, initially, the $\{110\}\langle 1\bar{1}0\rangle$ slip systems are slightly active, besides the dominant slip systems on the (100) plane. In a later stage of the deformation process, the slip systems on the {110} plane become more active in both the Sachs- and the $\hat{\boldsymbol{U}}$-inclusion model. For all models, most (100) poles, which represent the crystallographic slip planes of the two easiest slip systems, are moving towards the compression direction, with, for the Sachs-inclusion model, a maximum intensity of poles at

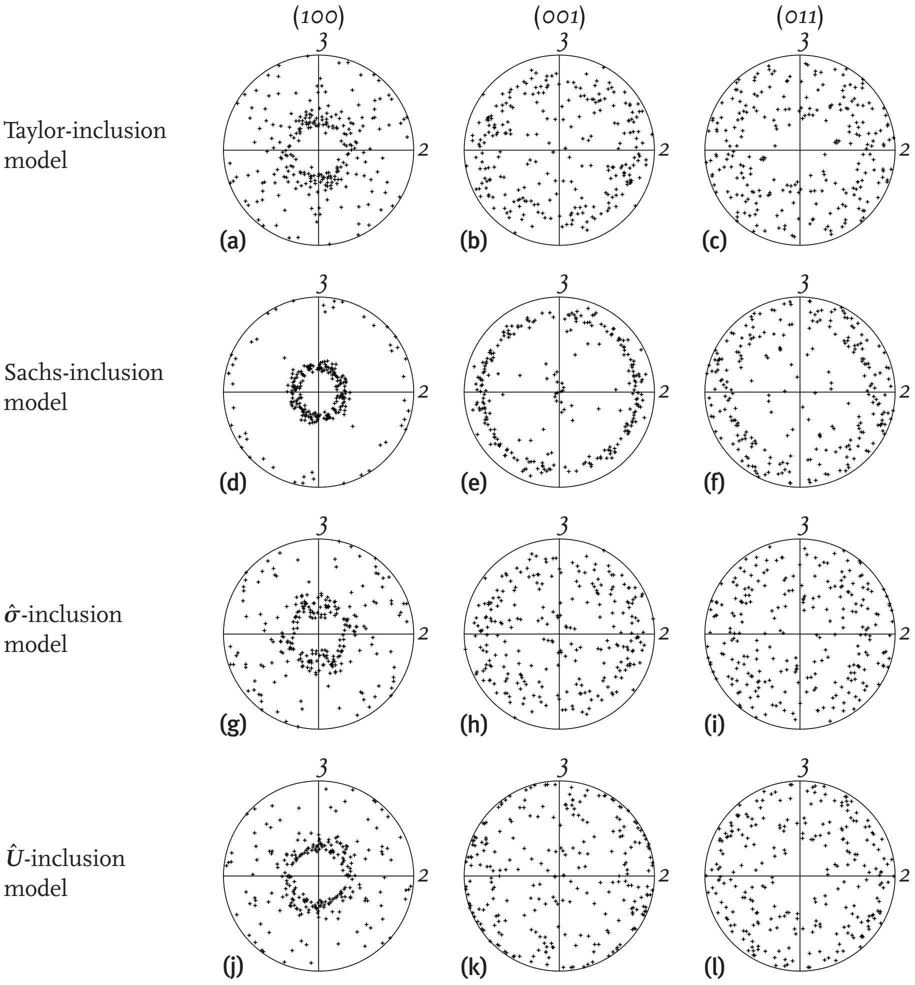

Figure 4.12 / Crystallographic textures as predicted by (a)–(c) the Taylor-inclusion model, (d)–(f) the Sachs-inclusion model, (g)–(i) the $\hat{\boldsymbol{\sigma}}$-inclusion model, and (j)–(l) the $\hat{\boldsymbol{U}}$-inclusion model, for HDPE subjected to uniaxial compression at a mesoscopically imposed strain $\dot{\varepsilon} t = 0.75$.

an altitude angle of 20°–25° with the loading direction, which again is in agreement with experimental results of Bartczak et al. (1992b). In the Taylor-inclusion model however, a more diffuse pattern is formed, with most poles at an altitude angle $> 25°$. In Figure 4.13, the trajectories and the corresponding angular velocities of the (100) poles are shown. The Sachs-inclusion model exhibits a more structured pattern for the crystallographic pole trajectories. However it shows more variation in the length of the trajectories since only relatively weak inclusions are active, in contrast to the Taylor-inclusion model, where all inclusions are forced to be active. Since, in the latter model, slip occurs on planes other

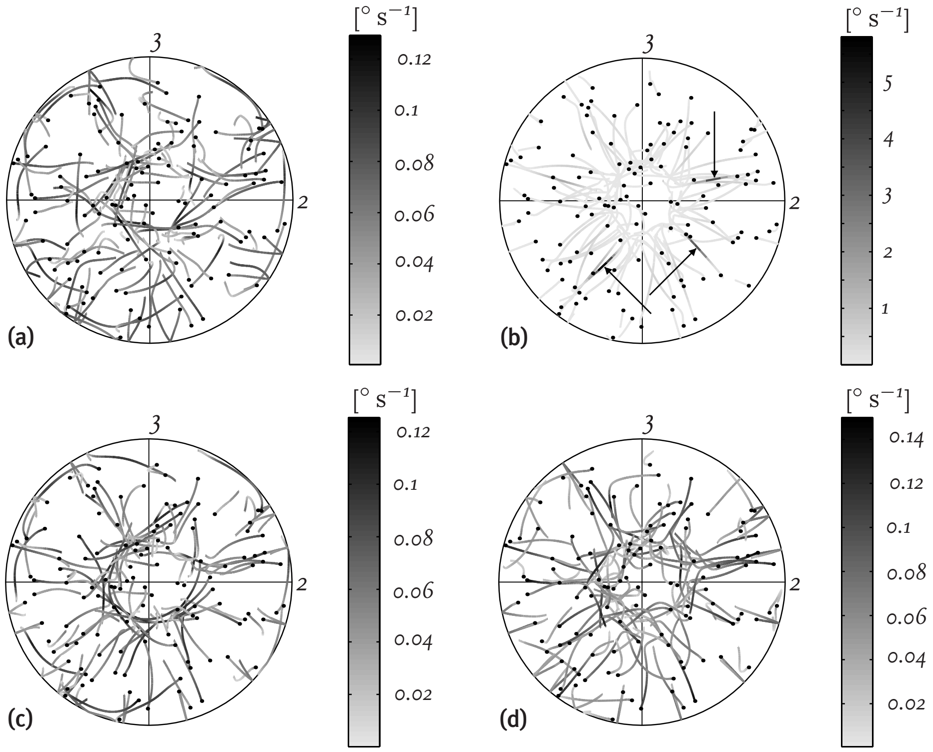

Figure 4.13 / Crystallographic (100) pole trajectories as predicted by (a) the Taylor-inclusion model, (b) the Sachs-inclusion model, (c) the $\hat{\boldsymbol{\sigma}}$-inclusion model, and (d) the $\hat{U}$-inclusion model, for HDPE subjected to uniaxial compression up to a mesoscopically imposed strain $\dot{\varepsilon}t = 0.75$. The dots denote the initial position of the poles and the gray values represent the angular velocity of each pole. For the Sachs-inclusion model, the arrows indicate the inclusions that induce the stress-dips.

than the principal slip plane (100), the direction of the pole trajectories is more diverse. For the Sachs-inclusion model, the (100) poles approaching the compression direction are found to change direction when attaining an angle of approximately 20°–25°. Therefore, apparently the initial goal, which is the compression direction, is not reached, which is also observed in the experiments by Bartczak et al. (1992b). This alteration of the direction of the trajectories corresponds to the activation of less easy slip systems, mainly the $\{110\}\langle 1\bar{1}0\rangle$ slip systems. The stress-dips that were observed in the Sachs-inclusion model are accompanied by temporarily large rates of deformation in few inclusions, corresponding to large polar angular velocities for these inclusions in Figure 4.13 (indicated by the arrows). This phenomenon is not observed for the Taylor- and the hybrid-inclusion models.

In Figure 4.14, the morphological texture, i.e. the orientation of the lamellar normals, is shown for each interaction model. In all models, the normals of the inclusion interfaces are migrating towards the compression direction, with, for the Taylor-, Sachs- and $\hat{\boldsymbol{\sigma}}$-inclusion models, a maximum intensity of normals in the center of the pole figure. The Sachs-inclusion model exhibits a slightly sharper texture than the Taylor-inclusion model. In the $\hat{\boldsymbol{U}}$-inclusion model, the compression axis is not reached.

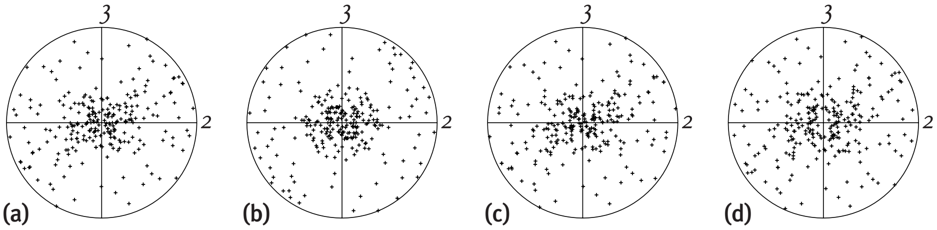

Figure 4.14 / Morphological texture for HDPE subjected to uniaxial compression at mesoscopically imposed strain $\dot{\varepsilon}t = 0.75$, for (a) the Taylor-inclusion model, (b) the Sachs-inclusion model, (c) the $\hat{\boldsymbol{\sigma}}$-inclusion model, and (d) the $\hat{\boldsymbol{U}}$-inclusion model.

The normalized stress–strain behavior of the $\hat{\boldsymbol{U}}$-inclusion model is shown in Figure 4.15(a) for different strain rates. This strain rate-dependency is in reasonably good agreement with experimental results of G'Sell et al. (1992) and Hiss et al. (1999). Figure 4.15(b) exhibits an approximately linear relation between $\ln(\bar{\sigma}^{\mathrm{eq}}/\tau_0)$ and $\ln(\dot{\varepsilon}/\dot{\gamma}_0)$, as dictated by the plastic power law behavior of both the crystalline and the amorphous phase. The mesoscopically observed strain rate sensitivity coefficient $\bar{m} = \left[\mathrm{d}\ln(\bar{\sigma}^{\mathrm{eq}}/\tau_0)/\mathrm{d}\ln(\dot{\varepsilon}/\dot{\gamma}_0)\right]_{\varepsilon}$ is found to be 0.09 for $\dot{\varepsilon}t = 0.25$, which is slightly below the corresponding coefficient of the individual phases, $1/n^{\pi} = 0.11$ (with $\pi = \mathrm{a, c}$). A similar dependency is obtained for the other inclusion models.

The stress–strain curves of various polyethylenes were split into five different ranges by Hiss et al. (1999). The transition points are located at similar strain-values, and are associated with (i) the onset of isolated slip processes, (ii) collective activity of slip, (iii) the beginning of crystallite fragmentation, and (iv) chain disentanglement. The underlying microstructural assumptions of the composite inclusion model are appropriate only up to the third transition point, at $\varepsilon \approx 0.6$, after which the lamellae begin to disintegrate. At larger strains, the applicability of the model becomes questionable.

4.7 Loading cycles

In this section, the behavior of the four inclusion models is investigated during consecutive loading, unloading and reloading. The previously considered high density polyethy-

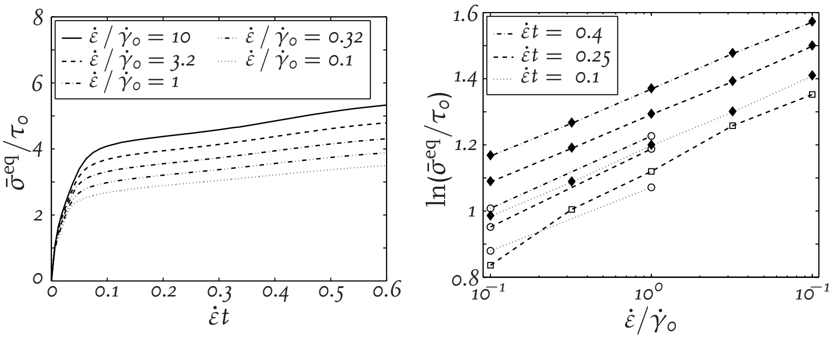

(a) **(b)**

Figure 4.15 / (a) The rate-dependency of the normalized equivalent mesoscopic stress $\bar{\sigma}^{\mathrm{eq}}/\tau_0$ vs. the imposed mesoscopic strain $\dot{\varepsilon}t$ and (b) the normalized equivalent mesoscopic stress vs. the normalized mesoscopically imposed strain rate $\dot{\varepsilon}/\dot{\gamma}_0$, for HDPE in uniaxial compression with $\dot{\lambda}/\lambda = -\dot{\varepsilon}$, as predicted by the $\hat{\boldsymbol{U}}$-inclusion model (indicated by closed diamonds) and obtained from experimental (tensile) data from G'Sell et al. (1992), indicated by open circles, and Hiss et al. (1999), indicated by open squares.

lene material with the initially random orientations as represented in Figure 4.6 is first subjected to uniaxial compression at constant strain rate with $\dot{\lambda}/\lambda = -\dot{\varepsilon}$ and $\dot{\varepsilon} = 10^{-3}$ s^{-1}. Then, at a certain mesoscopic strain level, the direction of the mesoscopic deformation is reversed and the material is unloaded gradually with $\dot{\lambda}/\lambda = \dot{\varepsilon}$ until the mesoscopically observed stress is fully released ($\bar{\sigma}_{11} \geq 0$). Following this unloading step, the material is reloaded at the same strain rate. This unloading–reloading cycle is repeated at higher strains. The mesoscopic stress–strain behavior during these cycles is presented in Figure 4.16 for each interaction model. For polyethylene, commonly a hysteresis loop is found during unloading and subsequent reloading (Sargent and Shinozaki, 1977; Hiss et al., 1999; Hobeika et al., 2000). For the Sachs-inclusion model, the predicted stress–strain curve does not show this hysteresis loop. Since the Sachs-inclusion model does not enforce interinclusion compatibility, the unloading can be accommodated fully elastically, resulting in an approximately linear release of stress. Consequently, the material in each inclusion reloads along the same path. After yielding, the stress–strain curve returns to the continuous-loading curve. The elastic nature of the unloading–reloading of the Sachs-inclusion model is shown in Figure 4.17, which plots the phase-volume-averaged plastic strain for each phase as a function of $\dot{\varepsilon}t$. For the Sachs-inclusion model, no plastic deformation is observed during unloading or during reloading (until rejoining the original curve). In the other interaction models, the interinclusion compatibility conditions enforce a partially plastic unloading in the crystalline phase, as is demonstrated for the first unloading–reloading cycle in Figure 4.17 for the $\hat{\boldsymbol{U}}$-inclusion model. For the Taylor-inclusion and $\hat{\boldsymbol{\sigma}}$-inclusion models, initially only small hysteresis loops can be ob-

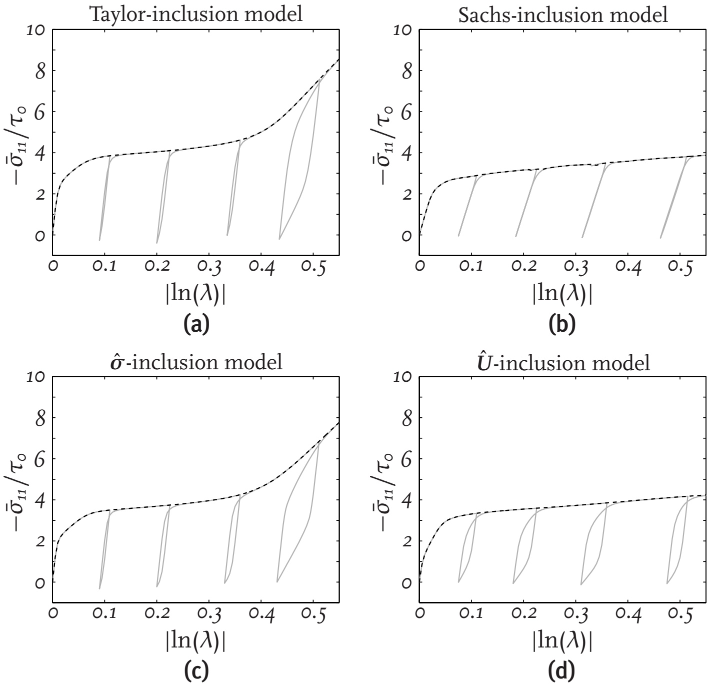

Figure 4.16 / The mesoscopic stress–strain behavior for loading, unloading and reloading of polyethylene in uniaxial compression, predicted by various interaction models. The dashed lines represent the stress–strain response for continuous uniaxial compression.

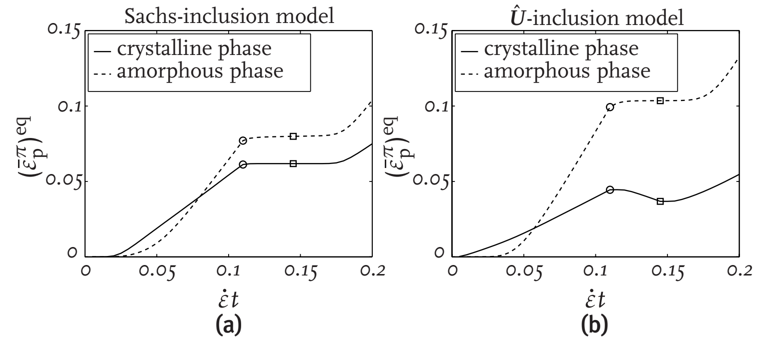

Figure 4.17 / The equivalent logarithmic strain measure of the phase-volume-averaged plastic deformation during sequentially loading, unloading and reloading for (a) the Sachs-inclusion model and (b) the $\hat{\boldsymbol{U}}$-inclusion model. The onset of unloading and reloading is denoted by circles and squares, respectively.

served. Also, after each unloading–reloading cycle, the stress–strain curve returns to the continuous-loading curve. After the strong textural hardening has set in ($\dot{\varepsilon}t > 0.4$), a considerably larger hysteresis loop is found. This is attributed to a continuation of unloading after the relatively weak inclusions have reached a relaxed state. During this stage of local reverse loading, plastic deformation occurs in the crystalline phases of the concerning inclusions. The $\hat{\boldsymbol{U}}$-inclusion model resembles best the experimentally observed behavior. In this model, local–global interactions for both deformation and stress are imposed. These mixed conditions, in combination with the amorphous/crystalline interactions, prevent the unloading from being fully elastic. During unloading, significant plastic deformations occur in the crystalline phase, as is shown in Figure 4.17. Consequently, the subsequent reloading step, which is initially elastic, follows a different path.

Since in the foregoing the $\hat{\boldsymbol{U}}$-inclusion model was found to exclude the deficiencies of the Taylor- and the Sachs-inclusion models, and appears to be superior in cyclic loading, in the remaining of this thesis only the $\hat{\boldsymbol{U}}$-inclusion model will be used.

4.8 Effect of crystallinity

The basic element of the presented elasto-viscoplastic composite inclusion model consists of a layered structure of amorphous and crystalline domains with relative thicknesses f^a and $f^c = 1 - f^a$, respectively. The influence of the crystallinity f^c on the normalized equivalent mesoscopic stress, $\bar{\sigma}^{eq}/\tau_0$, for uniaxial compression, using the $\hat{\boldsymbol{U}}$-inclusion model, is presented in Figure 4.18. An increase of both initial stiffness and yield stress with increasing crystallinity level can be observed. Since postyield hardening is found to be approximately independent of the amount of crystallinity, at higher strains, the curves differ mainly by a vertical shift, corresponding to experimental observations (Kennedy et al., 1994).

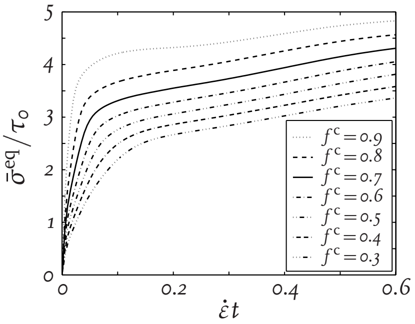

Figure 4.18 / The influence of the crystallinity on the normalized equivalent mesoscopic stress $\bar{\sigma}^{eq}/\tau_0$ vs. the imposed mesoscopic strain $\dot{\varepsilon}t$ for HDPE in uniaxial compression as predicted by the $\hat{\boldsymbol{U}}$-inclusion model.

In Figure 4.19(a), the mesoscopically predicted initial modulus, $\bar{E}$, obtained in uniaxial compression, with the $\hat{\boldsymbol{U}}$-inclusion model, is shown as a function of the crystallinity f^c, as well as experimental data by Crist et al. (1989). The value for $\bar{E}$ corresponds reasonably well to the experimental data for $f^c = 0.7$, since in the present work, this crystallinity level was used as the reference level for the selection of material parameters. The dependence of the initial modulus on the crystallinity, as predicted by the $\hat{\boldsymbol{U}}$-inclusion model, is significantly smaller than can be deduced from the Crist et al. data. The relatively strong influence of f^c on $\bar{E}$ is attributed by Crist et al. to a dependence of the amorphous modulus on the crystal thickness. An alternative explanation was offered by Doyle (2000), whose finite element model of alternating amorphous and crystalline layers provides a quantitatively good prediction of the dependence of the elastic modulus on the crystallinity for higher crystallinities. The deviation at lower crystallinities was attributed to a relaxation of the mechanical constraints due to a change in aspect ratio of lamellae. The change of nature of the interactions at low crystallinity (an amorphous matrix with randomly oriented lamellae) suggests the use of a more Sachslike approach. The effect of the crystallinity on the yield stress, as well as postyield stress is shown in Figure 4.19(b). The yield stress is assumed to be given by the intersection of the initial and 5 percent strain tangents of the mesoscopic equivalent stress–strain curve, as shown in the insert of the figure. The dependence of the yield stress on crystallinity, becoming less pronounced for crystallinities lower than 0.6, corresponds reasonably well with the effect experimentally observed (Crist et al., 1989).

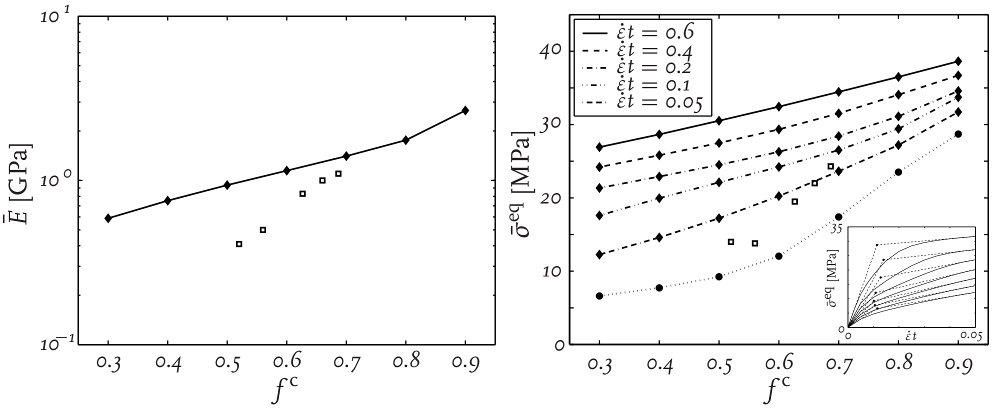

(a) (b)

Figure 4.19 / The influence of crystallinity f^c on (a) the mesoscopically predicted initial modulus $\bar{E}$ and (b) the mesoscopically observed equivalent mesoscopic stress $\bar{\sigma}^{eq}$, at various mesoscopic strain levels, in uniaxial compression, as predicted by the $\hat{\boldsymbol{U}}$-inclusion model (indicated by closed diamonds). The closed circles indicate yield stresses, obtained as shown in the insert. Experimental (tensile) data for the initial modulus and yield stress, from Crist et al. (1989), are represented by open squares.

The effect of crystallinity on the unloading and subsequent reloading in uniaxial compression is given in Figure 4.20, for the $\hat{\boldsymbol{U}}$-inclusion model. For each cycle, unloading occurs first via an initial tangent and after a certain transition zone, via a much lower secondary tangent. A similar behavior is found during reloading. Besides the effect of crystallinity on the stress level at the start of unloading, decreasing f^c has a lowering effect on the initial unloading tangent and a stronger decreasing effect on the secondary tangent. The energy dissipation during an unloading–reloading cycle, i.e. the area enclosed by a hysteresis loop, is found to have a maximum for a crystallinity level of approximately 50 percent.

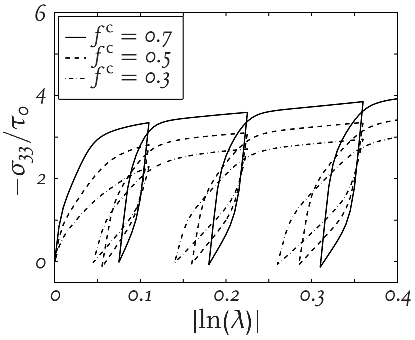

Figure 4.20 / The influence of crystallinity f^c on the mesoscopic stress–strain behavior for loading, unloading and reloading of polyethylene in uniaxial compression, predicted by the $\hat{\boldsymbol{U}}$-inclusion model.

4.9 Evolution of anisotropy

Although the material considered here is initially randomly oriented, and thus is initially quasi-isotropic, the mechanical properties will evolve in an anisotropic manner upon deformation, due to the evolution of crystallographic and morphological texture. This is illustrated by immediate reloading in compression and in shear along different axes, where the initial deformation was uniaxial compression in the $\boldsymbol{e}_1$-direction up to $\dot{\varepsilon} t = 0.6$, followed by unloading to a stress-free state at $t^\star$. Compressive reloading is applied in the basic $\boldsymbol{e}_i$-directions as $\bar{U}_{ii}(t) = \lambda^\star \, \bar{U}_{ii}(t^\star)$, with $\lambda^\star = \exp[-\dot{\varepsilon}(t - t^\star)]$, whereas plane stress ij-shearing is obtained by prescribing the appropriate rotation-neutralized components of $\bar{\boldsymbol{F}} = [\boldsymbol{I} + \gamma^\star \boldsymbol{e}_j \boldsymbol{e}_i] \cdot \bar{\boldsymbol{U}}(t^\star)$, with $\gamma^\star = \sqrt{3}\, \dot{\varepsilon}\, (t - t^\star)$. The normalized stress–strain behavior obtained is displayed in Figure 4.21. In compression, the yield stress in the two transverse directions is significantly reduced with respect to the initial loading direction,

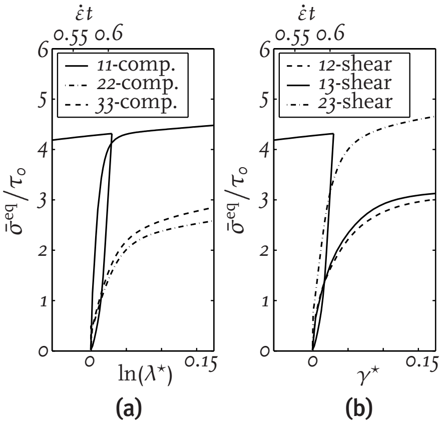

Figure 4.21 / Anisotropy in reloading (lower axis) after loading and unloading (upper axis) of initially isotropic material.

and is even below the initial yield stress. For 23-shearing, the flow stress approximately equals the flow stress for compressive reloading in the initial loading direction. In the other shear directions, the material yields at a substantially reduced stress level, with a more nonlinear elastic behavior.

4.10 Conclusions

An elasto-viscoplastic model for the constitutive behavior of semicrystalline polymers has been developed. The model is based on (a simplified representation of) the underlying morphology and deformation mechanisms of this material. As a representative microstructural element, a two-phase layered composite inclusion has been used, based on the lamellar structure that is commonly observed in semicrystalline polymers. Both the crystalline and the amorphous phase are participating in the composite inclusion model, mechanically coupled by enforcing compatibility and traction continuity on the interface between the crystalline lamella and the corresponding amorphous layer. For both phases, micromechanically-based constitutive models have been used within the framework of an elasto-viscoplastic decomposition of the deformation gradient. The local inclusion-averaged deformation and stress fields are related to the mesoscopic fields of the aggregate using four interaction models: a Taylor approach; a Sachs approach; and two hybrid Taylor/Sachs approaches.

This work extends earlier work of Lee et al. (1993a) by including the important effects of the elastic behavior of the constituent phases. To facilitate the use of elasto-viscoplastic constitutive models, the framework in which the composite inclusion model is formulated, deviates from that of Lee et al.. The new model formulates compatibility and averaging schemes in terms of deformation gradients of the respective phases, whereas the Lee et al. model was a rate formulation. Due to dilatation effects, the volume fractions of both the inclusions and the individual phases are allowed to change upon deformation. In order to obtain the correct volume-averaged volumetric response, the deformation gradients are scaled. A solution procedure is used, which is based on solving a set of nonlinear equations for the elastic deformation gradients of the constituent phases. The uniaxial compression of initially isotropic high density polyethylene is taken as a case study. The choice of the interaction model appears to be rather critical in the predictions. For HDPE in uniaxial deformation, application of the Taylor-inclusion model leads to unreasonably high values of the stress in certain inclusions, resulting in modulus and yield strength predictions that are relatively high and also predicting excessive hardening to occur at relatively modest strain. The Sachs-inclusion model however, assumes a weakened measure of kinematical compatibility, and thus circumvents the difficulty of unfavorably oriented inclusions. The crystallographic textures obtained in this model seem to be in agreement with experimental observations. However, the stress–strain behavior of the Sachs-inclusion model shows a number of temporary reductions due to the existence of relatively weakly oriented inclusions. The hybrid $\hat{\boldsymbol{\sigma}}$-inclusion model shows largely the same behavior as the Taylor-inclusion model. The hybrid $\hat{\boldsymbol{U}}$-inclusion model however, appears to exclude the deficiencies of the Taylor- and the Sachs-inclusion models, whereas in the Lee et al. work, the hybrid interaction laws were concluded to give results similar to the classical Sachs-type interaction law. Furthermore, the stress–strain behavior during unloading–reloading cycles shows the superiority of the $\hat{\boldsymbol{U}}$-inclusion model over the alternatives.

The new model is able to simulate the mesoscopic elasticity, the rate-dependent plasticity, and the unloading behavior of semicrystalline polymers, based on the elasto-viscoplastic micromechanics of the material. With this model, the influence of crystallinity on the mesoscopic stress–strain behavior has been studied. The dependence of initial modulus, yield stress and postyield behavior on the crystallinity corresponds reasonably well to experimentally observed effects, as reported in the literature. Additionally, the effect of crystallinity on the behavior during unloading–reloading cycles is investigated. The dissipated energy during a cycle is found to have a maximum for about 50 percent crystallinity. The ability of the model to capture the effects of a textured microstructure giving rise to anisotropic mechanical behavior was demonstrated by simulating axial and shear loading in different directions on a pretextured microstructure.

The model presented, capturing the elasto-viscoplastic micromechanics of both the amorphous and the crystalline phase, as well as the morphological structure, offers new possibilities to study the mechanics of semicrystalline polymers, particularly, the anisotropic mesoscopic stiffness and deformation resistances for preferentially oriented semicrystalline polymers as commonly present in thin films and coatings as well as in particle-modified polymers. In Chapter 6, the composite inclusion model will be used to simulate intraspherulitic deformation and stress, whereas in Chapter 7, the model will be employed to study the matrix deformation in particle-toughened semicrystalline materials. For these purposes, an aggregate of composite inclusions will be used as a representative microstructural unit at each integration point of a finite element formulation. Some aspects of the finite element implementation will be presented in Chapter 5.

CHAPTER FIVE

Bridge to the macroscopic level[1]

Abstract / In this chapter, some aspects concerning the implementation of the composite inclusion model into a finite element formulation are presented. The influence of the aggregate-size, the tangent operator, and a subincremental procedure are discussed.

5.1 Introduction

In this thesis, a multiscale approach is used for modeling the micromechanics of particle-modified semicrystalline polymers. The different levels involved are schematically shown in Figure 5.1. At the microscopic level, a structure of individual crystalline lamellae, interspersed with amorphous domains is identified. A bridge to the mesoscopic level, where the semicrystalline matrix material consists of aggregates of these constituent phases, is formed by the composite inclusion model, which was presented in Chapter 4. At the macroscopic level, the particle-modified material consists of a polymeric matrix with randomly dispersed particles or voids. This two-phase system is modeled by finite elements. A micro–meso–macrolevel bridge is obtained by using an aggregate of composite inclusions in each integration point of a finite element model. A bridge to the engineering level, at which the material can be considered to be homogeneous, could be obtained by a multilevel finite element procedure (e.g. Smit et al., 1998; Smit, 1998; Kouznetsova et al., 2001, 2002; Kouznetsova, 2002). However, this step is not pursued in this work.

In this chapter, some aspects concerning the use and the implementation of the composite inclusion model in a finite element context are presented. In Chapter 4, the $\hat{\boldsymbol{U}}$-

---

[1] This chapter is partly reproduced from Van Dommelen et al. (2001).

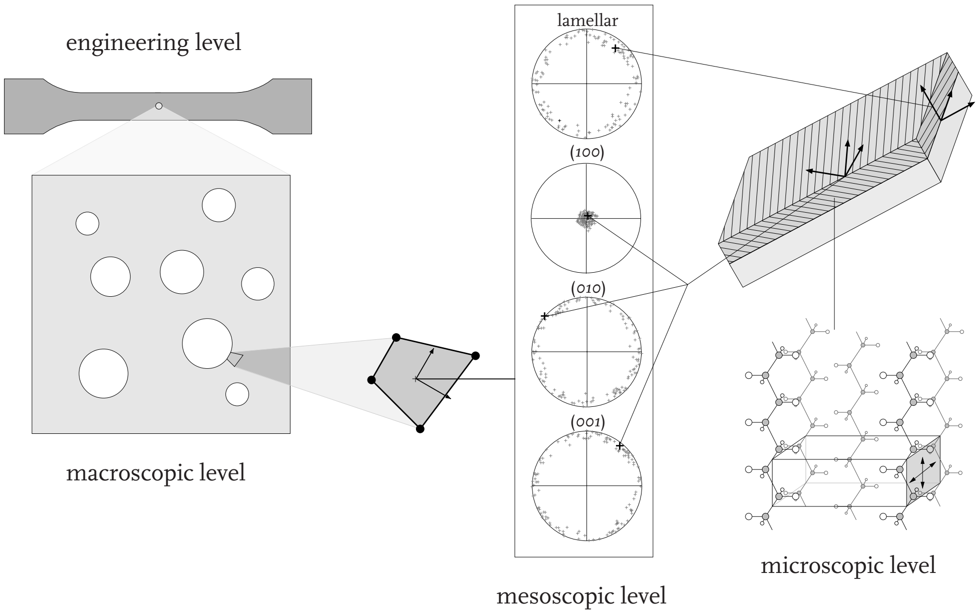

Figure 5.1 / The various levels involved in the multiscale model.

inclusion model was concluded to be the most effective of the interaction models considered for the material of interest. Therefore, in the remaining of this thesis, only the $\hat{U}$-inclusion model will be used and the term *composite inclusion model* will implicitly refer to this interaction model.

5.2 Influence of aggregate-size

The composite inclusion model can be used to simulate the mechanical behavior of initially isotropic semicrystalline material by taking a randomly generated set of initial crystallographic orientations. The number of inclusions within an aggregate should be sufficiently large, in order to expel the influence of the particular set of initial orientations, and to have truly isotropic material behavior. The influence of the aggregate-size (i.e. the number of composite inclusions N_{I}) on the equivalent mesoscopic stress, $\bar{\sigma}^{\mathrm{eq}}$, as a function of the imposed mesoscopic strain is represented in Figures 5.2 and 5.3. The term *mesoscopic* is used for the aggregate of inclusions. In this application, the initially isotropic HDPE material is subjected to constant strain rate uniaxial tension with $\lambda(t) = \exp(\dot{\varepsilon} t)$ and $\dot{\varepsilon} = 10^{-3}\ \mathrm{s}^{-1}$.

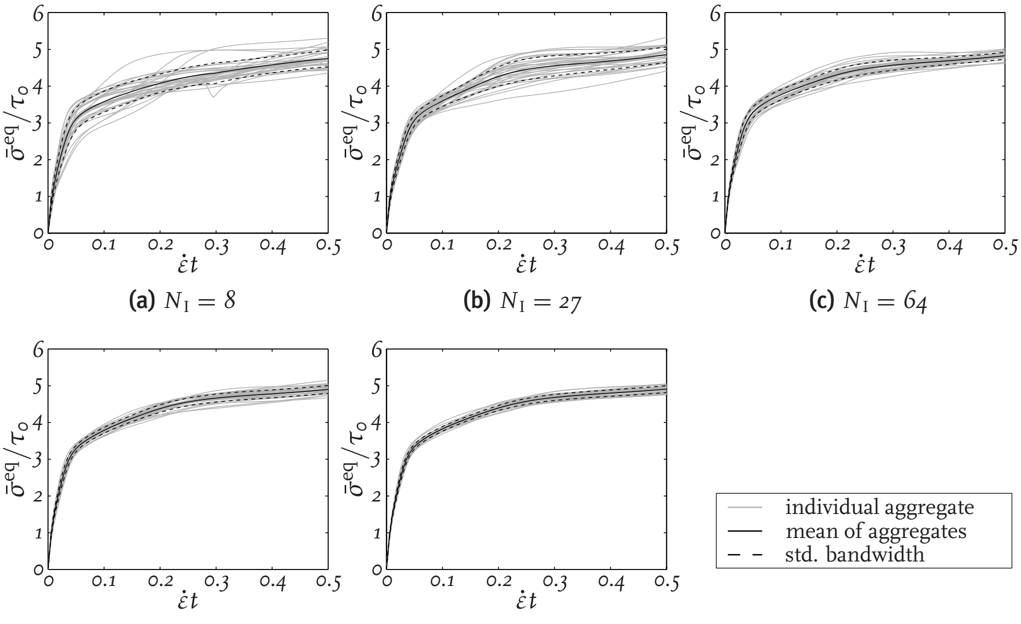

(a) $N_{\rm I} = 8$ (b) $N_{\rm I} = 27$ (c) $N_{\rm I} = 64$

(d) $N_{\rm I} = 125$ (e) $N_{\rm I} = 216$

Figure 5.2 / The normalized equivalent mesoscopic stress in uniaxial tension for the $\hat{U}$-inclusion model for different aggregate-sizes. The gray lines represent the stress–strain curves for 30 individual, randomly generated, aggregates, for each aggregate-size. The solid black lines are the mean equivalent stresses for each aggregate-size, whereas the dashed black lines indicate the corresponding standard deviation bandwidth.

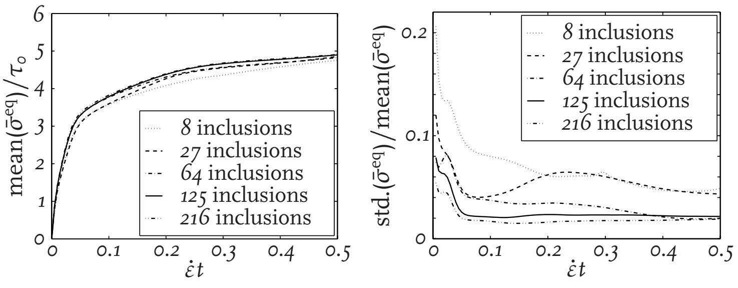

(a) (b)

Figure 5.3 / (a) The normalized mean equivalent mesoscopic stress and (b) the relative standard deviation of the equivalent mesoscopic stress as a function of the mesoscopically imposed strain for different numbers of inclusions. For each aggregate-size, 30 different sets of randomly generated inclusions are used.

For the smallest aggregate-size, with $N_{\mathrm{I}} = 8$, a relatively large scatter in the stress–strain response is found. After an imposed strain of $\dot{\varepsilon}t = 0.5$, the standard deviation of the mesoscopic equivalent stress of 30 different sets of randomly generated aggregates reaches a value of 5 percent of the mean stress. For an aggregate-size of $N_{\mathrm{I}} = 27$, and $\dot{\varepsilon}t \geq 0.2$, approximately similar standard deviations are found. A significantly smaller scatter of mesoscopic stress–strain behavior is obtained for aggregates with 64 inclusions, with a standard deviation of 2 percent of the mean stress at $\dot{\varepsilon}t = 0.5$. An aggregate-size of 125 inclusions results, in the plastic region, in an approximately constant relative standard deviation of about 2 percent of the mean equivalent stress. A further increase of the aggregate-size, to 216 inclusions, slightly decreases the standard deviation bandwidth, with no further significant effect on the mean stress–strain curve.

When used in a finite element simulation, in each integration point, the material is represented by an aggregate of inclusions. In order to simulate the behavior of initially isotropic semicrystalline material, a sufficiently large aggregate must be used. However, since an entire composite inclusion model is solved in each integration point, for each iteration of the global iterative process, calculation times tend to become extensive. Therefore, for the aggregate-size, a compromise of a sufficiently large aggregate with respect to statistical considerations which is small enough for acceptable computation times should be pursued. Based on these considerations, an aggregate-size of 64 inclusions will be used in the finite element simulations that are presented in the remaining of this thesis.

5.3 Finite element implementation

In Chapter 4, the composite inclusion aggregate has been discussed, which represents a numerical, micromechanically based constitutive model for semicrystalline polymeric materials. In this section, some aspects of the implementation of this constitutive model in a finite element context will be outlined. An overview of the numerical procedure is shown in Figure 5.4, where Φ_j symbolically represents the equations that constitute the composite inclusion model and $\breve{\boldsymbol{\sigma}}$ are extra unknowns that are introduced for efficiency reasons (see Appendix A).

5.3.1 Tangent operator

The composite inclusion model, as discussed in Chapter 4, gives, for an integration point, the Cauchy stress $\bar{\boldsymbol{\sigma}}$, i.e. the volume-averaged stress of an aggregate, for a given deformation gradient $\bar{\boldsymbol{F}}$, the volume-averaged deformation of the aggregate. Since the relationship between these two quantities is intrinsically nonlinear, at the finite element level, an iterative procedure is used (HKS, 2001). For this purpose, the Jacobian ${}^4\bar{\mathcal{K}}$ is determined,

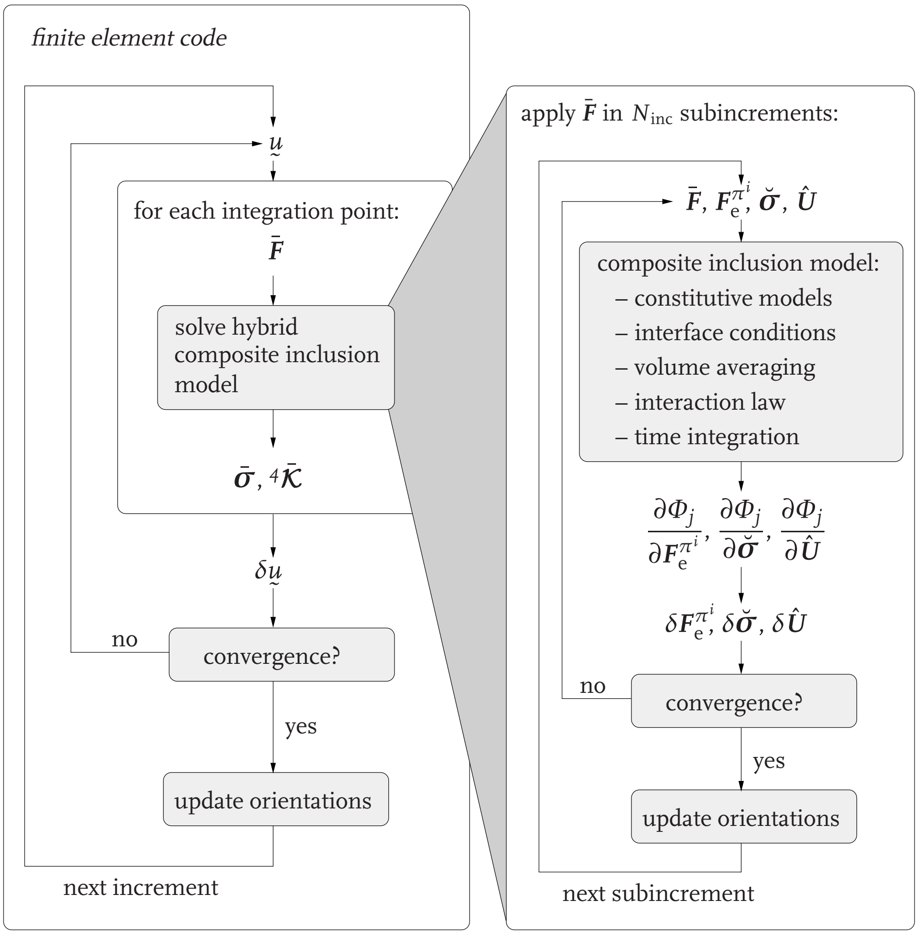
finite element code
$\underset{\sim}{u}$
for each integration point:
$\bar{F}$
solve hybrid composite inclusion model
$\bar{\boldsymbol{\sigma}}, {}^4\bar{\mathcal{K}}$
$\delta\underset{\sim}{u}$
no
convergence?
yes
update orientations
next increment
apply $\bar{F}$ in N_{inc} subincrements:
$\bar{F}, F_e^{\pi^i}, \breve{\boldsymbol{\sigma}}, \hat{U}$
composite inclusion model:
– constitutive models
– interface conditions
– volume averaging
– interaction law
– time integration
$\frac{\partial\Phi_j}{\partial F_e^{\pi^i}}, \frac{\partial\Phi_j}{\partial\breve{\boldsymbol{\sigma}}}, \frac{\partial\Phi_j}{\partial\hat{U}}$
$\delta F_e^{\pi^i}, \delta\breve{\boldsymbol{\sigma}}, \delta\hat{U}$
no
convergence?
yes
update orientations
next subincrement

Figure 5.4 / FEM implementation scheme.

which is defined as:

$$\delta\bar{\boldsymbol{\sigma}} = {}^4\bar{\mathcal{K}} : \delta\bar{F} \tag{5.1}$$

The mesoscopic Cauchy stress following from the composite inclusion model can be functionally written as

$$\bar{\boldsymbol{\sigma}} = \bar{\boldsymbol{\sigma}}(F_e^{\pi^i} | i = 1, \ldots, N_{\text{I}}; \pi = \text{a, c}), \tag{5.2}$$

where $\boldsymbol{F}_{\mathrm{e}}^{\pi^i}$ are the elastic deformation gradients of the crystalline and amorphous domains of the N_{I} composite inclusions and remain to be determined. For a given $\bar{\boldsymbol{F}}$ [2], the a priori unknown elastic deformation gradients $\boldsymbol{F}_{\mathrm{e}}^{\pi^i}$ (corresponding to $18N_{\mathrm{I}}$ unknowns) are obtained by solving a set of coupled nonlinear equations, which is summarized in Section 5 of Appendix A and can be symbolically written as

$$\Phi_j(\bar{\boldsymbol{F}},\hat{\boldsymbol{U}},\breve{\boldsymbol{\sigma}},\boldsymbol{F}_{\mathrm{e}}^{\pi^i}|i=1,\ldots,N_{\mathrm{I}};\pi=\mathrm{a},\mathrm{c})=0 \quad ; \quad j=1,\ldots,18N_{\mathrm{I}}+12. \tag{5.3}$$

In these equations, also the 12 extra unknowns $\hat{\boldsymbol{U}}$ and $\breve{\boldsymbol{\sigma}}$ appear, corresponding to the auxiliary stretchlike variables and the unprescribed macroscopic stress components, respectively. The Jacobian ${}^4\bar{\mathcal{K}}$ in Equation (5.1) can be written as

$$^4\bar{\mathcal{K}}=\sum_{i=1}^{N_{\mathrm{I}}}\sum_{\pi=\mathrm{a},\,\mathrm{c}}\frac{\mathrm{d}\bar{\boldsymbol{\sigma}}}{\mathrm{d}\boldsymbol{F}_{\mathrm{e}}^{\pi^i}}:\frac{\mathrm{d}\boldsymbol{F}_{\mathrm{e}}^{\pi^i}}{\mathrm{d}\bar{\boldsymbol{F}}}, \tag{5.4}$$

where the derivatives $\mathrm{d}\bar{\boldsymbol{\sigma}}/\mathrm{d}\boldsymbol{F}_{\mathrm{e}}^{\pi^i}$ can be determined straightforwardly and are also required for the iterative solution of the composite inclusion model itself. The derivatives $\mathrm{d}\boldsymbol{F}_{\mathrm{e}}^{\pi^i}/\mathrm{d}\bar{\boldsymbol{F}}$ remain to be determined. For all variations of $\bar{\boldsymbol{F}}$, the $18N_{\mathrm{I}}+12$ functionalities in Equation (5.3) should remain 0. Thus, a set of linear equations for the derivatives $\mathrm{d}\hat{\boldsymbol{U}}/\mathrm{d}\bar{\boldsymbol{F}}$; $\mathrm{d}\breve{\boldsymbol{\sigma}}/\mathrm{d}\bar{\boldsymbol{F}}$ and $\mathrm{d}\boldsymbol{F}_{\mathrm{e}}^{\pi^i}/\mathrm{d}\bar{\boldsymbol{F}}$ in the direction with $\mathrm{d}\Phi_j/\mathrm{d}\bar{\boldsymbol{F}}=\boldsymbol{O}$ is obtained by

$$\frac{\mathrm{d}\Phi_j}{\mathrm{d}\bar{\boldsymbol{F}}}=\frac{\partial\Phi_j}{\partial\bar{\boldsymbol{F}}}+\frac{\partial\Phi_j}{\partial\hat{\boldsymbol{U}}}:\frac{\mathrm{d}\hat{\boldsymbol{U}}}{\mathrm{d}\bar{\boldsymbol{F}}}+\frac{\partial\Phi_j}{\partial\breve{\boldsymbol{\sigma}}}:\frac{\mathrm{d}\breve{\boldsymbol{\sigma}}}{\mathrm{d}\bar{\boldsymbol{F}}}+\sum_{i=1}^{N_{\mathrm{I}}}\sum_{\pi=\mathrm{a},\,\mathrm{c}}\frac{\partial\Phi_j}{\partial\boldsymbol{F}_{\mathrm{e}}^{\pi^i}}:\frac{\mathrm{d}\boldsymbol{F}_{\mathrm{e}}^{\pi^i}}{\mathrm{d}\bar{\boldsymbol{F}}}=\boldsymbol{O} \quad ; \quad j=1,\ldots,18N_{\mathrm{I}}+12. \tag{5.5}$$

After solving this set of equations, the Jacobian ${}^4\bar{\mathcal{K}}$ is obtained by substitution of $\mathrm{d}\boldsymbol{F}_{\mathrm{e}}^{\pi^i}/\mathrm{d}\bar{\boldsymbol{F}}$ in Equation (5.4).

5.3.2 Subincrementation

The Newton–Raphson procedure that is used to solve the composite inclusion model, for each iteration of the global (FEM) incremental procedure, requires that the steps in which the deformation $\bar{\boldsymbol{F}}$ is applied are small enough, depending on the internal state of the concerning aggregate. In order to prevent a dramatic reduction of the global increment size, the deformation gradient $\bar{\boldsymbol{F}}$ is applied in a number of subincrements for those integration points that require smaller steps. For this purpose, let the incremental mesoscopic deformation gradient, between time steps t_n and t_{n+1}, be decomposed as

---

[2] The implementation presented here is limited to 3D, plane strain, and axisymmetric calculations. For plane stress simulations, mixed conditions for $\bar{\boldsymbol{F}}$ and $\bar{\boldsymbol{\sigma}}$ are prescribed. For all 2D assumptions, however, the composite inclusion model remains essentially three-dimensional.

$$\bar{\boldsymbol{F}}_{\text{inc}} = \bar{\boldsymbol{R}}_{\text{inc}} \cdot \bar{\boldsymbol{U}}_{\text{inc}} \quad \text{with} \quad \bar{\boldsymbol{F}}(t_{n+1}) = \bar{\boldsymbol{F}}_{\text{inc}} \cdot \bar{\boldsymbol{F}}(t_n). \tag{5.6}$$

First, the incremental stretch is applied. For this purpose, assume that within a stretch increment, the time-dependency of the deformation gradient can be written as

$$\bar{\boldsymbol{F}}(\tau) = (\bar{\boldsymbol{U}}_{\text{inc}})^{\frac{\tau - t_n}{\Delta t}} \cdot \bar{\boldsymbol{F}}(t_n) \quad ; \quad t_n \leq \tau \leq t_{n+1} \quad ; \quad \Delta t = t_{n+1} - t_n. \tag{5.7}$$

Then, the incremental deformation is applied in the following N_{inc} subincrements i:

$$\bar{\boldsymbol{F}}(\tau_i) = \left(\bar{\boldsymbol{U}}_{\text{inc}}\right)^{\frac{i}{N_{\text{inc}}}} \cdot \bar{\boldsymbol{F}}(t_n) \quad ; \quad i = 1, \ldots, N_{\text{inc}} \quad ; \quad \tau_i = t_n + \frac{i}{N_{\text{inc}}} \Delta t. \tag{5.8}$$

Finally, the incremental rotation $\bar{\boldsymbol{R}}_{\text{inc}}$ is applied:

$$\bar{\boldsymbol{F}}(t_{n+1}) = \bar{\boldsymbol{R}}_{\text{inc}} \cdot \bar{\boldsymbol{F}}(\tau_{N_{\text{inc}}}) \quad \text{and} \quad \bar{\boldsymbol{\sigma}}(t_{n+1}) = \bar{\boldsymbol{R}}_{\text{inc}} \cdot \bar{\boldsymbol{\sigma}}(\tau_{N_{\text{inc}}}) \cdot \bar{\boldsymbol{R}}_{\text{inc}}^{\mathrm{T}}. \tag{5.9}$$

Also, the appropriate orientation-dependent state variables are updated with the incremental rotation tensor.

5.3.3 Finite element package

The composite inclusion model is implemented in the finite element package ABAQUS (HKS, 2001). Thereby the previously discussed numerical aspects have been applied within the `UMAT` subroutine, using a geometrically nonlinear formulation.

5.3.4 Output

In the remaining chapters, the following mesoscopic measure of plastic deformation magnitude is used as an output quantity:

$$\bar{\varepsilon}_{\mathrm{p}}^{\mathrm{mag}} = \sqrt{\frac{2}{3} \bar{\boldsymbol{\varepsilon}}_{\mathrm{p}} : \bar{\boldsymbol{\varepsilon}}_{\mathrm{p}}} \quad \text{with} \quad \bar{\boldsymbol{\varepsilon}}_{\mathrm{p}} = \ln(\bar{\boldsymbol{U}}_{\mathrm{p}}), \tag{5.10}$$

where $\bar{\boldsymbol{U}}_{\mathrm{p}}$ is obtained from a right polar decomposition of the following mesoscopic plastic deformation gradientlike quantity:

$$\bar{\boldsymbol{F}}_{\mathrm{p}} = \bar{\boldsymbol{F}}_{\mathrm{e}}^{-1} \cdot \bar{\boldsymbol{F}}. \tag{5.11}$$

The mesoscopic deformation gradient tensor $\bar{\boldsymbol{F}}$ is given by Equations (4.20) and (4.21). A similar volume-averaging procedure is used to obtain $\bar{\boldsymbol{F}}_{\mathrm{e}}$.

CHAPTER SIX

Intraspherulitic deformation[1]

Abstract / The multiscale composite inclusion model is used to investigate the mechanics of intraspherulitic deformation of polyethylene. The model establishes a link between the macroscopic and the microscopic level. The averaged fields of an aggregate of composite inclusions, having preferential orientations, constitute the behavior of the intraspherulitic material. The spherulitic macrostructure is modeled by finite elements and loaded under uniaxial and plane strain conditions. Heterogeneous intraspherulitic deformation, with strain concentrations in the centers, results from the anisotropic structure within each spherulite.

6.1 Introduction

When cooled from the melt, many polymers, such as for example polyethylene, possess a semicrystalline structure with often a spherulitic morphology (Bassett and Hodge, 1981; Bassett et al., 1981; G'Sell and Dahoun, 1994). Considered from a central point, each spherulite consists of a radial assembly of thin twisted crystalline lamellae which are separated by amorphous layers. Any macroscopically homogeneous deformation of these materials is accommodated by various deformation mechanisms in the heterogeneous microstructure. For a better understanding of the mechanical behavior of semicrystalline materials, a link between the macroscopic and microscopic levels should be established.

A review of the structure and the microscopic deformation mechanisms of polyethylene spherulites is given in Lin and Argon (1994). Experimental investigations of intraspherulitic deformation processes have been carried out for thin films. Both affine and nonaffine deformation models of spherulites were proposed by Wilchinsky (1964). Hay and Keller (1965) found spherulitic deformation to consist mostly of a combination of homogeneous and inhomogeneous deformation. The latter was found to occur predominantly within spherulites in the equatorial region (the *equator* denotes the region where the radial direction is perpendicular to the loading direction, as schematically shown in Figure 6.1) by (*100*)[*001*] slip, causing a rotation of crystals around the ***b***-axis for appropriately oriented crystals, and between spherulites in the polar regions (the *pole* is defined as the region of the spherulite where the radial direction is aligned with the loading axis) of the boundary. Deformations in the equatorial area were observed to be higher than in the polar area, with the strain becoming very large towards the center of the spherulite. Neck formation across the transverse diameter in spherulitic films of polyethylene was reported Keith and Padden (1959). Kobayashi and Nagasawa (1966) used a rigid/plastic Hill yield criterion to model the heterogeneous distribution of deformation in a spherulite. Wang (1974) attributed the inhomogeneous deformation primarily to the anisotropic structure of the spherulite, and secondarily to the mechanical interactions between spherulites. Based on a linearly elastic model of a spherulite, Wang found the stress and strain to approach infinity in the spherulitic center, and the strain in the equatorial region to be larger than in the polar region. In the inclined 45° area, the deformation was dominated by shear strain. Allan and Bevis (1977, 1980) reported the occurrence of twinning in the equatorial regions of thin films of polyethylene spherulites. They subdivided the spherulitic domain into three regions: (i) the equatorial region, (ii) the region where the angle between the radial direction and the tensile axis ranges from 30° to 55°, here referred to as the *inclined* region, and (iii) the polar area. The ***b***-axis governs the deformation behavior in all three regions, with a tendency to align the ***c***-direction towards the tensile axis. The primary mode of deformation is interlamellar slip, followed by intralamellar slip. The polar region was concluded to possess a larger deformation resistance with respect to the loading direction than the other regions. Aboulfaraj et al. (1995) found the deformation to be initiated near the center of polypropylene spherulites, and observed little deformation in the polar region and the largest strains in the equatorial area. A finite element model of alternating amorphous and crystalline layers was presented by Doyle (2000) for polyethylene, and appeared to provide a quantitatively good prediction of the dependence of the elastic modulus on the crystallinity for relatively high crystallinities.

---

[1] This chapter is based on Van Dommelen et al. (2003a).

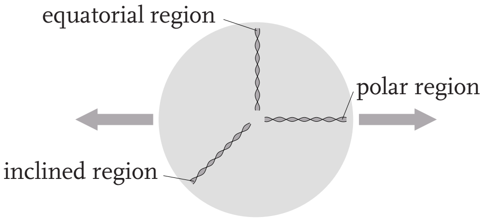

Figure 6.1 / Definition of regions in a spherulite.

In this chapter, a multiscale numerical model is used to investigate the mechanics of intraspherulitic deformation in polyethylene. For this purpose, a distinction between three different scales is made, as is schematically shown in Figure 6.2. Macroscopically, a structure of multiple spherulites is considered, which will be modeled by finite elements. Different RVE models are used for either uniaxial or plane strain deformation. In each material point within a spherulite, referred to as the mesoscopic level, an assembly of twisted, and locally parallel lamellae is assumed. The mechanical behavior of this assembly is modeled by the polycrystalline composite inclusion model (see Chapter 4). The basic element of this model is a two-phase layered structure of a crystalline and an amorphous domain. Constitutive properties are assigned to the components at this microscopic level. The microstructural behavior is linked to the mesoscopic and the macroscopic scale.

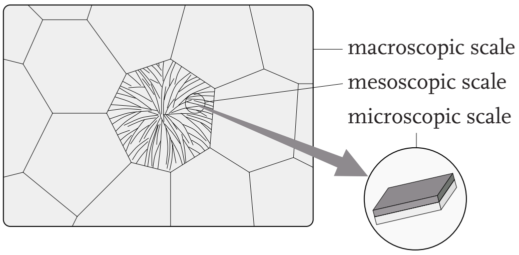

Figure 6.2 / Schematic illustration of a polyspherulitic structure with one spherulite highlighted, and an indication of the various modeling levels.

6.2 Mesoscopic scale: composite inclusion model

In this section, the anisotropy of a bundle of polyethylene lamellae, as predicted by the composite inclusion model, will be investigated. For this purpose, an aggregate of preferentially oriented composite inclusions will be subjected to various deformation modes.

6.2.1 Deformation modes

An aggregate of composite inclusions (at the mesoscopic scale), represented by a set of crystallographic orientations and corresponding lamellar orientations, will be subjected to constant strain rate uniaxial tension in the three basic directions $\boldsymbol{e}_i$ of a material associated coordinate system:

$$\bar{\boldsymbol{R}} = \boldsymbol{I} \quad ; \qquad \bar{U}_{ii} = \lambda(t) \quad ; \qquad i = 1 \vee i = 2 \vee i = 3, \tag{6.1}$$

with

$$\lambda(t) = \exp(\dot{\varepsilon} t), \tag{6.2}$$

where $\dot{\varepsilon}$ is set equal to the material reference shear rate $\dot{\gamma}_0$, $\bar{\boldsymbol{R}}$ is the mesoscopic rotation tensor, and $\bar{\boldsymbol{U}}$ is the corresponding right stretch tensor. Furthermore, the components of the mesoscopic Cauchy stress tensor $\bar{\boldsymbol{\sigma}}$ should satisfy:

$$\bar{\sigma}_{jj} = \bar{\sigma}_{12} = \bar{\sigma}_{13} = \bar{\sigma}_{23} = 0 \quad ; \qquad j \in \{1,2,3 | \, j \neq i\}. \tag{6.3}$$

In another test case, pure shear deformation is applied by prescribing one of the basic shear components ij of the (symmetric) right stretch tensor:

$$\bar{\boldsymbol{R}} = \boldsymbol{I} \quad ; \qquad \bar{U}_{ij} = \gamma(t) \quad ; \qquad ij = 12 \ \vee \ ij = 13 \ \vee \ ij = 23, \tag{6.4}$$

with

$$\gamma(t) = \frac{1}{2}\sqrt{3}\,\dot{\gamma}_0 t, \tag{6.5}$$

and

$$\bar{\sigma}_{11} = \bar{\sigma}_{22} = \bar{\sigma}_{33} = \bar{\sigma}_{kl} = 0 \quad ; \qquad kl \in \{12,13,23 | \, kl \neq ij\}. \tag{6.6}$$

6.2.2 Intraspherulitic material

A schematic illustration of the structure of an isolated spherulite is shown in Figure 6.3(a). Crystalline lamellae, interspersed with amorphous regions, grow in an approximately radial direction from a central nucleus (e.g. G'Sell and Dahoun, 1994; Lin and Argon, 1994; Allan and Bevis, 1977). This rather complicated structure will be approximated by assuming that all lamellae have grown in a perfectly radial direction with respect to the center, represented by a local coordinate system with its 1-axis in

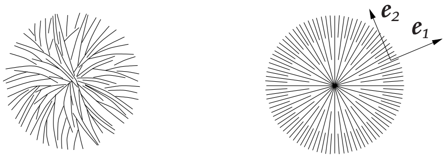

(a) (b)

Figure 6.3 / (a) Structure of an isolated spherulite (after G'Sell and Dahoun, 1994), and (b) simplified model.

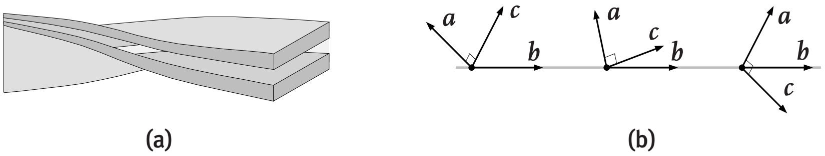

Figure 6.4 / (a) Twisting of a lamella (after Allan and Bevis, 1977), and (b) orientation of the crystallographic directions in a lamella.

the radial direction, as is shown in Figure 6.3(b). For polyethylene spherulites, having an orthorhombic lattice, this growth direction corresponds with the crystallographic (010)-direction, with a twist around this **b**-axis, as schematically depicted in Figure 6.4(a). Consequently, the principal crystallographic **a** and **c**-axes, the latter corresponding to the molecular chain direction, exhibit a rotation around the **b**-axis, as shown in Figure 6.4(b). As a representative mesoscopical unit for the intraspherulitic material of melt-crystallized high density polyethylene (HDPE), a bundle of radiating lamellae with multiple twisting periods is assumed. Therefore, the mesoscopic constitutive behavior will show a fiber symmetry around the local 1-direction. This material is modeled by an aggregate of composite inclusions with preferential initial orientations of the crystallographic domains, where the (010) poles are, except for an additional randomness, parallel to the 1-direction. The distribution of orientations of the principal lattice directions is represented in Figure 6.5(a)–(c) for 125 composite inclusions. The initial angle between $\boldsymbol{c}_0$ and $\boldsymbol{n}_0^I$ is set at 35°, corresponding to the {201} planes (see Chapter 4). Consequently, the lamellar normals are approximately perpendicular to the spherulitic radial direction. The initial orientations of the lamellar normals are shown in Figure 6.5(d).

The obtained equivalent mesoscopic stress, $\bar{\sigma}^{eq}$, as a function of the imposed deformation, when loaded in the different modes, as previously described, is represented in Figure 6.5(e) and (f). The results are normalized by the lowest slip resistance $\tau_0 = 8$ MPa. The constitutive behavior at the mesoscopic scale should be transversely isotropic with the fiber symmetry direction corresponding to the spherulitic radial direction. Therefore, all differences (at the mesoscopic scale) in mechanical response in the 22 and 33 tensile deformation modes and the 12 and 13 shear modes are of statistical origin. The viscoplastic part of the crystalline constitutive model provides eight distinct slip systems for polyethylene (Bartczak et al., 1992a). However, when loaded in the **b**-direction, only the $\{110\}\langle 1\bar{1}0\rangle$ slip systems can accommodate plastic crystalline deformation, whereas the (100) slip planes, having the lowest slip resistance, are not activated. As a consequence, an increased yield stress in the 1-direction is observed. In the plastic range, the ratio of $\bar{\sigma}_{11}/\bar{\sigma}_{22}$ is approximately 1.4. The direction in which yield resistance is elevated will be in line with the tensile direction in the polar areas of a spherulite under tension, and perpendicular to the tensile direction in the equatorial region.

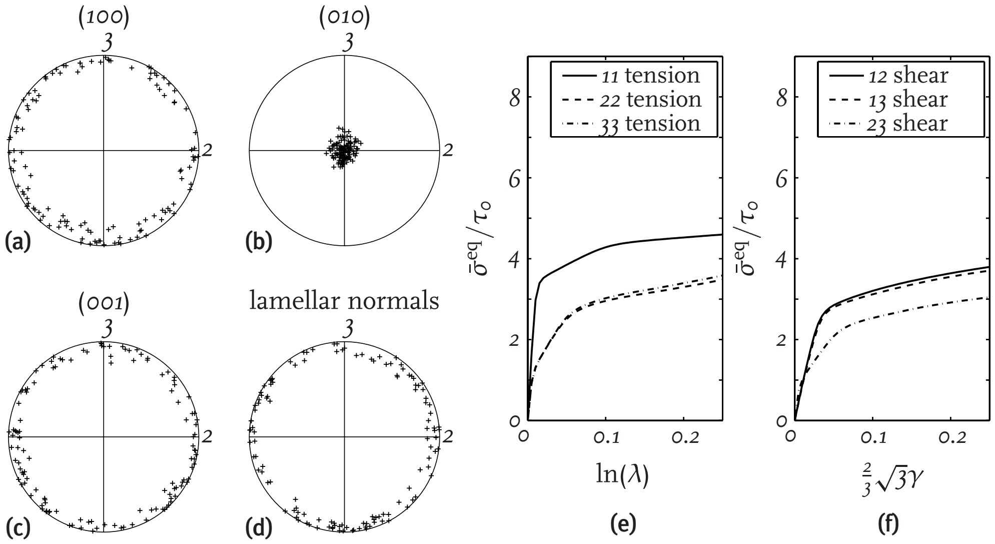

Figure 6.5 / Equal area projection pole figures with (a)–(c) the principal crystallographic lattice directions, and (d) the lamellar normals of a set of orientations representing intraspherulitic material and (e), (f) the normalized equivalent mesoscopic stress $\bar{\sigma}^{\mathrm{eq}}/\tau_0$, vs. the imposed deformation for tension and shear, respectively, in the basic material directions as predicted by the composite inclusion model.

6.3 Macroscopic scale: spherulitic models

A macroscopic structure with multiple spherulites is modeled by finite elements. Different representative volume element (RVE) models are used for for either uniaxial or plane strain deformation. For the latter, also the irregularity of the structure is accounted for.

6.3.1 Axisymmetric RVE

An axisymmetric RVE model of a staggered array (referred to as the *SA model*) of spherulites is considered, which was previously used for the simulation of particle-toughened polymers by Socrate and Boyce (2000) and by Tzika et al. (2000) and which resembles a body centered tetragonal stacking. A schematic representation of the RVE, with $L_0 = R_0$, is shown in Figure 6.6(a). A spherulitic center is assumed to be located in point C_1. Figure 6.6(b) shows the location of neighboring RVEs and the corresponding arrangement of spherulites. The spherulites are assumed to be the result of a uniform radial crystal growth; i.e. the spherulitic boundaries are located such that the distances to the nearest centers are equal. The staggered arrangement of spherulites is realized by subjecting the RVE to anti-symmetry conditions (with respect to point M) along the outer

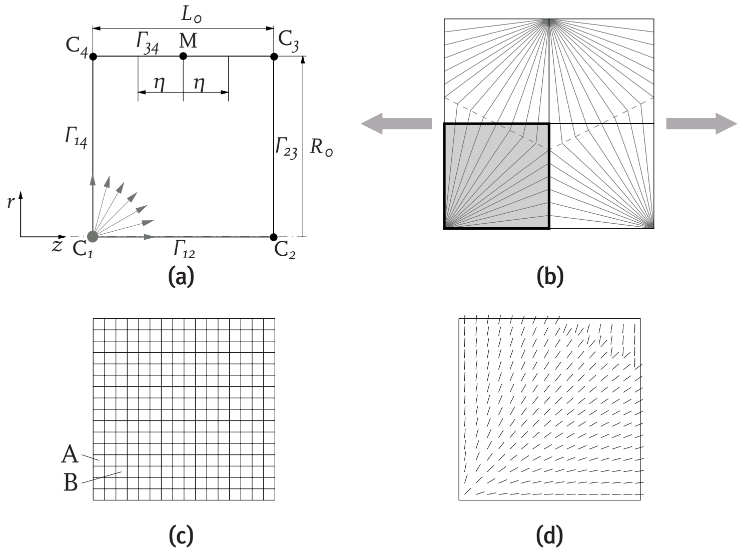

(a) (b) (c) (d)

Figure 6.6 / (a) Schematic visualization of the axisymmetric RVE model of a staggered array of spherulites, (b) the RVE with three neighboring RVEs, (c) the finite element mesh and (d) local material orientations.

radius (Tvergaard, 1996, 1998). A similar RVE has been employed for the simulation of particle-modified material in Chapter 2, where the applied boundary conditions have been discussed (Equations (2.6) to (2.11), with C_5 coinciding with C_1).

The finite element mesh of the axisymmetric SA model is visualized in Figure 6.6(c). Further on, microscopic responses will be shown for the elements that are marked A and B. In each integration point of the 256 reduced integration four-noded bilinear elements, a local coordinate system $\boldsymbol{e}_i$ is generated. The local 1-directions are shown in Figure 6.6(d). In the local coordinate system of each integration point, a unique set of initial crystallographic and lamellar orientations was generated, similar to the distribution that was shown in Figure 6.5(a)–(d), where the local 1-directions correspond to the view direction of the pole figures.

6.3.2 Irregular plane strain RVE

To account for the irregular nature of spherulitic semicrystalline material, also a plane strain RVE with randomly dispersed spherulites (referred to as the *RD model*) is used, see Figure 6.7(a). Full compatibility of each opposite boundary pair is assumed. The corresponding kinematic and natural boundary tyings (Smit et al., 1998) and the loading boundary conditions have been discussed in Chapter 2 (Equation (2.12) to (2.17)).

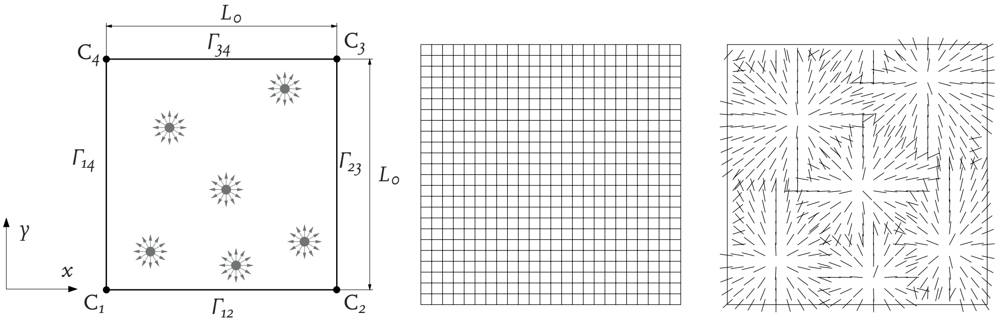

(a) (b) (c)

Figure 6.7 / (a) Schematic visualization of the plane strain RVE with an irregular distribution of spherulite centers, (b) finite element mesh and (c) local material orientations.

A structure with 6 irregularly dispersed spherulitic nuclei is taken. The mesh with 576 four-noded bilinear reduced integration plane strain elements is shown in Figure 6.7(b). A local orientation field is generated by taking the local *1*-direction towards the closest nucleus, taking into account the periodicity of the structure, and is shown in Figure 6.7(c). Again, spherulitic boundaries are located at an equal distance to the two closest nuclei.

The periodic twisting in the radial direction is modeled by employing in each integration point an aggregate of composite inclusions with a fiber symmetry around the global *1*-direction, with the ***b***-axes oriented parallel to each other. A more refined model would be obtained by assuming the length scale of an aggregate to be smaller than the wave length of twisting, i.e. if the twisting nature would be macroscopically modeled rather than mesoscopically. However, this approach would require considerably more refined finite element meshes, and is therefore not pursued in this work.

6.4 Intraspherulitic deformation and stress

In this section, the multiscale model will be used to investigate intraspherulitic deformation and stress. Both RVE models, as described in the previous section, are used. In each integration point a (unique) set of orientations with a similar distribution as in Figure 6.5(a)–(d), representing a bundle of twisted lamellae, is assumed. The local (fiber) symmetry directions correspond to the *1*-directions as described in Section 6.3. In each integration point, 64 composite inclusions per aggregate are used.

6.4.1 Axisymmetry

The axisymmetric SA model represents a polyethylene spherulite, with an initial crystallinity of $f^c = 0.7$, under uniaxial loading conditions. In Figure 6.8, the obtained fields of the magnitude of plastic deformation, $\bar{\varepsilon}_{\mathrm{p}}^{\mathrm{mag}} = \sqrt{\frac{2}{3}\bar{\boldsymbol{\varepsilon}}_{\mathrm{p}} : \bar{\boldsymbol{\varepsilon}}_{\mathrm{p}}}$, with $\bar{\boldsymbol{\varepsilon}}_{\mathrm{p}}$ a mesoscopic plastic strain tensor, are shown for different levels of macroscopically imposed deformation $\dot{\varepsilon}t$. Plastic deformation is found to be initiated in the center of the spherulite, and spreads out initially in the equatorial direction. At somewhat larger strains, the deformation remains predominantly concentrated in the center, and spreads out with an angle in the range of 0°–35° with the equator, forming a lobe at 35°. Moreover, a small concentration of deformation is found at the spherulite boundary.

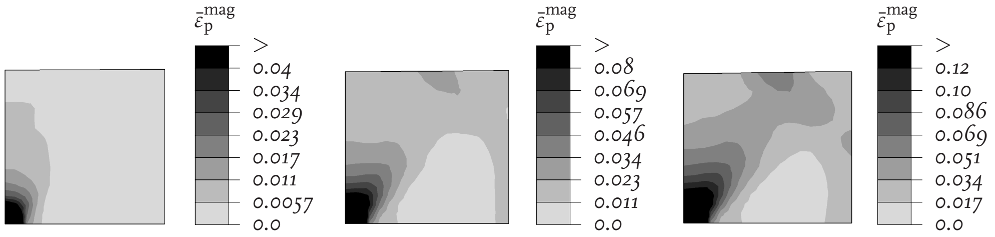

(a) (b) (c)

Figure 6.8 / Intraspherulitic magnitude of the plastic deformation, $\bar{\varepsilon}_{\mathrm{p}}^{\mathrm{mag}}$, at (a) $\dot{\varepsilon}t = 0.025$, (b) $\dot{\varepsilon}t = 0.05$, and (c) $\dot{\varepsilon}t = 0.075$, for the axisymmetric SA model.

Some selected microscopic texture evolutions and deformation quantities in the points A and B (as defined in Figure 6.6(c)) for the SA model are shown in Figure 6.9 and 6.10, respectively. In the pole figures showing the evolution of crystallographic and morpho-

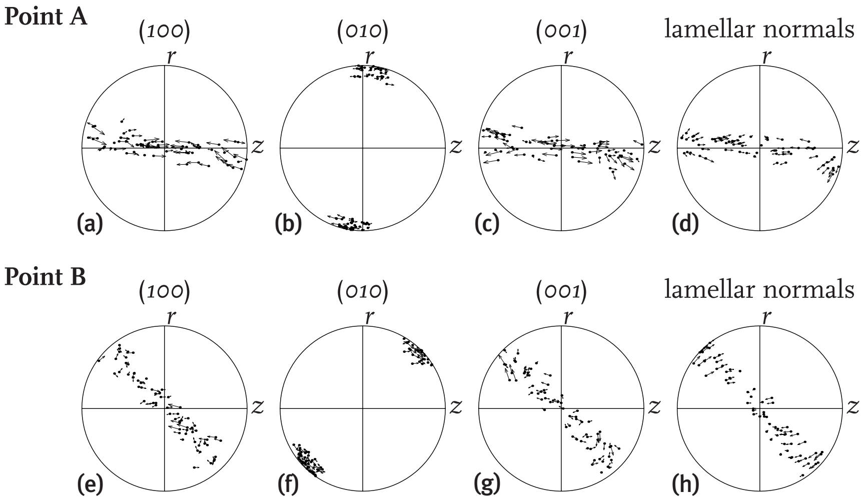

Figure 6.9 / Texture evolution in selected points of the axisymmetric SA model, at $\dot{\varepsilon}t = 0.075$.

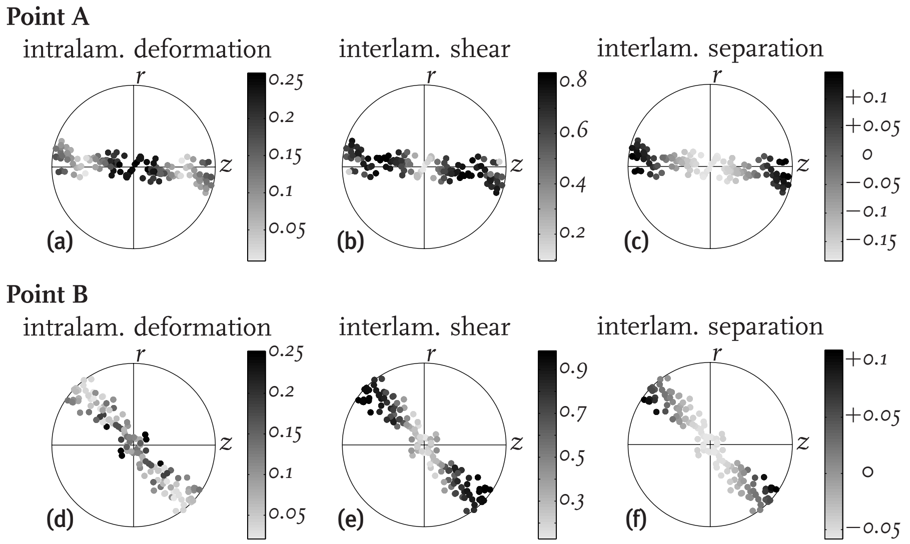

Figure 6.10 / Microscopic deformation results in selected points of the axisymmetric SA model, at $\dot{\varepsilon}t = 0.075$.

logical texture (Figure 6.9), each initial orientation is represented by a dot. The arrow connects it with the corresponding final orientation, which is located at the arrow-head. In the pole figures showing microscopic deformation quantities (Figure 6.10), the location of each dot denotes the initial orientation of the lamellar normal of an inclusion and its gray intensity represents the value of the indicated quantity for the inclusion. The latter pole figures are enriched by also mapping each pole in reflection with respect to the central point of the plot. The view direction is the macroscopic out-of-plane direction. *Intralamellar* deformation of the ith inclusion is represented by the magnitude of deformation of the crystalline phase, $(\varepsilon^{\mathrm{c}^i})^{\mathrm{mag}} = \sqrt{\frac{2}{3}\boldsymbol{\varepsilon}^{\mathrm{c}^i} : \boldsymbol{\varepsilon}^{\mathrm{c}^i}}$, with $\boldsymbol{\varepsilon}^{\mathrm{c}^i} = \ln(\boldsymbol{U}^{\mathrm{c}^i})$. For the amorphous deformation, a distinction is made between *interlamellar shear* and *interlamellar separation*. Let $\boldsymbol{\gamma}^{\mathrm{a}^i}$ be a material vector in the amorphous phase of inclusion i, with $\boldsymbol{\gamma}_0^{\mathrm{a}^i} = \boldsymbol{n}_0^{\mathrm{I}^i}$. Then, interlamellar shear is assumed to be represented by the angle (in radians) between the convected material vector, $\boldsymbol{\gamma}^{\mathrm{a}^i} = \boldsymbol{F}^{\mathrm{a}^i} \cdot \boldsymbol{n}_0^{\mathrm{I}^i}$, and the current lamellar normal, $\boldsymbol{n}^{\mathrm{I}^i}$. Lamellar separation is represented by $\ln(\lambda_{\mathrm{nn}}^{\mathrm{a}^i})$, with $\lambda_{\mathrm{nn}}^{\mathrm{a}^i} = \boldsymbol{n}^{\mathrm{I}^i} \cdot \boldsymbol{\gamma}^{\mathrm{a}^i}$.

Most (100) poles of point A, which is located in the equatorial region of the spherulite, migrate away from the tensile direction, whereas the (001) poles are moving towards the loading axis, and the (010) poles show little activity. The patterns result from deformation primarily on the (100)[001] slip system, which is the most easily activated slip system. For a small number of inclusions, also the $\{110\}\langle 1\bar{1}0\rangle$ slip systems are active. All lamellar normals are moving away from the tensile direction. The microscopic mode of deformation is found to depend on the local orientation of the lamellar normal with respect to the loading axis, as can be observed in Figure 6.10. Intralamellar crystallographic deformation is found to occur predominantly for composite inclusions with their lamellar normals almost perpendicular to the tensile direction, whereas interlamellar shear is present for inclusions with their normals either inclined to or parallel to the loading direction. For the latter orientations, also interlamellar separation is observed. In Figure 6.11, a schematic overview of the occurrence of these deformation modes is depicted. Point B is located in a region where the angle between the radial direction and the axis of loading is 45°. In this point, significant intralamellar crystallographic slip occurs only in few composite inclusions. For these domains, predominantly the (100)[010] slip system is active. Interlamellar deformation is present for those inclusions that have a relatively small angle between their lamellar normal and the loading direction (i.e. in the outer region of the pole figures). In the polar region, crystallographic slip occurs predominantly on the (100)[010] and $\{110\}\langle 1\bar{1}0\rangle$ slip systems.

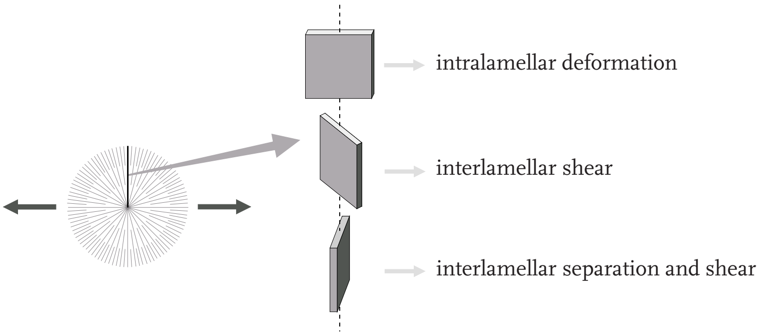

Figure 6.11 / Schematic overview of microscopic deformation modes in the equatorial region.

The normalized equivalent mesoscopic stress, $\bar{\sigma}^{\mathrm{eq}}/\tau_0$, and the normalized mesoscopic hydrostatic pressure, $\bar{p}/\tau_0$, are represented in Figure 6.12, as well as the direction and magnitude of the normalized in-plane principal stress, $\bar{\sigma}_{\max}/\tau_0$. Deviatoric stresses are concentrated primarily in the center of the spherulite. Also in the polar region near the boundary, slightly elevated equivalent stresses are found. Large tensile triaxial stresses are observed near the spherulitic boundary, and in the equatorial area, becoming larger towards the boundary. Maximum principal stresses are larger in regions of either elevated deviatoric or elevated triaxial stress, i.e. in the center of the spherulite and near the boundary, in the equatorial region. The direction of the maximum principal stress is approximately aligned with the loading direction in the entire spherulite, with a small deviation in the center and near the inclined boundary.

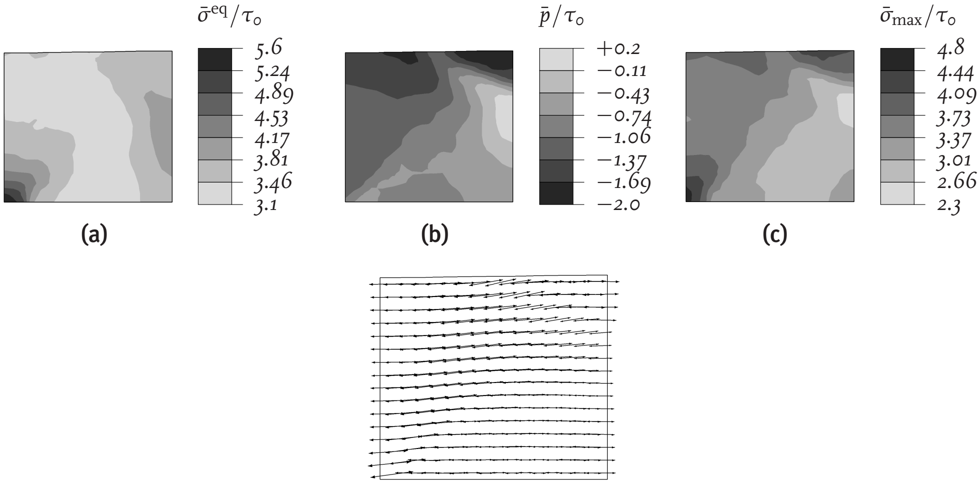

(a) (b) (c)

(d)

Figure 6.12 / (a) Normalized equivalent stress, $\bar{\sigma}^{\mathrm{eq}}/\tau_0$, (b) normalized hydrostatic pressure, $\bar{p}/\tau_0$, and (c), (d) magnitude and direction of the normalized maximum in-plane principal stress, $\bar{\sigma}_{\max}/\tau_0$, at $\dot{\varepsilon}t = 0.075$, for the axisymmetric SA model.

The dependence of the macroscopic volume-averaged axial stress $\langle\bar{\sigma}_{zz}\rangle$, versus the imposed deformation, on the crystallinity f^{c}, is represented in Figure 6.13(a) for the axisymmetric SA model. An increase of both initial stiffness and yield stress with increasing crystallinity level can be observed. The influence of the crystallinity on the macroscopic yield stress is presented in Figure 6.13(b). The yield stress is assumed to be given by the intersection of the initial and 5 percent strain tangents of the macroscopic stress–strain curve, as shown in the insert of the figure. The stresses are found to be somewhat larger than as obtained by the composite inclusion model in Chapter 4.

Although the macroscopic deformation of spherulitic material, and the corresponding stress field, may appear homogeneous, due to the heterogeneity of the meso- and microstructure, local concentrations of stress are present, even in the absence of defects. The axisymmetric SA model, that is employed in the foregoing, predicts for uniaxial tension a normalized macroscopic triaxial stress of $\langle\bar{p}\rangle/\tau_0 = -1.12$, at $\dot{\varepsilon}t = 0.075$. It can be observed from Figure 6.12(b), that this is accompanied by a minimum normalized mesoscopic hydrostatic stress of $\bar{p}/\tau_0 = -2.0$, which is found near the spherulite boundary. The corresponding microscopic normalized triaxial stresses in the amorphous and crystalline domains, p^{π^i}/τ_0 with $\pi = \mathrm{a}, \mathrm{c}$, are shown in *inverse* pole figures in Figure 6.14, where the location of each dot represents the relative orientation of the tensile direction with respect to the crystallographic coordinate system of the corresponding inclusion. The view direction is the crystallographic ***b***-axis and the gray intensity represents the magnitude of the normalized hydrostatic pressure. In the figures, 1000 randomly se-

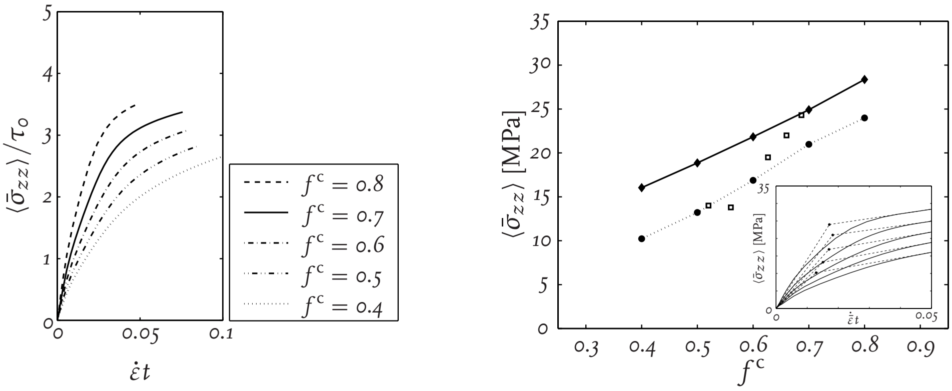

(a) (b)

Figure 6.13 / The influence of the crystallinity, f^c, on (a) the normalized volume-averaged axial stress, $\langle\bar{\sigma}_{zz}\rangle/\tau_0$, vs. the imposed deformation, $\dot{\varepsilon}t$, and (b) the volume-averaged axial stress at $\dot{\varepsilon}t = 0.05$ (closed diamonds) and yield stresses (closed circles, obtained as shown in the insert), for the axisymmetric SA model. Experimental results from Crist et al. (1989), are represented by open squares.

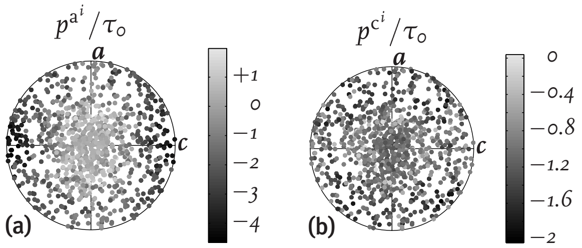

Figure 6.14 / Inverse equal area pole figures of the normalized hydrostatic pressure, p^{π^i}/τ_0, at $\dot{\varepsilon}t = 0.075$, in (a) the amorphous domains and (b) the crystalline phases.

lected composite inclusions are displayed. Maximum tensile triaxial stresses are found in the amorphous domains for loading perpendicular to the ***b***-axis, i.e. in the equatorial region. In this region, maximum values are found for inclusions that are located near the boundary and near the center, and with the molecular chain axis parallel to the tensile direction.

6.4.2 Plane strain

The multispherulite RD model is used to investigate the intra- and interspherulitic deformation of semicrystalline material under plane strain loading conditions. In Figure 6.15, the mesoscopic deformation and stress fields obtained are displayed for this model. Plastic deformation is initiated in the center of all spherulites. At larger strains, weak

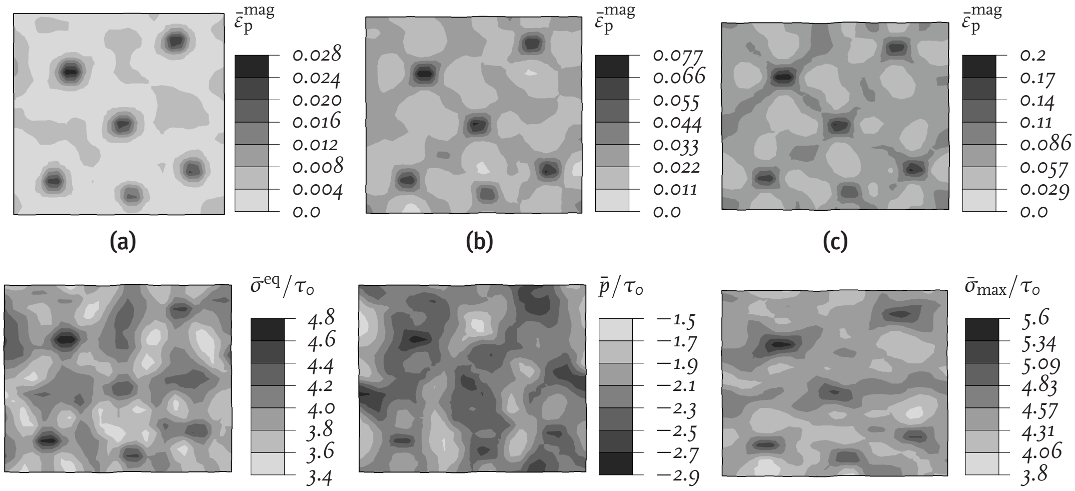

(a) (b) (c)

(d) (e) (f)

Figure 6.15 / Intraspherulitic plastic deformation, $\bar{\varepsilon}_\mathrm{p}^\mathrm{mag}$, at (a) $\dot{\varepsilon}t = 0.025$, (b) $\dot{\varepsilon}t = 0.05$, and (c) $\dot{\varepsilon}t = 0.1$, and (d) normalized equivalent stress, $\bar{\sigma}^\mathrm{eq}/\tau_0$, (e) normalized hydrostatic pressure, $\bar{p}/\tau_0$, and (f) normalized maximum in-plane principal stress, $\bar{\sigma}_\mathrm{max}/\tau_0$, at $\dot{\varepsilon}t = 0.1$, for the plane strain RD model.

deformation bands appear in the inclined regions, as well as near some spherulite boundaries. Stress concentrations are observed in the centers, spreading out in the macroscopic loading direction and the free direction, and at the boundaries. In contrast to the uniaxial unit cell simulations, tensile triaxial stresses are concentrated in the centers, spreading out in the inclined direction, and at some boundaries. Maximum principal stresses are found predominantly in the centers, spreading out towards the loading direction.

More detailed results of intraspherulitic deformation under plane strain conditions are obtained with the model with a staggered spherulite arrangement. For this purpose, plane strain elements are used for the model that was shown in Figure 6.6. Compatibility within the staggered array of spherulites is imposed by using linear anti-symmetry conditions in the r-direction along the outer radius, replacing Equation (2.7). The results obtained with the plane strain SA model are shown in Figure 6.16, and compare reasonably well with the multispherulite model with an irregular stacking of spherulites, indicating that the inhomogeneous behavior is primarily governed by the anisotropic structure within the individual spherulites, and to a lesser degree from the interactions between irregularly distributed spherulites.

Some selected microscopic texture evolutions and deformation quantities are shown in Figure 6.17 and 6.18, respectively, for the plane strain SA model. In the area of concentrated plastic deformation, i.e. in the inclined direction, where point B is situated, most slip occurs on the (100)[010] transverse slip system and additionally also on the chain slip

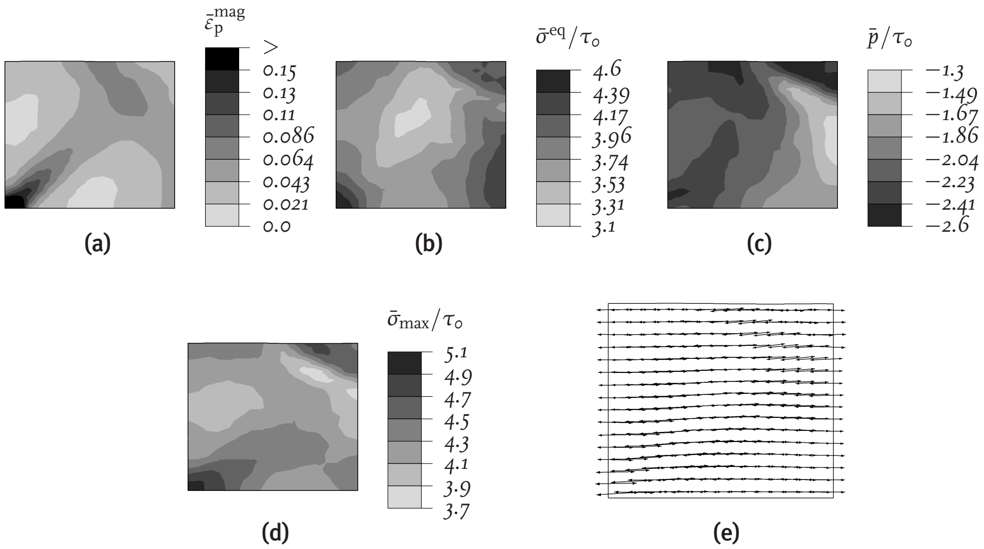

Figure 6.16 / (a) Plastic deformation, $\bar{\varepsilon}_p^{mag}$, (b) normalized equivalent stress, $\bar{\sigma}^{eq}/\tau_0$, (c) normalized hydrostatic pressure, $\bar{p}/\tau_0$, and (d), (e) direction and magnitude of the normalized maximum in-plane principal stress, $\bar{\sigma}_{max}/\tau_0$, at $\dot{\varepsilon}t = 0.075$, for the plane strain SA model.

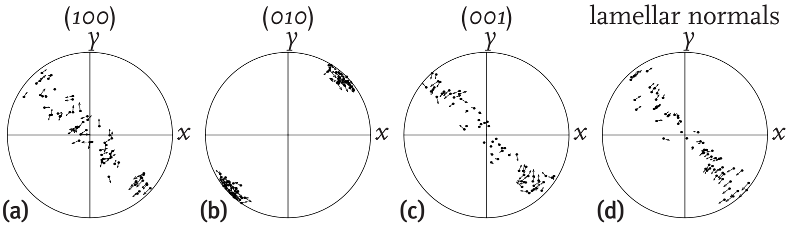

Figure 6.17 / Texture evolution in point B of the plane strain SA model, at $\dot{\varepsilon}t = 0.075$.

systems. Deformation in the equatorial area (point A) of the spherulite is substantially smaller than for the axisymmetric unit cell. Particularly, interlamellar shear in inclusions with their lamellar normals away from the tensile direction is considerably smaller as a consequence of the plane strain condition. In this area, intralamellar deformation occurs mainly by slip on the (100)[001] chain slip system.

6.5 Comparison with the mesoscopic model

In Chapter 4, a multispherulitic structure has been modeled by a mesoscopic composite inclusion model with randomly oriented composite inclusions. In the current chapter, the same structure is represented by a more refined macroscopic finite element model,

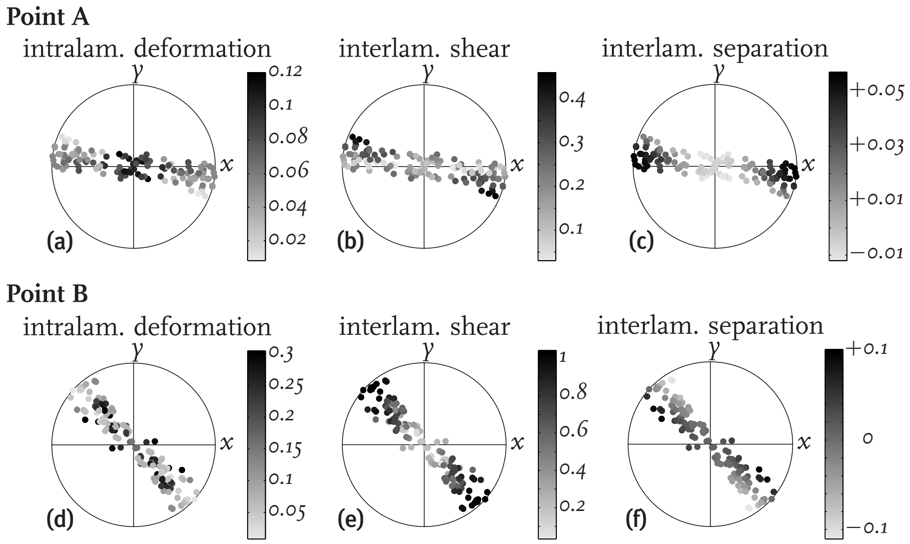

Figure 6.18 / Microscopic deformation results in selected points of the plane strain SA model, at $\dot{\varepsilon}t = 0.075$.

also taking into account the geometrical structure of the spherulites. In this section, a comparison of the microscopic results obtained for these two models is given. For this purpose, the composite inclusion model (referred to as *CI model*) of Chapter 4 is used for an aggregate of 343 initially randomly oriented composite inclusions in uniaxial tension with $\dot{\lambda}/\lambda = \dot{\varepsilon}$, and $\dot{\varepsilon} = 10^{-3}\ \mathrm{s}^{-1}$, up to the same macroscopic strain level as the multiscale finite element model of spherulites (axisymmetric SA model, Section 6.4.1), which consists of 256 times 64 composite inclusions.

In the foregoing, the local mode of deformation was found to be dependent on the orientation of the crystallographic ***b***-axis and on the lamellar normal orientation, i.e. on the full three-dimensional orientation of the composite inclusion. Moreover, the radial coordinate within the spherulite was found to determine the amount of strain. The latter effect is not represented in the mesoscopic CI model. Since the tensile direction is a symmetry direction for uniaxial loading, thus only one axis of the global coordinate system being relevant, and the orientations of all three crystallographic axes being of interest, the dependence of the microscopic results on the three-dimensional orientation of the inclusions is shown in the *inverse* pole figures in Figure 6.19, where the location of each dot represents the relative orientation of the tensile direction with respect to the crystallographic coordinate system of the corresponding inclusion. The view direction is the crystallographic ***b***-axis and the gray intensity represents the value of the indicated deformation quantity for each inclusion. For the finite element model, 1000 randomly selected composite inclusions are displayed, whereas the inverse pole figures for the mesoscopic

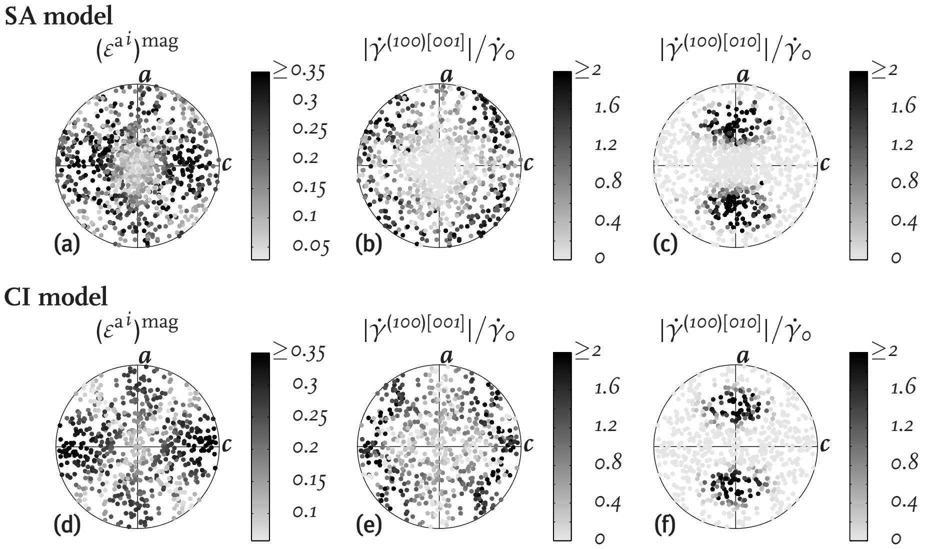

Figure 6.19 / Inverse equal area pole figures of various microscopic deformation measures in (a)–(c) the macroscopic finite element model and (d)–(f) the mesoscopic composite inclusion model, at $\dot{\varepsilon}t = 0.075$.

composite inclusion model are enriched by reflecting each pole with respect to the center of the figure. The amount of amorphous deformation is represented in Figure 6.19(a) and (d) by $(\varepsilon^{a^i})^{\mathrm{mag}} = \sqrt{\frac{2}{3}\boldsymbol{\varepsilon}^{a^i} : \boldsymbol{\varepsilon}^{a^i}}$, with $\boldsymbol{\varepsilon}^{a^i} = \ln(\boldsymbol{U}^{a^i})$. For both models, the amorphous deformation is small if the ***b***-direction is aligned with the axis of loading (i.e. in the polar region of the spherulite) or when the loading axis is inclined between ***a*** and ***c***. Due to the geometrically induced strain concentration in the center of the spherulite in the SA model, peak values are considerably higher, falling outside the chosen limits of the scale bar. In Figure 6.19, also the normalized shear rates of the two slip systems with the lowest slip resistance are represented. In both models, the (100)[001] chain slip system is *inactive* when the loading direction is close to the ***b***-direction or the ***a***-direction. When loaded parallel to the molecular chain axes, the SA model shows relatively large (100)[001] shear rates, an effect which is not observed in the CI model. The transverse slip system on the (100) plane is *active* only when the principal axis of loading corresponds to a certain direction in the ab-plane. Also for this slip system, the two models are in good agreement. Therefore, it can be concluded that although the geometrical effect of the anisotropic structure within a spherulite, causing strain concentration in the center, is not present in the mesoscopic composite inclusion model, the microscopic deformation mechanisms observed are in reasonably good agreement with the finite element model.

6.6 Influence of spherulite size for particle-modified systems

In this thesis, the influence of locally anisotropic structures in particle-modified semicrystalline polymers is numerically investigated. Starting-point was the hypothesis that the matrix material possesses a preferential orientation near the particle/matrix interface due to transcrystallization. The brittle–to–tough transition was assumed to be controlled by the ratio of the anisotropic layer thickness and the average interparticle distance. In the absence of transcrystallized layers, the matrix material of a particle-modified semicrystalline polymeric system is assumed to possess a spherulitic structure. In Figure 6.20, this is depicted for two different length scales. At a relatively small length scale, the average spherulitic diameter approximately equals the average interparticle distance. Thus, an alternative length scale parameter can be defined as the ratio of the average spherulite size and the average interparticle distance. However, although intraspherulitic material is generally anisotropic, this ratio is unable to explain the existence of a critical interparticle distance. Retrospectively, the requirements for toughening by local anisotropy (see Chapter 2) were (i) a radially oriented structure, and (ii) a sufficient amount of anisotropy with reduced *12* and *13* shear strengths. Neither requirements are satisfied for the system as represented in Figure 6.20(a). Since the amount of anisotropy within a spherulite is relatively low, the geometrical effects of the voided structure will dominate over the effects of the intraspherulitic anisotropy.

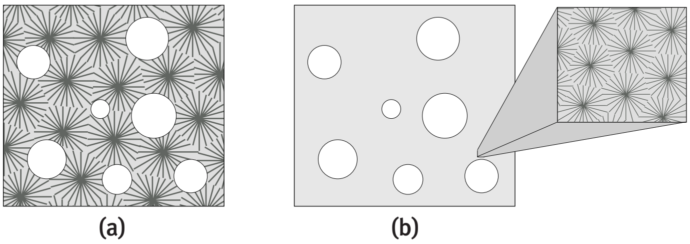

Figure 6.20 / Spherulitic structure in particle-modified material at (a) a small length scale and (b) a large length scale.

6.7 Conclusions

A three-level numerical model was used to study intraspherulitic deformation and stresses for semicrystalline polyethylene. The twisted lamellar structure of spherulitic material was represented by an aggregate of preferentially oriented two-phase composite inclusions within each material point of macroscopic finite element models of a spherulitic structure. Deformations were found to be initiated in the center, spreading out in the approximate equatorial region for uniaxial loading conditions and in inclined directions for plane strain loading. Inhomogeneous deformations were found to develop mainly as a consequence of the anisotropic structure within each spherulite, and to a lesser degree from the interactions between irregularly distributed spherulites. The deformations were linked to microstructural processes as interlamellar deformation and intralamellar crystallographic slip. Besides the dependence on the orientation of the spherulitic radial direction, the local mode of deformation depends on the phase of twisting, i.e. on the interface normal orientation. Deviatoric stress concentrations were found in the center and near the polar boundary. Tensile triaxial stresses are largest near the radial boundary of the spherulite. The anisotropy within a spherulitic structure was concluded to be unable to explain the length scale effects in particle-modified material.

CHAPTER SEVEN

Particle-modified semicrystalline material[1]

Abstract / The multiscale model is used to investigate the effect of a specific microstructural morphology on the mechanical behavior of particle-modified high density polyethylene systems. The anisotropy of material with preferential orientations is investigated. A transcrystallized microstructure is found to have a limited effect on matrix shear yielding and to alter the triaxial stress field. An alternative hypothesized microstructure is used to demonstrate the possible influence of processing conditions.

7.1 Introduction

The present-day notion of the toughening mechanism in semicrystalline materials is based on the criterion proposed by Wu (1985), which states that a sharp brittle–to–tough transition occurs for nylon/rubber blends when the average interparticle matrix ligament thickness is reduced below a critical value. A physical explanation of the absolute length parameter was offered by Muratoğlu et al. (1995a,c), who recognized the brittle–to–tough transition as a true material feature, which was attributed to thin layers of preferentially oriented material, with a reduced plastic shear resistance. Therefore, local anisotropy is due to the crystallization behavior of the matrix which is influenced by the rubber/matrix interface, leading to a layer of parallel crystalline lamellae, with the crystalline planes having the lowest plastic resistance parallel to the interface.

In Chapter 2, idealized polymeric matrix material was modeled by anisotropic Hill plasticity, and various representative volume elements were used to describe the system containing dispersed voids. It has been shown that local plastic anisotropy of matrix material around the voids can effectively replace localization by dispersed shear yielding and change the occurring hydrostatic stresses, potentially leading to toughened material behavior. However, to achieve these improvements, a morphology must be pursued that (i) has a radially oriented structure around the dispersed particles, and (ii) provides a sufficiently large amount of anisotropy with reduced *12* and *13* shear resistances. Moreover, in Chapter 3, the efficiency of this mechanism was found to be affected by the presence of hard filler particles.

---

[1] This chapter is partly reproduced from Van Dommelen et al. (2003d) and Van Dommelen et al. (2003f).

To investigate the possibility that a particular microstructure satisfies the above-mentioned requirements, a micromechanically-based numerical model for the elasto-viscoplastic deformation and texture evolution of semicrystalline polymers has been developed (Chapter 4) and will be used to simulate the behavior of particle-modified high density polyethylene (HDPE). For the analysis of these systems, a distinction between three different scales is made, as schematically depicted in Figure 1.8 of the introductory chapter. The constitutive properties of the material components are characterized at the microscopic scale. At this level, the individual crystallographic lamellae and amorphous layers are identified and are modeled as elasto-viscoplastic. The crystalline lamellae are assumed to deform plastically by crystallographic slip, whereas plastic flow of the amorphous phase is modeled as a rate-dependent process with strain hardening resulting from molecular orientation. At the mesoscopic scale, an aggregate of individual phases is considered, which can be a spherulite or a sheaflike aggregate of preferentially oriented material. To bridge between those scales, the composite inclusion model is used. The microscopic deformation and stress fields are related to the mesoscopic fields of the aggregate by a hybrid interaction law. At the macroscopic scale, for particle-modified materials, a structure of dispersed particles and matrix material can be identified. At this level, the system is represented by a finite element model using various representative volume elements, as suggested by the Hill-type simulations of Chapter 2. A bridge to the mesoscopic level is obtained by using an aggregate of composite inclusions as a representative microstructural unit in each integration point. The effect of transcrystallized orientations of matrix material versus randomly oriented material on both mesoscopic and microscopic results is investigated. A limited shear yielding effect of transcrystallized orientations is observed. Further improved properties are obtained for a hypothesized microstructure (which may be the result of process conditions) if loaded in the appropriate direction.

7.2 Anisotropy of preferentially oriented material

In the next sections, the full multiscale model will be used to examine the effect of the microstructural morphology on the mechanics of particle-modified systems. First, in this section, the anisotropy, at the mesoscopic level, of (microscopically) preferentially oriented material, as predicted by the composite inclusion model, is investigated.

7.2.1 Randomly oriented material

The local spherulitic structure of melt-crystallized HDPE is represented by an aggregate of 125 composite inclusions with randomly generated initial orientations of the crystallographic phases, having an orthorhombic lattice. The distribution of orientations of the principal lattice directions is represented in Figure 7.1(a)–(c). The initial angle between $\boldsymbol{c}_0$ and $\boldsymbol{n}_0^{\mathrm{I}}$ is set at 35°, corresponding to the $\{201\}$ planes (see Chapter 4). The initial orientations of the lamellar normals are shown in Figure 7.1(d). Since the distribution of the crystallographic orientations is random, the mechanical behavior of this aggregate will be quasi isotropic. The aggregate is subjected to the boundary conditions for different deformation modes as described in Section 6.2.1; the obtained equivalent mesoscopic stress, $\bar{\sigma}^{\mathrm{eq}}$, as a function of the imposed deformation, is represented in Figure 7.1(e) and (f). The equivalent stresses are normalized by the lowest slip resistance $\tau_0 = 8$ MPa. The number of inclusions within an aggregate should be sufficiently large, in order to expel the influence of the particular set of initial inclusions, and to mimic a truly isotropic material

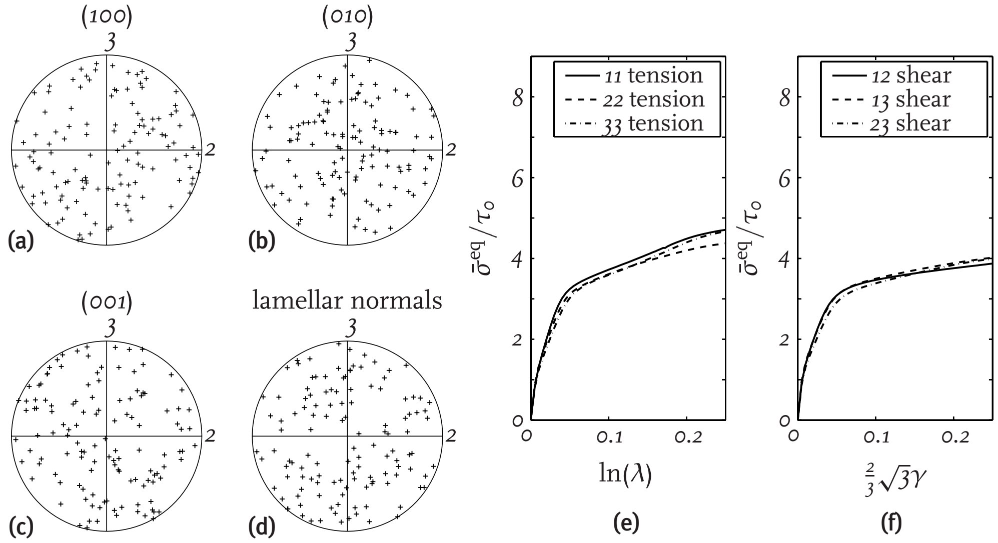

Figure 7.1 / Equal area projection pole figures representing (a)–(c) the principal crystallographic lattice directions, and (d) the lamellar normals of a random set of orientations and (e), (f) the normalized equivalent mesoscopic stress $\bar{\sigma}^{\mathrm{eq}}/\tau_0$, vs. the imposed deformation for tension and shear, respectively in the mesoscopic basic directions as predicted by the composite inclusion model.

behavior. Here, the number of inclusions that comprise an aggregate is limited to 125, hence a quasi isotropic response is obtained. The influence of the aggregate size on the mesoscopic behavior was examined in Chapter 5.

7.2.2 Transcrystallized material

The criterion for toughness of semicrystalline polymers, which was initially proposed by Muratoğlu et al. (1995c) for nylon/rubber blends and which was extended to HDPE with rubber or calcium carbonate fillers by Bartczak et al. (1999a,b), is based on the presence of transcrystallized matrix material around well-dispersed particles. A similar morphology, namely unidirectionally grown crystalline lamellae, was found in polymeric material crystallized on planar substrates (Muratoğlu et al., 1995a; Bartczak et al., 1999c). For thin HDPE films, crystallized on rubber and calcium carbonate substrates, Bartczak et al. (1999c) found a sheaflike morphology of the lamellae, which were oriented preferentially edge-on against the substrate, resulting from a surface-induced crystallization. The (100) planes, containing the two crystallographic slip systems with the lowest slip resistance, $(100)[001]$ and $(100)[010]$, were found to be directed preferentially parallel to the plane of the film with a random orientation of the molecular chains within this plane. The lamellar normals were either parallel to the plane of the substrate or somewhat tilted with respect to the plane. However, twisting of lamellae was found to be substantially reduced. The preferred crystallographic planes for the crystalline/amorphous interface remain unclear for this morphology. It can be assumed that these planes are still of the $\{h0l\}$-type. The observation by Bartczak et al. (1999c) that crystal growth is unidirectional with little divergence sideways, and the reduction of lamellar twisting, suggest a smaller angle between the crystallographic chain direction $\boldsymbol{c}$ and the lamellar normal $\boldsymbol{n}^{\mathrm{I}}$ than observed in randomly crystallized material. Here, the plane of the crystalline/amorphous interface is assumed to be of the $\{102\}$-type, corresponding to an initial chain tilt angle of 9.7°. Besides the crystallographic and lamellar orientations, all microscopic material properties are assumed to be identical to the properties of the randomly crystallized material. A set of crystallographic orientations is generated with the (100) poles preferentially aligned in the direction of the normal of the substrate, with a certain random deviation from the substrate normal direction. Furthermore, a random rotation around this normal direction is applied. Therefore, the mechanical properties at the mesoscopic scale can be expected to be transversely isotropic with the (fiber) symmetry direction corresponding to the substrate normal direction. All differences in mechanical response in the 22 and 33 tensile directions and the 12 and 13 shear directions will be of statistical origin. After a set of crystallographic orientations has generated, the lamellar normals are obtained as described above. In Figure 7.2(a)–(d), the orientations of a set of 125 composite inclusions are displayed. The view direction of the equal area pole figures is the substrate normal direction. This direction is the preferred direction for the (100) poles. In Fig-

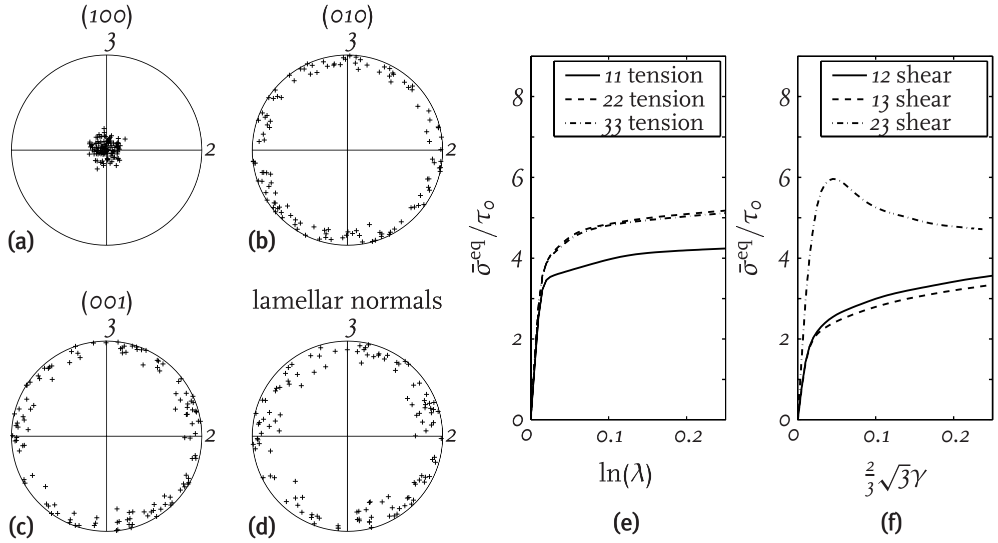

Figure 7.2 / Equal area projection pole figures representing (a)–(c) the principal crystallographic lattice directions, and (d) the lamellar normals of a set of transcrystallized orientations and (e), (f) the normalized equivalent mesoscopic stress $\bar{\sigma}^{eq}/\tau_0$, vs. the imposed deformation for tension and shear, respectively, in the basic material directions as predicted by the composite inclusion model.

ure 7.2(e) and (f), the corresponding mesoscopic stress–strain response of the composite inclusion model is shown in the basic tensile and shear directions. With respect to the randomly oriented aggregate, the equivalent stresses in the transverse tensile directions are increased. The reduction of the 12 and 13 shear resistances is related to these tensile 22 and 33 resistances. The ratio of transverse tensile and 12/13 shear resistances at the onset of yielding is of the order of 2. At higher strains, this ratio decreases to approximately 1.5. Simulations with an anisotropic Hill plasticity model (Chapter 2) showed that for the effectiveness of the toughening mechanism under investigation, a larger amount of anisotropy would be necessary. A sharper texture, however, does not increase the R_{22}/R_{12} anisotropy ratio.

7.3 Macroscopic models

For particle-modified materials, a structure of dispersed particles and matrix material can be identified. The system is described by a finite element model of a representative volume element (RVE). The blended system, having a three-dimensional nature, is simplified to a two-dimensional RVE, for which two different approaches are used (see

Chapter 2). In order to capture the important effects of the essentially irregular nature of particle-dispersed systems, a plane strain RVE with randomly dispersed particles (referred to as the *RD model*) is used, where the cavitated particles are represented by voids. In Figure 7.3(a), a schematic illustration of this RVE is shown. The periodicity assumption requires full compatibility of each opposite boundary pair (Smit et al., 1999). The corresponding essential and natural boundary tyings and the applied tensile loading conditions were discussed in Chapter 2 (Equation (2.12) to (2.17)). A similar structure as was used in the Hill-type simulations in Chapter 2 is adopted, containing 20 volume percent irregularly dispersed voids. The mesh with 565 four-noded bilinear reduced integration plane strain elements is shown in Figure 7.3(b). An orientation field is generated by taking the local 1-directions perpendicular to the closest void/matrix interface, respecting the periodicity of the structure, as shown in Figure 7.3(c).

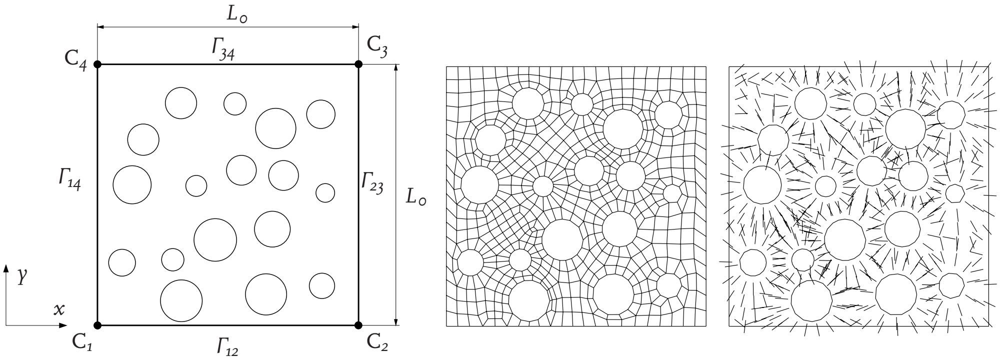

(a) **(b)** **(c)**

Figure 7.3 / (a) Schematic visualization of a multiparticle plane strain RVE, (b) finite element mesh, and (c) local material orientations.

For the representation of the triaxial stress state around a particle, an axisymmetric RVE model of a staggered array of particles (referred to as the *SA model*) is considered, which was previously used for the study of the micromechanics of particle-modified polymers by Socrate and Boyce (2000) and by Tzika et al. (2000) and which resembles a body centered tetragonal stacking of particles. A schematic representation of the RVE, with $L_0 = R_0$, is shown in Figure 7.4(a) and (b), where the cavitated particle is represented as a void. The RVE is subjected to anti-symmetry conditions (with respect to point M) along the outer radius. The periodicity conditions and tensile loading conditions applied were presented in Chapter 2 (Equations (2.6) to (2.11)). The finite element mesh of the SA model, with 20 volume percent voids, is visualized in Figure 7.4(c). In each integration point of the 196 reduced integration four-noded bilinear elements, a local coordinate system is generated, such that the local 1-directions are again perpendicular to the closest void surface, as is shown in Figure 7.4(d).

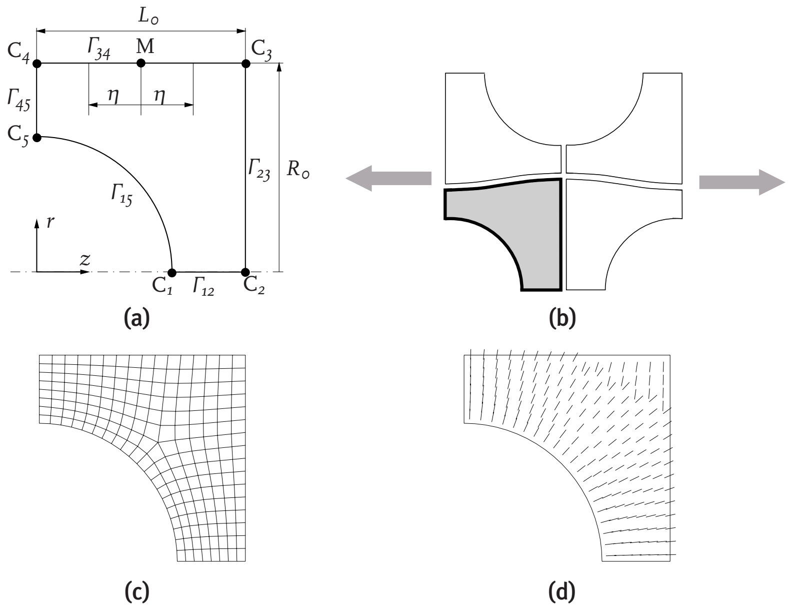

Figure 7.4 / (a) Schematic visualization of an axisymmetric RVE model of a staggered array of particles, (b) its position with respect to three neighboring RVEs in a deformed state, (c) finite element mesh and (d) local material orientations.

7.4 Effect of transcrystallized anisotropy on toughness

In this section, the full multiscale model will be used to investigate the effect of a transcrystallized orientation on the deformation of particle-modified systems. Both RVE models, as described in the previous section, are applied, with in each integration point either an aggregate of randomly generated orientations or a (unique) set of orientations with a similar distribution as in Figure 7.2. For the latter situation, the local (fiber) symmetry directions correspond to the 1-directions as described in Section 7.3. In each integration point, 64 composite inclusions per aggregate are used.

In Figure 7.5, for the plane strain RD model, the obtained fields of the magnitude of plastic deformation, $\bar{\varepsilon}_p^{\mathrm{mag}} = \sqrt{\frac{2}{3}\bar{\boldsymbol{\varepsilon}}_p : \bar{\boldsymbol{\varepsilon}}_p}$, are shown for $\dot{\varepsilon}t = 0.025$. For the large scale RVE, containing randomly oriented, and thus quasi isotropic, matrix material, plastic deformation is localized in particle-bridging paths, percolating through the matrix, approximately perpendicular to the loading direction. The small scale RVE, having transcrystallized orientations, shows more widespread localized plastic deformation, with also shear bands in relatively thick interparticle ligaments, in the 30° to 50° direction with respect to the particle poles (the term *pole* refers to the location where the particle/matrix interface normals are aligned with the loading direction). In the relatively thin ligaments, still localized deformation is observed. In Figures 7.6 and 7.7, the magnitude of the plastic deforma-

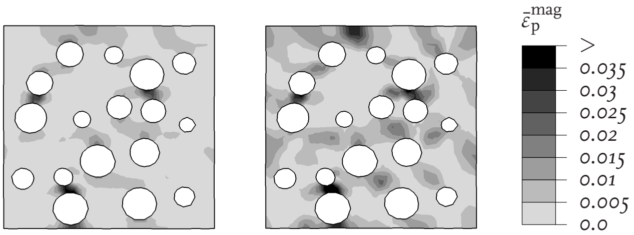

(a) (b)

Figure 7.5 / The influence of radially oriented anisotropy on the magnitude of the plastic deformation, $\bar{\varepsilon}_\text{p}^\text{mag}$, for the RD model, at $\dot{\varepsilon}t = 0.025$, with (a) randomly generated initial orientations, and (b) transcrystallized preferential orientations.

tion is shown for $\dot{\varepsilon}t = 0.05$, as well as some selected microscopic texture evolutions and deformation quantities in two integration points, for random and transcrystallized initial orientations, respectively. For both situations, most plastic deformation is concentrated in relatively thin interparticle ligaments. The presence of a layer of preferentially crystallized material with significant thickness around cavitated rubber particles does have some effect on the mechanism of matrix shear yielding. This effect is, however, limited due to the relatively small level of anisotropy in the material.

In the pole figures showing the evolution of crystallographic and morphological texture, the initial orientation of each composite inclusion is represented by a dot. The arrow connects it with the corresponding final orientation, which is located at the arrow-head. In the pole figures showing microscopic deformation quantities, the location of each dot denotes the initial orientation of the lamellar normal of an inclusion and its gray intensity represents the value of the indicated quantity for the inclusion. To enrich the information shown in the latter pole figures, the mirror location of each pole with respect to the central point of the plot is also given. The view direction is the macroscopic out-of-plane direction. The term *intralamellar* deformation is employed for the magnitude of the deformation of the crystalline phase. For the amorphous deformation, a distinction is made between so-called *interlamellar shear* and *interlamellar separation* (as defined in Chapter 6). The integration point indicated by A in Figures 7.6 and 7.7, represents, for the initially randomly oriented material, a material point in the highly localized zone. Since this integration point is located in the equatorial area (the *equator* is defined as the area where the particle/matrix interface normal is perpendicular to the loading direction), the local 1-direction is almost perpendicular to the global loading direction. The microscopic results for this point show moderate crystallographic deformation, mainly for inclusions with their lamellar normals close to the local 1-direction. The (100) poles, which represent the planes containing the two most easily activated slip systems, migrate towards a direction which is approximately 40° away from the local 1-direction. The lamellar normals are moving towards the same direction, with the largest activity for lamellar poles

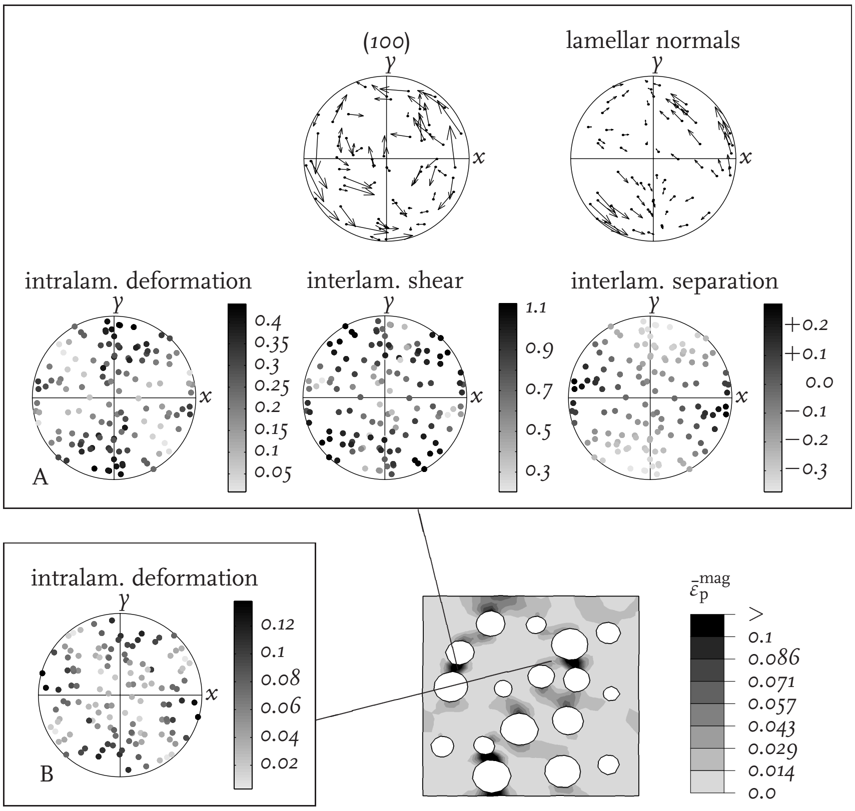

Figure 7.6 / The magnitude of the plastic deformation, $\bar{\varepsilon}_\mathrm{p}^\mathrm{mag}$, and selected microscopic results for the RD model, at $\dot{\varepsilon}t = 0.05$, with randomly generated initial orientations.

initially far from the target direction. Amorphous deformations are relatively large, with interlamellar shear predominantly in inclusions with their crystalline/amorphous interface approximately 45° inclined with the loading direction. Interlamellar separation is found predominantly in inclusions with their interface normals perpendicular to the local 1-direction. For the RVE with transcrystallized orientations (Figure 7.7), deformation is still localized in the ligament containing integration point A. In this point, the maximum intralamellar (crystallographic) deformation has increased with respect to the quasi isotropic material, whereas both maximum interlamellar shear and separation have decreased. Crystallographic deformation is concentrated in inclusions with their lamellar normals perpendicular to the loading direction. Also in integration point B, the maximum intralamellar deformations are approximately doubled, whereas the magnitude of the interlamellar deformations is comparable to the isotropic situation.

In Figures 7.8 and 7.9, the normalized hydrostatic pressure $\bar{p}/\tau_0$, as well as some selected microscopic texture evolutions and deformation quantities in two integration points, are shown for the SA model, with random and transcrystallized initial orientations, respec-

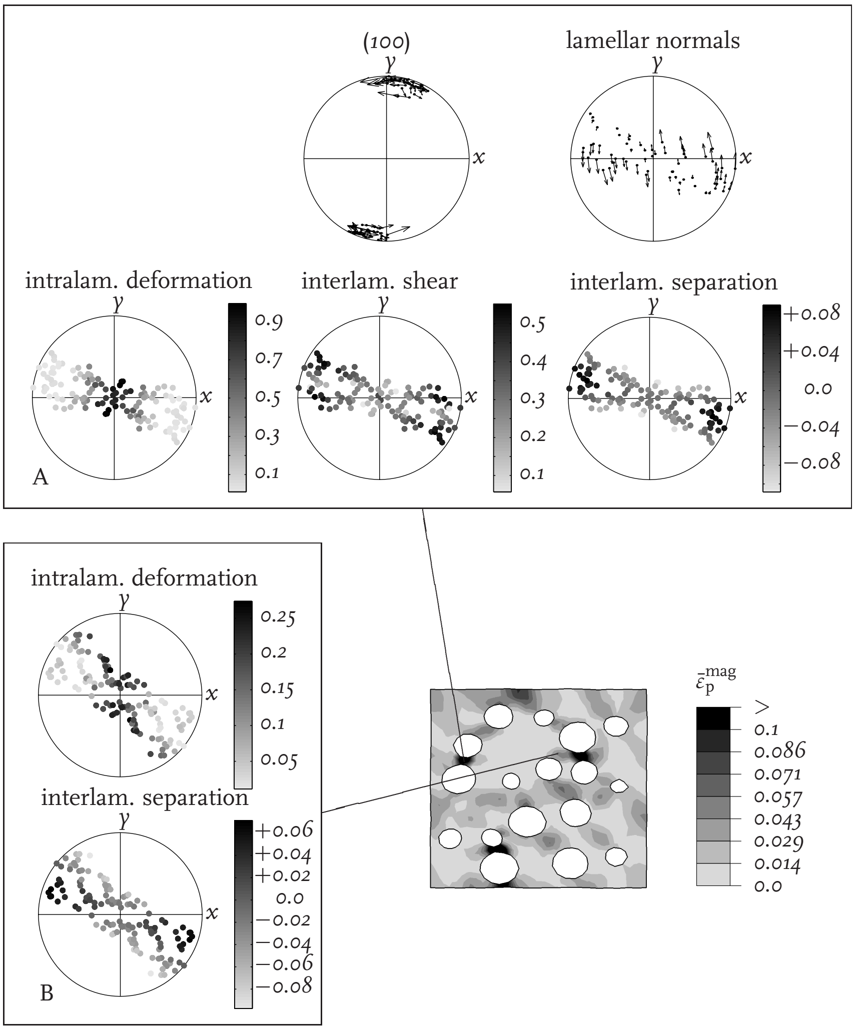

Figure 7.7 / The magnitude of the plastic deformation, $\bar{\varepsilon}_\mathrm{p}^\mathrm{mag}$, and selected microscropic results for the RD model, at $\dot{\varepsilon}t = 0.05$, with transcrystallized initial orientations.

tively. The region of peak tensile triaxial stresses is located in the matrix material near the polar region for the preferentially oriented material, rather than in the equator area, as is observed for the randomly oriented material. In the equator region, the hydrostatic pressures remain negative; however, the absolute values are reduced with respect to the quasi isotropic material. In Figure 7.10, the direction and the magnitude of the normalized maximum in-plane principal stress, $\bar{\sigma}_\mathrm{max}/\tau_0$, are shown for the SA model. For the large scale, quasi isotropic material, the maximum principal stresses are found to be negligible in the polar region, whereas for the small scale configuration, with transcrystallized ori-

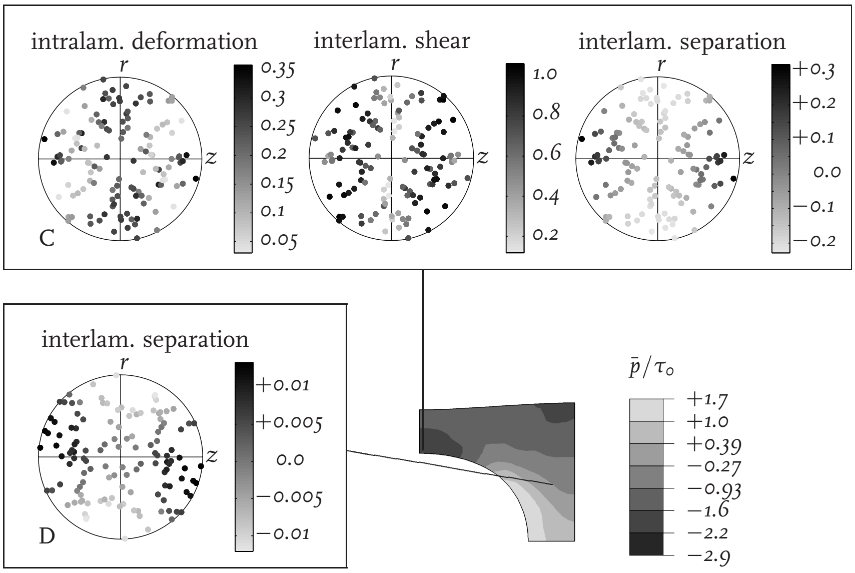

Figure 7.8 / The normalized hydrostatic pressure, $\bar{p}/\tau_0$, and selected microscopic results for the SA model, at $\dot{\varepsilon}t = 0.1$, with randomly generated initial orientations.

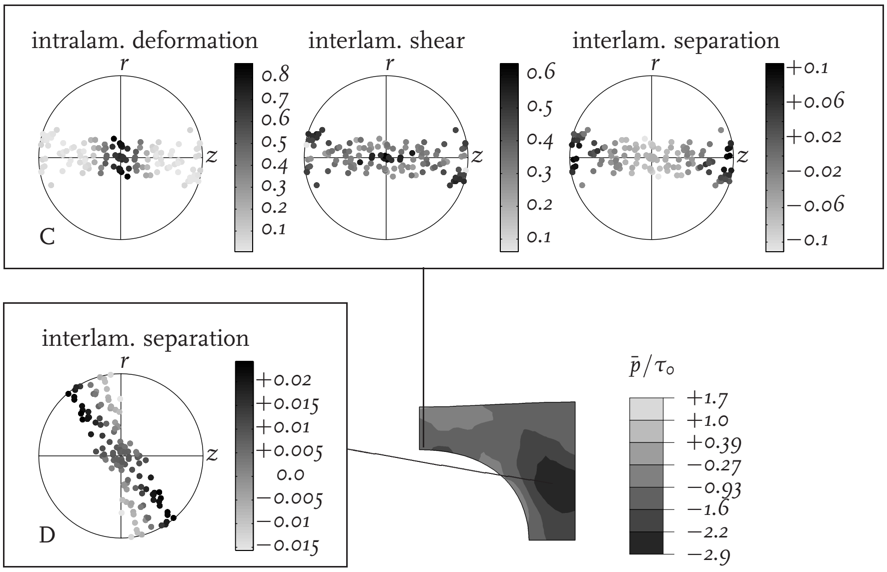

Figure 7.9 / The normalized hydrostatic pressure, $\bar{p}/\tau_0$, and selected microscopic results for the SA model, at $\dot{\varepsilon}t = 0.1$, with transcrystallized initial orientations.

entations, also in this region, maximum principal stresses are significant. In the equator region, maximum values are slightly increased with respect to the principal stresses in the isotropic material.

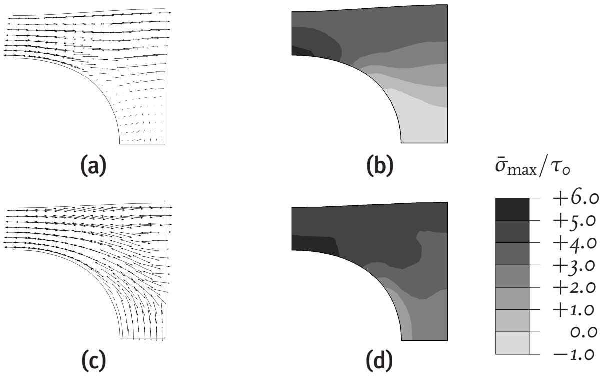

Figure 7.10 / The direction and the magnitude of the normalized maximum in-plane principal stress, $\bar{\sigma}_{\max}/\tau_0$, for the SA model, at $\dot{\varepsilon}t = 0.1$, with (a)–(b) randomly generated orientations, (c)–(d) transcrystallized preferential orientations.

For the initially randomly oriented configuration, in integration point C, which is located in the equatorial region, the intralamellar deformations are relatively small, and are found predominantly for inclusions with their lamellar normals either perpendicular or parallel to the loading direction. In the remaining inclusions, interlamellar shear is considerably large and a significant amount of interlamellar separation is found for inclusions with their lamellar normals aligned with the loading direction. For these inclusions, the preferred direction of possible craze growth, perpendicular to the direction of the maximum principal stress (Kramer, 1983), is parallel to the crystalline/amorphous interface. For the material with transcrystallized initial orientations, the maximum intralamellar deformations are more than doubled with respect to the randomly oriented material for inclusions with their lamellar normal perpendicular to the loading direction. Interlamellar deformations are considerably reduced. For integration point D, which is located in a high tensile triaxial stress area, lamellar separations remain small.

In polymeric materials, the principal mechanisms leading to deformation and fracture (Kausch et al., 1999) are shear yielding of matrix material, voiding and the occurrence of crazelike features (Michler and Godehardt, 2000; Narisawa and Ishikawa, 1990) under triaxial stress conditions, and brittle fracture of the matrix by chain scission, induced by high tensile principal stresses. Whether or not the material will show toughened behavior will depend on which of these phenomena will predominantly occur. Massive shear yielding, with energy-absorbing inelastic deformation, will have a beneficial effect on toughening. However, for the transcrystallized orientation currently considered, the increase of matrix shear yielding (replacing strain localization) is limited. Intralamellar deformation is favored over interlamellar deformation. In the quasi isotropic material, crazelike features may be initiated in the equator region, where the peak tensile triaxial stresses are maximal, and significant interlamellar separation occurs. Since they will grow perpendicular to the direction of maximum principal stress, the growth direction will be transversely to the macroscopic tensile direction. These crazes may act as precursors to cracks, ultimately leading to failure. For the material having transcrystallized preferential orientations, in this region the negative hydrostatic pressures and interlamellar separation are reduced, diminishing the chance of craze initiation. On the other hand, in the polar region, for this material, relatively large tensile triaxial stresses are found, possibly initiating voids. However, interlamellar separation remains small at this location. In this area, the growth direction of possible crazes will be in the direction of macroscopic loading, and crazing may become an energy-absorbing mechanism. Therefore, transcrystallized orientations may lead to some degree of toughening, however, the effect is limited by the relatively small amount of anisotropy.

7.5 Alternative microstructure

In the previous section, a fully radially oriented, transcrystallized, microstructure was shown to have a beneficial, but limited effect on the mechanics of deformation in particle-modified systems. This was due to the relatively small reduction in yield strength in the local *12* and *13* shear directions. A further decrease of these shear yield strengths would increase matrix shear yielding. Alternatively, an increase of the local *22* tensile yield strength, would have a similar effect, since concurrently it reduces the strengths in shear.

A small flow-related crystallographic orientation was found by Bartczak et al. (1999b) in HDPE with calcium carbonate fillers. The importance of process conditions was demonstrated by Schrauwen et al. (2001a,b, 2002), who found toughness to be dominated by flow-induced effects. A row structure of polyethylene lamellae was found in extruded alternating high density polyethylene and polystyrene thin layers by Pan et al. (1990). The long axes of the lamellae, which are the crystallographic ***b***-axes, were oriented in the plane of the layers and perpendicular to the extrusion direction. The ***a***-directions were found to be predominantly normal to the layer surface and lamellar surface normals were aligned with the direction of flow. Moreover, only partial twisting was observed. In thicker layers, an unoriented structure was observed, similar to bulk polyethylene, with the corresponding lamellar twisting.

In this section, the effect of a hypothetical microstructure, with preferential orientations that may be the result of an influence of the process conditions on the crystallization of matrix material, will be investigated for a voided macrostructure. The transcrystallized preferential orientations as used previously, were axisymmetric with respect to the local *1*-direction, i.e. within the plane of the particle/matrix interface, the orientation was assumed to be random. This is schematically shown in Figure 7.11(a), where all transverse orientations are represented in a discoid structure (Muratoğlu et al., 1995a). Here,

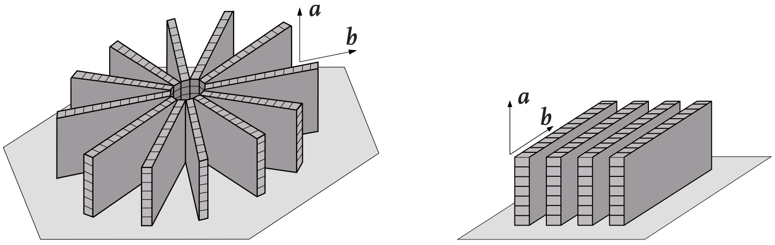

(a) (b)

Figure 7.11 / (a) Transversely isotropic transcrystallized material and (b) transcrystallized material with an additional row structure.

an additional preferential orientation of the molecular chains and the lamellar normals in the local 2-direction is assumed (see Figure 7.11(b)). The lamellar row structure obtained thereby may be the result of an influence of the flow on the crystallization behavior, and resembles the structure that was reported by Pan et al. (1990). Again, the crystallographic $\{102\}$ planes are assumed to constitute the crystalline/amorphous interface, with an initial tilt angle of 9.7°. In Figure 7.12, a generated set of 125 composite inclusion orientations of this type are displayed. The stress–strain behavior obtained when this aggregate of composite inclusions is subjected to tension and shear in the basic material directions is shown in Figure 7.12(e) and (f). Because of the lack of a fiber symmetry in this material, large differences between the 22 and 33 tensile loading configurations are found. With respect to the transcrystallized orientations (Figure 7.2), the yield strength in the 22-direction has considerably increased, whereas the 33 yield strength is reduced. At $\ln(\lambda) = 0.05$ and $\frac{2}{3}\sqrt{3}\gamma = 0.05$, the ratio of the 22 tensile and 12 shear yield strength is 3.4. The ratio of the 22 tensile resistance and the 12 shear resistance of transcrystallized material is 3.0. When material with this microstructural morphology would, in a particle-dispersed system, be oriented appropriately with respect to the loading conditions, an additional beneficial effect on the amount of matrix shear yielding may be expected.

A microstructure of matrix material around well-dispersed voided particles is hypothesized that consists of lamellar crystals that are nucleated at the particle/matrix interface. An influence of processing conditions is assumed for matrix material in the equatorial regions (with respect to the flow direction). This hypothetical morphology is realized by assigning aggregates of composite inclusions with crystallographic and morphological orientations similar to the orientation set in Figure 7.12 to specific elements of the finite element meshes which were previously used for the RD model and the SA model. These elements are located in the equatorial areas with respect to the flow direction. For the remaining elements, again transcrystallized orientations are assumed (similar to Figure 7.2). In Figure 7.13, the assigned flow-influenced areas are shown for both models, for either flow in the loading direction or flow perpendicular to the loading direction. In each integration point, the local 1-directions are assumed to be radially oriented with re-

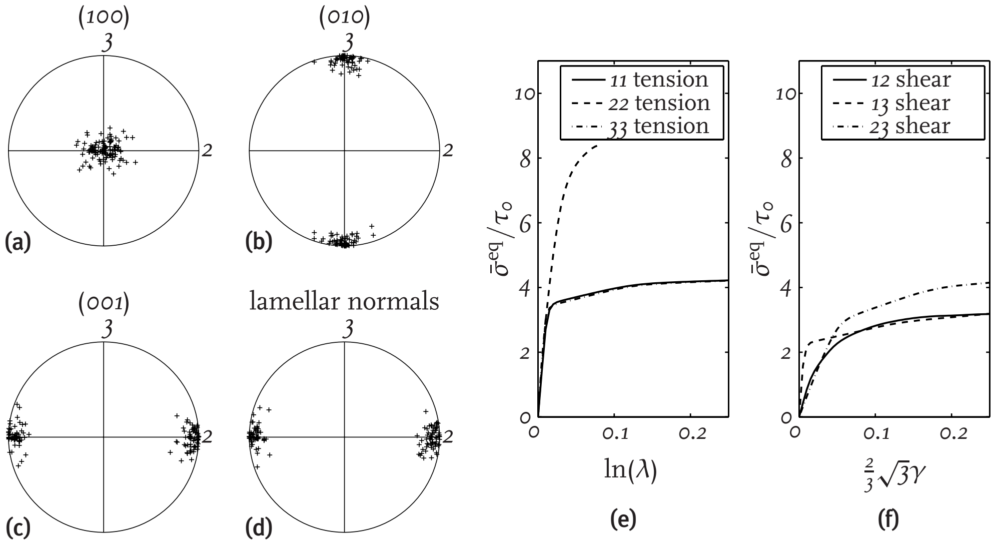

Figure 7.12 / Equal area projection pole figures representing (a)–(c) the principal crystallographic lattice directions, and (d) the lamellar normals of an anisotropic set of orientations with an assumed influence of processing conditions and (e), (f) the normalized equivalent mesoscopic stress $\bar{\sigma}^{eq}/\tau_0$, vs. the imposed deformation for tension and shear, respectively, in the basic material directions as predicted by the composite inclusion model.

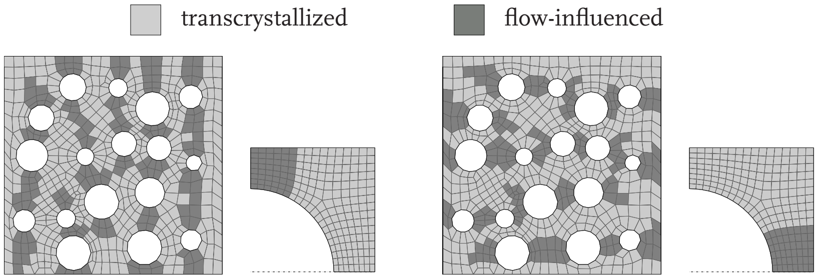

(a) FD: ↔ **(b)** FD: ↔ **(c)** FD: ↕ **(d)** FD: ↕

Figure 7.13 / Assumed influence of flow on crystallization, with (a)–(b) flow in the loading direction and (c)–(d) flow perpendicular to the loading direction. The flow direction (FD) is indicated by the arrows.

spect to the nearest particle, as was previously used for the transcrystallized situation. In Figure 7.14, the effect of this microstructure on the obtained field of plastic deformation is shown for the RD model at $\dot{\varepsilon}t = 0.035$. In this figure, also the fully transcrystallized situation is represented. When the macroscopic loading is applied perpendicular to the

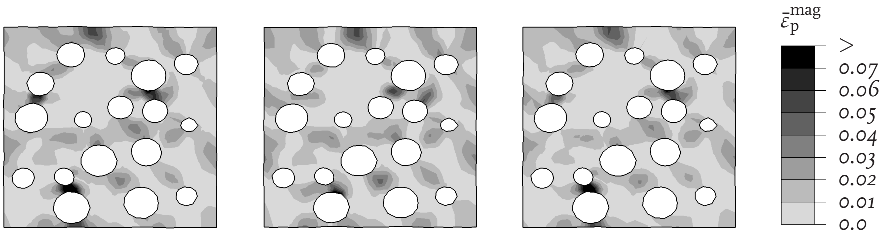

(a) **(b)** FD: ↔ **(c)** FD: ↕

Figure 7.14 / The influence of (a) transcrystallized orientations and (b), (c) flow-influenced orientations on the magnitude of the plastic deformation, $\bar{\varepsilon}_\mathrm{p}^\mathrm{mag}$, for the RD model, at $\dot{\varepsilon}t = 0.035$, with (b) flow in the loading direction, (c) flow perpendicular to the loading direction. The flow direction (FD) is indicated by the arrows.

flow direction, no significant effect of the flow-influenced orientations can be observed, compared to fully transcrystallized material. However, when the RVE is loaded in the direction of the flow, the plastic deformation is no longer localized in the relatively thin interparticle ligaments, but occurs predominantly in the matrix material, away from the particle surfaces and at the particle surface at an inclined location.

In Figure 7.15(a), the normalized hydrostatic pressure field is represented for the SA model, loaded in the flow direction. Results for the material loaded perpendicular to the flow direction are not shown because of the similarity with the fully transcrystallized situation. As for the fully transcrystallized situation, the area of peak tensile hydrostatic stress is relocated from the equatorial region for the quasi isotropic material to the matrix material near the particle pole. Figure 7.15(b) and (c) show the normalized maximum in-plane principal stress for the SA model with the influence of flow in the loading direction. The largest maximum principal stresses are again observed in the equatorial area.

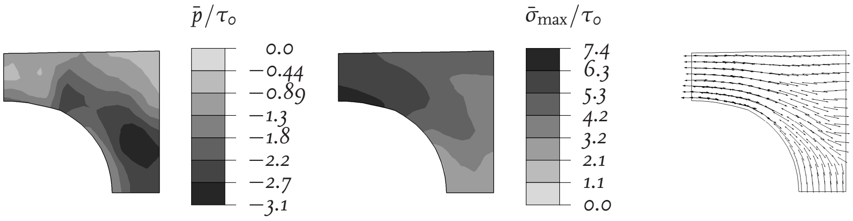

(a) **(b)** **(c)**

Figure 7.15 / (a) The normalized hydrostatic pressure, $\bar{p}/\tau_0$ and (b), (c) the magnitude and the direction of the normalized maximum in-plane principal stress, $\bar{\sigma}_\mathrm{max}/\tau_0$, for the SA model, at $\dot{\varepsilon}t = 0.075$, with the influence of flow in the loading direction.

Thus, the hypothesized microstructure with local material orientations that may result from an influence of process conditions on crystallization may increase the toughening effects, if loaded in the appropriate direction with respect to the flow direction. Then, localization of deformation is replaced by dispersed shear yielding. Although an hypothesized microstructure is used, whereas the actual microstructure induced by the flow is unknown, this example demonstrates the possible importance of the processing conditions for the particle-toughening of semicrystalline material.

7.6 Conclusions

A physically-based mechanism for the toughening of semicrystalline polymeric materials by the dispersion of particles relies on the presence of a layer of anisotropic transcrystallized material around the particles (Muratoğlu et al., 1995c; Bartczak et al., 1999a,b). In this chapter, a multiscale model was used to investigate the effect of preferentially oriented matrix material in HDPE blended with rubber particles, which were assumed to be cavitated. The particle-dispersed system was described by both a plane strain RVE model with irregularly dispersed voids and by an axisymmetric RVE model with an assumed regular stacking of voids, which were loaded in constant strain rate tension. In each integration point of the finite element model, an aggregate of composite inclusions has been used as a representative microstructural element that provides the constitutive behavior of the material at the mesoscopic level. Constitutive properties were assigned at the microstructural level to the amorphous and the crystalline domains. Besides these properties, the mesoscopic constitutive behavior was affected by the crystallographic and lamellar orientations of the composite inclusions. By using preferential initial orientations, a mesoscopically anisotropic constitutive behavior was obtained.

Simulations on voided polymeric material with a large average interparticle matrix ligament thickness, having quasi isotropic constitutive behavior at a mesoscopic level, showed a strongly localized deformation, along a path through the matrix, perpendicular to the loading direction. Large tensile triaxial stresses were found in the equator region (with respect to the loading direction) near the particles. In this area, interlamellar separations were relatively large. A particle-modified system having a relatively small average interparticle matrix ligament thickness has been realized by using initially preferentially oriented lamellae, with the crystallographic (*100*) planes approximately parallel to the void/matrix interface. For this system, a more dispersed field of plastic deformation was found, induced by a small relative reduction of the shear yield strength. Moreover, a relocation of the tensile triaxial stresses in the polar region, where deformation by interlamellar separation remains small, was observed, diminishing the likeliness of initiation and growth of critical crazelike features in the amorphous domains. These phenomena could indeed lead to some degree of toughening of the particle-modified material if the interparticle distance is small. However, with the level of anisotropy as predicted by the composite inclusion model, the effects of these locally preferential orientations remain limited. Simulations on idealized polymeric material, modeled by anisotropic Hill plasticity (Chapter 2), showed a much larger potential of local anisotropy for toughening of particle-dispersed semicrystalline materials, if the amount of anisotropy would be sufficiently large.

The level, and thereby the effect of local anisotropy was found to be improved if an additional hypothetical possibly flow-induced row structure of the transcrystallized lamellae was assumed in certain regions. When loaded in the direction of the macroscopic flow, plastic deformation was no longer localized in relatively thin interparticle ligaments, but was dispersed through the matrix. This massive shear yielding, in combination with the effects on craze-initiating conditions, will have a further beneficial influence on the behavior of this material, however, only if loaded in the appropriate direction. Although the employed microstructure was hypothetical, the calculations demonstrated the important role of processing conditions in particle-toughening of semi-crystalline polymers.

CHAPTER EIGHT

Conclusions and recommendations[1]

Abstract / The main ideas, methods and conclusions of this thesis are recapitulated. Retrospectively, the initial hypothesis concerning the mechanism of particle-toughening of semicrystalline polymers is evaluated. Recommendations for future work are given.

8.1 Conclusions

In this thesis, the hypothesis that local anisotropy in particle-modified polymeric systems may lead to macroscopically toughened behavior was investigated by numerical methods. The anisotropy is assumed to be induced by a specific microstructure, which results from preferred crystallization of the polymeric matrix material. The role of the particles in this mechanism is (i) to create a microstructure with anisotropic constitutive behavior during crystallization, and additionally (ii) to provoke local stress concentrations during loading, thereby inducing extensive matrix shear yielding. The validity of this hypothesis has been investigated by micromechanical modeling methods. Thereby, the crystallization behavior was left out of consideration, and the starting-point was an estimated microstructure for the particle-modified system.

The effect of matrix material with a reduced yield strength in the local shear directions around well-dispersed voids has been investigated by finite element simulations for idealized systems. The fictitious polymeric material was modeled in the context of anisotropic Hill plasticity. The three-dimensional structure of the voided material was simplified by the introduction of two different micromechanical models. The applicability of these computationally two-dimensional models was assessed by comparison with full three-dimensional simulations. The calculations confirmed that the mechanism as proposed by Muratoğlu et al. (1995c) could indeed lead to toughened material behavior. Required for toughening by this mechanism is apparently (i) a structure of well-dispersed voided particles; (ii) locally anisotropic material, radially oriented with respect to the nearest void surface; and (iii) sufficiently reduced shear yield strengths. If these requirements are satisfied, local plastic anisotropy of matrix material around the voids can effectively replace localization by dispersed shear yielding and can relocate the occurring tensile triaxial stresses at the particle poles, potentially leading to toughened material behavior.

---

[1] This chapter is partly based on Van Dommelen et al. (2003e).

A similar modeling approach was used to investigate the influence of rubber and mineral filler particles on this toughening mechanism. The use of mineral filler particles for toughening of polymeric materials requires debonding in order to prevent excessive negative hydrostatic pressures. These debonded hard particles show a relocation of tensile triaxial stresses to the particle polar areas by local anisotropy, similarly to anisotropic voided systems, with the maximum principal stresses directed such that crazes or microcracks are expected to propagate parallel to the loading direction. Moreover, the anisotropy-induced shear yielding mechanism is affected by the presence of stiff inclusions. Although some effect of the anisotropy was observed, the mechanism of toughening by local anisotropy is considered to be less effective for nonadhering hard particles, which have the advantage of increasing the blend modulus, than for low stiffness rubber fillers.

Thereafter, to investigate whether the requirements for the toughening mechanism can be achieved by a transcrystallized microstructure, a micromechanically-based numerical model for the elasto-viscoplastic deformation and texture evolution of semicrystalline polymers was developed and used to simulate the behavior of particle-modified high density polyethylene (HDPE). For these blended polymeric systems, a distinction between three different scales has been made. The constitutive properties of the distinguishable material components were characterized at the microscopic scale. At the mesoscopic scale, an aggregate of individual phases was considered. To bridge between those scales, a composite inclusion model has been formulated. The model is based on (a simplified representation of) the underlying morphology and deformation mechanisms of this material. As a representative microstructural element, a two-phase layered composite inclusion has been used, with a lamellar structure as is commonly observed in semicrystalline polymers. Both the crystalline and the amorphous phase are represented in the composite inclusion model and are mechanically coupled at the interface. For both phases, micromechanically-based constitutive models have been used. The local inclusion-averaged deformation and stress fields are related to the mesoscopic fields of the aggregate using an interaction model. Due to the anisotropy of the materials under investigation, a proper choice of the interaction law, bridging between the microscopic and the mesoscopic scales, was found to be crucial. A hybrid interaction model was chosen, that compromises between local compatibility and local equilibrium. In the model, the effect of transcrystallization on microscopic properties other than orientation, such as crystallinity and amorphous and crystalline constitutive behavior (e.g. as a result of the lamellar thickness), are not accounted for.

The composite inclusion model was used to evaluate intraspherulitic deformation and stress. The spherulitic macrostructure was modeled by finite elements and loaded under uniaxial and plane strain conditions. Heterogeneous intraspherulitic deformation, with strain concentrations in the spherulitic centers, was found to result from the anisotropic structure within each spherulite.

Finally, a full multiscale model was used to investigate the effect of preferentially oriented matrix material in HDPE blended with rubber particles, which were represented by voids. In this model, the structure–property relationship is addressed at various levels: (i) the arrangement of chain segments, represented in the constitutive behavior of the individual phases; (ii) the arrangement of the lamellae, influencing the response of the polymeric matrix material; and (iii) the particle-modified macroscopic structure. Simulations on voided polymeric material with a large average interparticle matrix ligament thickness, having quasi isotropic constitutive behavior at the mesoscopic level, showed strongly localized deformation. Maximum tensile triaxial stresses were found in the equator regions near the particles. A particle-modified system having a relatively small average interparticle matrix ligament thickness was realized by using initially preferentially oriented lamellae, with the crystallographic (*100*) planes approximately parallel to the void/matrix interface. For this system, a more dispersed field of plastic deformation was found, induced by a relative reduction of the shear yield strength. Moreover a relocation of the peak tensile triaxial stresses to the polar region was observed, diminishing the initiation and growth of critical crazelike features in the amorphous domains. These phenomena could indeed lead to some degree of toughening of the particle-modified material when the interparticle distance is small. However, with the level of anisotropy as predicted by the composite inclusion model, the effects of these locally preferred orientations remained limited. The simulations on idealized polymeric materials, modeled by anisotropic Hill plasticity, showed a substantially increased potential capacity of local anisotropy for toughening of particle-dispersed semicrystalline materials, if the amount of anisotropy was sufficiently large.

The level, and thereby the effect of local anisotropy was more pronounced by assuming a hypothetical additional row structure of the transcrystallized lamellae in certain regions, which might be the result of the processing history. When loaded in the direction of the macroscopic flow, plastic deformation was no longer localized in relatively thin interparticle ligaments, but was largely distributed through the matrix. This shear yielding, in combination with the effects on craze-initiating conditions, has a further beneficial effect on the mechanical behavior of this material, however only when loaded in the appropriate direction.

Based on these simulations, Figure 1.5, which was the starting-point of this work, illustrating the potential of rubber and mineral fillers for improving mechanical properties by the hypothesized mechanism, can be further refined. This refinement is displayed in Figure 8.1. Whereas in the reference (large scale) isotropic system, tensile triaxial stresses

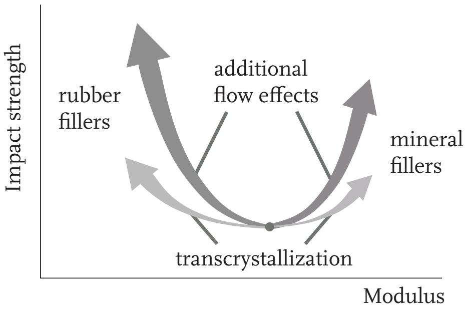

Figure 8.1 / The influence of voids (cavitated rubber) vs. hard (mineral) particles in combination with microstructure-induced anisotropy on the mechanical properties.

were found in the particle equator areas, for all anisotropic (small scale) systems, maximum negative pressures were observed in the polar area. For these systems, crazelike events are expected to propagate in the loading direction. For rubber-filled systems, transcrystallized layers had a limited effect on matrix shearing, whereas the presence of row-structured material more efficiently changed the mode of deformation to dispersed shear yielding. However, the mechanism of toughening by local anisotropy was concluded to be less effective for nonadhering hard particles.

8.2 Recommendations

In this thesis, the mechanical behavior of particle-modified semicrystalline materials is numerically modeled at various scales. Many assumptions and simplifications have been made. In this section, some aspects are discussed that may be focused on in future work.

8.2.1 Composite inclusion model

A micromechanically-based model has been developed for the constitutive behavior of semicrystalline polymers. A hybrid local–global interaction law was used, which compromises between interinclusion compatibility and equilibrium. For the $\hat{\boldsymbol{U}}$-inclusion model with a sharp initial texture (e.g. parallel interface normals $\boldsymbol{n}_0^{\mathrm{I}^i}$), the span

$$\{\, \boldsymbol{e}_{0j}^{\mathrm{I}^i} \otimes \boldsymbol{n}_0^{\mathrm{I}^i} \mid i = 1, \ldots, N_{\mathrm{I}}\,;\, j = 1, \ldots, 3 \,\} \tag{8.1}$$

does not have a full rank and some components of $\hat{\boldsymbol{U}}$ may be indeterminate. The same holds for the span

$$\{\, \boldsymbol{e}_{j}^{\mathrm{I}^i} \otimes \boldsymbol{x}_k^{\mathrm{I}^i} \mid i = 1, \ldots, N_{\mathrm{I}}\,;\, j = 1, \ldots, 3\,;\, k = 1,2 \,\}, \tag{8.2}$$

in the $\hat{\boldsymbol{\sigma}}$-inclusion model in combination with a sharp current texture, which may yield some components of $\hat{\boldsymbol{\sigma}}$ indeterminate. In case of a strongly evolved morphological texture, the well-posedness of the boundary conditions for the individual composite inclusions in the $\hat{\boldsymbol{U}}$-inclusion model (Equations (4.36) and (4.37)) and the $\hat{\boldsymbol{\sigma}}$-inclusion model (Equations (4.33) and (4.34)) degenerates. Therefore, the nature of the hybrid interaction laws limits the strain range that is numerically attainable. An alternative (hybrid) interaction law, with a different basis for assigning interinclusion compatibility and equilibrium conditions and/or less severe constraints on the rotation tensor could evade some of these limitations. Such a formulation may possibly be based on nominal stresses. Then, both interinclusion compatibility and interinclusion equilibrium may be based on the interface orientation in the reference configuration, such as for example:

$$
\begin{aligned}
{}^4\mathcal{P}^{\mathrm{I}^i}_{\mathrm{x_o}} : \boldsymbol{T}^{\mathrm{I}^i} &= {}^4\mathcal{P}^{\mathrm{I}^i}_{\mathrm{x_o}} : \bar{\boldsymbol{T}} \quad ; \quad i = 1,\ldots,N_{\mathrm{I}}, && (8.3)\\
{}^4\mathcal{P}^{\mathrm{I}^i}_{\mathrm{n_o}} : \boldsymbol{F}^{\mathrm{I}^i} &= {}^4\mathcal{P}^{\mathrm{I}^i}_{\mathrm{n_o}} : \hat{\boldsymbol{F}} \quad ; \quad i = 1,\ldots,N_{\mathrm{I}}, && (8.4)
\end{aligned}
$$

with $\boldsymbol{T}$ the first Piola–Kirchhoff stress tensor.

Furthermore, in the current hybrid composite inclusion interaction models, the assignment of Taylorlike and Sachslike interactions is based on the directions in which the equilibrium and compatibility conditions within the basic element are enforced. A different approach that could be pursued may involve assigning the directions of interinclusion compatibility and equilibrium on the basis of the intrainclusion principal anisotropy directions. Then, the Sachslike interaction for a certain composite inclusion could be enforced either in the plastically constrained directions of the crystallographic phase, or in the relatively stiff principal directions of the entire composite inclusion. Similarly, the Taylorlike interactions could be assigned to the weak directions within the basic element of the model. Moreover, a composite inclusion model in a rate formulation may be more suitable for large strain usage and addresses the conditions of consistency in a more appropriate way.

Elasto-viscoplastic generalizations of the constitutive models that were used by Lee et al. (1993a) have been chosen. The selection of the appropriate constitutive model for the noncrystalline domain and the characterization of material parameters may deserve additional attention. At relatively large strains, the crystalline phase may exhibit phenomena other than accounted for in the model, such as a degradation of the crystalline structure, twinning, or stress-induced martensitic transformation (e.g. Gent and Madan, 1989; Lin and Argon, 1994; G'Sell and Dahoun, 1994). Some of these aspects may be incorporated into the model.

8.2.2 Spherulitic modeling

In the current models of spherulitic structures (Chapter 6), the boundaries between spherulites are assumed to have an infinitely small thickness. They are merely present by the virtue of changes in local material orientation, and therefore have no physical properties. A finite thickness may be assigned to these boundaries which can be modeled with a distinct constitutive behavior. Furthermore, more detailed finite element models of spherulitic structures, with a macroscopic modeling of lamellar twisting, may be employed, as well as three-dimensional unit cell models (e.g. Danielson et al., 2002).

8.2.3 Particle-modified systems

For large strain investigations of particle-toughening of semicrystalline polymers, a phenomenological constitutive model may be preferred from a computational point of view. Such a model may involve anisotropic elasticity, anisotropic yielding and postyield hardening, with distinct compressive and tensile behavior, and rate dependence. An efficient finite element implementation of this model would allow for more detailed studies of particle-modified semicrystalline materials.

Future investigations could include a more appropriate particle/matrix interface model, high triaxiality loading conditions, and other particle geometries and size distributions. The process of the cavitation of rubber inclusions could be modeled (Steenbrink and Van der Giessen, 1999). Furthermore, for quantitative predictions of brittle/tough behavior, failure criteria for crazing (e.g. Tijssens et al., 2000; Estevez et al., 2000; Socrate et al., 2001) and brittle fracture should be included. The conditions of crazing in glassy polystyrene have been characterized by a combination of microindentation and numerical modeling by Van Melick et al. (2003); Van Melick (2002). The incorporation of thermal expansion in the composite inclusion model is discussed in Van Dommelen et al. (2000b). Using the thermo-elasto-viscoplastic composite inclusion model, the effect of residual thermal stresses in particle-modified systems may be examined. The influence of transcrystallization on microscopic properties other than orientation, such as crystallinity and amorphous and crystalline constitutive behavior is neglected in the current model; however may be substantial. This effect may be quantified and incorporated in the model for transcrystallized material. Moreover the effect of transcrystallization on the resistance to void nucleation may be of interest.

Three-dimensional simulations are preferred for a correct representation of many aspects of particle-modified systems, as was demonstrated in Chapter 2. For efficiency reasons, different two-dimensional models have been used instead. Using a phenomenological model for the anisotropic constitutive behavior of semicrystalline material allows full three-dimensional computations. Multilevel finite element methods (e.g. Smit et al., 1998; Smit, 1998; Kouznetsova et al., 2001, 2002; Kouznetsova, 2002) could provide a link to the engineering scale (see Figure 5.1). However, in combination with the micromechanically-based composite inclusion model, these computations would require enormous computational effort. Therefore, for this application, also a phenomenological model would be recommended.

A possible effect of processing conditions has been established. Experimental investigations should further clarify the microstructure and its origin that causes toughened behavior (see Schrauwen, 2003). The potential of alternative microstructures for toughening of semicrystalline material may be studied, as well as the possibility to realize these morphologies.

Finally, in this thesis, a hypothesis that was based on experimental findings in the literature has been evaluated entirely by numerical modeling methods. Therefore, the conclusions are valid only within the restrictions of the modeling assumptions. Experimental studies should verify the validity of these conclusions for real material systems.

APPENDIX A

Composite inclusion model

Abstract / The sets of equations that compose the composite inclusion model with its various interaction laws are summarized.

A.1 Introduction

In this appendix, the nonlinear equations of the composite inclusion model (see Chapter 4) that are simultaneously solved for each increment are symbolically given for each inclusion interaction assumption. The mesoscopic rotation tensor $\bar{\boldsymbol{R}}$ is assumed to be fully prescribed. Furthermore, N_σ components of the mesoscopic Cauchy stress tensor, $\bar{\boldsymbol{\sigma}}$, and the $6 - N_\sigma$ nonassociated components of the mesoscopic right stretch tensor, $\bar{\boldsymbol{U}}$, are prescribed. Let these components be given by

$$\check{\boldsymbol{\sigma}} = {}^4\mathcal{P}_\sigma : \bar{\boldsymbol{\sigma}} \quad \text{and} \quad \check{\boldsymbol{U}} = {}^4\mathcal{P}_\mathrm{U} : \bar{\boldsymbol{U}}, \tag{A.1}$$

respectively, with

$${}^4\mathcal{P}_\sigma + {}^4\mathcal{P}_\mathrm{U} = {}^4\mathcal{I}. \tag{A.2}$$

In Table A.1, the unknown variables for each inclusion interaction model are summarized. For all interaction models, both the amorphous and the crystalline elastic deformation gradients are considered as unknowns. The microscopic deformation and stress fields of inclusion i can then be symbolically written as (see Figure 4.5):

$$\boldsymbol{F}^{\pi^i} = \boldsymbol{F}^{\pi^i}(\boldsymbol{F}_\mathrm{e}^{\pi^i}) \quad ; \quad \pi = \mathrm{a, c}, \quad \text{and} \quad \boldsymbol{F}^{\mathrm{I}^i} = \sum_{\pi=\mathrm{a,\ c}} f_\mathrm{o}^{\pi^i} \boldsymbol{F}^{\pi^i}(\boldsymbol{F}_\mathrm{e}^{\pi^i}), \tag{A.3}$$

$$\boldsymbol{\sigma}^{\pi^i} = \boldsymbol{\sigma}^{\pi^i}(\boldsymbol{F}_\mathrm{e}^{\pi^i}) \quad ; \quad \pi = \mathrm{a, c}, \quad \text{and} \quad \boldsymbol{\sigma}^{\mathrm{I}^i} = \sum_{\pi=\mathrm{a,\ c}} f^{\pi^i} \boldsymbol{\sigma}^{\pi^i}(\boldsymbol{F}_\mathrm{e}^{\pi^i}), \tag{A.4}$$

Model	Unknowns	Number of unknowns
Taylor-inclusion	$\boldsymbol{F}_{\rm e}^{{\rm c}^i}, \boldsymbol{F}_{\rm e}^{{\rm a}^i};\ i = 1,\dots,N_{\rm I}$	$18N_{\rm I}$
Sachs-inclusion	$\boldsymbol{F}_{\rm e}^{{\rm c}^i}, \boldsymbol{F}_{\rm e}^{{\rm a}^i};\ i = 1,\dots,N_{\rm I}$	$18N_{\rm I}$
$\hat{\boldsymbol{\sigma}}$-inclusion	$\boldsymbol{F}_{\rm e}^{{\rm c}^i}, \boldsymbol{F}_{\rm e}^{{\rm a}^i};\ i = 1,\dots,N_{\rm I}$	$18N_{\rm I}$
	$\hat{\boldsymbol{\sigma}}$	6
	$\breve{\boldsymbol{U}} = {}^4\mathcal{P}_\sigma : \bar{\boldsymbol{U}}$	N_σ
$\hat{\boldsymbol{U}}$-inclusion	$\boldsymbol{F}_{\rm e}^{{\rm c}^i}, \boldsymbol{F}_{\rm e}^{{\rm a}^i};\ i = 1,\dots,N_{\rm I}$	$18N_{\rm I}$
	$\hat{\boldsymbol{U}}$	6
	$\breve{\boldsymbol{\sigma}} = {}^4\mathcal{P}_{\rm U} : \bar{\boldsymbol{\sigma}}$	$6 - N_\sigma$

Table A.1 / The unknown variables and the number of unknowns in each composite inclusion model.

respectively. In the $\hat{\boldsymbol{\sigma}}$-inclusion and the $\hat{\boldsymbol{U}}$-inclusion model, an auxiliary unknown stress tensor $\hat{\boldsymbol{\sigma}}$ or stretch tensor $\hat{\boldsymbol{U}}$, respectively, is defined. Moreover, for numerical efficiency, the unprescribed mesoscopic stretch components or unprescribed mesoscopic stress components are considered as unknowns for the $\hat{\boldsymbol{\sigma}}$-inclusion or the $\hat{\boldsymbol{U}}$-inclusion model, respectively, and are denoted by $\breve{\boldsymbol{U}}$ and $\breve{\boldsymbol{\sigma}}$. Consequently, a strong reduction of the number of nonzero elements in the matrix $\underline{K} = {\rm d}\underset{\sim}{\Phi}/{\rm d}\underset{\sim}{u}$ is obtained, where $\underset{\sim}{\Phi}$ symbolically contains the complete set of equations to be solved, whereas the unknowns are stored in the column $\underset{\sim}{u}$. The unknowns are determined by simultaneously solving the set of $18N_{\rm I}$ equations for the Taylor- and the Sachs-inclusion model, the set of $18N_{\rm I} + N_\sigma + 6$ equations for the $\hat{\boldsymbol{\sigma}}$-inclusion model or the set of $18N_{\rm I} - N_\sigma + 12$ equations for the $\hat{\boldsymbol{U}}$-inclusion model. The complete sets of equations are given in the following sections.

A.2 Taylor-inclusion model

- Intrainclusion equilibrium ($3N_{\rm I}$ scalar eqns.):

$$ {}^4\mathcal{P}_{\rm n}^{{\rm I}^i} : \boldsymbol{\sigma}^{{\rm c}^i} = {}^4\mathcal{P}_{\rm n}^{{\rm I}^i} : \boldsymbol{\sigma}^{{\rm a}^i} \quad ; \quad i = 1,\dots,N_{\rm I} \tag{A.5} $$

- Volume-averaging of stress (N_σ scalar eqns.):

$$ {}^4\mathcal{P}_\sigma : \sum_{i=1}^{N_{\rm I}} f^{{\rm I}^i} \boldsymbol{\sigma}^{{\rm I}^i} = {}^4\mathcal{P}_\sigma : \bar{\boldsymbol{\sigma}} = \breve{\boldsymbol{\sigma}} \tag{A.6} $$

- Intrainclusion compatibility ($6N_{\mathrm{I}}$ scalar eqns.):

$$ {}^4\mathcal{P}^{\mathrm{I}^i}_{\mathrm{x}_0} : \boldsymbol{F}^{\mathrm{c}^i} = {}^4\mathcal{P}^{\mathrm{I}^i}_{\mathrm{x}_0} : \boldsymbol{F}^{\mathrm{a}^i} \quad ; \quad i = 1, \dots, N_{\mathrm{I}} \tag{A.7} $$

- Interinclusion compatibility and volume-averaging of deformation ($6N_{\mathrm{I}} - N_\sigma$ scalar eqns.):

$$ \begin{align} {}^4\mathcal{P}_{\mathrm{U}} : \boldsymbol{U}^{\mathrm{I}^i} &= {}^4\mathcal{P}_{\mathrm{U}} : \bar{\boldsymbol{U}} = \check{\boldsymbol{U}} \quad ; \quad i = 1, \dots, N_{\mathrm{I}} \quad (N_{\mathrm{I}}[6 - N_\sigma] \text{ scalar eqns.}) \tag{A.8} \\ {}^4\mathcal{P}_\sigma : \boldsymbol{U}^{\mathrm{I}^i} &= {}^4\mathcal{P}_\sigma : \boldsymbol{U}^{\mathrm{I}^{i+1}} \quad ; \quad i = 1, \dots, N_{\mathrm{I}} - 1 \quad (N_\sigma[N_{\mathrm{I}} - 1] \text{ scalar eqns.}) \tag{A.9} \end{align} $$

- Prescribed rotations ($3N_{\mathrm{I}}$ scalar eqns.):

$$ \boldsymbol{R}^{\mathrm{I}^i} = \bar{\boldsymbol{R}} \quad ; \quad i = 1, \dots, N_{\mathrm{I}} \tag{A.10} $$

A.3 Sachs-inclusion model

- Intrainclusion equilibrium ($3N_{\mathrm{I}}$ scalar eqns.):

$$ {}^4\mathcal{P}^{\mathrm{I}^i}_{\mathrm{n}} : \boldsymbol{\sigma}^{\mathrm{c}^i} = {}^4\mathcal{P}^{\mathrm{I}^i}_{\mathrm{n}} : \boldsymbol{\sigma}^{\mathrm{a}^i} \quad ; \quad i = 1, \dots, N_{\mathrm{I}} \tag{A.11} $$

- Interinclusion equilibrium and volume-averaging of stress ($6[N_{\mathrm{I}} - 1] + N_\sigma$ scalar eqns.):

$$ \begin{align} {}^4\mathcal{P}_\sigma : \boldsymbol{\sigma}^{\mathrm{I}^i} &= {}^4\mathcal{P}_\sigma : \bar{\boldsymbol{\sigma}} = \check{\boldsymbol{\sigma}} \quad ; \quad i = 1, \dots, N_{\mathrm{I}} \quad (N_{\mathrm{I}} N_\sigma \text{ scalar eqns.}) \tag{A.12} \\ {}^4\mathcal{P}_{\mathrm{U}} : \boldsymbol{\sigma}^{\mathrm{I}^i} &= {}^4\mathcal{P}_{\mathrm{U}} : \boldsymbol{\sigma}^{\mathrm{I}^{i+1}} \quad ; \quad i = 1, \dots, N_{\mathrm{I}} - 1 \tag{A.13} \\ & \qquad\qquad ([N_{\mathrm{I}} - 1][6 - N_\sigma] \text{ scalar eqns.}) \notag \end{align} $$

- Intrainclusion compatibility ($6N_{\mathrm{I}}$ scalar eqns.):

$$ {}^4\mathcal{P}^{\mathrm{I}^i}_{\mathrm{x}_0} : \boldsymbol{F}^{\mathrm{c}^i} = {}^4\mathcal{P}^{\mathrm{I}^i}_{\mathrm{x}_0} : \boldsymbol{F}^{\mathrm{a}^i} \quad ; \quad i = 1, \dots, N_{\mathrm{I}} \tag{A.14} $$

- Volume-averaging of deformation ($6 - N_\sigma$ scalar eqns.):

$$ {}^4\mathcal{P}_{\mathrm{U}} : \left(\frac{\bar{J}}{J_\Sigma} \right)^{\frac{1}{3}} \sum_{i=1}^{N_{\mathrm{I}}} f_0^{\mathrm{I}^i} \boldsymbol{U}^{\mathrm{I}^i} = {}^4\mathcal{P}_{\mathrm{U}} : \bar{\boldsymbol{U}} = \check{\boldsymbol{U}} \tag{A.15} $$

- Prescribed rotations ($3N_{\mathrm{I}}$ scalar eqns.):

$$ \boldsymbol{R}^{\mathrm{I}^i} = \bar{\boldsymbol{R}} \quad ; \quad i = 1, \dots, N_{\mathrm{I}} \tag{A.16} $$

A.4 $\hat{\sigma}$-inclusion model

- Intrainclusion equilibrium ($3N_{\mathrm{I}}$ scalar eqns.):

$$ {}^4\mathcal{P}_{\mathrm{n}}^{\mathrm{I}^i} : \boldsymbol{\sigma}^{\mathrm{c}^i} = {}^4\mathcal{P}_{\mathrm{n}}^{\mathrm{I}^i} : \boldsymbol{\sigma}^{\mathrm{a}^i} \quad ; \quad i = 1, \ldots, N_{\mathrm{I}} \tag{A.17} $$

- Interinclusion equilibrium ($3N_{\mathrm{I}}$ scalar eqns.):

$$ {}^4\mathcal{P}_{\mathrm{x}}^{\mathrm{I}^i} : \boldsymbol{\sigma}^{\mathrm{I}^i} = {}^4\mathcal{P}_{\mathrm{x}}^{\mathrm{I}^i} : \hat{\boldsymbol{\sigma}} \quad ; \quad i = 1, \ldots, N_{\mathrm{I}} \tag{A.18} $$

- Volume-averaging of stress (N_σ scalar eqns.):

$$ {}^4\mathcal{P}_\sigma : \sum_{i=1}^{N_{\mathrm{I}}} f^{\mathrm{I}^i} \boldsymbol{\sigma}^{\mathrm{I}^i} = {}^4\mathcal{P}_\sigma : \bar{\boldsymbol{\sigma}} = \check{\boldsymbol{\sigma}} \tag{A.19} $$

- Intrainclusion compatibility ($6N_{\mathrm{I}}$ scalar eqns.):

$$ {}^4\mathcal{P}_{\mathrm{x}_\mathrm{o}}^{\mathrm{I}^i} : \boldsymbol{F}^{\mathrm{c}^i} = {}^4\mathcal{P}_{\mathrm{x}_\mathrm{o}}^{\mathrm{I}^i} : \boldsymbol{F}^{\mathrm{a}^i} \quad ; \quad i = 1, \ldots, N_{\mathrm{I}} \tag{A.20} $$

- Interinclusion compatibility ($3N_{\mathrm{I}}$ scalar eqns.):

$$ {}^4\mathcal{P}_{\mathrm{n}_\mathrm{o}}^{\mathrm{I}^i} : \boldsymbol{U}^{\mathrm{I}^i} = {}^4\mathcal{P}_{\mathrm{n}_\mathrm{o}}^{\mathrm{I}^i} : (\check{\boldsymbol{U}} + \breve{\boldsymbol{U}}) \quad ; \quad i = 1, \ldots, N_{\mathrm{I}} \tag{A.21} $$

- Volume-averaging of deformation (6 scalar eqns.):

$$ \left(\frac{\bar{J}}{J_\Sigma} \right)^{\frac{1}{3}} \sum_{i=1}^{N_{\mathrm{I}}} f_{\mathrm{o}}^{\mathrm{I}^i} \boldsymbol{U}^{\mathrm{I}^i} = \check{\boldsymbol{U}} + \breve{\boldsymbol{U}} \tag{A.22} $$

- Prescribed rotations ($3N_{\mathrm{I}}$ scalar eqns.):

$$ \boldsymbol{R}^{\mathrm{I}^i} = \bar{\boldsymbol{R}} \quad ; \quad i = 1, \ldots, N_{\mathrm{I}} \tag{A.23} $$

A.5 $\hat{U}$-inclusion model

- Intrainclusion equilibrium ($3N_{\mathrm{I}}$ scalar eqns.):

$$ {}^4\mathcal{P}_{\mathrm{n}}^{\mathrm{I}^i} : \boldsymbol{\sigma}^{\mathrm{c}^i} = {}^4\mathcal{P}_{\mathrm{n}}^{\mathrm{I}^i} : \boldsymbol{\sigma}^{\mathrm{a}^i} \quad ; \quad i = 1, \ldots, N_{\mathrm{I}} \tag{A.24} $$

- Interinclusion equilibrium ($3N_{\mathrm{I}}$ scalar eqns.):

$$ {}^4\mathcal{P}_{\mathrm{x}}^{\mathrm{I}^i} : \boldsymbol{\sigma}^{\mathrm{I}^i} = {}^4\mathcal{P}_{\mathrm{x}}^{\mathrm{I}^i} : (\check{\boldsymbol{\sigma}} + \breve{\boldsymbol{\sigma}}) \quad ; \quad i = 1, \ldots, N_{\mathrm{I}} \tag{A.25} $$

- Volume-averaging of stress (6 scalar eqns.):

$$\sum_{i=1}^{N_\mathrm{I}} f^{\mathrm{I}^i} \boldsymbol{\sigma}^{\mathrm{I}^i} = \breve{\boldsymbol{\sigma}} + \check{\boldsymbol{\sigma}} \tag{A.26}$$

- Intrainclusion compatibility ($6N_\mathrm{I}$ scalar eqns.):

$$^4\boldsymbol{\mathcal{P}}^{\mathrm{I}^i}_{\mathrm{x}_o} : \boldsymbol{F}^{\mathrm{c}^i} = {}^4\boldsymbol{\mathcal{P}}^{\mathrm{I}^i}_{\mathrm{x}_o} : \boldsymbol{F}^{\mathrm{a}^i} \quad ; \quad i = 1, \ldots, N_\mathrm{I} \tag{A.27}$$

- Interinclusion compatibility ($3N_\mathrm{I}$ scalar eqns.):

$$^4\boldsymbol{\mathcal{P}}^{\mathrm{I}^i}_{\mathrm{n}_o} : \boldsymbol{U}^{\mathrm{I}^i i} = {}^4\boldsymbol{\mathcal{P}}^{\mathrm{I}^i}_{\mathrm{n}_o} : \hat{\boldsymbol{U}} \quad ; \quad i = 1, \ldots, N_\mathrm{I} \tag{A.28}$$

- Volume-averaging of deformation ($6 - N_\sigma$ scalar eqns.):

$$^4\boldsymbol{\mathcal{P}}_\mathrm{U} : \left(\frac{\bar{J}}{J_\Sigma}\right)^{\frac{1}{3}} \sum_{i=1}^{N_\mathrm{I}} f^{\mathrm{I}^i}_o \boldsymbol{U}^{\mathrm{I}^i} = {}^4\boldsymbol{\mathcal{P}}_\mathrm{U} : \bar{\boldsymbol{U}} = \check{\boldsymbol{U}} \tag{A.29}$$

- Prescribed rotations ($3N_\mathrm{I}$ scalar eqns.):

$$\boldsymbol{R}^{\mathrm{I}^i} = \bar{\boldsymbol{R}} \quad ; \quad i = 1, \ldots, N_\mathrm{I} \tag{A.30}$$

Bibliography

Aboulfaraj, M., G'Sell, C., Ulrich, B., and Dahoun, A. (1995). In situ observation of the plastic deformation of polypropylene spherulites under uniaxial tension and simple shear in the scanning electron microscope. *Polymer*, **36**, 731–742.

Ahzi, S., Lee, B. J., and Asaro, R. J. (1994). Plasticity and anisotropy evolution in crystalline polymers. *Materials Science and Engineering A*, **189**, 35–44.

Allan, P. and Bevis, M. (1977). Deformation processes in thin melt-cast films of high-density polyethylene I. Experimental methods and deformation processes in the equatorial regions of spherulites. *Philosophical Magazine*, **35**, 405–430.

Allan, P. and Bevis, M. (1980). Deformation processes in thin melt-cast films of high-density polyethylene II. Deformation processes in the non-equatorial regions of spherulites. *Philosophical Magazine A*, **41**, 555–572.

Argon, A. S. (1997). Morphological mechanisms and kinetics of large-strain plastic deformation and evolution of texture in semi-crystalline polymers. *Journal of Computer-Aided Materials Design*, **4**, 75–98.

Argon, A. S., Cohen, R. E., Gebizlioglu, O. S., and Schwier, C. E. (1983). Crazing in block copolymers and blends. H.-H. Kausch (ed.). *Advances in Polymer Science*, **52/53**, 275–334. Springer-Verlag, Berlin.

Argon, A. S., Cohen, R. E., and Mower, T. M. (1994). Mechanisms of toughening brittle polymers. *Materials Science and Engineering A*, **176**, 79–90.

Arruda, E. M. and Boyce, M. C. (1993). A three-dimensional constitutive model for the large stretch behavior of rubber elastic material. *Journal of the Mechanics and Physics of Solids*, **41**, 389–412.

Asaro, R. J. and Needleman, A. (1985). Texture development and strain hardening in rate dependent polycrystals. *Acta Metallurgica*, **33**, 923–953.

Bartczak, Z., Argon, A. S., and Cohen, R. E. (1992a). Deformation mechanisms and plastic resistance in single-crystal-textured high-density polyethylene. *Macromolecules*, **25**, 5036–5053.

Bartczak, Z., Cohen, R. E., and Argon, A. S. (1992b). Evolution of the crystalline texture of high-density polyethylene during uniaxial compression. *Macromolecules*, **25**, 4692–4704.

Bartczak, Z., Argon, A. S., Cohen, R. E., and Weinberg, M. (1999a). Toughness mechanism in semi-crystalline polymer blends: I. High-density polyethylene toughened with rubbers. *Polymer*, **40**, 2331–2346.

Bartczak, Z., Argon, A. S., Cohen, R. E., and Weinberg, M. (1999b). Toughness mechanism in semi-crystalline polymer blends: II. High-density polyethylene toughened with calcium carbonate filler particles. *Polymer*, **40**, 2347–2365.

Bartczak, Z., Argon, A. S., Cohen, R. E., and Kowalewski, T. (1999c). The morphology and orientation of polyethylene in films of sub-micron thickness crystallized in contact with calcite and rubber substrates. *Polymer*, **40**, 2367–2380.

Bassett, D. C. and Hodge, A. M. (1981). On the morphology of melt-crystallized polyethylene I. Lamellar profiles. *Proceedings of the Royal Society of London A*, **377**, 25–37.

BASSETT, D. C., HODGE, A. M., and OLLEY, R. H. (1981). On the morphology of melt-crystallized polyethylene II. Lamellae and their crystallization conditions. *Proceedings of the Royal Society of London A*, **377**, 39–60.

BERGSTRÖM, J. S. and BOYCE, M. C. (1998). Constitutive modeling of the large strain time-dependent behavior of elastomers. *Journal of the Mechanics and Physics of Solids*, **46**, 931–954.

BERGSTRÖM, J. S. and BOYCE, M. C. (2001). Deformation of elastomeric networks: relation between molecular level deformation and classical statistical mechanics models of rubber elasticity. *Macromolecules*, **34**, 614–626.

BICERANO, J. and SEITZ, J. T. (1996). Molecular origins of toughness in polymers. C. B. ARENDS (ed.). *Polymer toughening*, 1–59. Marcel Dekker, New York.

BORGGREVE, R. J. M., GAYMANS, R. J., SCHUIJER, J., and INGEN HOUSZ, J. F. (1987). Brittle-tough transition in nylon-rubber blends: effect of rubber concentration and particle size. *Polymer*, **28**, 1489–1496.

BOYCE, M. C., PARKS, D. M., and ARGON, A. S. (1988). Large inelastic deformation of glassy polymers. Part I: Rate dependent constitutive model. *Mechanics of Materials*, **7**, 15–33.

BOYCE, M. C., MONTAGUT, E. L., and ARGON, A. S. (1992). Thermomechanical coupling on the cold drawing process of glassy polymers. *Polymer Engineering and Science*, **32**, 1073–1085.

CHACKO, V. P., KARASZ, F. E., FARRIS, R. J., and THOMAS, E. L. (1982). Morphology of $CaCO_3$-filled polyethylenes. *Journal of Polymer Science: Part B: Polymer Physics*, **20**, 2177–2195.

CHOY, C. L. and LEUNG, W. P. (1985). Elastic moduli of ultradrawn polyethylene. *Journal of Polymer Science: Part B: Polymer Physics*, **23**, 1759–1780.

COTTON, J. D., KAUFMAN, M. J., and NOEBE, R. D. (1991). A simplified method for determining the number of independent slip systems in crystals. *Scripta Metallurgica et Materialia*, **25**, 2395–2398.

CRIST, B., FISHER, C. J., and HOWARD, P. R. (1989). Mechanical properties of model polyethylenes: tensile elastic modulus and yield stress. *Macromolecules*, **22**, 1709–1718.

DAHOUN, A., CANOVA, G. R., MOLINARI, A., PHILIPPE, M. J., and G'SELL, C. (1991). The modelling of large strain textures and stress-strain relations of polyethylene. *Textures and Microstructures*, **14–18**, 347–354.

DANIELSON, M., PARKS, D. M., and BOYCE, M. C. (2002). Three-dimensional micromechanical modeling of voided polymeric materials. *Journal of the Mechanics and Physics of Solids*, **50**, 351–379.

DIJKSTRA, K. and TEN BOLSCHER, G. H. (1994). Nylon-6/rubber blends. Part III. Stresses in and around rubber particles and cavities in a nylon matrix. *Journal of Materials Science*, **29**, 4286–4293.

VAN DOMMELEN, J. A. W., BREKELMANS, W. A. M., and BAAIJENS, F. P. T. (1999a). Computational visco-plasticity for crystals lacking five independent slip systems. In *Proceedings of the Fifteenth Annual Meeting of the Polymer Processing Society*, 's-Hertogenbosch, The Netherlands.

VAN DOMMELEN, J. A. W., BREKELMANS, W. A. M., and BAAIJENS, F. P. T. (1999b). Computational visco-plasticity for crystals lacking five independent slip systems. In *Proceedings of the European Conference on Computational Mechanics*, München, Germany.

VAN DOMMELEN, J. A. W., BREKELMANS, W. A. M., and BAAIJENS, F. P. T. (2000a). Computational visco-plasticity for kinematically constrained crystals. *International Journal for Numerical Methods in Engineering*, **48**, 1311–1330.

VAN DOMMELEN, J. A. W., PARKS, D. M., BOYCE, M. C., BREKELMANS, W. A. M., and BAAIJENS, F. P. T. (2000b). Micromechanical modeling of the thermo-elasto-viscoplastic behavior of semi-crystalline polymers. In *Proceedings of the European Congress on Computational Methods in Applied Sciences and Engineering*, Barcelona, Spain.

VAN DOMMELEN, J. A. W., PARKS, D. M., BOYCE, M. C., BREKELMANS, W. A. M., and BAAIJENS, F. P. T. (2001). Multi-scale modeling of the constitutive behavior of semi-crystalline polymers. In *Proceedings of the European Conference on Computational Mechanics*, Cracow, Poland.

VAN DOMMELEN, J. A. W., BREKELMANS, W. A. M., and BAAIJENS, F. P. T. (2002a). Micromechanics of particle-modified semi-crystalline materials. In *Proceedings of the Fifth World Conference on Computational Mechanics*, Vienna, Austria.

VAN DOMMELEN, J. A. W., BREKELMANS, W. A. M., and BAAIJENS, F. P. T. (2002b). Micromechanics of particle-modified semi-crystalline materials. In *Proceedings of the Eighteenth Annual Meeting of the Polymer Processing Society*, Guimarães, Portugal.

VAN DOMMELEN, J. A. W., PARKS, D. M., BOYCE, M. C., BREKELMANS, W. A. M., and BAAIJENS, F. P. T. (2003a). Micromechanical modeling of intraspherulitic deformation of polymers. In preparation.

VAN DOMMELEN, J. A. W., BREKELMANS, W. A. M., and BAAIJENS, F. P. T. (2003b). Micromechanical modeling of particle-toughening of polymers by locally induced anisotropy. *Mechanics of Materials*. Accepted.

VAN DOMMELEN, J. A. W., PARKS, D. M., BOYCE, M. C., BREKELMANS, W. A. M., and BAAIJENS, F. P. T. (2003c). Micromechanical modeling of the elasto-viscoplastic behavior of semi-crystalline polymers. *Journal of the Mechanics and Physics of Solids*, **51**, 519–541.

VAN DOMMELEN, J. A. W., BREKELMANS, W. A. M., and BAAIJENS, F. P. T. (2003d). Multiscale modeling of particle-modified polyethylene. *Journal of Materials Science*. Submitted.

VAN DOMMELEN, J. A. W., BREKELMANS, W. A. M., and BAAIJENS, F. P. T. (2003e). Multiscale modeling of particle-modified semicrystalline materials. In *Proceedings of the 12th International Conference on Deformation, Yield and Fracture of Polymers*, Churchill College, Cambridge, UK.

VAN DOMMELEN, J. A. W., BREKELMANS, W. A. M., and BAAIJENS, F. P. T. (2003f). Multiscale modeling of particle-modified semicrystalline polymers. In *Proceedings of the Second M.I.T. Conference on Computational Fluid and Solid Mechanics*, Cambridge, USA.

VAN DOMMELEN, J. A. W., BREKELMANS, W. A. M., and BAAIJENS, F. P. T. (2003g). A numerical investigation of the potential of rubber and mineral particles for toughening of semicrystalline polymers. *Computational Materials Science*. Accepted.

DOYLE, M. J. (2000). On the effect of crystallinity on the elastic properties of semicrystalline polyethylene. *Polymer Engineering and Science*, **40**, 330–335.

ELSNER, G., KEMPF, J., BARTHA, J. W., and WAGNER, H. H. (1990). Anisotropy of thermal expansion of thin polyimide films. *Thin Solid Films*, **185**, 189–197.

ESTEVEZ, R., TIJSSENS, M. G. A., and VAN DER GIESSEN, E. (2000). Modeling of the competition between shear yielding and crazing in glassy polymers. *Journal of the Mechanics and Physics of Solids*, **48**, 2585–2617.

EVERS, L. P., PARKS, D. M., BREKELMANS, W. A. M., and GEERS, M. G. D. (2001). Enhanced modeling of hardening in crystal plasticity for FCC metals. *Journal de Physique IV*, **11**, 179–186.

EVERS, L. P., PARKS, D. M., BREKELMANS, W. A. M., and GEERS, M. G. D. (2002). Crystal plasticity model with enhanced hardening by geometrically necessary dislocation accumulation. *Journal of the Mechanics and Physics of Solids*, **50**, 2403–2424.

FRIEDRICH, K. (1983). Crazes and shear bands in semi-crystalline thermoplastics. H.-H. KAUSCH (ed.). *Advances in Polymer Science*, **52/53**, 225–274. Springer-Verlag, Berlin.

FUKUI, T., KIKUCHI, Y., and INOUE, T. (1991). Elastic-plastic analysis of the toughening mechanism in rubber-modified nylon: matrix yielding and cavitation. *Polymer*, **32**, 2367–2371.

GALESKI, A., BARTCZAK, Z., ARGON, A. S., and COHEN, R. E. (1992). Morphological alterations during texture-producing plastic plane strain compression of high-density polyethylene. *Macromolecules*, **25**, 5705–5718.

GAUTAM, S., BALIJEPALLI, S., and RUTLEDGE, G. C. (2000). Molecular simulations of the interlamellar phase in polymers: effect of chain tilt. *Macromolecules*, **33**, 9136–9145.

GENT, A. N. and MADAN, S. (1989). Plastic yielding of partially crystalline polymers. *Journal of Polymer Science: Part B: Polymer Physics*, **27**, 1529–1542.

GROVES, W. G. and KELLY, A. (1963). Independent slip systems in crystals. *The Philosophical Magazine*, **8**, 877–887.

G'SELL, C. and DAHOUN, A. (1994). Evolution of microstructure in semi-crystalline polymers under large plastic deformation. *Materials Science and Engineering A*, **175**, 183–199.

G'SELL, C., HIVER, J. M., DAHOUN, A., and SOUAHI, A. (1992). Video-controlled tensile testing of polymers and metals beyond the necking point. *Journal of Materials Science*, **27**, 5031–5039.

HKS (2001). *ABAQUS/Standard User's Manual, version 6.2*. Hibbitt, Karlsson & Sorensen, Inc., Pawtucket, Rhode Island, USA.

HALL, R. (1991). Computer modelling of rubber-toughened plastics: random placement of monosized core-shell particles in a polymer matrix and interparticle distance calculations. *Journal of Materials Science*, **26**, 5631–5636.

HAY, I. L. and KELLER, A. (1965). Polymer deformation in terms of spherulites. *Kolloid-Zeitschrift und Zeitschrift für Polymere*, **204**, 43–74.

HILL, R. (1950). *The Mathematical Theory of Plasticity*. Oxford University Press, London.

HILL, R. (1972). On constitutive macro-variables for heterogeneous solids at finite strain. *Proceedings of the Royal Society of London A*, **326**, 131–147.

HISS, R., HOBEIKA, S., LYNN, S., and STROBL, G. (1999). Network stretching, slip processes, and fragmentation of crystallites during uniaxial drawing of polyethylene and related copolymers. A comparative study. *Macromolecules*, **32**, 4390–4403.

HOBEIKA, S., LYNN, C., MEN, Y., and STROBL, G. (2000). A general scheme for describing tensile deformations of polyethylenes, derived from video-controlled stretching tests and WAXS. In *Proceedings of the 11th International Conference on Deformation, Yield and Fracture of Polymers*, 83–86, Churchill College, Cambridge, UK.

HUTCHINSON, J. W. (1976). Bounds and self-consistent estimates for creep of polycrystalline materials. *Proceedings of the Royal Society of London A*, **348**, 101–127.

KAUSCH, H.-H., GENSLER, R., GREIN, CH., PLUMMER, C. J. G., and SCARAMUZZINO, P. (1999). Crazing in semicrystalline thermoplastics. *Journal of Macromolecular Science – Physics*, **B38**, 803–815.

KEITH, H. D. and PADDEN, F. J. (1959). Deformation mechanisms in crystalline polymers. *Journal of Polymer Science*, **41**, 525–528.

KELLER, A. and SAWADA, S. (1964). On the interior morphology of bulk polyethylene. *Die Makromolekulare Chemie*, **74**, 190–221.

KENNEDY, M. A., PEACOCK, A. J., and MANDELKERN, L. (1994). Tensile properties of crystalline polymers: linear polyethylene. *Macromolecules*, **27**, 5297–5310.

KIM, G.-M., LEE, D.-H., HOFFMANN, B., KRESSLER, J., and STÖPPELMANN, G. (2001). Influence of nanofillers on the deformation process in layered silicate/polyamide-12 nanocomposites. *Polymer*, **42**, 1095–1100.

KOBAYASHI, K. and NAGASAWA, T. (1966). Mechanical properties of polyethylene crystals. II. Deformation process of spherulite. *Journal of Polymer Science: Part C*, **15**, 163–183.

KOCKS, U. F., TOMÉ, C. N., and WENK, H.-R. (1998). *Texture and Anisotropy: Preferred Orientations in Polycrystals and their Effect on Materials Properties*. Cambridge University Press, Cambridge, UK.

KOUZNETSOVA, V. (2002). *Computational homogenization for the multi-scale analysis of multi-phase materials*. Ph.D. thesis, Eindhoven University of Technology, The Netherlands.

KOUZNETSOVA, V., BREKELMANS, W. A. M., and BAAIJENS, F. P. T. (2001). An approach to micro-macro modeling of heterogeneous materials. *Computational mechanics*, **27**, 37–48.

KOUZNETSOVA, V., GEERS, M. G. D., and BREKELMANS, W. A. M. (2002). Multi-scale constitutive modelling of heterogeneous materials with a gradient-enhanced computational homogenization scheme. *International Journal for Numerical Methods in Engineering*, **54**, 1235–1260.

KRAMER, E. J. (1983). Microscopic and molecular fundamentals of crazing. H.-H. KAUSCH (ed.). *Advances in Polymer Science*, **52/53**, 1–56. Springer-Verlag, Berlin.

LEE, B. J., PARKS, D. M., and AHZI, S. (1993a). Micromechanical modeling of large plastic deformation and texture evolution in semi-crystalline polymers. *Journal of the Mechanics and Physics of Solids*, **41**, 1651–1687.

LEE, B. J., ARGON, A. S., PARKS, D. M., AHZI, S., and BARTCZAK, Z. (1993b). Simulation of large strain plastic deformation and texture evolution in high density polyethylene. *Polymer*, **34**, 3555–3575.

LEE, B. J., AHZI, S., and ASARO, R. J. (1995). On the plasticity of low symmetry crystals lacking five independent slip systems. *Mechanics of Materials*, **20**, 1–8.

LEE, B. J., AHZI, S., and PARKS, D. M. (1999). Intermediate modeling of polycrystal plasticity. In *Proceedings of Plasticity '99: The Seventh International Symposium on Plasticity and its Current Applications*, Cancun, Mexico.

LEE, B. J., AHZI, S., and PARKS, D. M. (2002). Bicrystal-based modeling of plasticity in FCC Metals. *Journal of Engineering Materials and Technology*, **124**, 27–40.

LEE, E. H. (1969). Elastic-plastic deformation at finite strains. *Journal of Applied Mechanics: Transactions of the ASME*, **36**, 1–6.

LIN, L. and ARGON, A. S. (1994). Structure and plastic deformation of polyethylene. *Journal of Materials Science*, **29**, 294–323.

LOYENS, W. and GROENINCKX, G. (2002). Ultimate mechanical properties of rubber toughened semicrystalline PET at room temperature. *Polymer*, **43**, 5679–5691.

LOYENS, W. and GROENINCKX, G. (2003). Rubber toughened semicrystalline PET: influence of the matrix properties and test temperature. *Polymer*, **44**, 123–136.

MANDELKERN, L. and ALAMO, R. G. (1999). Polyethylene, linear high-density. J. E. MARK (ed.). *Polymer Data Handbook*, 493–507. Oxford University Press, New York.

MARGOLINA, A. and WU, S. (1988). Percolation model for brittle-tough transition in nylon/rubber blends. *Polymer*, **29**, 2170–2173.

VAN MELICK, H. G. H. (2002). *Deformation and failure of polymer glasses.* Ph.D. thesis, Eindhoven University of Technology, The Netherlands.

VAN MELICK, H. G. H., BRESSERS, O. F. J. T., DEN TOONDER, J. M. J., GOVAERT, L. E., and MEIJER, H. E. H. (2003). A micro-indentation method for probing the craze-initiation stress in glassy polymers. *Polymer*, **44**. Accepted.

MICHLER, G. H. (1999). Micromechanics of polymers. *Journal of Macromolecular Science – Physics*, **B38**, 787–802.

MICHLER, G. H. and GODEHARDT, R. (2000). Deformation mechanisms of semicrystalline polymers on the submicron scale. *Crystal Research and Technology*, **35**, 863–875.

VON MISES, R. (1928). Mechanik der plastischen Formänderung von Kristallen. *Zeitschrift für angewandte Mathematik und Mechanik*, **8**, 161–185.

MURATOĞLU, O. K., ARGON, A. S., and COHEN, R. E. (1995a). Crystalline morphology of polyamide-6 near planar surfaces. *Polymer*, **36**, 2143–2152.

MURATOĞLU, O. K., ARGON, A. S., COHEN, R. E., and WEINBERG, M. (1995b). Microstructural processes of fracture of rubber-modified polyamides. *Polymer*, **36**, 4771–4786.

MURATOĞLU, O. K., ARGON, A. S., and COHEN, R. E. (1995c). Toughening mechanism of rubber-modified polyamides. *Polymer*, **36**, 921–930.

NAM, P. H., MAITI, P., OKAMOTO, M., KOTAKA, T., HASEGAWA, N., and USUKI, A. (2001). A hierarchical structure and properties of intercalated polypropylene/clay nanocomposites. *Polymer*, **42**, 9633–9640.

NARISAWA, I. and ISHIKAWA, M. (1990). Crazing in semicrystalline thermoplastics. H.-H. KAUSCH (ed.). *Advances in Polymer Science*, **91/92**, 353–391. Springer-Verlag, Berlin.

NIKOLOV, S. and DOGHRI, I. (1998). Micro/macro modeling and simulation of polyethylene in small strains. In *Proceedings of the Fourth World Congress on Computational Mechanics*, Buenos Aires, Argentina.

NIKOLOV, S. and DOGHRI, I. (2000). A micro/macro constitutive model for the small-deformation behavior of polyethylene. *Polymer*, **41**, 1883–1891.

NIKOLOV, S., DOGHRI, I., PIERARD, O., ZEALOUK, L., and GOLDBERG, A. (2002). Multi-scale constitutive modeling of the small deformations of semi-crystalline polymers. *Journal of the Mechanics and Physics of Solids*, **50**, 2275–2302.

ORTIZ, M., REPETTO, E. A., and STAINIER, L. (2000). A theory of subgrain dislocation structures. *Journal of Mechanics and Physics of Solids*, **48**, 2077–2114.

PAN, S. J., IM, J., HILL, M. J., KELLER, A., HILTNER, A., and BAER, E. (1990). Structure of ultrathin polyethylene layers in multilayer films. *Journal of Polymer Science: Part B: Polymer Physics*, **28**, 1105–1119.

PARKS, D. M. and AHZI, S. (1990). Polycrystalline plastic deformation and texture evolution for crystals lacking five independent slip systems. *Journal of the Mechanics and Physics of Solids*, **38**, 701–724.

PEACOCK, A. J. (2000). *Handbook of Polyethylene: Structures, Properties, and Applications*. Marcel Dekker, New York.

PETERLIN, A. (1971). Molecular model of drawing polyethylene and polypropylene. *Journal of Molecular Science*, **6**, 490–508.

PETERMANN, J. (1996). Morphology in oriented semicrystalline polymers. S. FAKIROV (ed.). *Oriented Polymer Materials*, 167–183. Hütig & Wepf, Basel; Heidelberg; New York.

PETERMANN, J. and EBENER, H. (1999). On the micromechanics of plastic deformation in semicrystalline polymers. *Journal of Macromolecular Science – Physics*, **B38**, 837–846.

RAMSTEINER, F. and HECKMANN, W. (1985). Mode of deformation in rubber-modified polyamide. *Polymer Communications*, **200**, 199–200.

RYBNIKÁŘ, F. (1981). Interactions in the system polyethylene–solid filler. *Journal of Macromolecular Science – Physics*, **B19**, 1–11.

RYBNIKÁŘ, F. (1989). Orientation in Composite of Polypropylene and Talc. *Journal of Applied Polymer Science*, **38**, 1479–1490.

SACHS, G. (1928). Zur Ableitung einer Fließbedingung. *Zeitschrift des Vereines Deutscher Ingenieure*, **72**, 734–736.

SÁNCHEZ-SOLÍS, A., ESTRADA, M. R., CRUZ, J., and MANERO, O. (2000). On the properties and processing of polyethylene terephthalate/styrene-butadiene rubber blend. *Polymer Engineering and Science*, **40**, 1216–1225.

SARGENT, C. M. and SHINOZAKI, D. M. (1977). On the shape of stress-strain curves of polyethylene. *Scripta Metallurgica*, **11**, 401–404.

SCHIMANSKI, T. (2002). *High-performance polypropylene structures for eco-friendly, fully recyclable composites*. Ph.D. thesis, Eindhoven University of Technology, The Netherlands.

SCHOENFELD, S. E., AHZI, S., and ASARO, R. J. (1995). Elastic-plastic crystal mechanics for low symmetry crystals. *Journal of the Mechanics and Physics of Solids*, **43**, 415–446.

SCHRAUWEN, B. A. G. (2003). *Deformation and failure of semi-crystalline polymer systems: influence of micro and molecular structure*. Ph.D. thesis, Eindhoven University of Technology.

SCHRAUWEN, B. A. G., GOVAERT, L. E., and MEIJER, H. E. H. (2001a). Toughness of high-density polyethylene with hard filler particles. In *Proceedings of the Seventeenth Annual Meeting of the Polymer Processing Society*, Montreal, Canada.

SCHRAUWEN, B. A. G., GOVAERT, L. E., PETERS, G. W. M., and MEIJER, H. E. H. (2001b). The influence of flow induced crystallization on the impact toughness of high-density polyethylene. In *Proceedings of the International Conference on Flow Induced Crystallization of Polymers*, Salerno, Italy.

SCHRAUWEN, B. A. G., GOVAERT, L. E., PETERS, G. W. M., and MEIJER, H. E. H. (2002). The influence of flow-induced crystallization on the impact toughness of high-density polyethylene. *Macromolecular Symposia*, **185**, 89–102.

SMIT, R. J. M. (1998). *Toughness of heterogeneous polymeric systems: A modeling approach*. Ph.D. thesis, Eindhoven University of Technology, The Netherlands.

SMIT, R. J. M., BREKELMANS, W. A. M., and MEIJER, H. E. H. (1998). Prediction of the mechanical behavior of non-linear heterogeneous systems by multi-level finite element modeling. *Computer Methods in Applied Mechanics and Engineering*, **155**, 181–192.

SMIT, R. J. M., BREKELMANS, W. A. M., and MEIJER, H. E. H. (1999). Prediction of the large-strain mechanical response of heterogeneous polymer systems: local and global deformation behaviour of a representative volume element of voided polycarbonate. *Journal of the Mechanics and Physics of Solids*, **47**, 201–221.

SMIT, R. J. M., BREKELMANS, W. A. M., and MEIJER, H. E. H. (2000a). Predictive modelling of the properties and toughness of polymeric materials. Part I. Why is polystyrene brittle and polycarbonate tough? *Journal of Materials Science*, **35**, 2855–2867.

SMIT, R. J. M., BREKELMANS, W. A. M., and MEIJER, H. E. H. (2000b). Predictive modelling of the properties and toughness of polymeric materials. Part II. Effect of microstructural properties on the macroscopic response of rubber-modified polymers. *Journal of Materials Science*, **35**, 2869–2879.

SMIT, R. J. M., BREKELMANS, W. A. M., and MEIJER, H. E. H. (2000c). Predictive modelling of the properties and toughness of polymeric materials. Part III. Simultaneous prediction of micro- and macrostructural deformation of rubber-modified polymers. *Journal of Materials Science*, **35**, 2881–2892.

SOCRATE, S. and BOYCE, M. C. (2000). Micromechanics of toughened polycarbonate. *Journal of the Mechanics and Physics of Solids*, **48**, 233–275.

SOCRATE, S., BOYCE, M. C., and LAZZERI, A. (2001). A micromechanical model for multiple crazing in high impact polystyrene. *Mechanics of Materials*, **33**, 155–175.

STEENBRINK, A. C. and VAN DER GIESSEN, E. (1999). On cavitation, post-cavitation and yield in amorphous polymer–rubber blends. *Journal of the Mechanics and Physics of Solids*, **47**, 843–876.

TAYLOR, G. I. (1938). Plastic strain in metals. *Journal of the Institute of Metals*, **62**, 307–324.

THIO, Y. S., ARGON, A. S., COHEN, R. E., and WEINBERG, M. (2002). Toughening of isotactic polypropylene with $CaCO_3$ particles. *Polymer*, **43**, 3661–3674.

TIJSSENS, M. G. A., VAN DER GIESSEN, E., and SLUYS, L. J. (2000). Modeling of crazing using a cohesive surface methodology. *Mechanics of Materials*, **32**, 19–35.

TVERGAARD, V. (1996). Effect of void size difference on growth and cavitation instabilities. *Journal of the Mechanics and Physics of Solids*, **44**, 1237–1253.

TVERGAARD, V. (1998). Interaction of very small voids with larger voids. *International Journal of Solids and Structures*, **30**, 3989–4000.

TZIKA, P. A., BOYCE, M. C., and PARKS, D. M. (2000). Micromechanics of deformation in particle-toughened polyamides. *Journal of the Mechanics and Physics of Solids*, **48**, 1893–1930.

WANG, T. T. (1974). Morphology and mechanical properties of crystalline polymers. III. Deformation of spherulites in polyethylene. *Journal of Polymer Science: Polymer Physics Edition*, **12**, 145–158.

WEBER, G. G. (1988). *Computational procedures for a new class of finite deformation elastic-plastic constitutive equations*. Ph.D. thesis, Department of Mechanical Engineering, Massachusetts Institute of Technology, Cambridge, USA.

WILBRINK, M. W. L., ARGON, A. S., COHEN, R. E., and WEINBERG, M. (2001). Toughenability of nylon-6 with $CaCO_3$ filler particles: new findings and general principles. *Polymer*, **42**, 10155–10180.

WILCHINSKY, Z. W. (1964). Orientation in crystalline polymers related to deformation. *Polymer*, **5**, 271–281.

WU, S. (1985). Phase structure and adhesion in polymer blends: a criterion for rubber toughening. *Polymer*, **26**, 1855–1863.

WU, S. (1988). A generalized criterion for rubber toughening: the critical matrix ligament thickness. *Journal of Applied Polymer Science*, **35**, 549–561.

YOUNG, R. J. (1988). Screw dislocation model for yield in polyethylene. *Materials Forum*, **11**, 210–216.

YOUNG, R. J. and BOWDEN, P. B. (1974). Twinning and martensitic transformations in oriented high-density polyethylene. *The Philosophical Magazine*, **29**, 1061–1073.

ZUIDERDUIN, W. C. J., WESTZAAN, C., HUÉTINK, J., and GAYMANS, R. J. (2003). Toughening of polypropylene with calcium carbonate particles. *Polymer*, **44**, 261–275.

Samenvatting

Een veel gebruikte methode om de taaiheid van semi-kristallijne polymeren te verhogen, is het inmengen van rubberdeeltjes. Het huidige begrip van het onderliggende taaiheidsbevorderende mechanisme in deze semi-kristallijne materialen is gebaseerd op een criterium, dat stelt dat taai gedrag ontstaat indien de gemiddelde matrix-ligamentdikte tussen de deeltjes kleiner is dan een bepaalde kritische waarde. Deze waarde wordt beschouwd als een intrinsieke materiaaleigenschap en wordt toegekend aan dunne lagen van getranskristalliseerd materiaal in de microstructurele morfologie. De doelstelling van dit onderzoek is met behulp van numerieke methoden de invloed van de microstructuur op het microscopische, mesoscopische en macroscopische gedrag van deeltjesgemodificeerde semi-kristallijne materialen te onderzoeken, in het bijzonder het effect van lagen met een voorkeursoriëntatie.

De mogelijkheden van lokale anisotropie rondom gedispergeerde deeltjes voor het verbeteren van de materiaaleigenschappen worden onderzocht voor een geïdealiseerd materiaal uitgaande van anisotrope Hill-plasticiteit. Het systeem, bestaande uit matrixmateriaal met ingemengde rubberdeeltjes, wordt beschreven met een eindige elementen model van een representatief volume-element (RVE). Het systeem bevat een lengteparameter, gedefinieerd als de verhouding tussen de gemiddelde afstand tussen de deeltjes en een intrinsieke materiaal-karakteristieke afstand. Deze lengteparameter is in de berekeningen vertegenwoordigd door de aanwezigheid van een anisotrope laag met een specifieke dikte rondom de gedispergeerde deeltjes. De toepasbaarheid van verschillende typen RVE modellen voor deeltjesgemodificeerde semi-kristallijne materialen is onderzocht. Daarbij zijn driedimensionale simulaties als referentie gebruikt. De berekeningen tonen aan dat lokale anisotropie van het matrixmateriaal rondom de deeltjes gelokaliseerde deformatie vervangt door verdeelde plastische deformatie in afschuifbanden en de aard van de optredende hydrostatische spanningen verandert. Echter, om deze verbeteringen te bereiken, dient een microstructuur gerealiseerd te worden met voldoende mate van anisotropie. De effectiviteit van het taaiheidsmechanisme blijkt echter beperkt te worden door de aanwezigheid van harde deeltjes.

Om te onderzoeken of deze anisotropie bereikt kan worden met een getranskristalliseerde microstructuur, is een model voor het mechanische gedrag van semi-kristallijne materialen ontwikkeld, dat gebaseerd is op de onderliggende morfologie. De gevolgde procedure omvat analyses op drie niveau's. De constitutieve eigenschappen van het matrixmateriaal worden gekarakteriseerd op het microscopische niveau, waar de individuele kristallijne en amorfe fasen geïdentificeerd worden. Op het mesoscopische niveau wordt een aggregaat van individuele fasen beschouwd, zoals een sferuliet of een bundelvormige verzameling met voorkeursoriëntaties. Om de bijbehorende lengteschalen te overbruggen is een model met gelaagde bicomposiete inclusies geformuleerd. Iedere inclusie bestaat uit een kristallijn lamel, dat verondersteld wordt plastisch te deformeren door kristallografische slip en een amorfe laag. Een interactiemodel koppelt de lokale deformatie- en spanningsvelden van de inclusies aan de mesoscopische velden van het aggregaat. Uniaxiale compressie van initieel isotroop HDPE wordt gebruikt om het gedrag van diverse interactiemodellen te evalueren. Op basis van de evaluatie is een hybride interactiemodel gekozen, dat een compromis vormt tussen lokale compatibiliteit en lokaal evenwicht.

Een volledige overbrugging van micro–meso–macroniveau wordt verkregen door een verzameling van composiete inclusies in ieder integratiepunt van een macroscopisch eindige elementen model te gebruiken. Het meerschalige model is gebruikt om de mechanica van intraspherulitische deformatie van polyethyleen te simuleren. Tenslotte zijn meerschalige berekeningen uitgevoerd voor deeltjesgemodificeerd HDPE materiaal. Getranskristalliseerde oriëntaties laten een beperkt effect op het gedrag van de matrix zien. Verbeterde eigenschappen in een specifieke belastingsrichting worden verkregen voor een verondersteld alternatieve, gedeeltelijk stromingsgeïnduceerde, microstructuur.

Dankwoord / Acknowledgements

Hierbij wil ik allen die de afgelopen vier jaar betrokken zijn geweest bij mij en bij mijn werkzaamheden hartelijk danken. Een speciaal woord van dank gaat naar Marcel Brekelmans voor de begeleiding gedurende het gehele project en voor de bijdrage bij de totstandkoming van dit proefschrift. Zijn altijd kritische kijk op de zaken en zinvolle opmerkingen waren van grote waarde. Ook Frank Baaijens wil ik danken voor het vertrouwen dat hij altijd heeft getoond en voor het bieden van de mogelijkheid om dit onderzoek te verrichten. Hij was het die mij de kans heeft geboden om enige tijd te werken bij het Massachusetts Institute of Technology (MIT).

The period that I worked at the MIT has proven to be of vital importance for this research project. There, the foundations of this work were laid. Many thanks go to Mary Boyce and David Parks for putting the project on the right track. Many aspects of this work were based on their vision and ideas. Their enthousiasm and encouragements were always a great stimulation.

Marc Geers en Han Meijer dank ik voor de nuttige suggesties en de laatste correcties. Eveneens een woord van dank gaat naar Leon Govaert, Bernard Schrauwen en Lambert van Breemen voor de prettige samenwerking, en naar Leo Wouters en Patrick van Brakel voor hun ondersteuning.

De afgelopen jaren, ben ik steeds nauw betrokken geweest bij de “Metals Forming”-groep (what’s in a name?). Alle mensen daarvan dank ik hartelijk voor de immer plezierige werksfeer. Verder wil ik de *two brothers on the fourth floor*, Rens Evers en Roy Engelen, bedanken voor hun vriendschap. Als drie-eenheid hebben we samen veel meegemaakt, waardoor iedere dag weer de moeite waard was om naar Eindhoven te rijden. De periode die ik met Rens in Boston heb doorgebracht was onvergetelijk. Tevens wil ik onze overige kamergenoten in de loop der jaren, Ruchi Rastogi, Anita Mol en Marjolein van Lieshout, bedanken.

Als afwisseling van de dagelijkse geestelijke inspanning was de regelmatige sportieve in(/ont)spanning bij zowel H6 als het overheidsteam van vitaal belang. Daarvoor dank aan alle teamgenoten. Tenslotte, wil ik mijn familie bedanken voor alle steun en vertrouwen...

Hans van Dommelen,
Eindhoven, februari 2003.

Curriculum Vitae

Hans van Dommelen was born on October 14, 1975 in Eindhoven, The Netherlands. In 1994, he finished his secondary education at the Carolus Borromeus College in Helmond. From 1994 until 1999 he studied Mechanical Engineering at the Eindhoven University of Technology. During his study, he did a traineeship at Philips Research in Eindhoven, and became interested in the field of micromechanics of materials. He received his master's degree in 1999 on the subject of computational polymer crystal plasticity. In that year he started his Ph.D. research on the micromechanics of semicrystalline polymers, as a part of the Dutch Polymer Institute (DPI) program, in the Materials Technology group of the Eindhoven University of Technology. Part of this research was conducted at the Department of Mechanical Engineering of the Massachusetts Institute of Technology (MIT) in Cambridge, USA.